Position Estimation for PMSMs at Any Speed Using the Zero-Sequence Voltage and Modified Space Vector Modulation

Dissertation zur Erlangung des Grades des Doktors der Ingenieurwissenschaften der Naturwissenschaftlich-Technischen Fakultät der Universität des Saarlandes

von
Klaus Schuhmacher

Saarbrücken
2022

Tag des Kolloquiums:	05.10.2022
Dekan:	Prof. Dr. Jörn Erik Walter
Berichterstatter:	Prof. Dr.-Ing. Matthias Nienhaus Juniorprof. Dr. Gianluca Rizzello
Vorsitz:	Prof. Dr.-Ing. Michael Vielhaber
Akad. Beisitzer:	Dr. Michael Roland

Preface

The following thesis has been written during my time as a Doctoral Researcher at the Laboratory of Actuation Technology (LAT) at the Universität des Saarlandes. I would like to thank my supervisor Prof. Dr. Matthias Nienhaus and all of my current and former colleages at the LAT for the fruitful collaborations and discussions.

Special thanks go to a handful of people whose work helped to make possible or facilitate the preparation and conduction of the experimental investigations. Stephan Kleen designed the custom motor that was used in many of the experiments in this thesis. He also put into operation the real-time control for the used motor test bench and prepared the automated test cycles. Daniel Merl contributed a large part to the development of the custom motor control board used in this thesis. A software for data acquisition and visualization from Dr. Emanuele Grasso and Niklas König helped significantly to gather real-time data from the custom motor control board in an efficient and comfortable way.

The final thanks goes to my girlfriend Kristin Stoffel, for her continued love and support.

Klaus Schuhmacher

Abstract

Anisotropy-based estimation techniques enable position and speed estimation for synchronous and induction machines down to low speeds and standstill. One possible approach consists of exciting the machine with special pulse patterns and measuring the zero-sequence voltage which requires access to the neutral point of a star-connected machine but can in return enable high signal-to-noise ratios. This thesis focuses in particular on permanent magnet synchronous machines and aims to contribute to the understanding of fundamental relations through a mathematical analysis of the underlying anisotropy information as well as to practical aspects that include initial polarity detection, usable pulse patterns and investigations on certain non-ideal effects which real machines exhibit. Experimentally achieved estimation results using real machines are presented, which demonstrate in particular low noise content and little dependence on rotor speed.

Kurzfassung

Anisotropiebasierte Schätzverfahren ermöglichen Positions- und Drehzahlschätzung für Synchron- und Induktionsmaschinen bis hin zu niedrigen Drehzahlen und Stillstand. Ein möglicher Ansatz besteht darin, die Maschine mit speziellen Pulsmustern anzuregen und die Nullspannung zu messen, was den Zugang zum Sternpunkt einer im Stern verschalteten Maschine erfordert, dafür aber hohe Signal-Rausch-Verhältnisse ermöglichen kann. Diese Arbeit konzentriert sich insbesondere auf Permanentmagnet-Synchronmaschinen und möchte durch eine mathematische Analyse der zugrundeliegenden Anisotropie-Information zum Verständnis grundlegender Zusammenhänge beitragen sowie zu praktischen Aspekten, darunter die Erkennung der anfänglichen Polarität, verwendbare Pulsmuster und Untersuchungen zu bestimmten nicht-idealen Effekten, welche bei realen Maschinen auftreten. Es werden experimentell erzielte Ergebnisse der Schätzung bei realen Maschinen vorgestellt, die insbesondere einen geringen Rauschanteil und eine geringe Abhängigkeit von der Rotordrehzahl aufzeigen.

Contents

1. Introduction

1.1. Motivation

Permanent magnet synchronous machines (PMSMs) are known for their favorable properties concerning dynamic behavior, efficiency and power density. Previously used in particular in high-performance industry applications such as machine tools and robotics, they are becoming increasingly widespread in a broad range of applications that include traction and automotive applications, electrical mobility, more electric aircraft, renewable power generation, and home appliances [BCC+14], with particular interest in the lower power ranges.

In a modern electrical drive, PMSMs are typically controlled via field-oriented control, independently controlling the current in the direction of the permanent magnet flux and in the direction orthogonal to that, commonly known as the axes 'd' and 'q'. To perform the coordinate transformations required for this, the rotor position must be known at all times. Additionally, knowledge of the rotor speed is required to decouple the current control in the two axes and, of course, for use in a superordinate speed control loop. In conventional drives, the position and speed information is obtained through the use of position sensors, such as optical or magnetic encoders or resolvers. "Sensorless control" aims to replace such sensors by techniques that estimate the position using only measurements of currents and/or voltages associated with the machine. Possible benefits of sensorless control are reduction of size and cost of the overall electrical drive system. In addition to the size and cost of the position sensor itself, its cabling and installation also contribute to the overall expenses, which sensorless techniques aim to eliminate. Another benefit can be an increase of reliability due to the omission of the position sensor or because sensorless control can be used as a backup mechanism in case of sensor failure.

There exists a wide variety of sensorless techniques in the scientific literature. In the last three decades, research works have concentrated on anisotropy-based techniques. The terms saliency-based or signal-injection-based are often used with the same meaning. Anisotropy-based techniques allow to extend position estimation into the low speed

region down to standstill, where previous methods had failed. The focus of this thesis lies on anisotropy-based position estimation for PMSMs using the zero-sequence voltage, which is measurable by accessing a machine's neutral point. Compared to the more common techniques which use current measurements, measurements of the zero-sequence voltage have the potential to provide anisotropy signals with higher signal-to-noise ratios. Furthermore, this work focuses on an excitation of the machine through the discrete voltage vectors that are applied by the switching inverter. This offers a large transient excitation and is realized by means of modified space vector modulation. It also enables a direct calculation of the estimated position and does not require the use of analogous bandpass filters like in approaches that rely on an injection of sinusoidal signals.

1.2. Contributions

At the beginning it should be emphasized that the general approach of estimating the position based on measurements of the zero-sequence voltage during certain switching states of the inverter and a direct position calculation has already been described in a few other scientific works, both for PMSMs and induction machines. Therefore, it is not a new contribution of this work. Instead, the following points are considered to be essential contributions of this thesis:

1. A comprehensive and thoughtful mathematical analysis of the anisotropy information available in the zero-sequence voltage is presented. One example concerns the reference frame used. While zero-sequence voltage based techniques were usually modeled in the 'abc' reference frame, the '$\alpha\beta0$' reference frame is extensively used in this thesis, which in many occasions leads to more descriptive equations. It also enables basic comparisons of the available anisotropy information with the one that can be obtained via current measurements, since current-based techniques are almost exclusively modeled in the '$\alpha\beta$' or 'dq' frame.

2. A computationally efficient function for position calculation, which does not neglect harmonic components that are systematically created in the inductance ratios for the most commonly assumed anisotropy model, is given.

3. A thorough investigation on five different modified modulation strategies suitable for the pursued estimation approach is conducted. Investigated aspects include the respective reduction in achievable voltage vector magnitudes, the introduction of

harmonics in the line-to-line voltages and differences in the estimation results. The investigations include two novel strategies that employ only a minimum number of voltage vectors for measurements and that have favorable properties.

4. The possibility of capacitive coupling of external disturbances onto the neutral point is discussed and demonstrated on a real motor. To the knowledge of the author, the effect has not been described so far, but appropriate countermeasures like grounding or isolating the motor showed to be an important aspect in ensuring reliable estimation results.

5. A novel procedure for initial polarity detection is described. Unlike previous approaches, it evaluates the magnitude of the inductance ratio vector obtained through zero-sequence voltage measurements. Since it uses the same anisotropy information as the position estimation method looked at here, it can easily be combined with it and also benefits from the high signal-to-noise ratio.

6. Experimental results for a custom prototype PMSM and a commercially available PMSM are presented, allowing an assessment of the characteristics of the considered estimation technique and showing dependencies on speed and currents.

1.3. Outline

This thesis is structured as follows. In chapter 2, the stationary and rotating reference frames as well as a simplified machine and inverter model are defined. In chapter 3, the physical background and a state of the art of sensorless control techniques using magnetic anisotropy information is presented. The anisotropy information that is available in the zero-sequence voltage is analyzed in general and for particular special cases of a fundamental wave inductance model in chapter 4. Additionally, comparisons to the anisotropy information available via current measurements are drawn and parasitic capacitive effects that affect the measurement of the zero-sequence voltage are discussed. Chapter 5 covers the estimation of the position from the acquired anisotropy information and discusses the effects of magnetic saturation and secondary anisotropies. The procedure for initial polarity detection is also described there. In chapter 6, the different possibilities for modifying the space vector modulation in favor of the estimation technique are discussed and compared. After that, experimental results for one selected modulation strategy are presented in chapter 7. Finally, the work is rounded off with a conclusion.

2. Machine and Inverter Model

2.1. Reference Frames

When modeling three-phase electrical machines, different coordinate systems are typically used to obtain advantageous mathematical representations. In the following, the reference frames used throughout this work and the transformation matrices between these are defined.

The 'abc' frame is the physical coordinate system that is directly related to the physical quantities in the three phases 'a', 'b' and 'c', such as voltages, currents and flux linkages. These phase quantities can be transformed into a reference frame with two orthogonal axes 'α' and 'β' and a so-called zero-sequence axis denoted with '0'. This transformation of a vector of phase quantities $\boldsymbol{x}$ is well-known as the Clarke transform. It is defined in its amplitude invariant matrix form by

$$\underbrace{\begin{bmatrix} x_\alpha \\ x_\beta \\ x_0 \end{bmatrix}}_{\boldsymbol{x}^\mathrm{s}} = \underbrace{\begin{bmatrix} \frac{2}{3} & -\frac{1}{3} & -\frac{1}{3} \\ 0 & \frac{1}{\sqrt{3}} & -\frac{1}{\sqrt{3}} \\ \frac{1}{3} & \frac{1}{3} & \frac{1}{3} \end{bmatrix}}_{\boldsymbol{T}_\mathrm{C}} \underbrace{\begin{bmatrix} x_\mathrm{a} \\ x_\mathrm{b} \\ x_\mathrm{c} \end{bmatrix}}_{\boldsymbol{x}^\mathrm{p}} \tag{2.1}$$

with the inverse transformation

$$\underbrace{\begin{bmatrix} x_\mathrm{a} \\ x_\mathrm{b} \\ x_\mathrm{c} \end{bmatrix}}_{\boldsymbol{x}^\mathrm{p}} = \underbrace{\begin{bmatrix} 1 & 0 & 1 \\ -\frac{1}{2} & \frac{\sqrt{3}}{2} & 1 \\ -\frac{1}{2} & -\frac{\sqrt{3}}{2} & 1 \end{bmatrix}}_{\boldsymbol{T}_\mathrm{C}^{-1}} \underbrace{\begin{bmatrix} x_\alpha \\ x_\beta \\ x_0 \end{bmatrix}}_{\boldsymbol{x}^\mathrm{s}} \tag{2.2}$$

where

$$\boldsymbol{T}_\mathrm{C}\boldsymbol{T}_\mathrm{C}^{-1} = \boldsymbol{T}_\mathrm{C}^{-1}\boldsymbol{T}_\mathrm{C} = \boldsymbol{I} \ . \tag{2.3}$$

In the last equation, $\boldsymbol{I}$ is the 3x3 identity matrix. As is visible in (2.1), the zero-sequence

Table 2.1.: Reference frames.

Reference frame		Components	Matrices	Vectors
stationary, general	-	-	$\boldsymbol{X}$	$\boldsymbol{x}$
stationary, physical	-	a, b, c	$\boldsymbol{X}^{\mathrm{p}}$	$\boldsymbol{x}^{\mathrm{p}}$
stationary, orthogonal	full	α, β, 0	$\boldsymbol{X}^{\mathrm{s}}$	$\boldsymbol{x}^{\mathrm{s}}$
	reduced	α, β	$\boldsymbol{X}^{\mathrm{s*}}$	$\boldsymbol{x}^{\mathrm{s*}}$
rotating	full	d, q, 0	$\boldsymbol{X}^{\mathrm{r}}$	$\boldsymbol{x}^{\mathrm{r}}$
	reduced	d, q	$\boldsymbol{X}^{\mathrm{r*}}$	$\boldsymbol{x}^{\mathrm{r*}}$

component provides the mean value of a vector's components in the physical reference frame:

$$x_0 = \frac{1}{3}\left(x_{\mathrm{a}} + x_{\mathrm{b}} + x_{\mathrm{c}}\right) \ . \tag{2.4}$$

In symmetric three-phase systems, the zero-sequence components of both the phase voltages and the phase currents are zero, allowing for a reduction of the vectors to two dimensions without loss of information. In most cases, the zero-sequence components are also simply not of interest. The approach pursued in this thesis, however, explicitly uses the zero-sequence voltage, i.e. the mean of the phase voltages in the 'abc' reference frame:

$$u_0 = \frac{1}{3}\left(u_{\mathrm{a}} + u_{\mathrm{b}} + u_{\mathrm{c}}\right) \ . \tag{2.5}$$

Therefore, the zero-sequence axis must be included in the electrical machine model.

When working with vectors and matrices, superscripts will be used to denote the coordinate system in which quantities are expressed according to Table 2.1. When the zero-sequence axis is omitted, the reduced vector or matrix is additionally denoted with an asterisk. The components of vectors and matrices are denoted with a respective subscript. A superscript is not given for the scalar components of vectors and matrices to avoid redundant information and to streamline the equations. In some occasions, a vector without superscript will be used to generally refer to a vector or matrix in a stationary frame.

In stationary operation, the voltages, currents and flux linkages in a balanced synchronous machine are typically symmetrical sinusoidal quantities. They form three-phase systems rotating at the same frequency as the so-called 'electrical rotor angle' φ, which is related to the mechanical rotor angle φ_{m} via the number of pole pairs, p:

$$\varphi = p\varphi_{\mathrm{m}} \ . \tag{2.6}$$

By moving to a coordinate system that rotates synchronously to the rotor, these quantities become approximately constant. In the case of PMSMs, the axes of this rotating coordinate system are the direct axis 'd' and the quadrature axes 'q'. They are obtained by rotating the α- and β-axes by φ, so that the d-axis is aligned with the flux of the permanent magnets, as shown in Fig. 2.1. The representation in d- and q-coordinates are the basis of field-oriented control that is widely used in modern drive systems. The transformation is performed with a rotation matrix known as the Park transform:

$$\underbrace{\begin{bmatrix} x_\mathrm{d} \\ x_\mathrm{q} \\ x_0 \end{bmatrix}}_{\boldsymbol{x}^\mathrm{r}} = \underbrace{\begin{bmatrix} \cos(\varphi) & \sin(\varphi) & 0 \\ -\sin(\varphi) & \cos(\varphi) & 0 \\ 0 & 0 & 1 \end{bmatrix}}_{\boldsymbol{T}_\mathrm{P}(\varphi)} \underbrace{\begin{bmatrix} x_\alpha \\ x_\beta \\ x_0 \end{bmatrix}}_{\boldsymbol{x}^\mathrm{s}} \tag{2.7}$$

$$\underbrace{\begin{bmatrix} x_\alpha \\ x_\beta \\ x_0 \end{bmatrix}}_{\boldsymbol{x}^\mathrm{s}} = \underbrace{\begin{bmatrix} \cos(\varphi) & -\sin(\varphi) & 0 \\ \sin(\varphi) & \cos(\varphi) & 0 \\ 0 & 0 & 1 \end{bmatrix}}_{\boldsymbol{T}_\mathrm{P}^{-1}(\varphi)} \underbrace{\begin{bmatrix} x_\mathrm{d} \\ x_\mathrm{q} \\ x_0 \end{bmatrix}}_{\boldsymbol{x}^\mathrm{r}} \tag{2.8}$$

$$\boldsymbol{T}_\mathrm{P}(\varphi)\boldsymbol{T}_\mathrm{P}^{-1}(\varphi) = \boldsymbol{T}_\mathrm{P}{}^{-1}(\varphi)\boldsymbol{T}_\mathrm{P}(\varphi) = \boldsymbol{I}\ . \tag{2.9}$$

Note that the zero-sequence component remains unchanged in this transformation.

Because the rotor position changes with time, the rotation matrix is time-dependent. The time derivative of the rotation matrix and its inverse are

$$\frac{\mathrm{d}}{\mathrm{d}t}\boldsymbol{T}_\mathrm{P}(\varphi) = \omega \begin{bmatrix} -\sin(\varphi) & \cos(\varphi) & 0 \\ -\cos(\varphi) & -\sin(\varphi) & 0 \\ 0 & 0 & 0 \end{bmatrix} = \omega \begin{bmatrix} 0 & 1 & 0 \\ -1 & 0 & 0 \\ 0 & 0 & 0 \end{bmatrix} \boldsymbol{T}_\mathrm{P}(\varphi) = \omega \boldsymbol{J}\boldsymbol{T}_\mathrm{P}(\varphi) \tag{2.10}$$

and

$$\frac{\mathrm{d}}{\mathrm{d}t}\boldsymbol{T}_\mathrm{P}^{-1}(\varphi) = \omega \begin{bmatrix} -\sin(\varphi) & -\cos(\varphi) & 0 \\ \cos(\varphi) & -\sin(\varphi) & 0 \\ 0 & 0 & 0 \end{bmatrix} = \omega \begin{bmatrix} 0 & -1 & 0 \\ 1 & 0 & 0 \\ 0 & 0 & 0 \end{bmatrix} \boldsymbol{T}_\mathrm{P}^{-1}(\varphi) = \omega \boldsymbol{J}^\mathrm{T}\boldsymbol{T}_\mathrm{P}^{-1}(\varphi) \tag{2.11}$$

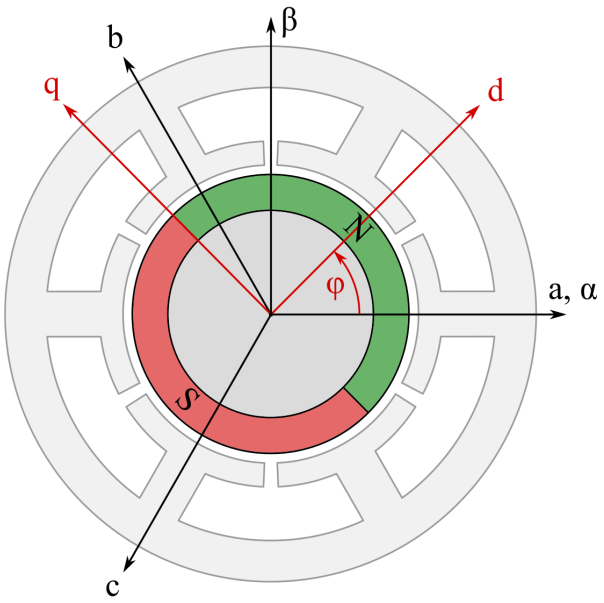

Figure 2.1.: Reference Frames in a PMSM.

with the clockwise 90° rotation matrix $\boldsymbol{J}$ and its transposed matrix $\boldsymbol{J}^{\mathrm{T}}$

$$\boldsymbol{J} = \begin{bmatrix} 0 & 1 & 0 \\ -1 & 0 & 0 \\ 0 & 0 & 0 \end{bmatrix}, \quad \boldsymbol{J}^{\mathrm{T}} = \begin{bmatrix} 0 & -1 & 0 \\ 1 & 0 & 0 \\ 0 & 0 & 0 \end{bmatrix} \tag{2.12}$$

and with the electrical angular frequency

$$\omega = \frac{\mathrm{d}}{\mathrm{d}t}\varphi \, . \tag{2.13}$$

2.2. Electrical Model

2.2.1. Stationary Coordinates

This work assumes a three-phase star-connected PMSM with accessible neutral point that is supplied by a three-phase two-level switching inverter as shown in Fig. 2.2. The voltages at the machine terminals and at the neutral point are expressed with reference to the negative rail of the DC link. The phase voltages of the machine are the difference

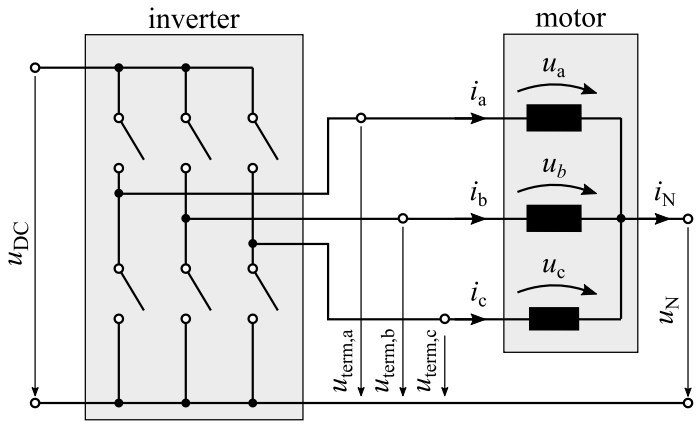

Figure 2.2.: Voltages and currents for a three-phase star-connected motor that is connected to a switching inverter.

between the voltages at the machine terminals and the neutral point:

$$\begin{aligned} u_a &= u_{term,a} - u_N \\ u_b &= u_{term,b} - u_N \\ u_c &= u_{term,c} - u_N \ . \end{aligned} \tag{2.14}$$

In vectorial notation, these equations can be expressed by

$$\boldsymbol{u}^p = \boldsymbol{u}^p_{term} - u_N \begin{bmatrix} 1 \\ 1 \\ 1 \end{bmatrix} \tag{2.15}$$

where

$$\boldsymbol{u}^p = \begin{bmatrix} u_a \\ u_b \\ u_c \end{bmatrix}, \quad \boldsymbol{u}^p_{term} = \begin{bmatrix} u_{term,a} \\ u_{term,b} \\ u_{term,c} \end{bmatrix} \ . \tag{2.16}$$

Transforming (2.15) with the Clarke transform leads to

$$\boldsymbol{T}_\mathrm{C}\boldsymbol{u}^\mathrm{p} = \boldsymbol{T}_\mathrm{C}\boldsymbol{u}^\mathrm{p}_\mathrm{term} - u_\mathrm{N}\boldsymbol{T}_\mathrm{C}\begin{bmatrix}1\\1\\1\end{bmatrix} \tag{2.17}$$

$$\boldsymbol{u}^\mathrm{s} = \boldsymbol{u}^\mathrm{s}_\mathrm{term} - u_\mathrm{N}\begin{bmatrix}0\\0\\1\end{bmatrix} \tag{2.18}$$

with

$$\boldsymbol{u}^\mathrm{s} = \begin{bmatrix}u_\alpha\\u_\beta\\u_0\end{bmatrix},\ \boldsymbol{u}^\mathrm{s}_\mathrm{term} = \begin{bmatrix}u_{\mathrm{term},\alpha}\\u_{\mathrm{term},\beta}\\u_{\mathrm{term},0}\end{bmatrix} = \begin{bmatrix}u_\alpha\\u_\beta\\u_{\mathrm{term},0}\end{bmatrix}\ . \tag{2.19}$$

The α- and β-components are identical for $\boldsymbol{u}^\mathrm{s}$ and $\boldsymbol{u}^\mathrm{s}_\mathrm{term}$. The zero-sequence voltage u_0 however is the difference between the mean voltage applied at the machine terminals and the neutral point voltage:

$$u_0 = \frac{1}{3}\left(u_\mathrm{a} + u_\mathrm{b} + u_\mathrm{c}\right) \tag{2.20}$$

$$= u_{\mathrm{term},0} - u_\mathrm{N}\ . \tag{2.21}$$

Or, if expressed the other way, u_N differs from the mean voltage applied at the terminals by the zero-sequence voltage:

$$u_\mathrm{N} = u_{\mathrm{term},0} - u_0\ . \tag{2.22}$$

When the neutral point is left open or is measured with high impedance, no current can flow through it so that the zero-sequence current in a star-connected machine must always be zero:

$$i_0 = \frac{1}{3}i_\mathrm{N} = \frac{1}{3}\left(i_\mathrm{a} + i_\mathrm{b} + i_\mathrm{c}\right) = \frac{1}{3}\begin{bmatrix}1 & 1 & 1\end{bmatrix}\boldsymbol{i}^\mathrm{p} = 0 \tag{2.23}$$

$$\boldsymbol{i}^\mathrm{p} = \begin{bmatrix}i_\mathrm{a}\\i_\mathrm{b}\\i_\mathrm{c}\end{bmatrix}\ . \tag{2.24}$$

For the zero-sequence voltage u_0, this is however not generally true. It can be different from zero when the machine is not symmetric, for example due to differing inductances that are the core of anisotropy-based approaches. The exact conditions will be analyzed

in chapter 4.

The electrical part of a three-phase synchronous machine is described by the following equation, where $\boldsymbol{u}$ is the vector of the phase voltages, $\boldsymbol{R}$ is the resistance matrix, $\boldsymbol{i}$ is the vector of the phase currents[1] and $\boldsymbol{\Psi}$ is the vector of the phases' flux linkages:

$$\boldsymbol{u} = \boldsymbol{R}\boldsymbol{i} + \frac{\mathrm{d}}{\mathrm{d}t}\boldsymbol{\Psi} \ . \tag{2.25}$$

In the 'abc' coordinate system we obtain

$$\begin{bmatrix} u_\mathrm{a} \\ u_\mathrm{b} \\ u_\mathrm{c} \end{bmatrix} = \boldsymbol{R} \begin{bmatrix} i_\mathrm{a} \\ i_\mathrm{b} \\ i_\mathrm{c} \end{bmatrix} + \frac{\mathrm{d}}{\mathrm{d}t} \begin{bmatrix} \Psi_\mathrm{a} \\ \Psi_\mathrm{b} \\ \Psi_\mathrm{c} \end{bmatrix} \ . \tag{2.26}$$

The resistance matrix is assumed constant and diagonal in the physical reference frame:

$$\boldsymbol{R}^\mathrm{p} = \begin{bmatrix} R_\mathrm{a} & 0 & 0 \\ 0 & R_\mathrm{b} & 0 \\ 0 & 0 & R_\mathrm{c} \end{bmatrix} \ . \tag{2.27}$$

In a permanent magnet synchronous machine such as the exemplary machine in Fig. 2.3, both the rotor magnets and the currents in the stator coils contribute to the flux linkage vector. Accordingly, the flux linkages are a function of both the position and the currents, but also depend on previous magnetization due to magnetic hysteresis. Under the simplifying assumption of linear superposition however, the total flux linkage vector is usually separated into the flux linkages caused by the permanent magnets and those caused by the currents in the stator inductances.

$$\boldsymbol{\Psi}(\varphi, \boldsymbol{i}) = \boldsymbol{\Psi}_\mathrm{PM}(\varphi) + \boldsymbol{\Psi}_\mathrm{s}(\varphi) \tag{2.28}$$

$$= \boldsymbol{\Psi}_\mathrm{PM}(\varphi) + \boldsymbol{L}(\varphi)\,\boldsymbol{i} \ . \tag{2.29}$$

The inductance matrix $\boldsymbol{L}$ is considered as a symmetrical and invertible matrix. Further, it is assumed here to be only position-dependent. The nonlinear and hysteretic behavior are, at least at this point, neglected to obtain a model that can be used for analyzing fundamental relations. Generally, the basic principle of most estimation techniques is

[1] It should be noted that in a star-connected machine, the phase currents are identical to the line currents, i.e. the currents flowing from the switching nodes of the inverter to the motor terminals. Therefore, no distinction between these is necessary.

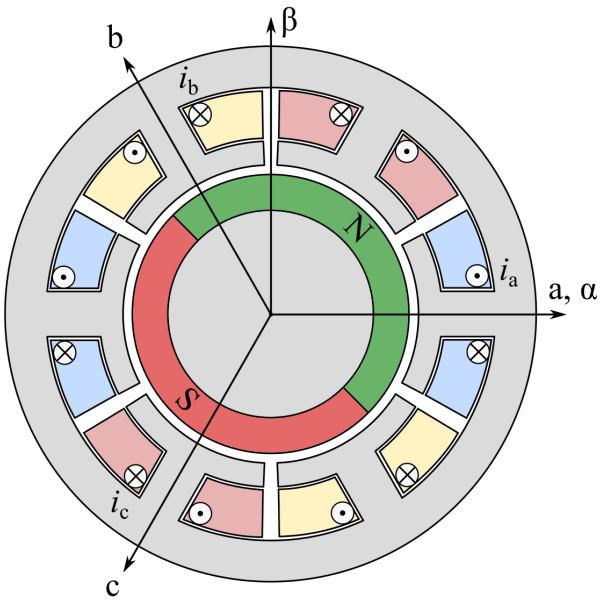

Figure 2.3.: Schematic cross-section of a two-pole permanent magnet synchronous machine with three phases a, b, c and surface mounted magnets.

based on simplified models to allow wide applicability to different machines. In practice, the inductance matrix is particularly current-dependent which needs to be considered for operation under (varying) load conditions, therefore this aspect will be brought up again in section 5.2 and in chapter 7.

Inserting (2.29) into (2.25), we obtain

$$\boldsymbol{u} = \boldsymbol{R}\boldsymbol{i} + \frac{\mathrm{d}}{\mathrm{d}t}\left(\boldsymbol{L}\left(\varphi\right)\boldsymbol{i}\right) + \frac{\mathrm{d}}{\mathrm{d}t}\boldsymbol{\Psi}_{\mathrm{PM}}\left(\varphi\right) \tag{2.30}$$

$$= \boldsymbol{R}\boldsymbol{i} + \boldsymbol{L}\left(\varphi\right)\left(\frac{\mathrm{d}}{\mathrm{d}t}\boldsymbol{i}\right) + \left(\frac{\mathrm{d}}{\mathrm{d}t}\boldsymbol{L}\left(\varphi\right)\right)\boldsymbol{i} + \frac{\mathrm{d}}{\mathrm{d}t}\boldsymbol{\Psi}_{\mathrm{PM}}\left(\varphi\right) \ . \tag{2.31}$$

In the physical coordinates 'abc', the equation is written as

$$\boldsymbol{u}^{\mathrm{p}} = \boldsymbol{R}^{\mathrm{p}}\boldsymbol{i}^{\mathrm{p}} + \boldsymbol{L}^{\mathrm{p}}\left(\varphi\right)\left(\frac{\mathrm{d}}{\mathrm{d}t}\boldsymbol{i}^{\mathrm{p}}\right) + \left(\frac{\mathrm{d}}{\mathrm{d}t}\boldsymbol{L}^{\mathrm{p}}\left(\varphi\right)\right)\boldsymbol{i}^{\mathrm{p}} + \frac{\mathrm{d}}{\mathrm{d}t}\boldsymbol{\Psi}^{\mathrm{p}}_{\mathrm{PM}}\left(\varphi\right) \tag{2.32}$$

$$\begin{bmatrix} u_{\mathrm{a}} \\ u_{\mathrm{b}} \\ u_{\mathrm{c}} \end{bmatrix} = \boldsymbol{R}^{\mathrm{p}} \begin{bmatrix} i_{\mathrm{a}} \\ i_{\mathrm{b}} \\ i_{\mathrm{c}} \end{bmatrix} + \boldsymbol{L}^{\mathrm{p}}\left(\varphi\right)\left(\frac{\mathrm{d}}{\mathrm{d}t}\begin{bmatrix} i_{\mathrm{a}} \\ i_{\mathrm{b}} \\ i_{\mathrm{c}} \end{bmatrix}\right) + \left(\frac{\mathrm{d}}{\mathrm{d}t}\boldsymbol{L}^{\mathrm{p}}\left(\varphi\right)\right)\begin{bmatrix} i_{\mathrm{a}} \\ i_{\mathrm{b}} \\ i_{\mathrm{c}} \end{bmatrix} + \frac{\mathrm{d}}{\mathrm{d}t}\begin{bmatrix} \Psi_{\mathrm{PM,a}}\left(\varphi\right) \\ \Psi_{\mathrm{PM,b}}\left(\varphi\right) \\ \Psi_{\mathrm{PM,c}}\left(\varphi\right) \end{bmatrix} \ . \tag{2.33}$$

In the inductance matrix

$$\boldsymbol{L}^{\mathrm{p}}(\varphi) = \begin{bmatrix} L_{\mathrm{aa}}(\varphi) & L_{\mathrm{ab}}(\varphi) & L_{\mathrm{ca}}(\varphi) \\ L_{\mathrm{ab}}(\varphi) & L_{\mathrm{bb}}(\varphi) & L_{\mathrm{bc}}(\varphi) \\ L_{\mathrm{ca}}(\varphi) & L_{\mathrm{bc}}(\varphi) & L_{\mathrm{cc}}(\varphi) \end{bmatrix} \tag{2.34}$$

inductances with equal subscripts denote self-inductances, whereas inductances with different subscripts denote mutual inductances.

For reasons of readability, the position dependencies will no longer be explicitly stated in the further course of this work.

By splitting the derivative of the inductance matrix and the flux linkage vector in (2.33) into derivatives with respect to the position and derivatives of the position with respect to time, the electrical rotor speed $\omega = \mathrm{d}\varphi/\mathrm{d}t$ can be factored out:

$$\boldsymbol{u}^{\mathrm{p}} = \boldsymbol{R}^{\mathrm{p}}\boldsymbol{i}^{\mathrm{p}} + \boldsymbol{L}^{\mathrm{p}}\left(\frac{\mathrm{d}}{\mathrm{d}t}\boldsymbol{i}^{\mathrm{p}}\right) + \left(\frac{\mathrm{d}\varphi}{\mathrm{d}t}\frac{\mathrm{d}}{\mathrm{d}\varphi}\boldsymbol{L}^{\mathrm{p}}\right)\boldsymbol{i}^{\mathrm{p}} + \frac{\mathrm{d}\varphi}{\mathrm{d}t}\frac{\mathrm{d}}{\mathrm{d}\varphi}\boldsymbol{\Psi}^{\mathrm{p}}_{\mathrm{PM}} \tag{2.35}$$

$$= \boldsymbol{R}^{\mathrm{p}}\boldsymbol{i}^{\mathrm{p}} + \boldsymbol{L}^{\mathrm{p}}\left(\frac{\mathrm{d}}{\mathrm{d}t}\boldsymbol{i}^{\mathrm{p}}\right) + \omega \cdot \left(\left(\frac{\mathrm{d}}{\mathrm{d}\varphi}\boldsymbol{L}^{\mathrm{p}}\right)\boldsymbol{i}^{\mathrm{p}} + \frac{\mathrm{d}}{\mathrm{d}\varphi}\boldsymbol{\Psi}^{\mathrm{p}}_{\mathrm{PM}}\right). \tag{2.36}$$

Accordingly, the phase voltages consist of resistive voltages, voltages induced by current changes and voltages induced by rotor movement. Multiplying with $\boldsymbol{T}_{\mathrm{C}}$ on the left side leads to

$$\boldsymbol{T}_{\mathrm{C}}\boldsymbol{u}^{\mathrm{p}} = \boldsymbol{T}_{\mathrm{C}}\boldsymbol{R}^{\mathrm{p}}\boldsymbol{i}^{\mathrm{p}} + \boldsymbol{T}_{\mathrm{C}}\boldsymbol{L}^{\mathrm{p}}\left(\frac{\mathrm{d}}{\mathrm{d}t}\boldsymbol{i}^{\mathrm{p}}\right) + \omega \cdot \left(\boldsymbol{T}_{\mathrm{C}}\left(\frac{\mathrm{d}}{\mathrm{d}\varphi}\boldsymbol{L}^{\mathrm{p}}\right)\boldsymbol{i}^{\mathrm{p}} + \frac{\mathrm{d}}{\mathrm{d}\varphi}\boldsymbol{T}_{\mathrm{C}}\boldsymbol{\Psi}^{\mathrm{p}}_{\mathrm{PM}}\right) \tag{2.37}$$

$$\boldsymbol{u}^{\mathrm{s}} = \boldsymbol{T}_{\mathrm{C}}\boldsymbol{R}^{\mathrm{p}}\boldsymbol{i}^{\mathrm{p}} + \boldsymbol{T}_{\mathrm{C}}\boldsymbol{L}^{\mathrm{p}}\left(\frac{\mathrm{d}}{\mathrm{d}t}\boldsymbol{i}^{\mathrm{p}}\right) + \omega \cdot \left(\boldsymbol{T}_{\mathrm{C}}\left(\frac{\mathrm{d}}{\mathrm{d}\varphi}\boldsymbol{L}^{\mathrm{p}}\right)\boldsymbol{i}^{\mathrm{p}} + \frac{\mathrm{d}}{\mathrm{d}\varphi}\boldsymbol{\Psi}^{\mathrm{s}}_{\mathrm{PM}}\right)\ . \tag{2.38}$$

Replacing $\boldsymbol{i}^{\mathrm{p}}$ by $\boldsymbol{T}_{\mathrm{C}}^{-1}\boldsymbol{i}^{\mathrm{s}}$, (2.38) is rewritten to

$$\boldsymbol{u}^{\mathrm{s}} = \boldsymbol{T}_{\mathrm{C}}\boldsymbol{R}^{\mathrm{p}}\boldsymbol{T}_{\mathrm{C}}^{-1}\boldsymbol{i}^{\mathrm{s}} + \boldsymbol{T}_{\mathrm{C}}\boldsymbol{L}^{\mathrm{p}}\boldsymbol{T}_{\mathrm{C}}^{-1}\left(\frac{\mathrm{d}}{\mathrm{d}t}\boldsymbol{i}^{\mathrm{s}}\right) + \omega \cdot \left(\boldsymbol{T}_{\mathrm{C}}\left(\frac{\mathrm{d}}{\mathrm{d}\varphi}\boldsymbol{L}^{\mathrm{p}}\right)\boldsymbol{T}_{\mathrm{C}}^{-1}\boldsymbol{i}^{\mathrm{s}} + \frac{\mathrm{d}}{\mathrm{d}\varphi}\boldsymbol{\Psi}^{\mathrm{s}}_{\mathrm{PM}}\right)\ . \tag{2.39}$$

The resistance and inductance matrix for describing the motor equations in the 'αβ0' frame are therefore given by

$$\boldsymbol{R}^{\mathrm{s}} = \boldsymbol{T}_{\mathrm{C}}\boldsymbol{R}^{\mathrm{p}}\boldsymbol{T}_{\mathrm{C}}^{-1} \tag{2.40}$$

and

$$\boldsymbol{L}^{\mathrm{s}} = \boldsymbol{T}_{\mathrm{C}}\boldsymbol{L}^{\mathrm{s}}\boldsymbol{T}_{\mathrm{C}}^{-1}\ . \tag{2.41}$$

The following relations hold between the inductances in the 'αβ0' and the 'abc' reference frame:

$$L_{\alpha\alpha} = \frac{1}{6}\left(4L_{\mathrm{aa}} + L_{\mathrm{bb}} + L_{\mathrm{cc}} - 4L_{\mathrm{ab}} + 2L_{\mathrm{bc}} - 4L_{\mathrm{ca}}\right) \tag{2.42}$$

$$L_{\beta\beta} = \frac{1}{2}\left(L_{\mathrm{bb}} + L_{\mathrm{cc}} - 2L_{\mathrm{bc}}\right) \tag{2.43}$$

$$L_{00} = \frac{1}{3}\left(L_{\mathrm{aa}} + L_{\mathrm{bb}} + L_{\mathrm{cc}} + 2L_{\mathrm{bc}} + 2L_{\mathrm{ca}} + 2L_{\mathrm{ab}}\right) \tag{2.44}$$

$$L_{\alpha\beta} = L_{\beta\alpha} = \frac{1}{2\sqrt{3}}\left(L_{\mathrm{cc}} - L_{\mathrm{bb}} + 2L_{\mathrm{ab}} - 2L_{\mathrm{ca}}\right) \tag{2.45}$$

$$L_{0\alpha} = \frac{1}{2}L_{\alpha 0} = \frac{1}{6}\left(2L_{\mathrm{aa}} - L_{\mathrm{bb}} - L_{\mathrm{cc}} + L_{\mathrm{ab}} - 2L_{\mathrm{bc}} + L_{\mathrm{ca}}\right) \tag{2.46}$$

$$L_{0\beta} = \frac{1}{2}L_{\beta 0} = \frac{1}{2\sqrt{3}}\left(L_{\mathrm{bb}} - L_{\mathrm{cc}} + L_{\mathrm{ab}} - L_{\mathrm{ca}}\right)\ . \tag{2.47}$$

For the resistance matrix, the relations are somewhat simpler due to the diagonal form of $\boldsymbol{R}^{\mathrm{p}}$. It can be seen that coupling terms between the α-, β- and 0-axis may be present when the phase resistances in the 'abc' frame are not all equal:

$$R_{\alpha\alpha} = \frac{1}{6}\left(4R_{\mathrm{aa}} + R_{\mathrm{bb}} + R_{\mathrm{cc}}\right) \tag{2.48}$$

$$R_{\beta\beta} = \frac{1}{2}\left(R_{\mathrm{bb}} + R_{\mathrm{cc}}\right) \tag{2.49}$$

$$R_{00} = \frac{1}{3}\left(R_{\mathrm{aa}} + R_{\mathrm{bb}} + R_{\mathrm{cc}}\right) \tag{2.50}$$

$$R_{\alpha\beta} = R_{\beta\alpha} = \frac{1}{2\sqrt{3}}\left(R_{\mathrm{cc}} - R_{\mathrm{bb}}\right) \tag{2.51}$$

$$R_{0\alpha} = \frac{1}{2}R_{\alpha 0} = \frac{1}{6}\left(2R_{\mathrm{aa}} - R_{\mathrm{bb}} - R_{\mathrm{cc}}\right) \tag{2.52}$$

$$R_{0\beta} = \frac{1}{2}R_{\beta 0} = \frac{1}{2\sqrt{3}}\left(R_{\mathrm{bb}} - R_{\mathrm{cc}}\right)\ . \tag{2.53}$$

Consequently, the inductance and resistance matrices in the 'αβ0' coordinate system are of the form

$$\boldsymbol{L}^{\mathrm{s}} = \begin{bmatrix} L_{\alpha\alpha} & L_{\alpha\beta} & 2L_{0\alpha} \\ L_{\alpha\beta} & L_{\beta\beta} & 2L_{0\beta} \\ L_{0\alpha} & L_{0\beta} & L_{00}. \end{bmatrix}, \quad \boldsymbol{R}^{\mathrm{s}} = \begin{bmatrix} R_{\alpha\alpha} & R_{\alpha\beta} & 2R_{0\alpha} \\ R_{\alpha\beta} & R_{\beta\beta} & 2R_{0\beta} \\ R_{0\alpha} & R_{0\beta} & R_{00} \end{bmatrix}. \tag{2.54}$$

With the transformed resistance and inductance matrices, one obtains the voltage equation

in the 'αβ0' frame,

$$\boldsymbol{u}^{\mathrm{s}} = \boldsymbol{R}^{\mathrm{s}}\boldsymbol{i}^{\mathrm{s}} + \boldsymbol{L}^{\mathrm{s}}\left(\frac{\mathrm{d}}{\mathrm{d}t}\boldsymbol{i}^{\mathrm{s}}\right) + \omega \cdot \left(\left(\frac{\mathrm{d}}{\mathrm{d}\varphi}\boldsymbol{L}^{\mathrm{s}}\right)\boldsymbol{i}^{\mathrm{s}} + \frac{\mathrm{d}}{\mathrm{d}\varphi}\boldsymbol{\Psi}^{\mathrm{s}}_{\mathrm{PM}}\right). \tag{2.55}$$

Using (2.15) and (2.18), the voltages in the phases can finally be described in the 'abc' reference frame by

$$\boldsymbol{u}^{\mathrm{p}}_{\mathrm{term}} - u_{\mathrm{N}}\begin{bmatrix}1\\1\\1\end{bmatrix} = \boldsymbol{R}^{\mathrm{p}}\boldsymbol{i}^{\mathrm{p}} + \boldsymbol{L}^{\mathrm{p}}\left(\frac{\mathrm{d}}{\mathrm{d}t}\boldsymbol{i}^{\mathrm{p}}\right) + \omega \cdot \left(\left(\frac{\mathrm{d}}{\mathrm{d}\varphi}\boldsymbol{L}^{\mathrm{p}}\right)\boldsymbol{i}^{\mathrm{p}} + \frac{\mathrm{d}}{\mathrm{d}\varphi}\boldsymbol{\Psi}^{\mathrm{p}}_{\mathrm{PM}}\right) \tag{2.56}$$

and, similarly, in the 'αβ0' reference frame by

$$\boldsymbol{u}^{\mathrm{s}}_{\mathrm{term}} - u_{\mathrm{N}}\begin{bmatrix}0\\0\\1\end{bmatrix} = \boldsymbol{R}^{\mathrm{s}}\boldsymbol{i}^{\mathrm{s}} + \boldsymbol{L}^{\mathrm{s}}\left(\frac{\mathrm{d}}{\mathrm{d}t}\boldsymbol{i}^{\mathrm{s}}\right) + \omega \cdot \left(\left(\frac{\mathrm{d}}{\mathrm{d}\varphi}\boldsymbol{L}^{\mathrm{s}}\right)\boldsymbol{i}^{\mathrm{s}} + \frac{\mathrm{d}}{\mathrm{d}\varphi}\boldsymbol{\Psi}^{\mathrm{s}}_{\mathrm{PM}}\right). \tag{2.57}$$

2.2.2. Rotating Coordinates

The equations of the electrical model in the rotating coordinates are obtained by left-sided multiplication of the 'αβ0'-representation of (2.25) with $\boldsymbol{T}_{\mathrm{P}}$:

$$\boldsymbol{T}_{\mathrm{P}}\boldsymbol{u}^{\mathrm{s}} = \boldsymbol{T}_{\mathrm{P}}\left(\boldsymbol{R}^{\mathrm{s}}\boldsymbol{i}^{\mathrm{s}} + \frac{\mathrm{d}}{\mathrm{d}t}\boldsymbol{\Psi}^{\mathrm{s}}\right) \tag{2.58}$$

$$\boldsymbol{u}^{\mathrm{r}} = \boldsymbol{R}^{\mathrm{r}}\boldsymbol{i}^{\mathrm{r}} + \boldsymbol{T}_{\mathrm{P}}\left(\frac{\mathrm{d}}{\mathrm{d}t}\boldsymbol{\Psi}^{\mathrm{s}}\right) \tag{2.59}$$

$$= \boldsymbol{R}^{\mathrm{r}}\boldsymbol{i}^{\mathrm{r}} + \boldsymbol{T}_{\mathrm{P}}\left(\frac{\mathrm{d}}{\mathrm{d}t}\left(\boldsymbol{T}_{\mathrm{P}}^{-1}\boldsymbol{\Psi}^{\mathrm{r}}\right)\right) \tag{2.60}$$

$$= \boldsymbol{R}^{\mathrm{r}}\boldsymbol{i}^{\mathrm{r}} + \boldsymbol{T}_{\mathrm{P}}\left(\frac{\mathrm{d}}{\mathrm{d}t}\boldsymbol{T}_{\mathrm{P}}^{-1}\right)\boldsymbol{\Psi}^{\mathrm{r}} + \boldsymbol{T}_{\mathrm{P}}\boldsymbol{T}_{\mathrm{P}}^{-1}\left(\frac{\mathrm{d}}{\mathrm{d}t}\boldsymbol{\Psi}^{\mathrm{r}}\right) \tag{2.61}$$

$$= \boldsymbol{R}^{\mathrm{r}}\boldsymbol{i}^{\mathrm{r}} + \boldsymbol{T}_{\mathrm{P}}\omega\boldsymbol{J}^{\mathrm{T}}\boldsymbol{T}_{\mathrm{P}}^{-1}\boldsymbol{\Psi}^{\mathrm{r}} + \left(\frac{\mathrm{d}}{\mathrm{d}t}\boldsymbol{\Psi}^{\mathrm{r}}\right). \tag{2.62}$$

Note that $\boldsymbol{T}_{\mathrm{P}}\boldsymbol{J}^{\mathrm{T}}\boldsymbol{T}_{\mathrm{P}}^{-1} = \boldsymbol{J}^{\mathrm{T}}$, which further leads to

$$\boldsymbol{u}^{\mathrm{r}} = \boldsymbol{R}^{\mathrm{r}}\boldsymbol{i}^{\mathrm{r}} + \omega\boldsymbol{J}^{\mathrm{T}}\boldsymbol{\Psi}^{\mathrm{r}} + \left(\frac{\mathrm{d}}{\mathrm{d}t}\boldsymbol{\Psi}^{\mathrm{r}}\right). \tag{2.63}$$

The flux linkage vector and its derivative are described by:

$$\boldsymbol{\Psi}^{\mathrm{r}} = \boldsymbol{L}^{\mathrm{r}}\boldsymbol{i}^{\mathrm{r}} + \boldsymbol{\Psi}^{\mathrm{r}}_{\mathrm{PM}} \tag{2.64}$$

$$\frac{\mathrm{d}}{\mathrm{d}t}\boldsymbol{\Psi}^{\mathrm{r}} = \boldsymbol{L}^{\mathrm{r}}\left(\frac{\mathrm{d}}{\mathrm{d}t}\boldsymbol{i}^{\mathrm{r}}\right) + \left(\frac{\mathrm{d}}{\mathrm{d}t}\boldsymbol{L}^{\mathrm{r}}\right)\boldsymbol{i}^{\mathrm{r}} + \frac{\mathrm{d}}{\mathrm{d}t}\boldsymbol{\Psi}^{\mathrm{r}}_{\mathrm{PM}} \tag{2.65}$$

where the inductance matrix in the rotating reference frame is given by

$$\boldsymbol{L}^{\mathrm{r}} = \boldsymbol{T}_{\mathrm{P}}\boldsymbol{L}^{\mathrm{s}}\boldsymbol{T}_{\mathrm{P}}^{-1} \tag{2.66}$$

$$= \begin{bmatrix} L_{\mathrm{dd}} & L_{\mathrm{dq}} & 2L_{0\mathrm{d}} \\ L_{\mathrm{dq}} & L_{\mathrm{qq}} & 2L_{0\mathrm{q}} \\ L_{0\mathrm{d}} & L_{0\mathrm{q}} & L_{00} \end{bmatrix} \tag{2.67}$$

with the inverse transform

$$\boldsymbol{L}^{\mathrm{s}} = \boldsymbol{T}_{\mathrm{P}}^{-1}\boldsymbol{L}^{\mathrm{r}}\boldsymbol{T}_{\mathrm{P}} \ . \tag{2.68}$$

Inserting the transformation leads to

$$\boldsymbol{u}^{\mathrm{r}} = \boldsymbol{R}^{\mathrm{r}}\boldsymbol{i}^{\mathrm{r}} + \boldsymbol{L}^{\mathrm{r}}\left(\frac{\mathrm{d}}{\mathrm{d}t}\boldsymbol{i}^{\mathrm{r}}\right) + \left(\frac{\mathrm{d}}{\mathrm{d}t}\boldsymbol{L}^{\mathrm{r}}\right)\boldsymbol{i}^{\mathrm{r}} + \omega\boldsymbol{J}^{\mathrm{T}}\boldsymbol{\Psi}^{\mathrm{r}} + \frac{\mathrm{d}}{\mathrm{d}t}\boldsymbol{\Psi}^{\mathrm{r}}_{\mathrm{PM}} \tag{2.69}$$

$$= \boldsymbol{R}^{\mathrm{r}}\boldsymbol{i}^{\mathrm{r}} + \boldsymbol{L}^{\mathrm{r}}\left(\frac{\mathrm{d}}{\mathrm{d}t}\boldsymbol{i}^{\mathrm{r}}\right) + \left(\frac{\mathrm{d}}{\mathrm{d}t}\boldsymbol{L}^{\mathrm{r}}\right)\boldsymbol{i}^{\mathrm{r}} + \omega\boldsymbol{J}^{\mathrm{T}}\boldsymbol{L}^{\mathrm{r}}\boldsymbol{i}^{\mathrm{r}} + \omega\boldsymbol{J}^{\mathrm{T}}\boldsymbol{\Psi}^{\mathrm{r}}_{\mathrm{PM}} + \frac{\mathrm{d}}{\mathrm{d}t}\boldsymbol{\Psi}^{\mathrm{r}}_{\mathrm{PM}} \tag{2.70}$$

$$= \boldsymbol{R}^{\mathrm{r}}\boldsymbol{i}^{\mathrm{r}} + \boldsymbol{L}^{\mathrm{r}}\left(\frac{\mathrm{d}}{\mathrm{d}t}\boldsymbol{i}^{\mathrm{r}}\right) + \omega\left(\boldsymbol{J}^{\mathrm{T}}\boldsymbol{L}^{\mathrm{r}}\boldsymbol{i}^{\mathrm{r}} + \left(\frac{\mathrm{d}}{\mathrm{d}\varphi}\boldsymbol{L}^{\mathrm{r}}\right)\boldsymbol{i}^{\mathrm{r}} + \boldsymbol{J}^{\mathrm{T}}\boldsymbol{\Psi}^{\mathrm{r}}_{\mathrm{PM}} + \frac{\mathrm{d}}{\mathrm{d}\varphi}\boldsymbol{\Psi}^{\mathrm{r}}_{\mathrm{PM}}\right) \ . \tag{2.71}$$

Similar as in the stationary reference frames, the phase voltages are again expressed by resistive voltages, voltages induced by current changes and voltages induced by rotor movement.

2.2.3. Conventional Model

Compared to conventional electrical models of PMSMs, the model used in this work is kept more general in order to include asymmetries that may cause zero-sequence voltage terms. However, the conventional models that are commonly described in the 'dq' frame and found for example in [Kri01; Sch15] can easily be derived as a special case of this model, which is demonstrated in this section.

By assuming $\boldsymbol{\Psi}^{\mathrm{r}}_{\mathrm{PM}}$ as constant and with only a d-axis component, i.e.

$$\boldsymbol{\Psi}^{\mathrm{r}}_{\mathrm{PM}} = \begin{bmatrix} \Psi_{\mathrm{PM}} \\ 0 \\ 0 \end{bmatrix} = \text{const} \tag{2.72}$$

the term featuring its derivative in (2.71) becomes zero. Further, the phase resistances can be assumed as balanced, which allows to use a scalar resistance $\boldsymbol{R}$ in place of the resistance matrix. These two simplifications lead to

$$\boldsymbol{u}^{\mathrm{r}} = R\boldsymbol{i}^{\mathrm{r}} + \boldsymbol{L}^{\mathrm{r}} \left(\frac{\mathrm{d}}{\mathrm{d}t} \boldsymbol{i}^{\mathrm{r}} \right) + \omega \left(\boldsymbol{J}^{\mathrm{T}} \boldsymbol{L}^{\mathrm{r}} \boldsymbol{i}^{\mathrm{r}} + \left(\frac{\mathrm{d}}{\mathrm{d}\varphi} \boldsymbol{L}^{\mathrm{r}} \right) \boldsymbol{i}^{\mathrm{r}} + \boldsymbol{J}^{\mathrm{T}} \boldsymbol{\Psi}^{\mathrm{r}}_{\mathrm{PM}} \right). \tag{2.73}$$

Since conventional models do not include the zero-sequence axis, let us also consider only the d- and q-components of this equation. In combination with $i_0 = 0$, one can write

$$\begin{aligned} \begin{bmatrix} u_{\mathrm{d}} \\ u_{\mathrm{q}} \end{bmatrix} &= R \begin{bmatrix} i_{\mathrm{d}} \\ i_{\mathrm{q}} \end{bmatrix} + \begin{bmatrix} L_{\mathrm{dd}} & L_{\mathrm{dq}} \\ L_{\mathrm{dq}} & L_{\mathrm{qq}} \end{bmatrix} \begin{bmatrix} \frac{\mathrm{d}}{\mathrm{d}t} i_{\mathrm{d}} \\ \frac{\mathrm{d}}{\mathrm{d}t} i_{\mathrm{q}} \end{bmatrix} \\ &\quad + \omega \left(\begin{bmatrix} -L_{\mathrm{dq}} & -L_{\mathrm{qq}} \\ L_{\mathrm{dd}} & L_{\mathrm{dq}} \end{bmatrix} \begin{bmatrix} i_{\mathrm{d}} \\ i_{\mathrm{q}} \end{bmatrix} + \left(\frac{\mathrm{d}}{\mathrm{d}\varphi} \begin{bmatrix} L_{\mathrm{dd}} & L_{\mathrm{dq}} \\ L_{\mathrm{dq}} & L_{\mathrm{qq}} \end{bmatrix} \right) \begin{bmatrix} i_{\mathrm{d}} \\ i_{\mathrm{q}} \end{bmatrix} + \begin{bmatrix} 0 \\ \Psi_{\mathrm{PM}} \end{bmatrix} \right). \end{aligned} \tag{2.74}$$

The reduced inductance matrix in the 'dq' reference frame, which is a submatrix of the full inductance matrix $\boldsymbol{L}^{\mathrm{r}}$, is typically assumed to be independent of the position and with no mutual inductances:

$$\boldsymbol{L}^{\mathrm{r}*} = \begin{bmatrix} L_{\mathrm{dd}} = \text{const} & 0 \\ 0 & L_{\mathrm{qq}} = \text{const} \end{bmatrix}. \tag{2.75}$$

The equation therefore becomes

$$\begin{bmatrix} u_{\mathrm{d}} \\ u_{\mathrm{q}} \end{bmatrix} = R \begin{bmatrix} i_{\mathrm{d}} \\ i_{\mathrm{q}} \end{bmatrix} + \begin{bmatrix} L_{\mathrm{dd}} & 0 \\ 0 & L_{\mathrm{qq}} \end{bmatrix} \begin{bmatrix} \frac{\mathrm{d}}{\mathrm{d}t} i_{\mathrm{d}} \\ \frac{\mathrm{d}}{\mathrm{d}t} i_{\mathrm{q}} \end{bmatrix} + \omega \left(\begin{bmatrix} 0 & -L_{\mathrm{qq}} \\ L_{\mathrm{dd}} & 0 \end{bmatrix} \begin{bmatrix} i_{\mathrm{d}} \\ i_{\mathrm{q}} \end{bmatrix} + \begin{bmatrix} 0 \\ \Psi_{\mathrm{PM}} \end{bmatrix} \right) \tag{2.76}$$

and can further be written as the well-known equations for the phase voltages in the 'dq'

reference frame:

$$u_\mathrm{d} = Ri_\mathrm{d} + L_\mathrm{dd}\frac{\mathrm{d}}{\mathrm{d}t}i_\mathrm{d} - \omega L_\mathrm{qq}i_\mathrm{q} \tag{2.77}$$

$$u_\mathrm{q} = Ri_\mathrm{q} + L_\mathrm{qq}\frac{\mathrm{d}}{\mathrm{d}t}i_\mathrm{q} + \omega\left(L_\mathrm{dd}i_\mathrm{d} + \Psi_\mathrm{PM}\right) \ . \tag{2.78}$$

2.3. Torque Generation and Mechanical Model

The electromagnetic torque created by a synchronous machine can, according to [Kri01; Sch15], be described by

$$M_\mathrm{e} = \frac{3}{2}p\left(\Psi_\mathrm{d}i_\mathrm{q} - \Psi_\mathrm{q}i_\mathrm{d}\right) \ . \tag{2.79}$$

Under assumption of $L_\mathrm{dq} = L_\mathrm{qd} = 0$, and with $\Psi_\mathrm{d} = \Psi_\mathrm{PM}$ for a PMSM, the electromagnetic torque is found to be

$$M_\mathrm{e} = \frac{3}{2}p\left(\Psi_\mathrm{PM}i_\mathrm{q} + L_\mathrm{dd}i_\mathrm{d}i_\mathrm{q} - L_\mathrm{qq}i_\mathrm{q}i_\mathrm{d}\right) \tag{2.80}$$

$$= \frac{3}{2}p\left(\Psi_\mathrm{PM}i_\mathrm{q} + \left(L_\mathrm{dd} - L_\mathrm{qq}\right)i_\mathrm{d}i_\mathrm{q}\right) . \tag{2.81}$$

A simple strategy to control a PMSM consists of controlling i_d to zero. Assuming the machine parameters as constants, the electromagnetic torque is then proportional to the q-axis current.

To obtain the acceleration torque, the load torque M_ld needs to be subtracted from the electromagnetic torque. Thus, the angular acceleration of the motor shaft is obtained as

$$\frac{\mathrm{d}\omega_\mathrm{m}}{\mathrm{d}t} = \frac{1}{J}\left(M_\mathrm{e} - M_\mathrm{ld}\right) \tag{2.82}$$

where J is the moment of inertia and ω_m is the mechanical angular frequency

$$\omega_\mathrm{m} = \frac{\mathrm{d}}{\mathrm{d}t}\varphi_\mathrm{m} \ . \tag{2.83}$$

2.4. Inverter Switching States and Space Vector Modulation

Using a two-level three-phase switching inverter and assuming that none of the inverter outputs is kept floating, each machine terminal is connected either to the positive or the negative potential of the DC link. Using the negative potential as reference, the terminal voltages can be either at 0 or at u_DC. A total of eight different switching

Table 2.2.: Discrete voltage vectors for a three-phase switching inverter with all inverter legs conducting.

	$\boldsymbol{u}^{\mathrm{p}}_{\mathrm{term}}$			$\boldsymbol{u}^{\mathrm{s}}_{\mathrm{term}}$		
	a	b	c	α	β	0
$\boldsymbol{u}_0$	0	0	0	0	0	0
$\boldsymbol{u}_1$ (+a)	u_{DC}	0	0	$2/3u_{\mathrm{DC}}$	0	$1/3u_{\mathrm{DC}}$
$\boldsymbol{u}_2$ (−c)	u_{DC}	u_{DC}	0	$1/3u_{\mathrm{DC}}$	$1/\sqrt{3}u_{\mathrm{DC}}$	$2/3u_{\mathrm{DC}}$
$\boldsymbol{u}_3$ (+b)	0	u_{DC}	0	$-1/3u_{\mathrm{DC}}$	$1/\sqrt{3}u_{\mathrm{DC}}$	$1/3u_{\mathrm{DC}}$
$\boldsymbol{u}_4$ (−a)	0	u_{DC}	u_{DC}	$-2/3u_{\mathrm{DC}}$	0	$2/3u_{\mathrm{DC}}$
$\boldsymbol{u}_5$ (+c)	0	0	u_{DC}	$-1/3u_{\mathrm{DC}}$	$-1/\sqrt{3}u_{\mathrm{DC}}$	$1/3u_{\mathrm{DC}}$
$\boldsymbol{u}_6$ (−b)	u_{DC}	0	u_{DC}	$1/3u_{\mathrm{DC}}$	$-1/\sqrt{3}u_{\mathrm{DC}}$	$2/3u_{\mathrm{DC}}$
$\boldsymbol{u}_7$	u_{DC}	u_{DC}	u_{DC}	0	0	u_{DC}

states are therefore possible that can be associated to voltage vectors according to Table 2.2. To distinguish these from arbitrary voltage vectors, they are referred to as *discrete voltage vectors* in this thesis. Furthermore, the two vectors $\boldsymbol{u}_0$ and $\boldsymbol{u}_7$, where all machine terminals are connected to the same potential, are usually referred to as *zero vectors* because their α- and β- components are zero. The other six vectors are referred to as *active vectors*. They span a hexagonal area in the αβ-plane in which the realizable reference voltage vectors lie. Moreover, the active and zero voltage vectors divide this hexagonal area into six sectors as shown in Fig. 2.4.

To apply arbitrary reference voltage vectors to a machine via the switching inverter, modulation strategies must be used. The switching instants of the inverter switches are chosen in a way that the time averages of the terminal voltages in the αβ-plane equal the reference voltage vector, which is commanded by the current controller, over a certain period. The conventional approach to calculate the switching instants is space vector modulation (SVM). SVM uses the zero vectors and the two active vectors closest to the reference voltage vector and leads to relatively small current ripple. To differentiate it from modified SVMs that will be discussed in later parts of this thesis, the term *standard SVM* is used here. It will only be briefly described here but more information including the necessary calculations can be found for example in [KKB02; HL03].

The standard SVM defines the share of each of the two active voltage vectors and the overall share of the two zero vectors in a switching period T_{sw}. Since the two zero vectors are redundant, they offer a degree of freedom that can for example be used to minimize switching losses [KEZ91]. Fig. 2.5 shows an example of a reference voltage vector $\boldsymbol{u}_{\mathrm{r}}$ lying in sector I of the hexagon. It is synthesized by the two closest active voltage vectors

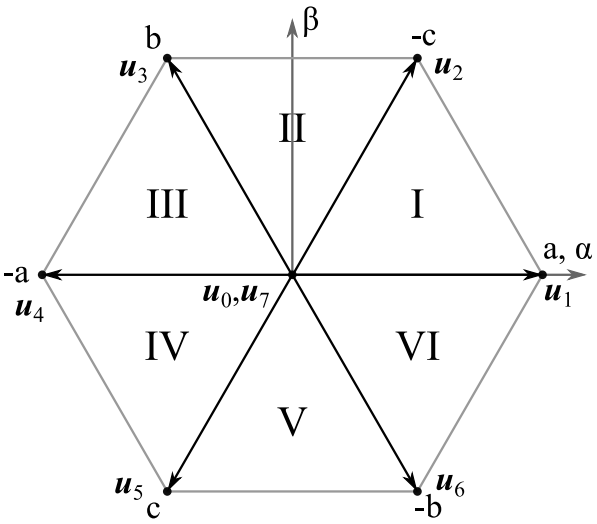

Figure 2.4.: The discrete voltage vectors and the hexagon of realizable reference voltage vectors in the αβ-plane.

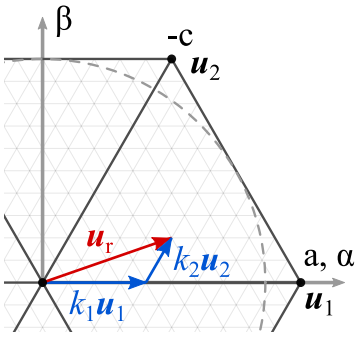

Figure 2.5.: Synthetization of a reference voltage vectors using standard SVM [SKMN21].

$\boldsymbol{u}_1$ and $\boldsymbol{u}_2$ whose share of a switching period are $k_1 = T_{\mathrm{u1}}/T_{\mathrm{sw}}$ and $k_2 = T_{\mathrm{u2}}/T_{\mathrm{sw}}$. The two zero vectors are applied for the rest of the switching period so that

$$T_{\mathrm{sw}} = T_{\mathrm{u0}} + T_{\mathrm{u1}} + T_{\mathrm{u2}} + T_{\mathrm{u7}} \ . \tag{2.84}$$

From the shares of the voltage vectors, the switching instants are calculated and from these in turn the three-phase pulse waveforms are generated. Most often, the standard SVM is realized with center-aligned pulses for the three phases. While a realization with

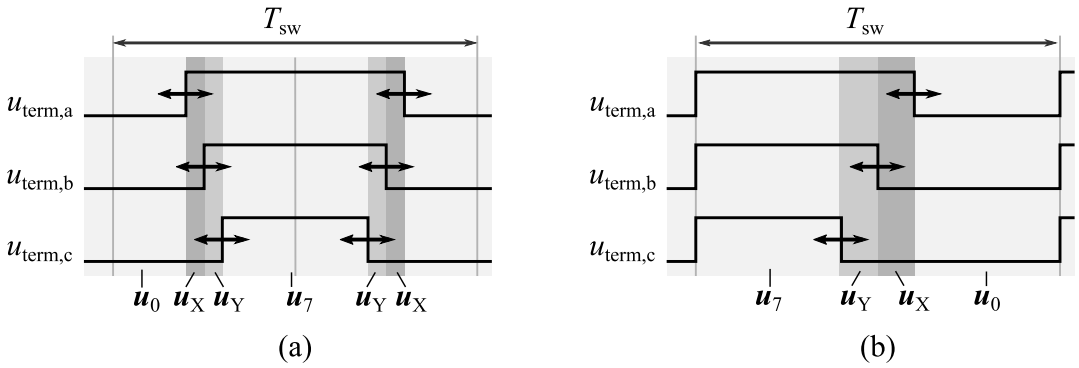

Figure 2.6.: Exemplary (a) center-aligned and (b) edge-aligned pulse patterns for a standard SVM

edge-aligned pulses is also possible, the number of active voltage vectors per switching period is effectively halved in comparison to center-aligned pulses and higher current ripple is produced [HL03] at the same switching frequency. Exemplary waveforms for a standard SVM with center- and edge-aligned pulses are shown in Figure 2.6. In the illustrated case, the zero vectors have been equally distributed.

3. Sensorless Control via Magnetic Anisotropy

3.1. Introduction to Sensorless Control of Synchronous and Induction Machines

In the field of electrical machines, the term *sensorless control* typically describes the approach of controlling a machine without the usage of position or speed sensors. While there are still sensors necessary that measure electrical quantities, this terminology has become so common in the scientific literature that deviating from this term may likely cause more confusion to potential readers than using it. Therefore, it is also used here with the aforementioned meaning in mind. Over the years, a vast amount of different sensorless techniques for synchronous and induction machines have been proposed and continuously been improved upon by the scientific community. For PMSMs, the techniques are usually divided into those that are based on the voltage induced by rotor movement – the back-electromotive force (BEMF) – and in those that are based on magnetic anisotropy.

Techniques based on the BEMF have been used for much longer and have found wide application in electrical drives. The BEMF in powered phases cannot be measured directly but its effect can be exploited by measuring the currents in the machine. Different approaches for position and speed estimation exist, such as flux and EMF estimators, Luenberger observers, extended Kalman filters and sliding mode observers [WVS19]. Further distinctions can be made between representations in stationary or estimated rotating reference frames. Differences between d- and q-axis inductances can be considered in the model, leading to an extended BEMF formulation. An overview as well as further literature on the various estimation techniques based on the BEMF can be found in review papers such as [BG10a; BG10b; WVS19].

The BEMF is proportional to rotor speed. Therefore, techniques that exploit the BEMF work well at medium and high rotor speeds. However, as speeds decrease, estimating

the position and/or speed becomes increasingly difficult and requires higher modeling effort and higher quality current measurements. Furthermore, estimation at standstill is generally not possible. In order to enable estimation of the rotor position even at low speed and standstill, a new category of estimation techniques has been established that is based on *magnetic anisotropy*. These techniques are described in the next section.

3.2. Techniques Based on Magnetic Anisotropy

3.2.1. Physical Background

Generally, anisotropy-based techniques make use of a position dependence of the machine inductances. In synchronous machines, the position dependence usually originates from one or both of two essential causes, namely the *geometry* of the rotor core and *magnetic saturation*.

The geometry of the rotor core may cause the magnetic circuits seen by each phase to vary over the rotor position due to varying effective air gaps and cross-sectional areas of the soft-magnetic material. Larger air gaps or smaller cross-sectional areas of the iron core lead to higher reluctance and therefore smaller differential inductance

$$L = \mathrm{d}\Psi/\mathrm{d}i \tag{3.1}$$

in a machine phase. A good example are synchronous reluctance machines (SynRM). This type of synchronous machines does not feature permanent magnets but a magnetic anisotropy that is typically created by an arrangement of flux barriers [VCC+00]. The principal relationship between current and flux in the d- and q-axis for such a machine is shown in Fig. 3.1(a). Here, the d-axis is defined as the axis that features the higher inductance.

Magnetic saturation on the other hand is caused by the nonlinear magnetic characteristics of the soft-magnetic core material. To understand this effect, one can consider a machine with surface mounted magnets (surface permanent magnet synchronous machine, SPMSM) and a symmetric rotor geometry. In the d-axis, which is aligned with the flux from the magnets, a bias exists in the flux level that saturates the material as shown in Fig. 3.1(b). The differential inductance is therefore smaller in the d-axis than it is for the q-axis, so that $L_{\mathrm{dd}} < L_{\mathrm{qq}}$. For PMSMs with surface-mounted permanent magnets, the anisotropy is caused primarily by saturation as this machine type does not feature inherent reluctance variation in the rotor core.

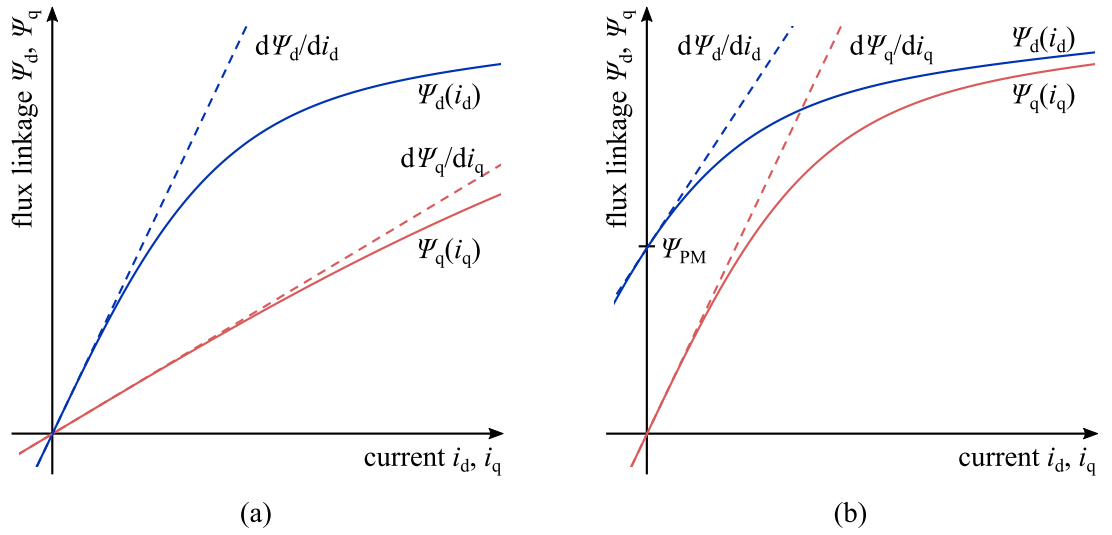

Figure 3.1.: Principal flux-current relationships and linearization at zero current for (a) a SynRM and (b) a SPMSM. The current in the respective other axis is held at zero.

Other motor types, such as machines with internal or buried permanent magnets, will typically feature a *combination* of geometry and saturation induced anisotropy. In general, the degree to which inductances vary depends strongly on the respective machine design and optimizing the design for sensorless operation is also a subject of scientific works, such as [AFG+16] and [KN17].

Similar to BEMF-based sensorless techniques, anisotropy-based techniques cannot be applied only to synchronous but also to induction machines to estimate the orientation of the rotor flux or the rotor position. While the same principle estimation techniques can generally be applied to both types of machines, different details may however have to be considered in each case.

Over the past three decades, a wide spectrum of different techniques based on magnetic anisotropies has been developed and refined in the scientific literature. The techniques differ essentially in excitation, measured quantities, signal processing and in their method to calculate the estimated position and speed as illustrated in Fig. 3.2. In the following, an overview of anisotropy-based techniques is presented which is divided into two sections. The first section covers techniques based on measurements of the line currents. In fact, most works concerning anisotropy-based approaches make use of current measurements, therefore it is meaningful to discuss the main concepts and certain advantages and

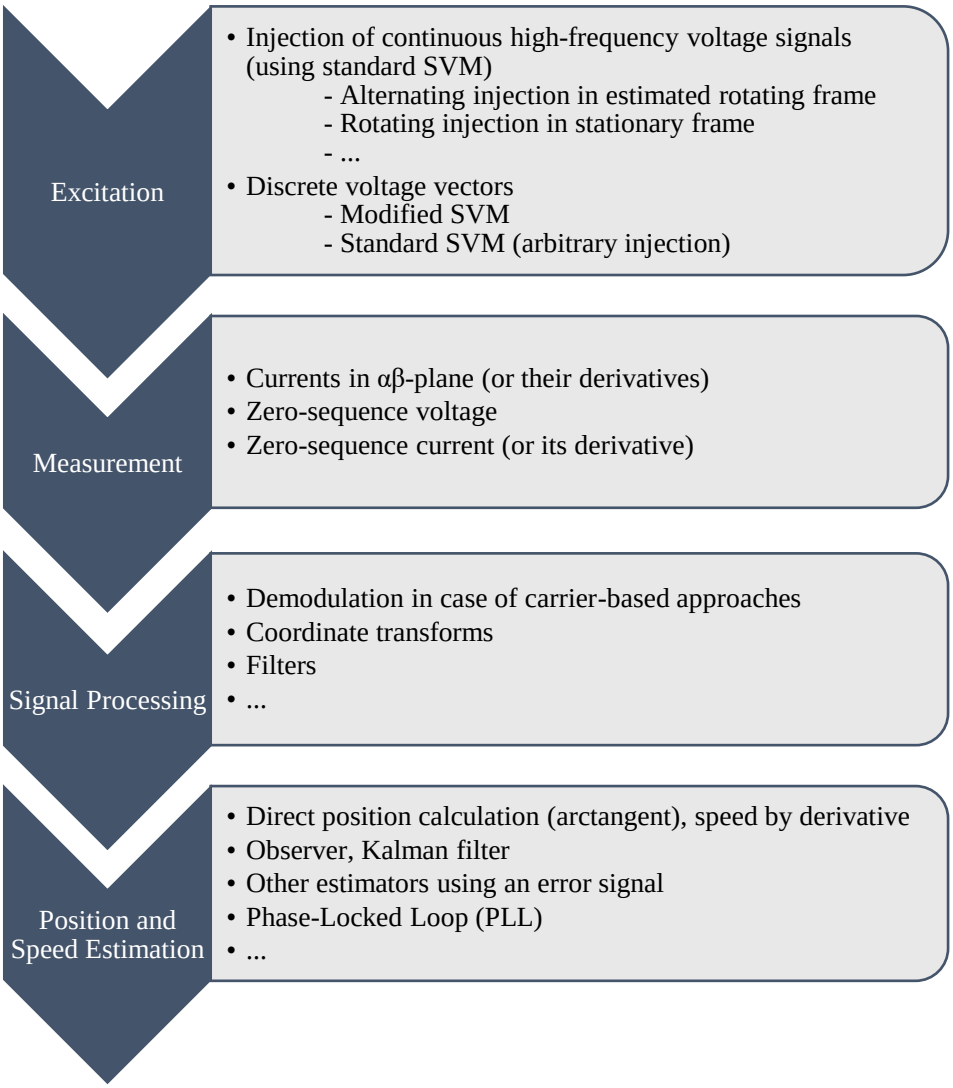

Figure 3.2.: Anisotropy-based techniques differ essentially in excitation, measured quantity, signal processing and the position and speed estimation approach.

disadvantages of techniques within this field. In the second section, techniques that use the zero-sequence voltage via the neutral point of a star-connected machine are discussed.

3.2.2. Techniques Based on Current Measurements

Techniques based on current measurements are the most common in the scientific literature. While there exist also techniques that exploit the zero-sequence current present in delta-connected machines, the vast majority uses the α- and β-axis currents (or the ones in the estimated d- and q-axis). The measurement of the zero-sequence current requires the integration of current sensors in series with the physical machine phases, whereas the α- and β-axis currents can be measured with conventionally placed current sensors, i.e. such in series with the inverter outputs or in the high or low sides of the inverter legs. Since such current sensors are present in virtually every electrical drive system, obvious advantages of these techniques are that there is usually no need for additional sensors and that they are usable with both star- and delta-connected machines. In this thesis, techniques based on the zero-sequence current are not further considered and when current-based techniques are mentioned, those based on the α- and β-axis currents are always meant.

The first technique based on magnetic anisotropies was the INFORM (Indirect Flux detection by Online Reactance Measurement) technique proposed by Schrödl in [Sch88] and [Sch96]. In the INFORM technique, the machine is excited with a specific pattern of discrete voltage vectors. The current change during these is measured by subtracting two current measurements for each vector. Since the current changes depend on the inductances, they contain the desired anisotropy information. In the original INFORM technique, the vectors were inserted between normal modulation periods used for the current control in regular intervals. After completing a measurement sequence, the estimated position can be directly calculated from the acquired anisotropy information using the *arctangent* function. A Kalman filter for the mechanical part of the model was used to improve the noisy position estimate [Sch96]. In later publications, alternative modulation strategies were introduced such as a strategy that minimizes the current deviation [RS04] and a strategy with only three active vectors for an application to magnetic bearings [NHHS14].

Techniques that use discrete voltage vectors as excitation usually require modification of the space vector modulation to ensure minimum durations for these vectors. In [PLK12], the authors proposed a concept called arbitrary injection that predicts the isotropic part of the current change by separate identification of the so-called isotropic admittance. This effectively reduces the number of unknowns in the relevant equations

by one[1]. As a result, an estimation without modification of the SVM becomes possible beyond a certain voltage threshold.

Another important group of anisotropy-based techniques is represented by high-frequency signal injection techniques. These inject voltages or, more rarely, currents at a frequency that is higher than the fundamental frequencies and lower than the switching frequency of the inverter. The two most important archetypes of this group are the alternating and the rotating injection and shall be described here briefly. Alternating injection typically involves injecting a sinusoidal voltage signal into the estimated d-axis of the machine. By using suitable filters, such as bandpass filters, the frequency component of the current that results from the injected signal is separated from the fundamental current component. The position can then be obtained for example by using the measured current response in the q-axis as an error signal that is controlled to zero with a PI controller [LKH03; Hol06]. In the case of rotating injection, a rotating voltage vector in stationary coordinates is injected. The interaction of this voltage vector with the anisotropy produces a negative-sequence current component in the measured current vector that is separated and used to estimate the position [JL95; BD11].

A significant advantage of the high-frequency injection techniques is that they do not require modification of the space vector modulation. The injected voltages are simply added to the reference voltages commanded by the current controller. However, there are some aspects to consider. A trade-off must be made when selecting the injection frequency. For low injection frequencies, the bandwidth of the current control must be reduced to ensure adequate frequency separation, which degrades dynamic performance. Additionally, the current ripple can result in audible noise and noticeable torque ripple. At higher injection frequencies, on contrast, the signal shape becomes increasingly distorted as the injection frequency approaches the switching frequency. Additionally, the amplitude of the high-frequency current response reduces due to the predominantly inductive impedance.

Generally, the obtainable signal-to-noise ratio is typically a significant drawback of current-based techniques, especially for motors that feature relatively small anisotropies. It is no secret that in order to obtain measurements of equivalent bandwidth and signal quality, more effort is required for current measurements than it is for voltage measurements. Moreover, the signal-to-noise ratio is adversely affected by the rather inefficient use of the ADC's conversion range. This is because the current slopes resulting

[1] see section 4.4.2

from a modified SVM, as well as the current response to a high frequency voltage injection, will usually be small in relation to the overall measurement range required for the fundamental current. Furthermore, in this small current ripple or high frequency current response, only a small part is actually position-dependent.

Different measures can be taken to improve the signal-to-noise ratio to a level that is sufficient for an adequate behavior in field-oriented control. The amount of excitation can be increased, which means an increase of the amplitude for injecting techniques or an increase in the duration of the discrete voltage vectors for techniques like INFORM. This goes however at the cost of increased audible noise and torque ripple and reduces the voltage that remains available for driving the machine. Alternatively, filters or mechanical observers can be used which however reduce the estimation bandwidth and therefore can worsen performance under transient conditions if too much filtering is necessary. In [Lan14], the use of current oversampling was suggested to estimate the current slope via linear regression, which significantly improves the approximation of the current slopes but requires fast ADCs and considerable computational power. For those techniques that require the current derivative, such as INFORM and the arbitrary injection approach, current derivative sensors can theoretically be used. However, the usage of two or three current derivative sensors additionally to the current sensors that are anyways needed for current control is usually too expensive and may easily exceed the costs of a mechanical position sensor. Generally, using higher quality current sensors can of course help improving the signal-to-noise ratio, however this also increases the cost and contradicts the idea of only using hardware that is necessary anyway.

3.2.3. Techniques Based on the Zero-Sequence Voltage

A possible alternative are techniques that obtain anisotropy information via the zero-sequence voltage. To measure the zero-sequence voltage, access to the neutral point of the machine and additional measurement circuitry is required, the latter of which will be discussed in the next chapter. Despite this extra effort, using the zero-sequence voltage to obtain anisotropy information typically provides a more attractive signal-to-noise ratio compared to current-based alternatives. One reason is the generally better measurability of voltages but what is probably more important is that a signal level and not its slope is measured and that the zero-sequence voltage is typically largely caused by the magnetic anisotropy so that the conversion range of the ADC can be efficiently used. For techniques based on the zero-sequence voltage, current sensors are required "only"

for the control of the d- and q-axis current and to compensate for current-dependent estimation errors. If this enables the use of less expensive current sensors compared to the previous group of techniques, the overall cost for achieving position estimates with an equivalent signal-to-noise ratio can potentially be significantly reduced.

The first authors to describe an anisotropy-based technique using the zero-sequence voltage were likely Holtz, Jiang and Pan in [JH97]. In the dissertation of Jiang [Jia00], the approach was described in more detail. The works focused on an application to induction machines and the zero-sequence voltage was measured during the application of opposing active voltage vectors to acquire the desired anisotropy information. Due to the relatively similar kind of excitation, the technique exhibits strong parallels to the INFORM technique.

In [Str19] and [TMH+11a; TMH+11b; TMM+12], a rather similar estimation approach has been described for the application to PMSMs under the name "Direct Flux Control" by Thiemann et al. Compared to [JH97; Jia00], a different pulse pattern and measurement sequence has been used, involving also zero vectors for the measurement. In [Man13], additional improvements have been presented, such as a signal transformation that can improve the position estimation and an alternative pulse pattern. It should be mentioned that [TMH+11a; TMH+11b; TMM+12; Man13] were found to contain a considerable amount of unsubstantiated or false statements so that the information provided there should be treated with additional care. As an example, in [TMH+11a] the authors claimed that, compared to works of Jiang and Pan, their approach does not need to separate secondary anisotropies by spatial filtering. However, this must be correctly attributed to the use of a permanent magnet machine with no significant secondary anisotropies and is not a result of the chosen pulse pattern or other differences in the estimation approach. Nevertheless, the works are included here as they still contain several relevant aspects such as the mentioned signal transformation.

Another noteworthy work was presented in [ITSA16]. The estimation approach is generally comparable to the works of the two previous researcher groups; yet, some differences exist. The zero-sequence voltage itself and not its differences between different voltage vectors was used, so that resistive and BEMF-related terms would not be eliminated. This approach is therefore suitable mainly for low speeds.

Similar to current-based techniques, there have also been works that inject high frequency voltage signals and measure the resulting high frequency response in the zero-sequence voltage. Using rotating injection, techniques have been proposed for estimating the orientation of the rotor flux [CST99] and the rotor position [BDGG05] in induction

machines and for estimating the rotor position in PMSMs [CSTT00]. Techniques to estimate the rotor position of a PMSM with an alternating injection were proposed in [XZ16a; XZ16b] for sinusoidal and square-wave voltage signals. It should be noted that, assuming only one or a few measurement per modulation period, analog filters such as bandpass filters or a combination of a notch and a lowpass filter [BDGG05] are necessary to separate the high frequency signal response, as the zero-sequence voltage signal will have a staircase shape due to the discrete switching states of the inverter. Additionally, because the signal frequency must lie below the switching frequency to be of approximately sinusoidal shape, the injected signal is more likely to fall into the audible frequency range and thus lead to audible noise.

During the work on this thesis, an additional noteworthy work has been published in [Wer18]. This work analyzes sensorless control of PMSMs using voltage measurements in general and zero-sequence voltage measurements in particular. The theoretical part of [Wer18] has clear parallels to the analysis conducted in this thesis, such as the usage of the '$\alpha\beta0$' and 'dq0' reference frames and comparisons with current-based anisotropy methods that become possible as a result. For experimental investigations, the work focused however on an excitation approach which can be implemented with standard modulators and on operation at low speed. Another work that is worth mentioning is [GMKN19], which introduced a model in the Laplace domain to describe the dynamic behavior of the neutral point voltage and suggested the use of an integrator circuit for the measurement of the zero-sequence voltage.

3.3. Summary

Anisotropy-based techniques allow to estimate the position of synchronuous and induction machines at any speed including low speeds and standstill. Most works make use of current measurements, since current sensors are anyway present in modern drive systems. However, measuring the zero-sequence voltage can be an interesting alternative. The main advantage of zero-sequence voltage based techniques is the attractive signal-to-noise ratio that can potentially be achieved due to the measurement of voltages instead of currents or current slopes and due to the more efficient use of the ADC.

Table 3.1 provides an overview of the publications discussed in the previous two sections, grouped by their measured quantities and by the kind of excitation. The number of publications provided for each group is not related to the number of works that exist in the scientific literature.

Table 3.1.: Measured quantities and kind of excitation for the references in this chapter.

		Measurement	
		currents ($\alpha\beta$)	zero-sequence voltage
Applicable to		star-connected machines delta-connected machines	star-connected machines
Excitation	discrete voltage vectors (PWM)	[Sch88], [Sch96], [PLK11], [Lan14], [Pau14]	[JH97], [Jia00], [HP02], [TMH+11b], [TMH+11a], [TMM+12], [Man13], [ITSA16], [Wer18], [Str19], [GMKN19]
	alternating injection	[LKH03], [Hol06]	[XZ16a], [XZ16b]
	rotating injection	[JL95]	[CST99], [CSTT00], [BDGG05]

4. Anisotropy Information in the Zero-Sequence Voltage

The physical principle that is exploited in anisotropy-based estimation techniques is the position dependence of a machines' inductances in stationary coordinates. The position-dependent inductances affect the relation between the voltages applied at the terminals and the current changes in the phases that is exploited in anisotropy-based techniques using current measurements. If the machine is star-connected, variations in the inductances can also cause changes in the zero-sequence voltage that can be exploited for the purpose of position estimation.

In this chapter, the anisotropy information obtainable via the zero-sequence voltage is analyzed. First, principle possibilities for the measurement of the zero-sequence voltage are described. Then, the relations between a machine's self- and mutual inductances, the voltages at the machine terminals and the resulting zero-sequence voltage are derived based on the machine model described in chapter 2. It becomes clear that for techniques based on the zero-sequence voltage the anisotropy information is contained in inductance ratios, which are given for the two stationary reference frames. The form of these inductance ratios is presented first for a general fundamental wave inductance matrix and then for selected special cases. The latter serve two purposes. On the one hand, they are used in chapter 5 to derive estimation functions that are free of machine parameters. On the other hand, they offer additional insights and reveal theoretical extreme cases where estimation is possible either only for current-based techniques or only for techniques based on the zero-sequence voltage. Key findings of the investigations in this chapter have already been published in [SKN19] and partially in [SGN19].

4.1. Measurement Approaches for the Zero-Sequence Voltage

To measure the zero-sequence voltages, there exist roughly three different possibilites that were described also in [BDGG05]. The first possibility is to measure all three phase

voltages individually and sum them according to

$$u_0 = u_\mathrm{a} + u_\mathrm{b} + u_\mathrm{c} \tag{4.1}$$

as was done for example in [Jia00]. While this is principally a straightforward approach, the individual measurement of the three voltages between the terminals and the neutral point results in considerable measurement effort. If the subsequent summation is done after conversion to the digital domain, the conversion range of the ADC will not be used efficiently because the zero-sequence voltage is usually rather small in relation to the DC link voltage. Summing the signals with analog circuitry before conversion is therefore preferable but further increases the complexity of the measurement circuit.

The second possibility is to measure only the voltage neutral point voltage with reference to a fixed potential such as the low potential or the midpoint of the DC link. According to (2.22), the relation between the zero-sequence voltage and the neutral point voltage is

$$u_\mathrm{N} = u_\mathrm{term,0} - u_0 \ . \tag{4.2}$$

During operation, the common-mode component $u_\mathrm{term,0}$ changes with the different inverter switching states and causes large jumps in the neutral point voltage. $u_\mathrm{term,0}$ can be assumed as known from the respective switching state and can be subtracted digitally from the measured neutral point voltage to obtain the (negative) zero-sequence voltage. Differences between the assumed and the actual $u_\mathrm{term,0}$, for example due to voltage drops over the power switches, can however lead to additional errors for such an approach. Another drawback with this approach is that the large varying DC components in u_N lead to an inefficient use of the ADC's resolution.

The last possibility consists of measuring the difference between the neutral point and an artificial neutral point as shown in Fig. 4.1. The artificial neutral point consists of three resistors connected to the machine terminals and replicates the common-mode component $u_\mathrm{term,0}$:

$$u_\mathrm{AN} = \frac{1}{3}\left(u_\mathrm{term,a} + u_\mathrm{term,b} + u_\mathrm{term,c}\right) = u_\mathrm{term,0} \ . \tag{4.3}$$

Accordingly, the difference of the two voltages is the negative zero-sequence voltage

$$u_\mathrm{NAN} = u_\mathrm{N} - u_\mathrm{AN} = u_\mathrm{N} - u_\mathrm{term,0} = -u_0 \ . \tag{4.4}$$

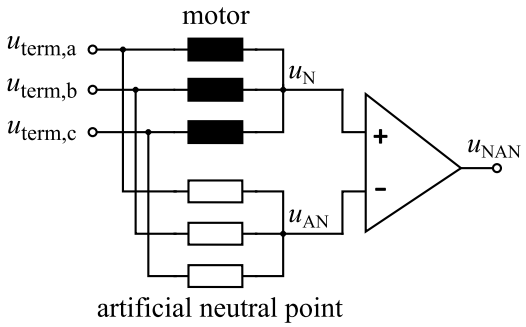

Figure 4.1.: Measuring the zero-sequence voltage as the difference between the motor neutral point and an artificial neutral point

In general, the analog subtraction of an artificial neutral point voltage is the approach that is most commonly used in recent works [BDGG05; Wer18]. Similar to the first approach, it includes an inherent removal of the common mode part $u_{\mathrm{term,0}}$ but the complexity of the measurement circuit is significantly reduced in comparison. For these reasons, this measurement approach is also used in this thesis. The actual measurement circuit will be described in more detail in section 6.6. As a convention, the term zero-sequence voltage will be used as a general term for both u_0 and u_{NAN} which differ only in sign.

For completeness, a particular variant that lies somewhere between the second and third approach shall be mentioned. In [ITSA16], two reference voltages at $u_{\mathrm{DC}}/3$ and $2 \cdot u_{\mathrm{DC}}/3$ were used for subtraction instead of an artificial neutral point. The two reference voltages corresponded to the levels of $u_{\mathrm{term,0}}$ at the switching states used for measurements and were created from u_{DC} via resistive voltage dividers. According to the authors, this approach allowed the use of less expensive amplifiers. However, two separate subtraction amplifiers and measurement paths are necessary. Voltage drops over the power switches are also not reflected in the reference voltages.

4.2. Analysis of Anisotropy Infomation in the Zero-Sequence Voltage

4.2.1. Analysis in the Physical Reference Frame 'abc'

Let us now analyze the anisotropy information that can be obtained from the zero-sequence voltage, starting with considerations in the 'abc' reference frame. Note that, for the moment, the inductance matrix is kept general to make some basic observations first. The position dependence of the inductance matrix is introduced subsequently in section 4.3.

According to equation (2.56), the phase voltages in the 'abc' reference frame are described by

$$\boldsymbol{u}^{\mathrm{p}} = \boldsymbol{R}^{\mathrm{p}}\boldsymbol{i}^{\mathrm{p}} + \boldsymbol{L}^{\mathrm{p}}\left(\frac{\mathrm{d}}{\mathrm{d}t}\boldsymbol{i}^{\mathrm{p}}\right) + \omega \cdot \left(\left(\frac{\mathrm{d}}{\mathrm{d}\varphi}\boldsymbol{L}^{\mathrm{r}}\right)\boldsymbol{i}^{\mathrm{p}} + \frac{\mathrm{d}}{\mathrm{d}\varphi}\boldsymbol{\Psi}^{\mathrm{p}}_{\mathrm{PM}}\right) \tag{4.5}$$

with

$$\boldsymbol{u}^{\mathrm{p}} = \boldsymbol{u}^{\mathrm{p}}_{\mathrm{term}} - u_{\mathrm{N}}\begin{bmatrix}1\\1\\1\end{bmatrix} . \tag{4.6}$$

When a switching event occurs at the inverter, the voltages at the machine terminals change almost instantly. The phase currents and the voltages that are induced by the rotor movement however stay almost unchanged directly before and after a switching event. Therefore, we can separate a voltage vector $\boldsymbol{u}_{\mathrm{slow}}$ including resistive voltage drops and the voltages induced by rotor movement, leading to

$$\boldsymbol{u}^{\mathrm{p}} = \boldsymbol{L}^{\mathrm{p}}\left(\frac{\mathrm{d}}{\mathrm{d}t}\boldsymbol{i}^{\mathrm{p}}\right) + \boldsymbol{u}^{\mathrm{p}}_{\mathrm{slow}} \tag{4.7}$$

$$\boldsymbol{u}^{\mathrm{p}}_{\mathrm{slow}} = \boldsymbol{R}^{\mathrm{p}}\boldsymbol{i}^{\mathrm{p}} + \omega\left(\left(\frac{\mathrm{d}}{\mathrm{d}\varphi}\boldsymbol{L}^{\mathrm{p}}\right)\boldsymbol{i}^{\mathrm{p}} + \frac{\mathrm{d}}{\mathrm{d}\varphi}\boldsymbol{\Psi}^{\mathrm{p}}_{\mathrm{PM}}\right) . \tag{4.8}$$

Generally, the terms in $\boldsymbol{u}^{\mathrm{p}}_{\mathrm{slow}}$ can be considered constant within short periods of time, in particular such that are shorter than a switching period. However, since the induced voltages scale with speed, this assumption becomes somewhat less accurate with increasing rotor speed.

By inserting (4.6) into (4.7), one obtains

$$\boldsymbol{u}_{\mathrm{term}}^{\mathrm{p}} - u_{\mathrm{N}} \begin{bmatrix} 1 \\ 1 \\ 1 \end{bmatrix} = \boldsymbol{L}^{\mathrm{p}} \left(\frac{\mathrm{d}}{\mathrm{d}t} \boldsymbol{i}^{\mathrm{p}} \right) + \boldsymbol{u}_{\mathrm{slow}}^{\mathrm{p}} \tag{4.9}$$

$$u_{\mathrm{N}} \begin{bmatrix} 1 \\ 1 \\ 1 \end{bmatrix} = \boldsymbol{u}_{\mathrm{term}}^{\mathrm{p}} - \boldsymbol{L}^{\mathrm{p}} \left(\frac{\mathrm{d}}{\mathrm{d}t} \boldsymbol{i}^{\mathrm{p}} \right) - \boldsymbol{u}_{\mathrm{slow}}^{\mathrm{p}} \ . \tag{4.10}$$

In the next step the derivatives of the currents are eliminated from the equation. By multiplying with the inverse inductance matrix on the left side,

$$u_{\mathrm{N}} \boldsymbol{L}^{\mathrm{p}^{-1}} \begin{bmatrix} 1 \\ 1 \\ 1 \end{bmatrix} = \boldsymbol{L}^{\mathrm{p}^{-1}} \cdot \left(\boldsymbol{u}_{\mathrm{term}}^{\mathrm{p}} - \boldsymbol{L}^{\mathrm{p}} \left(\frac{\mathrm{d}}{\mathrm{d}t} \boldsymbol{i}^{\mathrm{p}} \right) - \boldsymbol{u}_{\mathrm{slow}}^{\mathrm{p}} \right) \tag{4.11}$$

$$u_{\mathrm{N}} \boldsymbol{L}^{\mathrm{p}^{-1}} \begin{bmatrix} 1 \\ 1 \\ 1 \end{bmatrix} = \boldsymbol{L}^{\mathrm{p}^{-1}} \cdot \left(\boldsymbol{u}_{\mathrm{term}}^{\mathrm{p}} - \boldsymbol{u}_{\mathrm{slow}}^{\mathrm{p}} \right) - \frac{\mathrm{d}}{\mathrm{d}t} \boldsymbol{i}^{\mathrm{p}} \tag{4.12}$$

is obtained. Multiplying with the row vector $\begin{bmatrix} 1 & 1 & 1 \end{bmatrix}$ leads to

$$u_{\mathrm{N}} \begin{bmatrix} 1 & 1 & 1 \end{bmatrix} \boldsymbol{L}^{\mathrm{p}^{-1}} \begin{bmatrix} 1 \\ 1 \\ 1 \end{bmatrix} = \begin{bmatrix} 1 & 1 & 1 \end{bmatrix} \boldsymbol{L}^{\mathrm{p}^{-1}} \left(\boldsymbol{u}_{\mathrm{term}}^{\mathrm{p}} - \boldsymbol{u}_{\mathrm{slow}}^{\mathrm{p}} \right) - \begin{bmatrix} 1 & 1 & 1 \end{bmatrix} \left(\frac{\mathrm{d}}{\mathrm{d}t} \boldsymbol{i}^{\mathrm{p}} \right) \ . \tag{4.13}$$

Because

$$\begin{bmatrix} 1 & 1 & 1 \end{bmatrix} \left(\frac{\mathrm{d}}{\mathrm{d}t} \boldsymbol{i}^{\mathrm{p}} \right) = \frac{\mathrm{d}}{\mathrm{d}t} i_0 = 0 \tag{4.14}$$

this equation is simplified to

$$u_{\mathrm{N}} \begin{bmatrix} 1 & 1 & 1 \end{bmatrix} \boldsymbol{L}^{\mathrm{p}^{-1}} \begin{bmatrix} 1 \\ 1 \\ 1 \end{bmatrix} = \begin{bmatrix} 1 & 1 & 1 \end{bmatrix} \boldsymbol{L}^{\mathrm{p}^{-1}} \left(\boldsymbol{u}_{\mathrm{term}}^{\mathrm{p}} - \boldsymbol{u}_{\mathrm{slow}}^{\mathrm{p}} \right) \ . \tag{4.15}$$

The neutral point voltage is then finally obtained as

$$u_{\mathrm{N}} = \left(\begin{bmatrix} 1 & 1 & 1 \end{bmatrix} \boldsymbol{L}^{\mathrm{p}^{-1}} \begin{bmatrix} 1 \\ 1 \\ 1 \end{bmatrix} \right)^{-1} \begin{bmatrix} 1 & 1 & 1 \end{bmatrix} \boldsymbol{L}^{\mathrm{p}^{-1}} \left(\boldsymbol{u}^{\mathrm{p}}_{\mathrm{term}} - \boldsymbol{u}^{\mathrm{p}}_{\mathrm{slow}} \right) \tag{4.16}$$

$$u_{\mathrm{N}} = \boldsymbol{\kappa}^{\mathrm{p}} \left(\boldsymbol{u}^{\mathrm{p}}_{\mathrm{term}} - \boldsymbol{u}^{\mathrm{p}}_{\mathrm{slow}} \right) \tag{4.17}$$

with the inductance ratio vector

$$\boldsymbol{\kappa}^{\mathrm{p}} = \begin{bmatrix} \kappa_{\mathrm{a}} & \kappa_{\mathrm{b}} & \kappa_{\mathrm{c}} \end{bmatrix} = \left(\begin{bmatrix} 1 & 1 & 1 \end{bmatrix} \boldsymbol{L}^{\mathrm{p}^{-1}} \begin{bmatrix} 1 \\ 1 \\ 1 \end{bmatrix} \right)^{-1} \begin{bmatrix} 1 & 1 & 1 \end{bmatrix} \boldsymbol{L}^{\mathrm{p}^{-1}} \tag{4.18}$$

$$\begin{aligned} &= \frac{1}{L_{\mathrm{bb}}L_{\mathrm{cc}} + L_{\mathrm{aa}}L_{\mathrm{cc}} + L_{\mathrm{aa}}L_{\mathrm{bb}} - L_{\mathrm{bc}}^2 - L_{\mathrm{ca}}^2 - L_{\mathrm{ab}}^2} \\ &\quad +2\left(L_{\mathrm{ab}}L_{\mathrm{ca}} + L_{\mathrm{ab}}L_{\mathrm{bc}} + L_{\mathrm{bc}}L_{\mathrm{ca}} - L_{\mathrm{aa}}L_{\mathrm{bc}} - L_{\mathrm{bb}}L_{\mathrm{ca}} - L_{\mathrm{cc}}L_{\mathrm{ab}}\right) \\ &\quad \cdot \begin{bmatrix} L_{\mathrm{bb}}L_{\mathrm{cc}} - L_{\mathrm{cc}}L_{\mathrm{ab}} - L_{\mathrm{bb}}L_{\mathrm{ca}} + L_{\mathrm{ab}}L_{\mathrm{bc}} + L_{\mathrm{bc}}L_{\mathrm{ca}} - L_{\mathrm{bc}}^2 \\ L_{\mathrm{cc}}L_{\mathrm{aa}} - L_{\mathrm{aa}}L_{\mathrm{bc}} - L_{\mathrm{cc}}L_{\mathrm{ab}} + L_{\mathrm{bc}}L_{\mathrm{ca}} + L_{\mathrm{ca}}L_{\mathrm{ab}} - L_{\mathrm{ca}}^2 \\ L_{\mathrm{aa}}L_{\mathrm{bb}} - L_{\mathrm{bb}}L_{\mathrm{ca}} - L_{\mathrm{aa}}L_{\mathrm{bc}} + L_{\mathrm{ca}}L_{\mathrm{ab}} + L_{\mathrm{ab}}L_{\mathrm{bc}} - L_{\mathrm{ab}}^2 \end{bmatrix}^{\mathrm{T}} \end{aligned} \tag{4.19}$$

which is a row vector. It can be observed that the sum of the three inductance ratios is equal to one:

$$\kappa_{\mathrm{a}} + \kappa_{\mathrm{b}} + \kappa_{\mathrm{c}} = \frac{\begin{array}{l} L_{\mathrm{bb}}L_{\mathrm{cc}} + L_{\mathrm{aa}}L_{\mathrm{cc}} + L_{\mathrm{aa}}L_{\mathrm{bb}} - L_{\mathrm{bc}}^2 - L_{\mathrm{ca}}^2 - L_{\mathrm{ab}}^2 \\ +2\left(L_{\mathrm{ab}}L_{\mathrm{ca}} + L_{\mathrm{ab}}L_{\mathrm{bc}} + L_{\mathrm{bc}}L_{\mathrm{ca}} - L_{\mathrm{aa}}L_{\mathrm{bc}} - L_{\mathrm{bb}}L_{\mathrm{ca}} - L_{\mathrm{cc}}L_{\mathrm{ab}}\right) \end{array}}{\begin{array}{l} L_{\mathrm{bb}}L_{\mathrm{cc}} + L_{\mathrm{aa}}L_{\mathrm{cc}} + L_{\mathrm{aa}}L_{\mathrm{bb}} - L_{\mathrm{bc}}^2 - L_{\mathrm{ca}}^2 - L_{\mathrm{ab}}^2 \\ +2\left(L_{\mathrm{ab}}L_{\mathrm{ca}} + L_{\mathrm{ab}}L_{\mathrm{bc}} + L_{\mathrm{bc}}L_{\mathrm{ca}} - L_{\mathrm{aa}}L_{\mathrm{bc}} - L_{\mathrm{bb}}L_{\mathrm{ca}} - L_{\mathrm{cc}}L_{\mathrm{ab}}\right) \end{array}} = 1\,. \tag{4.20}$$

Moreover, for a symmetric motor with $L_{\mathrm{aa}} = L_{\mathrm{bb}} = L_{\mathrm{cc}}$ and $L_{\mathrm{ab}} = L_{\mathrm{bc}} = L_{\mathrm{ca}}$, the inductance ratios κ_{a}, κ_{b} and κ_{c} are exactly 1/3. We can therefore consider this the isotropic part of the inductance ratios and define an anisotropic inductance ratio vector

$$\boldsymbol{\kappa}^{\mathrm{p}}_{\Delta} = \begin{bmatrix} \kappa_{\mathrm{a}} - \frac{1}{3} & \kappa_{\mathrm{b}} - \frac{1}{3} & \kappa_{\mathrm{c}} - \frac{1}{3} \end{bmatrix} \tag{4.21}$$

which differs from a zero vector if the motor features a detectable magnetic anisotropy.

If we write the neutral point voltage as the difference of the mean voltage at the

terminals and the zero-sequence voltage

$$u_{\mathrm{N}} = u_{\mathrm{term},0} - u_0 \tag{4.22}$$

and insert this into equation (4.17), we obtain

$$\begin{aligned} u_0 &= -\boldsymbol{\kappa}^{\mathrm{p}} \left(\boldsymbol{u}^{\mathrm{p}}_{\mathrm{term}} - \boldsymbol{u}^{\mathrm{p}}_{\mathrm{slow}} \right) + u_{\mathrm{term},0} && (4.23)\\ &= -\boldsymbol{\kappa}^{\mathrm{p}} \left(\boldsymbol{u}^{\mathrm{p}}_{\mathrm{term}} - \boldsymbol{u}^{\mathrm{p}}_{\mathrm{slow}} \right) + \begin{bmatrix} \frac{1}{3} & \frac{1}{3} & \frac{1}{3} \end{bmatrix} \boldsymbol{u}^{\mathrm{p}}_{\mathrm{term}} && (4.24)\\ &= -\left(\boldsymbol{\kappa}^{\mathrm{p}} - \begin{bmatrix} \frac{1}{3} & \frac{1}{3} & \frac{1}{3} \end{bmatrix} \right) \boldsymbol{u}^{\mathrm{p}}_{\mathrm{term}} + \boldsymbol{\kappa}^{\mathrm{p}} \boldsymbol{u}^{\mathrm{p}}_{\mathrm{slow}} && (4.25)\\ &= -\boldsymbol{\kappa}^{\mathrm{p}}_{\Delta} \boldsymbol{u}^{\mathrm{p}}_{\mathrm{term}} + \boldsymbol{\kappa}^{\mathrm{p}} \boldsymbol{u}^{\mathrm{p}}_{\mathrm{slow}} \, . && (4.26) \end{aligned}$$

In the zero-sequence voltage, only the anisotropic part of the inductance ratios multiplies with the terminal voltage vector. Therefore, the measurement of the zero-sequence voltage is more useful than measuring the voltage between the neutral point and a fixed reference potential that was given by (4.17). The vector of slowly changing voltages, however, still multiplies with the overall inductance ratio vector.

Additionally, one important special case shall be considered here. By assuming a diagonal inductance matrix

$$\boldsymbol{L}^{\mathrm{p}} = \begin{bmatrix} L_{\mathrm{aa}} & 0 & 0 \\ 0 & L_{\mathrm{bb}} & 0 \\ 0 & 0 & L_{\mathrm{cc}} \end{bmatrix} \tag{4.27}$$

$\boldsymbol{\kappa}^{\mathrm{p}}$ is simplified significantly to

$$\begin{aligned} \boldsymbol{\kappa}^{\mathrm{p}} &= \frac{1}{L_{\mathrm{bb}}L_{\mathrm{cc}} + L_{\mathrm{aa}}L_{\mathrm{cc}} + L_{\mathrm{aa}}L_{\mathrm{bb}}} \begin{bmatrix} L_{\mathrm{bb}}L_{\mathrm{cc}} & L_{\mathrm{cc}}L_{\mathrm{aa}} & L_{\mathrm{aa}}L_{\mathrm{bb}} \end{bmatrix} && (4.28)\\ &= \begin{bmatrix} \frac{\frac{1}{L_{\mathrm{aa}}}}{\frac{1}{L_{\mathrm{aa}}} + \frac{1}{L_{\mathrm{bb}}} + \frac{1}{L_{\mathrm{cc}}}} & \frac{\frac{1}{L_{\mathrm{bb}}}}{\frac{1}{L_{\mathrm{aa}}} + \frac{1}{L_{\mathrm{bb}}} + \frac{1}{L_{\mathrm{cc}}}} & \frac{\frac{1}{L_{\mathrm{cc}}}}{\frac{1}{L_{\mathrm{aa}}} + \frac{1}{L_{\mathrm{bb}}} + \frac{1}{L_{\mathrm{cc}}}} \end{bmatrix} . && (4.29) \end{aligned}$$

4.2.2. Analysis in the Orthogonal Stator Frame 'αβ0'

The physical 'abc' frame enables direct relation to the three phases of the machine and the switching states of the inverter. However, for many considerations it is helpful to use the orthogonal stator frame 'αβ0' that can simplify some equations and make certain connections clearer.

According to (2.55), the phase voltages in the 'αβ0' frame were

$$\boldsymbol{u}^{\mathrm{s}} = \boldsymbol{R}^{\mathrm{s}}\boldsymbol{i}^{\mathrm{s}} + \boldsymbol{L}^{\mathrm{s}}\left(\frac{\mathrm{d}}{\mathrm{d}t}\boldsymbol{i}^{\mathrm{s}}\right) + \omega \cdot \left(\left(\frac{\mathrm{d}}{\mathrm{d}\varphi}\boldsymbol{L}^{\mathrm{s}}\right)\boldsymbol{i}^{\mathrm{s}} + \frac{\mathrm{d}}{\mathrm{d}\varphi}\boldsymbol{\Psi}^{\mathrm{s}}_{\mathrm{PM}}\right) . \tag{4.30}$$

Looking only at the zero-sequence voltage, i.e. the third component of this vectorial equation, one finds

$$\begin{aligned} u_0 = &\begin{bmatrix} R_{0\alpha} & R_{0\beta} & R_{00} \end{bmatrix}\boldsymbol{i}^{\mathrm{s}} + \begin{bmatrix} L_{0\alpha} & L_{0\beta} & L_{00} \end{bmatrix}\left(\frac{\mathrm{d}}{\mathrm{d}t}\boldsymbol{i}^{\mathrm{s}}\right) \\ &+ \omega\left(\left(\frac{\mathrm{d}}{\mathrm{d}\varphi}\begin{bmatrix} L_{0\alpha} & L_{0\beta} & L_{00} \end{bmatrix}\right)\boldsymbol{i}^{\mathrm{s}} + \frac{\mathrm{d}}{\mathrm{d}\varphi}\Psi_{\mathrm{PM},0}\right) . \end{aligned} \tag{4.31}$$

In combination with $i_0 = 0$, this simplifies to

$$u_0 = R_{0\alpha}i_\alpha + R_{0\beta}i_\beta + L_{0\alpha}\frac{\mathrm{d}}{\mathrm{d}t}i_\alpha + L_{0\beta}\frac{\mathrm{d}}{\mathrm{d}t}i_\beta + \omega \cdot \left(\left(\frac{\mathrm{d}}{\mathrm{d}\varphi}L_{0\alpha}\right)i_\alpha\left(\frac{\mathrm{d}}{\mathrm{d}t}L_{0\beta}\right)i_\beta + \frac{\mathrm{d}}{\mathrm{d}\varphi}\Psi_{\mathrm{PM},0}\right) . \tag{4.32}$$

From this equation it is clear that a zero-sequence voltage is only produced if there exist couplings with the zero-sequence axis in the resistance or inductance matrix or if there is a zero-sequence component in the voltage induced by the rotation of the permanent magnets.

Analogously to the procedure in the physical reference frame, we can separate the slowly changing voltage part in (4.30) and write

$$\boldsymbol{u}^{\mathrm{s}} = \boldsymbol{L}^{\mathrm{s}}\left(\frac{\mathrm{d}}{\mathrm{d}t}\boldsymbol{i}^{\mathrm{s}}\right) + \boldsymbol{u}^{\mathrm{s}}_{\mathrm{slow}} \tag{4.33}$$

$$\boldsymbol{u}^{\mathrm{s}}_{\mathrm{slow}} = \boldsymbol{R}^{\mathrm{s}}\boldsymbol{i}^{\mathrm{s}} + \omega\left(\left(\frac{\mathrm{d}}{\mathrm{d}\varphi}\boldsymbol{L}^{\mathrm{s}}\right)\boldsymbol{i}^{\mathrm{s}} + \frac{\mathrm{d}}{\mathrm{d}\varphi}\boldsymbol{\Psi}^{\mathrm{s}}_{\mathrm{PM}}\right) . \tag{4.34}$$

Equation (4.33) can be written as

$$\begin{bmatrix} u_\alpha \\ u_\beta \\ u_0 \end{bmatrix} = \begin{bmatrix} 0 \\ 0 \\ u_0 \end{bmatrix} + \begin{bmatrix} u_\alpha \\ u_\beta \\ 0 \end{bmatrix} = \boldsymbol{L}^{\mathrm{s}}\left(\frac{\mathrm{d}}{\mathrm{d}t}\boldsymbol{i}^{\mathrm{s}}\right) + \boldsymbol{u}^{\mathrm{s}}_{\mathrm{slow}} . \tag{4.35}$$

Note that $u_\alpha = u_{\mathrm{term},\alpha}$ and $u_\beta = u_{\mathrm{term},\beta}$ according to (2.19). Therefore, we can write

$$\begin{bmatrix} 0 \\ 0 \\ u_0 \end{bmatrix} = - \begin{bmatrix} u_{\mathrm{term},\alpha} \\ u_{\mathrm{term},\beta} \\ 0 \end{bmatrix} + \boldsymbol{L}^{\mathrm{s}} \left(\frac{\mathrm{d}}{\mathrm{d}t} \boldsymbol{i}^{\mathrm{s}} \right) + \boldsymbol{u}^{\mathrm{s}}_{\mathrm{slow}} \, . \tag{4.36}$$

By left-side multiplication with $\begin{bmatrix} 0 & 0 & 1 \end{bmatrix} \boldsymbol{L}^{\mathrm{s}^{-1}}$, one obtains

$$\begin{aligned} \begin{bmatrix} 0 & 0 & 1 \end{bmatrix} \boldsymbol{L}^{\mathrm{s}^{-1}} \begin{bmatrix} 0 \\ 0 \\ u_0 \end{bmatrix} = &- \begin{bmatrix} 0 & 0 & 1 \end{bmatrix} \boldsymbol{L}^{\mathrm{s}^{-1}} \begin{bmatrix} u_{\mathrm{term},\alpha} \\ u_{\mathrm{term},\beta} \\ 0 \end{bmatrix} + \begin{bmatrix} 0 & 0 & 1 \end{bmatrix} \boldsymbol{L}^{\mathrm{s}^{-1}} \boldsymbol{L}^{\mathrm{s}} \left(\frac{\mathrm{d}}{\mathrm{d}t} \boldsymbol{i}^{\mathrm{s}} \right) \\ &+ \begin{bmatrix} 0 & 0 & 1 \end{bmatrix} \boldsymbol{L}^{\mathrm{s}^{-1}} \boldsymbol{u}^{\mathrm{s}}_{\mathrm{slow}} \, . \end{aligned} \tag{4.37}$$

With $i_0 = 0$, one obtains

$$u_0 \begin{bmatrix} 0 & 0 & 1 \end{bmatrix} \boldsymbol{L}^{\mathrm{s}^{-1}} \begin{bmatrix} 0 \\ 0 \\ 1 \end{bmatrix} = - \begin{bmatrix} 0 & 0 & 1 \end{bmatrix} \boldsymbol{L}^{\mathrm{s}^{-1}} \left(\begin{bmatrix} u_{\mathrm{term},\alpha} \\ u_{\mathrm{term},\beta} \\ 0 \end{bmatrix} - \boldsymbol{u}^{\mathrm{s}}_{\mathrm{slow}} \right) \tag{4.38}$$

and finally

$$u_0 = - \left(\begin{bmatrix} 0 & 0 & 1 \end{bmatrix} \boldsymbol{L}^{\mathrm{s}^{-1}} \begin{bmatrix} 0 \\ 0 \\ 1 \end{bmatrix} \right)^{-1} \cdot \begin{bmatrix} 0 & 0 & 1 \end{bmatrix} \boldsymbol{L}^{\mathrm{s}^{-1}} \left(\begin{bmatrix} u_{\mathrm{term},\alpha} \\ u_{\mathrm{term},\beta} \\ 0 \end{bmatrix} - \boldsymbol{u}^{\mathrm{s}}_{\mathrm{slow}} \right). \tag{4.39}$$

By defining the admittance matrix $\boldsymbol{Y}^{\mathrm{s}}$ as the inverse of the inductance matrix

$$\boldsymbol{Y}^{\mathrm{s}} = \begin{bmatrix} Y_{\alpha\alpha} & Y_{\alpha\beta} & 2Y_{0\alpha} \\ Y_{\alpha\beta} & Y_{\beta\beta} & 2Y_{0\beta} \\ Y_{0\alpha} & Y_{0\beta} & Y_{00} \end{bmatrix} = \boldsymbol{L}^{\mathrm{s}^{-1}} \tag{4.40}$$

one can write

$$u_0 = -\frac{1}{Y_{00}} \begin{bmatrix} Y_{0\alpha} & Y_{0\beta} & Y_{00} \end{bmatrix} \cdot \left(\begin{bmatrix} u_{\mathrm{term},\alpha} \\ u_{\mathrm{term},\beta} \\ 0 \end{bmatrix} - \boldsymbol{u}^{\mathrm{s}}_{\mathrm{slow}} \right) \tag{4.41}$$

$$= -\boldsymbol{\kappa}^{\mathrm{s}} \cdot \left(\begin{bmatrix} u_{\mathrm{term},\alpha} \\ u_{\mathrm{term},\beta} \\ 0 \end{bmatrix} - \boldsymbol{u}^{\mathrm{s}}_{\mathrm{slow}} \right) \tag{4.42}$$

with the inductance ratio vector

$$\boldsymbol{\kappa}^{\mathrm{s}} = \begin{bmatrix} \kappa_\alpha & \kappa_\beta & 1 \end{bmatrix} = \begin{bmatrix} \frac{Y_{0\alpha}}{Y_{00}} & \frac{Y_{0\beta}}{Y_{00}} & 1 \end{bmatrix} . \tag{4.43}$$

u_0 can further be written as

$$u_0 = -\left(\boldsymbol{\kappa}^{\mathrm{s}} - \begin{bmatrix} 0 & 0 & 1 \end{bmatrix} \right) \begin{bmatrix} u_{\mathrm{term},\alpha} \\ u_{\mathrm{term},\beta} \\ u_{\mathrm{term},0} \end{bmatrix} + \boldsymbol{\kappa}^{\mathrm{s}} \boldsymbol{u}^{\mathrm{s}}_{\mathrm{slow}} \tag{4.44}$$

$$= -\left(\boldsymbol{\kappa}^{\mathrm{s}} - \begin{bmatrix} 0 & 0 & 1 \end{bmatrix} \right) \boldsymbol{u}^{\mathrm{s}}_{\mathrm{term}} + \boldsymbol{\kappa}^{\mathrm{s}} \boldsymbol{u}^{\mathrm{s}}_{\mathrm{slow}} \tag{4.45}$$

$$= -\boldsymbol{\kappa}^{\mathrm{s}}_{\Delta} \boldsymbol{u}^{\mathrm{s}}_{\mathrm{term}} + \boldsymbol{\kappa}^{\mathrm{s}} \boldsymbol{u}^{\mathrm{s}}_{\mathrm{slow}} \tag{4.46}$$

with the anisotropic inductance ratio vector

$$\boldsymbol{\kappa}^{\mathrm{s}}_{\Delta} = \begin{bmatrix} \kappa_\alpha & \kappa_\beta & 0 \end{bmatrix} . \tag{4.47}$$

The α- and β-components of the anisotropic inductance ratio vector $\boldsymbol{\kappa}^{\mathrm{s}}_{\Delta}$ are identical to those of the overall inductance ratio vector $\boldsymbol{\kappa}^{\mathrm{s}}$. Compared to the zero-sequence voltage, the neutral point voltage includes also the zero-sequence part of the terminal voltages

$$u_{\mathrm{N}} = -u_0 + u_{\mathrm{term},0} \tag{4.48}$$

$$= \left(\begin{bmatrix} \kappa_\alpha & \kappa_\beta & 0 \end{bmatrix} + \begin{bmatrix} 0 & 0 & 1 \end{bmatrix} \right) \boldsymbol{u}^{\mathrm{s}}_{\mathrm{term}} + \boldsymbol{\kappa}^{\mathrm{s}} \boldsymbol{u}^{\mathrm{s}}_{\mathrm{slow}} \tag{4.49}$$

$$= \boldsymbol{\kappa}^{\mathrm{s}} \boldsymbol{u}^{\mathrm{s}}_{\mathrm{term}} - \boldsymbol{\kappa}^{\mathrm{s}} \boldsymbol{u}^{\mathrm{s}}_{\mathrm{slow}} \tag{4.50}$$

$$= \boldsymbol{\kappa}^{\mathrm{s}} \left(\boldsymbol{u}^{\mathrm{s}}_{\mathrm{term}} - \boldsymbol{u}^{\mathrm{s}}_{\mathrm{slow}} \right) . \tag{4.51}$$

To gain some insight into the nature of the inductance ratios κ_α and κ_β, it is worth to

take a closer look at the inverse inductance matrix

$$\begin{aligned}\boldsymbol{Y}^{\mathrm{s}} = \boldsymbol{L}^{\mathrm{s}^{-1}} = &\frac{1}{L_{\alpha\alpha}L_{\beta\beta}L_{00} - 2L_{\alpha\alpha}L_{0\beta}^2 - 2L_{\beta\beta}L_{0\alpha}^2 - L_{00}L_{\alpha\beta}^2 + 4L_{\alpha\beta}L_{0\alpha}L_{0\beta}} \\ &\cdot \begin{bmatrix} L_{\beta\beta}L_{00} - 2L_{0\beta}^2 & 2L_{0\beta}L_{0\alpha} - L_{00}L_{\alpha\beta} & 2\left(L_{\alpha\beta}L_{0\beta} - L_{\beta\beta}L_{0\alpha}\right) \\ 2L_{0\beta}L_{0\alpha} - L_{00}L_{\alpha\beta} & L_{\alpha\alpha}L_{00} - 2L_{0\alpha}^2 & 2\left(L_{\alpha\beta}L_{0\alpha} - L_{\alpha\alpha}L_{0\beta}\right) \\ L_{\alpha\beta}L_{0\beta} - L_{\beta\beta}L_{0\alpha} & L_{\alpha\beta}L_{0\alpha} - L_{\alpha\alpha}L_{0\beta} & L_{\alpha\alpha}L_{\beta\beta} - L_{\alpha\beta}^2 \end{bmatrix}.\end{aligned} \tag{4.52}$$

Accordingly, the α- and β-components of the inductance ratio vector can be described by

$$\begin{aligned}\kappa_\alpha &= \frac{Y_{0\alpha}}{Y_{00}} = \frac{L_{\alpha\beta}L_{0\beta} - L_{\beta\beta}L_{0\alpha}}{L_{\alpha\alpha}L_{\beta\beta} - L_{\alpha\beta}^2} \\ \kappa_\beta &= \frac{Y_{0\beta}}{Y_{00}} = \frac{L_{\alpha\beta}L_{0\alpha} - L_{\alpha\alpha}L_{0\beta}}{L_{\alpha\alpha}L_{\beta\beta} - L_{\alpha\beta}^2}\end{aligned} \tag{4.53}$$

and u_{NAN} can finally be stated as

$$\begin{aligned}u_{\mathrm{NAN}} = -u_0 = &\begin{bmatrix} \frac{L_{\alpha\beta}L_{0\beta} - L_{\beta\beta}L_{0\alpha}}{L_{\alpha\alpha}L_{\beta\beta} - L_{\alpha\beta}^2} & \frac{L_{\alpha\beta}L_{0\alpha} - L_{\alpha\alpha}L_{0\beta}}{L_{\alpha\alpha}L_{\beta\beta} - L_{\alpha\beta}^2} & 0 \end{bmatrix} \boldsymbol{u}_{\mathrm{term}}^{\mathrm{s}} \\ &- \begin{bmatrix} \frac{L_{\alpha\beta}L_{0\beta} - L_{\beta\beta}L_{0\alpha}}{L_{\alpha\alpha}L_{\beta\beta} - L_{\alpha\beta}^2} & \frac{L_{\alpha\beta}L_{0\alpha} - L_{\alpha\alpha}L_{0\beta}}{L_{\alpha\alpha}L_{\beta\beta} - L_{\alpha\beta}^2} & 1 \end{bmatrix} \boldsymbol{u}_{\mathrm{slow}}^{\mathrm{s}}.\end{aligned} \tag{4.54}$$

Again, the dependence on mutual inductances with the zero-sequence axis can be observed. For $L_{0\alpha} = L_{0\beta} = 0$, the inductance ratios κ_α and κ_β would become zero and no anisotropy information would be available via the zero-sequence voltage.

4.2.3. Transformation of Inductance Ratios between the Stationary Reference Frames

To transform the inductance ratios from the physical to the orthogonal stator reference frame and vice versa, the Clarke transformation matrix can again be used. However, the transformation differs slightly from how voltages, currents and flux linkages are transformed and shall therefore be derived briefly. By equating (4.17) and (4.51),

$$\boldsymbol{\kappa}^{\mathrm{s}}\left(\boldsymbol{u}_{\mathrm{term}}^{\mathrm{s}} - \boldsymbol{u}_{\mathrm{slow}}^{\mathrm{s}}\right) = \boldsymbol{\kappa}^{\mathrm{p}}\left(\boldsymbol{u}_{\mathrm{term}}^{\mathrm{p}} - \boldsymbol{u}_{\mathrm{slow}}^{\mathrm{p}}\right) \tag{4.55}$$

is obtained. We can then transform the voltages using the known Clarke transformation. This gives

$$\boldsymbol{\kappa}^{\mathrm{s}} \left(\boldsymbol{T}_{\mathrm{C}} \boldsymbol{u}^{\mathrm{p}}_{\mathrm{term}} - \boldsymbol{T}_{\mathrm{C}} \boldsymbol{u}^{\mathrm{p}}_{\mathrm{slow}} \right) = \boldsymbol{\kappa}^{\mathrm{p}} \left(\boldsymbol{u}^{\mathrm{p}}_{\mathrm{term}} - \boldsymbol{u}^{\mathrm{p}}_{\mathrm{slow}} \right) \tag{4.56}$$

$$\boldsymbol{\kappa}^{\mathrm{s}} \boldsymbol{T}_{\mathrm{C}} \left(\boldsymbol{u}^{\mathrm{p}}_{\mathrm{term}} - \boldsymbol{u}^{\mathrm{p}}_{\mathrm{slow}} \right) = \boldsymbol{\kappa}^{\mathrm{p}} \left(\boldsymbol{u}^{\mathrm{p}}_{\mathrm{term}} - \boldsymbol{u}^{\mathrm{p}}_{\mathrm{slow}} \right) . \tag{4.57}$$

Transforming the inductance ratios between the two stationary frames can therefore be achieved using

$$\boldsymbol{\kappa}^{\mathrm{p}} = \boldsymbol{\kappa}^{\mathrm{s}} \boldsymbol{T}_{\mathrm{C}} \tag{4.58}$$

$$\boldsymbol{\kappa}^{\mathrm{s}} = \boldsymbol{\kappa}^{\mathrm{p}} \boldsymbol{T}_{\mathrm{C}}^{-1} . \tag{4.59}$$

4.2.4. Transient Behavior of the Zero-Sequence Voltage

Obviously, the zero-sequence voltage consists of a part that changes almost instantly when the terminals voltages are being switched and a second part that stays approximately unchanged if short time windows around such a switching event are considered:

$$u_{\mathrm{NAN}} = \boldsymbol{\kappa}_{\Delta} \boldsymbol{u}_{\mathrm{term}} - \boldsymbol{\kappa} \boldsymbol{u}_{\mathrm{slow}} . \tag{4.60}$$

The first part contains the desired anisotropy information whereas the second part is related to resistive imbalances and voltages induced by rotor movement. It can be considered as a disturbance and can be treated in one of two ways. It can either be neglected by considering only standstill and low-speed operation and assuming resistive imbalances to be small as in [ITSA16], or it can be systematically eliminated by considering only the response to a transient or high frequency excitation. Due to its usability in a much wider speed range, the latter approach is followed in this work.

To systematically eliminate $\boldsymbol{\kappa} \boldsymbol{u}_{\mathrm{slow}}$, a sequence of different discrete voltage vectors shall be applied within a short period. Consider for example two measurements at the time instants t_1 and t_2. If the time between these two instants is much smaller than the electrical time constants of the machine and the time for one electrical revolution, resistive voltage drops and voltages induced by rotor movement may be considered unchanged so that

$$\boldsymbol{u}^{\mathrm{s}}_{\mathrm{slow}}(t_1) \approx \boldsymbol{u}^{\mathrm{s}}_{\mathrm{slow}}(t_2) \tag{4.61}$$

in the 'αβ0' frame. The difference in the zero-sequence voltage between the two time

instants is

$$\Delta u_{\mathrm{NAN}} = u_{\mathrm{NAN}}(t_2) - u_{\mathrm{NAN}}(t_1) \tag{4.62}$$
$$= \boldsymbol{\kappa}^{\mathrm{s}}_{\Delta} \left(\boldsymbol{u}^{\mathrm{s}}_{\mathrm{term}}(t_2) - \boldsymbol{u}^{\mathrm{s}}_{\mathrm{term}}(t_1) \right) - \boldsymbol{\kappa}^{\mathrm{s}} \left(\boldsymbol{u}^{\mathrm{s}}_{\mathrm{slow}}(t_2) - \boldsymbol{u}^{\mathrm{s}}_{\mathrm{slow}}(t_1) \right) \tag{4.63}$$
$$\approx \boldsymbol{\kappa}^{\mathrm{s}}_{\Delta} \Delta \boldsymbol{u}^{\mathrm{s}}_{\mathrm{term}} - \boldsymbol{\kappa}^{\mathrm{s}} \cdot 0 \tag{4.64}$$

leaving only the information related to the anisotropy:

$$\Delta u_{\mathrm{NAN}} \approx \begin{bmatrix} \kappa_\alpha & \kappa_\beta & 0 \end{bmatrix} \Delta \boldsymbol{u}^{\mathrm{s}}_{\mathrm{term}} \tag{4.65}$$
$$= \kappa_\alpha \Delta u_{\mathrm{term},\alpha} + \kappa_\beta \Delta u_{\mathrm{term},\beta} \tag{4.66}$$

The analogous expression for the physical reference frame is found using the transformations in (2.1) and (4.59):

$$\Delta u_{\mathrm{NAN}} \approx \begin{bmatrix} \kappa_{\mathrm{a}} - \frac{1}{3} & \kappa_{\mathrm{b}} - \frac{1}{3} & \kappa_{\mathrm{c}} - \frac{1}{3} \end{bmatrix} \boldsymbol{T}_{\mathrm{C}}^{-1} \boldsymbol{T}_{\mathrm{C}} \Delta \boldsymbol{u}^{\mathrm{p}}_{\mathrm{term}} \tag{4.67}$$
$$= \begin{bmatrix} \kappa_{\mathrm{a}} - \frac{1}{3} & \kappa_{\mathrm{b}} - \frac{1}{3} & \kappa_{\mathrm{c}} - \frac{1}{3} \end{bmatrix} \Delta \boldsymbol{u}^{\mathrm{p}}_{\mathrm{term}} \, . \tag{4.68}$$

An example is given in Fig. 4.2. At the beginning, all phases are connected to the low potential of the inverter, then phase 'a' is switched. Accordingly, the differential

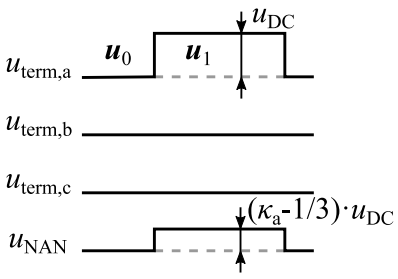

Figure 4.2.: Ideal response of u_{NAN} to a pulse on phase 'a'.

zero-sequence voltage between the two resulting voltage vectors is

$$\Delta u_{\mathrm{NAN,a}} = \begin{bmatrix} \kappa_\mathrm{a} - \frac{1}{3} & \kappa_\mathrm{b} - \frac{1}{3} & \kappa_\mathrm{c} - \frac{1}{3} \end{bmatrix} (\boldsymbol{u}_1 - \boldsymbol{u}_0) \tag{4.69}$$

$$= \begin{bmatrix} \kappa_\mathrm{a} - \frac{1}{3} & \kappa_\mathrm{b} - \frac{1}{3} & \kappa_\mathrm{c} - \frac{1}{3} \end{bmatrix} \begin{bmatrix} u_\mathrm{DC} \\ 0 \\ 0 \end{bmatrix} \tag{4.70}$$

$$= \left(\kappa_\mathrm{a} - \frac{1}{3} \right) u_\mathrm{DC} \, . \tag{4.71}$$

Clearly, it contains information about the a-component of the inductance ratio vector $\boldsymbol{\kappa}$.

4.2.5. Comparison with Anisotropy Information in Derivative of the Current Vector

To enable a fundamental comparison of estimation techniques using the zero-sequence voltage with those using the line currents, the underlying anisotropy information is presented in a similar manner. The starting point is again the simplified machine model in the 'αβ0' frame:

$$\begin{bmatrix} u_\alpha \\ u_\beta \\ u_0 \end{bmatrix} = \boldsymbol{R}^\mathrm{s} \begin{bmatrix} i_\alpha \\ i_\beta \\ i_0 \end{bmatrix} + \boldsymbol{L}^\mathrm{s} \frac{\mathrm{d}}{\mathrm{d}t} \begin{bmatrix} i_\alpha \\ i_\beta \\ i_0 \end{bmatrix} + \left(\frac{\mathrm{d}}{\mathrm{d}t} \boldsymbol{L}^\mathrm{s} \right) \begin{bmatrix} i_\alpha \\ i_\beta \\ i_0 \end{bmatrix} + \frac{\mathrm{d}}{\mathrm{d}t} \begin{bmatrix} \Psi_{\mathrm{PM},\alpha} \\ \Psi_{\mathrm{PM},\beta} \\ \Psi_{\mathrm{PM},0} \end{bmatrix} \, . \tag{4.72}$$

Because $i_0 = 0$ and $\mathrm{d}i_0/\mathrm{d}t = 0$ in a star-connected machine and because the zero-sequence voltage is not of interest for current-based techniques, one can consider only

$$\begin{bmatrix} u_\alpha \\ u_\beta \end{bmatrix} = \begin{bmatrix} R_{\alpha\alpha} & R_{\alpha\beta} \\ R_{\alpha\beta} & R_{\beta\beta} \end{bmatrix} \begin{bmatrix} i_\alpha \\ i_\beta \end{bmatrix} + \begin{bmatrix} L_{\alpha\alpha} & L_{\alpha\beta} \\ L_{\alpha\beta} & L_{\beta\beta} \end{bmatrix} \frac{\mathrm{d}}{\mathrm{d}t} \begin{bmatrix} i_\alpha \\ i_\beta \end{bmatrix} + \left(\frac{\mathrm{d}}{\mathrm{d}t} \begin{bmatrix} L_{\alpha\alpha} & L_{\alpha\beta} \\ L_{\alpha\beta} & L_{\beta\beta} \end{bmatrix} \right) \begin{bmatrix} i_\alpha \\ i_\beta \end{bmatrix} + \frac{\mathrm{d}}{\mathrm{d}t} \begin{bmatrix} \Psi_{\mathrm{PM},\alpha} \\ \Psi_{\mathrm{PM},\beta} \end{bmatrix} \tag{4.73}$$

and represent these reduced vectors and matrices by asterisk-denoted symbols:

$$\boldsymbol{u}^{\mathrm{s}*} = \boldsymbol{R}^{\mathrm{s}*} \boldsymbol{i}^{\mathrm{s}*} + \boldsymbol{L}^{\mathrm{s}*} \frac{\mathrm{d}}{\mathrm{d}t} \boldsymbol{i}^{\mathrm{s}*} + \left(\frac{\mathrm{d}}{\mathrm{d}t} \boldsymbol{L}^{\mathrm{s}*} \right) \boldsymbol{i}^{\mathrm{s}*} + \frac{\mathrm{d}}{\mathrm{d}t} \boldsymbol{\Psi}_\mathrm{PM}^{\mathrm{s}*} \, . \tag{4.74}$$

By rearranging for the derivative of the current vector, one obtains:

$$\frac{\mathrm{d}}{\mathrm{d}t} \boldsymbol{i}^{\mathrm{s}*} = \boldsymbol{L}^{\mathrm{s}*^{-1}} \left(\boldsymbol{u}^{\mathrm{s}*} - \boldsymbol{R}^{\mathrm{s}*} \boldsymbol{i}^{\mathrm{s}*} - \left(\frac{\mathrm{d}}{\mathrm{d}t} \boldsymbol{L}^{\mathrm{s}*} \right) \boldsymbol{i}^{\mathrm{s}*} - \frac{\mathrm{d}}{\mathrm{d}t} \boldsymbol{\Psi}_\mathrm{PM}^{\mathrm{s}*} \right) \, . \tag{4.75}$$

As with the zero-sequence voltage, the slowly changing voltage terms can be separated so that

$$\frac{\mathrm{d}}{\mathrm{d}t}\boldsymbol{i}^{\mathrm{s}*} = \boldsymbol{L}^{\mathrm{s}*^{-1}}\left(\boldsymbol{u}^{\mathrm{s}*} - \boldsymbol{u}^{\mathrm{s}*}_{\mathrm{slow}}\right) \tag{4.76}$$

with

$$\boldsymbol{u}^{\mathrm{s}*}_{\mathrm{slow}} = \boldsymbol{R}^{\mathrm{s}*}\boldsymbol{i}^{\mathrm{s}*} + \left(\frac{\mathrm{d}}{\mathrm{d}t}\boldsymbol{L}^{\mathrm{s}*}\right)\boldsymbol{i}^{\mathrm{s}*} + \frac{\mathrm{d}}{\mathrm{d}t}\boldsymbol{\Psi}^{\mathrm{s}*}_{\mathrm{PM}}\,. \tag{4.77}$$

Also similar to the zero-sequence voltage based approach, the slowly changing voltage terms can be eliminated by a subtraction of two measured current derivatives during different switching states [Sch96; Pau14] at time instants t_1 and t_2:

$$\begin{aligned}
\Delta\left(\frac{\mathrm{d}}{\mathrm{d}t}\boldsymbol{i}^{\mathrm{s}*}\right) &= \frac{\mathrm{d}}{\mathrm{d}t}\boldsymbol{i}^{\mathrm{s}*}(t_2) - \frac{\mathrm{d}}{\mathrm{d}t}\boldsymbol{i}^{\mathrm{s}*}(t_1) && (4.78)\\
&= \boldsymbol{L}^{\mathrm{s}*^{-1}}\left(\boldsymbol{u}^{\mathrm{s}*}(t_2) - \boldsymbol{u}^{\mathrm{s}*}_{\mathrm{slow}}\right) - \boldsymbol{L}^{\mathrm{s}*^{-1}}\left(\boldsymbol{u}^{\mathrm{s}*}(t_1) - \boldsymbol{u}^{\mathrm{s}*}_{\mathrm{slow}}\right) && (4.79)\\
&= \boldsymbol{L}^{\mathrm{s}*^{-1}}\Delta\boldsymbol{u}^{\mathrm{s}*} && (4.80)
\end{aligned}$$

with

$$\boldsymbol{L}^{\mathrm{s}*^{-1}} = \frac{1}{L_{\alpha\alpha}L_{\beta\beta} - L_{\alpha\beta}^2}\begin{bmatrix} L_{\beta\beta} & -L_{\alpha\beta} \\ -L_{\alpha\beta} & L_{\alpha\alpha} \end{bmatrix} \tag{4.81}$$

and

$$\Delta\boldsymbol{u}^{\mathrm{s}*} = \begin{bmatrix} u_\alpha(t_2) - u_\alpha(t_1) \\ u_\beta(t_2) - u_\beta(t_1) \end{bmatrix}. \tag{4.82}$$

In practice, the current derivatives are usually obtained by subtracting two current measurements or by linear regression. However, this is not considered further, because only the basic principle is of interest here. As mentioned earlier, the inverse of the reduced inductance matrix is often referred to as the admittance matrix

$$\boldsymbol{Y}^{\mathrm{s}*} = (\boldsymbol{L}^{\mathrm{s}*})^{-1} = \begin{bmatrix} Y^*_{\alpha\alpha} & Y^*_{\alpha\beta} \\ Y^*_{\alpha\beta} & Y^*_{\beta\beta} \end{bmatrix}\,. \tag{4.83}$$

It is clear that $\Delta(\mathrm{d}\boldsymbol{i}^{\mathrm{s}*}/\mathrm{d}t)$ depends only on $\boldsymbol{Y}^{\mathrm{s}*}$ and the α- and β- components of the applied voltage vectors and that $\boldsymbol{Y}^{\mathrm{s}*}$ contains the desired anisotropy information. Different to the anisotropy information in the zero-sequence voltage, the mutual inductances with the zero-sequence axis play no role here as they do not affect the α- and β-axis currents. Another difference lies in the fact that absolute and not relative information is obtained about the inductances. Already at this point it is therefore clear that the anisotropy

information exploited in the two groups of techniques cannot be identical. Further insight will be gained in the following sections by regarding particular special cases of fundamental wave inductance models.

4.3. Inductance Ratios Resulting from Fundamental Wave Inductance Models

The position dependence of the inductance matrix in the stationary reference frames is the core principle of anisotropy-based estimation techniques. To derive generally applicable estimation functions and structures, a fundamental wave inductance model is typically assumed for synchronous machines, which contains harmonic components of 2φ in the stationary frames and which results in constant self-inductances in the d- and q-axis of the machine. As discussed before, it is necessary to consider the full inductance matrix including in particular the mutual inductances with the zero-sequence axis to describe the anisotropy information in the zero-sequence voltage. In the following sections, the inductance ratios that result from fundamental wave inductance models shall be derived and compared to the anisotropy information available through current measurements. Four cases of position dependent inductance matrices are looked at for this purpose. At first, a general fundamental wave inductance model similar to the one used in [Wer18] is considered which has self- and mutual inductances in the physical reference frame that vary sinusoidally at two times the rotor frequency. Basic constraints are presented that limit the possible range of the included inductance coefficients from a physical perspective. After that, three special cases are discussed that allow to derive the required estimation functions and that provide additional insights.

4.3.1. General Fundamental Wave Inductance Model

The general fundamental wave inductance model in the abc reference frame is given by

$$\boldsymbol{L}^{\mathrm{p}} = \begin{bmatrix} L_0 + L_2\cos\left(2\varphi\right) & L_{\mathrm{m0}} + L_{\mathrm{m2}}\cos\left(2\left(\varphi - \frac{4\pi}{3}\right)\right) & L_{\mathrm{m0}} + L_{\mathrm{m2}}\cos\left(2\left(\varphi - \frac{2\pi}{3}\right)\right) \\ L_{\mathrm{m0}} + L_{\mathrm{m2}}\cos\left(2\left(\varphi - \frac{4\pi}{3}\right)\right) & L_0 + L_2\cos\left(2\left(\varphi - \frac{2\pi}{3}\right)\right) & L_{\mathrm{m0}} + L_{\mathrm{m2}}\cos\left(2\varphi\right) \\ L_{\mathrm{m0}} + L_{\mathrm{m2}}\cos\left(2\left(\varphi - \frac{2\pi}{3}\right)\right) & L_{\mathrm{m0}} + L_{\mathrm{m2}}\cos\left(2\varphi\right) & L_0 + L_2\cos\left(2\left(\varphi - \frac{4\pi}{3}\right)\right) \end{bmatrix}. \tag{4.84}$$

Transforming the matrix to the 'αβ0' frame using (2.41) leads to a matrix of the form

$$\boldsymbol{L}^{\mathrm{s}} = \begin{bmatrix} L_\Sigma + L_\Delta \cos(2\varphi) & L_\Delta \sin(2\varphi) & 2L_{\Delta 0} \cos(2\varphi) \\ L_\Delta \sin(2\varphi) & L_\Sigma - L_\Delta \cos(2\varphi) & -2L_{\Delta 0} \sin(2\varphi) \\ L_{\Delta 0} \cos(2\varphi) & -L_{\Delta 0} \sin(2\varphi) & L_{\Sigma 0} \end{bmatrix} \tag{4.85}$$

using an only slightly modified notation of the one used in [Wer18, p. 43]. The relation between the coefficients in the 'abc' reference frame and those in the 'αβ0' frame are described by

$$L_\Sigma = L_0 - L_{\mathrm{m}0} \tag{4.86}$$

$$L_\Delta = L_2/2 + L_{\mathrm{m}2} \tag{4.87}$$

$$L_{\Sigma 0} = L_0 + 2L_{\mathrm{m}0} \tag{4.88}$$

$$L_{\Delta 0} = L_2/2 - L_{\mathrm{m}2}/2\ . \tag{4.89}$$

Similarly, using (2.66), the corresponding matrix in the 'dq0' reference frame is found as

$$\boldsymbol{L}^{\mathrm{r}} = \begin{bmatrix} L_\Sigma + L_\Delta & 0 & 2L_{\Delta 0} \cos(3\varphi) \\ 0 & L_\Sigma - L_\Delta & -2L_{\Delta 0} \sin(3\varphi) \\ L_{\Delta 0} \cos(3\varphi) & -L_{\Delta 0} \sin(3\varphi) & L_{\Sigma 0} \end{bmatrix}. \tag{4.90}$$

The following inductance ratios result from this inductance model. In the 'abc' reference frame, by using (4.18), one receives

$$\boldsymbol{\kappa}^{\mathrm{p}} = \frac{1}{3} \frac{1}{L_\Sigma^2 - L_\Delta^2} \begin{bmatrix} L_\Sigma^2 - L_\Delta^2 - 2L_{\Delta 0} L_\Sigma \cos(2\varphi) + 2L_{\Delta 0} L_\Delta \cos(4\varphi) \\ L_\Sigma^2 - L_\Delta^2 - 2L_{\Delta 0} L_\Sigma \cos\left(2\left(\varphi - \frac{2\pi}{3}\right)\right) + 2L_{\Delta 0} L_\Delta \cos\left(4\left(\varphi - \frac{2\pi}{3}\right)\right) \\ L_\Sigma^2 - L_\Delta^2 - 2L_{\Delta 0} L_\Sigma \cos\left(2\left(\varphi - \frac{4\pi}{3}\right)\right) + 2L_{\Delta 0} L_\Delta \cos\left(4\left(\varphi - \frac{4\pi}{3}\right)\right) \end{bmatrix}^{\mathrm{T}} \tag{4.91}$$

$$= \begin{bmatrix} \frac{1}{3} & \frac{1}{3} & \frac{1}{3} \end{bmatrix} + \frac{2}{3} \frac{1}{L_\Sigma^2 - L_\Delta^2} \begin{bmatrix} -L_{\Delta 0} L_\Sigma \cos(2\varphi) + L_{\Delta 0} L_\Delta \cos(4\varphi) \\ -L_{\Delta 0} L_\Sigma \cos\left(2\left(\varphi - \frac{2\pi}{3}\right)\right) + L_{\Delta 0} L_\Delta \cos\left(4\left(\varphi - \frac{2\pi}{3}\right)\right) \\ -L_{\Delta 0} L_\Sigma \cos\left(2\left(\varphi - \frac{4\pi}{3}\right)\right) + L_{\Delta 0} L_\Delta \cos\left(4\left(\varphi - \frac{4\pi}{3}\right)\right) \end{bmatrix}^{\mathrm{T}} \tag{4.92}$$

whereas in the 'αβ0' frame, the inductance ratios can be obtained using (4.43) and (4.53):

$$\boldsymbol{\kappa}^{\mathrm{s}} = \frac{1}{L_{\Sigma}^2 - L_{\Delta}^2} \begin{bmatrix} -L_{\Delta 0} L_{\Sigma} \cos(2\varphi) + L_{\Delta 0} L_{\Delta} (\cos(4\varphi)) \\ L_{\Delta 0} L_{\Sigma} \sin(2\varphi) + L_{\Delta 0} L_{\Delta} (\sin(4\varphi)) \\ L_{\Sigma}^2 - L_{\Delta}^2 \end{bmatrix}^{\mathrm{T}} \tag{4.93}$$

$$= \frac{1}{L_{\Sigma}^2 - L_{\Delta}^2} \begin{bmatrix} -L_{\Delta 0} L_{\Sigma} \cos(-2\varphi) + L_{\Delta 0} L_{\Delta} (\cos(4\varphi)) \\ -L_{\Delta 0} L_{\Sigma} \sin(-2\varphi) + L_{\Delta 0} L_{\Delta} (\sin(4\varphi)) \\ L_{\Sigma}^2 - L_{\Delta}^2 \end{bmatrix}^{\mathrm{T}} . \tag{4.94}$$

It becomes clear that in addition to terms that vary with two times the rotor position, terms that vary with four times the rotor position also appear in the inductance ratios. The 2φ-component of the inductance ratio vector moves in the opposite direction of the rotor in the αβ-plane, whereas the 4φ-component moves in the same direction.

By reducing the fraction by L_{Σ}^2 , one can further write

$$\boldsymbol{\kappa}^{\mathrm{s}} = \frac{1}{1 - (L_{\Delta}/L_{\Sigma})^2} \begin{bmatrix} -(L_{\Delta 0}/L_{\Sigma}) \cos(-2\varphi) + \left(L_{\Delta 0} L_{\Delta}/{L_{\Sigma}}^2\right) (\cos(4\varphi)) \\ -(L_{\Delta 0}/L_{\Sigma}) \sin(-2\varphi) + \left(L_{\Delta 0} L_{\Delta}/{L_{\Sigma}}^2\right) (\sin(4\varphi)) \\ 1 - (L_{\Delta}/L_{\Sigma})^2 \end{bmatrix}^{\mathrm{T}} . \tag{4.95}$$

By defining κ_2^{s} and κ_4^{s} as the coefficients of the harmonic components varying with 2φ and 4φ, the inductance ratios can be expressed as

$$\begin{aligned} \kappa_{\alpha} &= \kappa_2^{\mathrm{s}} \cos(-2\varphi) + \kappa_4^{\mathrm{s}} \cos(4\varphi) \\ \kappa_{\beta} &= \kappa_2^{\mathrm{s}} \sin(-2\varphi) + \kappa_4^{\mathrm{s}} \sin(4\varphi) \end{aligned} \tag{4.96}$$

with

$$\kappa_2^{\mathrm{s}} = -\frac{(L_{\Delta 0}/L_{\Sigma})}{1 - (L_{\Delta}/L_{\Sigma})^2} \tag{4.97}$$

$$\kappa_4^{\mathrm{s}} = \frac{(L_{\Delta 0}/L_{\Sigma})\,(L_{\Delta}/L_{\Sigma})}{1 - (L_{\Delta}/L_{\Sigma})^2} . \tag{4.98}$$

The ratio of κ_4^{s} and κ_2^{s} is

$$\frac{\left|\kappa_4^{\mathrm{s}}\right|}{\left|\kappa_2^{\mathrm{s}}\right|} = \left|\frac{L_{\Delta}}{L_{\Sigma}}\right| = \frac{|L_{\Delta}|}{L_{\Sigma}} . \tag{4.99}$$

$L_{\Delta 0}/L_{\Sigma}$ instead appears as a common gain in both harmonic components. Therefore, it affects the overall magnitude of the anisotropy signals, but not their shape. It is

important to note here that, accordingly, the magnitude and shape of the anisotropy signals are decoupled in this general case of the inductance model.

Finally, to allow for basic comparisons with the anisotropy information available via current measurements, the admittance matrix in the 'αβ' reference frame shall be considered. Resulting from the fundamental wave inductance model, it is given by

$$\boldsymbol{Y}^{\mathrm{s}*} = \begin{bmatrix} Y^*_{\alpha\alpha} & Y^*_{\alpha\beta} \\ Y^*_{\alpha\beta} & Y^*_{\beta\beta} \end{bmatrix} = \begin{bmatrix} L_\Sigma + L_\Delta \cos(2\varphi) & L_\Delta \sin(2\varphi) \\ L_\Delta \sin(2\varphi) & L_\Sigma - L_\Delta \cos(2\varphi) \end{bmatrix}^{-1} \tag{4.100}$$

$$= \frac{1}{L_\Sigma^2 - L_\Delta^2} \begin{bmatrix} L_\Sigma - L_\Delta \cos(2\varphi) & -L_\Delta \sin(2\varphi) \\ -L_\Delta \sin(2\varphi) & L_\Sigma + L_\Delta \cos(2\varphi) \end{bmatrix} . \tag{4.101}$$

The following can be noted. Unlike the inductance ratios, the admittance matrix depends only on L_Δ and L_Σ but not on $L_{\Delta 0}$ and does not contain components that vary with four times the rotor frequency.

4.3.2. Constraints for the Inductance Coefficients

To restrict the range of feasible values, two basic constraints can be formulated for the inductance coefficients L_0, L_2, $L_{\mathrm{m}0}$, $L_{\mathrm{m}2}$ or, depending on the reference frame, L_Σ, L_Δ, $L_{\Delta 0}$. This is done by assuming positive self-inductances in the 'abc' and in the 'αβ' reference frame. The self-inductance in the zero-sequence axis is not considered here. As shown before, $L_{\Sigma 0}$ has no effect on the inductance ratios and, since no zero-sequence currents flow in the machine, it also doesn't affect the currents in the machine. Starting with the self-inductances in the 'abc' reference frame, the first constraint is immediately obtained by

$$|L_2| < L_0 . \tag{4.102}$$

Using (4.86)-(4.89), this constraint can alternatively be expressed as

$$|2L_\Delta + 4L_{\Delta 0}| < 2L_\Sigma + L_{\Sigma 0} . \tag{4.103}$$

If we assume that also the self-inductances in 'αβ' must always be positive, we obtain the second constraint

$$|L_\Delta| < L_\Sigma . \tag{4.104}$$

Using (4.86) and (4.87), this constraint can also be expressed as

$$|L_2/2 + L_{\mathrm{m}2}| < L_0 - L_{\mathrm{m}0} \,. \tag{4.105}$$

Expressing the above constraints as ratios leads to

$$\frac{|L_2|}{L_0} < 1 \tag{4.106}$$

$$\frac{|L_\Delta + 2L_{\Delta 0}|}{L_\Sigma + L_{\Sigma 0}/2} < 1 \tag{4.107}$$

for the first constraint and

$$\frac{|L_2/2 + L_{\mathrm{m}2}|}{L_0 - L_{\mathrm{m}0}} < 1 \tag{4.108}$$

$$\frac{|L_\Delta|}{L_\Sigma} < 1 \tag{4.109}$$

for the second constraint.

A last consideration shall be made for the special case $L_\Delta = L_{\Delta 0}$ and $L_\Sigma = L_{\Sigma 0}$. In this case, (4.107) becomes

$$\frac{|L_\Delta|}{L_\Sigma} < \frac{1}{2} \,. \tag{4.110}$$

4.3.3. Inductance Model with Negligible Mutual Inductances

It was shown that the inductance ratios that result from the general fundamental wave inductance model include both a term that varies at two times and a term that varies at four times the rotor position and that these are decoupled from each other. Without further knowledge about the machine, the position cannot be directly calculated. To enable position estimation of motors without identification procedures, it is expedient to consider special cases for which parameter-free estimation functions can be found. One possibility is to assume that the fluctuations of the mutual inductances are negligible, i.e. $L_{\mathrm{m}2} = 0$ and therefore

$$L_\Delta = L_{\Delta 0} = L_2/2 \,. \tag{4.111}$$

To simplify the following equations, we will assume also $L_{\mathrm{m}0} = 0$. As we have seen in section 4.3.1, only L_Σ, but not $L_{\Sigma 0}$, is relevant for the inductance ratios. Furthermore, an increase in $L_{\mathrm{m}0}$ has the same effect on L_Σ as a decrease in L_0. With this assumption,

L_Σ and $L_{\Sigma 0}$ both become equal to L_0 and one obtains

$$\boldsymbol{L}^{\mathrm{p}} = \begin{bmatrix} L_0 + L_2\cos(2\varphi) & 0 & 0 \\ 0 & L_0 + L_2\cos\left(2\left(\varphi - \frac{2\pi}{3}\right)\right) & 0 \\ 0 & 0 & L_0 + L_2\cos\left(2\left(\varphi - \frac{4\pi}{3}\right)\right) \end{bmatrix} \tag{4.112}$$

$$\boldsymbol{L}^{\mathrm{s}} = \begin{bmatrix} L_\Sigma + L_\Delta\cos(2\varphi) & L_\Delta\sin(2\varphi) & 2L_\Delta\cos(2\varphi) \\ L_\Delta\sin(2\varphi) & L_\Sigma - L_\Delta\cos(2\varphi) & -2L_\Delta\sin(2\varphi) \\ L_\Delta\cos(2\varphi) & -L_\Delta\sin(2\varphi) & L_\Sigma \end{bmatrix} \tag{4.113}$$

$$\boldsymbol{L}^{\mathrm{r}} = \begin{bmatrix} L_\Sigma + L_\Delta & 0 & 2L_\Delta\cos(3\varphi) \\ 0 & L_\Sigma - L_\Delta & -2L_\Delta\sin(3\varphi) \\ L_\Delta\cos(3\varphi) & -L_\Delta\sin(3\varphi) & L_\Sigma \end{bmatrix} . \tag{4.114}$$

This can be considered the anisotropy model that is found most often in the scientific literature for anisotropy-based techniques that use the zero-sequence voltage, featured also in a review paper [BD11]. The following inductance ratios are obtained as a result. In the 'abc' frame, one receives

$$\begin{aligned} \boldsymbol{\kappa}^{\mathrm{p}} = &\begin{bmatrix} \frac{1}{3} & \frac{1}{3} & \frac{1}{3} \end{bmatrix} \\ &+ \frac{2}{3}\frac{1}{1-(L_\Delta/L_\Sigma)^2}\begin{bmatrix} -(L_\Delta/L_\Sigma)\cos(2\varphi) + (L_\Delta/L_\Sigma)^2\cos(4\varphi) \\ -(L_\Delta/L_\Sigma)\cos\left(2\left(\varphi - \frac{2\pi}{3}\right)\right) + (L_\Delta/L_\Sigma)^2\cos\left(4\left(\varphi - \frac{2\pi}{3}\right)\right) \\ -(L_\Delta/L_\Sigma)\cos\left(2\left(\varphi - \frac{4\pi}{3}\right)\right) + (L_\Delta/L_\Sigma)^2\cos\left(4\left(\varphi - \frac{4\pi}{3}\right)\right) \end{bmatrix}^{\mathrm{T}} . \end{aligned} \tag{4.115}$$

In the 'αβ0' frame, one finds

$$\boldsymbol{\kappa}^{\mathrm{s}} = \frac{1}{1-(L_\Delta/L_\Sigma)^2}\begin{bmatrix} -(L_\Delta/L_\Sigma)\cos(-2\varphi) + (L_\Delta/L_\Sigma)^2\cos(4\varphi) \\ -(L_\Delta/L_\Sigma)\sin(-2\varphi) + (L_\Delta/L_\Sigma)^2\sin(4\varphi) \\ 1-(L_\Delta/L_\Sigma)^2 \end{bmatrix}^{\mathrm{T}} . \tag{4.116}$$

It becomes apparent, that the coefficients of the harmonic components in the inductance ratios depend only on the ratio of L_Δ and L_Σ for this anisotropy model. Therefore, one can define an *inductance variation ratio*

$$r = L_\Delta/L_\Sigma = \frac{L_2}{2L_0} . \tag{4.117}$$

The inductance ratios can then advantageously be expressed in the 'abc' frame by

$$\boldsymbol{\kappa}^{\mathrm{p}} = \begin{bmatrix} \frac{1}{3} & \frac{1}{3} & \frac{1}{3} \end{bmatrix} + \frac{2}{3}\frac{1}{\left(1-r^2\right)} \begin{bmatrix} -r\cos\left(2\varphi\right) + r^2\cos\left(4\varphi\right) \\ -r\cos\left(2\left(\varphi - \frac{2\pi}{3}\right)\right) + r^2\cos\left(4\left(\varphi - \frac{2\pi}{3}\right)\right) \\ -r\cos\left(2\left(\varphi - \frac{4\pi}{3}\right)\right) + r^2\cos\left(4\left(\varphi - \frac{4\pi}{3}\right)\right) \end{bmatrix}^{\mathrm{T}} \tag{4.118}$$

and in the 'αβ0' frame by

$$\boldsymbol{\kappa}^{\mathrm{s}} = \frac{1}{1-r^2} \begin{bmatrix} -r\cos\left(-2\varphi\right) + r^2\cos\left(4\varphi\right) \\ -r\sin\left(-2\varphi\right) + r^2\sin\left(4\varphi\right) \\ 1-r^2 \end{bmatrix}^{\mathrm{T}} . \tag{4.119}$$

Accordingly, κ_2^{s} and κ_4^{s} are given by

$$\kappa_2^{\mathrm{s}} = -\frac{r}{1-r^2} \tag{4.120}$$

$$\kappa_4^{\mathrm{s}} = \frac{r^2}{1-r^2} \tag{4.121}$$

and their ratio is

$$\frac{\left|\kappa_4^{\mathrm{s}}\right|}{\left|\kappa_2^{\mathrm{s}}\right|} = |r| \ . \tag{4.122}$$

It becomes apparent that the signal size and the signal shape are no longer decoupled, since both are determined only by $r = L_\Delta / L_\Sigma$. It also becomes clear that, under the made assumption for the inductance matrix, motors that have a higher inductance variation ratio and that should therefore be more suitable for position estimation are also expected to have a larger 4φ-component relative to the 2φ-component.

In Fig. 4.3, the variation of the shape of the inductance ratios is shown for different values of r with normalized signal magnitudes. As a result of the constraint in (4.110), the possible values of the inductance variation ratio are limited by $r_{\mathrm{min/max}} = \pm 0.5$. The theoretical maximum amplitudes are therefore

$$\left|\kappa_2^{\mathrm{s}}\left(r = \pm 0.5\right)\right| = \frac{0.5}{1-0.5^2} = \frac{2}{3} \tag{4.123}$$

and

$$\left|\kappa_4^{\mathrm{s}}\left(r = \pm 0.5\right)\right| = \frac{0.5^2}{1-0.5^2} = \frac{1}{3} \ . \tag{4.124}$$

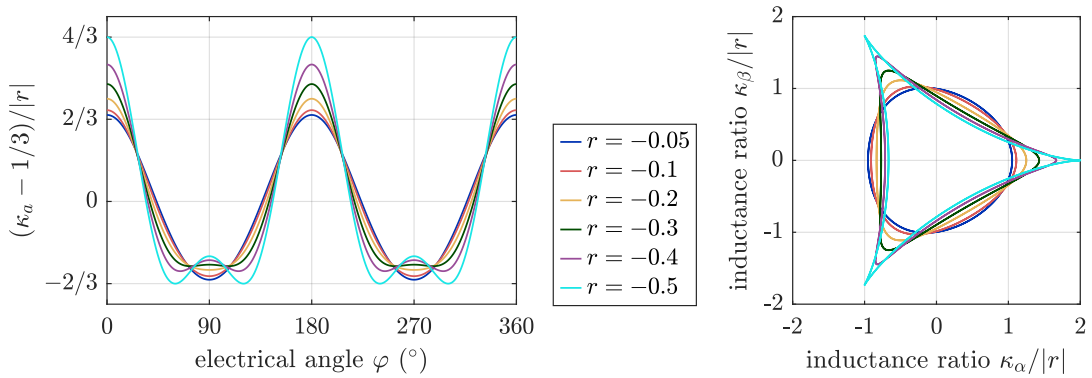

Figure 4.3.: Variation of the shapes of κ_a and $\boldsymbol{\kappa}^\mathrm{s}$ with r, magnitudes normalized by division by $|r|$.

The following relations exist between L_dd, L_qq, L_Σ and the inductance variation ratio r:

$$L_\mathrm{dd} = L_\Sigma \cdot (1 + r) \tag{4.125}$$

$$L_\mathrm{qq} = L_\Sigma \cdot (1 - r) \tag{4.126}$$

$$r = \frac{L_\mathrm{dd} - L_\mathrm{qq}}{L_\mathrm{dd} + L_\mathrm{qq}} \,. \tag{4.127}$$

However, it is important to remember that these relations result from the assumption of $L_\Delta = L_{\Delta 0}$.

4.3.4. Inductance Model with Diagonal Inductance Matrix in the Rotating Frame

Another interesting case to consider is

$$L_2 = L_\mathrm{m2} \Leftrightarrow L_{\Delta 0} = 0 \tag{4.128}$$

which in the 'dq0' frame leads to

$$\boldsymbol{L}^\mathrm{r} = \begin{bmatrix} L_\Sigma + L_\Delta & 0 & 0 \\ 0 & L_\Sigma - L_\Delta & 0 \\ 0 & 0 & L_{\Sigma 0} \end{bmatrix} . \tag{4.129}$$

When starting from the rotating coordinate system the above model is probably the most intuitive extension of the reduced inductance matrix to include the zero-sequence axis. Again, $L_\Sigma = L_{\Sigma 0}$ shall additionally be assumed for sake of simplicity. The inductance matrices in the 'αβ0' and 'abc' reference frame then become

$$\boldsymbol{L}^{\mathrm{s}} = \begin{bmatrix} L_\Sigma + L_\Delta \cos(2\varphi) & L_\Delta \sin(2\varphi) & 0 \\ L_\Delta \sin(2\varphi) & L_\Sigma - L_\Delta \cos(2\varphi) & 0 \\ 0 & 0 & L_\Sigma \end{bmatrix} \tag{4.130}$$

and

$$\boldsymbol{L}^{\mathrm{p}} = \begin{bmatrix} L_\Sigma + \frac{2}{3}L_\Delta \cos(2\varphi) & \frac{2}{3}L_\Delta \cos\left(2\left(\varphi - \frac{4\pi}{3}\right)\right) & \frac{2}{3}L_\Delta \cos\left(2\left(\varphi - \frac{2\pi}{3}\right)\right) \\ \frac{2}{3}L_\Delta \cos\left(2\left(\varphi - \frac{4\pi}{3}\right)\right) & L_\Sigma + \frac{2}{3}L_\Delta \cos\left(2\left(\varphi - \frac{2\pi}{3}\right)\right) & \frac{2}{3}L_\Delta \cos(2\varphi) \\ \frac{2}{3}L_\Delta \cos\left(2\left(\varphi - \frac{2\pi}{3}\right)\right) & \frac{2}{3}L_\Delta \cos(2\varphi) & L_\Sigma + \frac{2}{3}L_\Delta \cos\left(2\left(\varphi - \frac{4\pi}{3}\right)\right) \end{bmatrix}. \tag{4.131}$$

As a consequence of $L_{0\alpha} = L_{0\beta} = 0$, the resulting inductance ratios are

$$\begin{aligned} \kappa_\alpha &= 0 \\ \kappa_\beta &= 0\ . \end{aligned} \tag{4.132}$$

Obviously, no anisotropy information can be obtained through the zero-sequence voltage for a motor whose inductances conform to this model. Through current measurements, anisotropy information remains however available due to the different inductances in the d- and the q-axis.

4.3.5. Inductance Model with Vanishing Anisotropy Information in the Currents

The last special case that shall be considered here is

$$L_{\mathrm{m}2} = -L_2/2 \Leftrightarrow L_\Delta = 0\ . \tag{4.133}$$

For the inductances in the 'dq0' and 'αβ0' frames, this assumption leads to

$$\boldsymbol{L}^{\mathrm{r}} = \begin{bmatrix} L_\Sigma & 0 & 2L_{\Delta 0}\cos(3\varphi) \\ 0 & L_\Sigma & -2L_{\Delta 0}\sin(3\varphi) \\ L_{\Delta 0}\cos(3\varphi) & -L_{\Delta 0}\sin(3\varphi) & L_{\Sigma 0} \end{bmatrix} \tag{4.134}$$

and

$$\boldsymbol{L}^{\mathrm{s}} = \begin{bmatrix} L_\Sigma & 0 & 2L_{\Delta 0}\cos(2\varphi) \\ 0 & L_\Sigma & -2L_{\Delta 0}\sin(2\varphi) \\ L_{\Delta 0}\cos(2\varphi) & -L_{\Delta 0}\sin(2\varphi) & L_{\Sigma 0} \end{bmatrix}. \tag{4.135}$$

In this case, the inductances L_{dd} and L_{qq} become equal. Under the additional assumption of $L_\Sigma = L_{\Sigma 0}$, a corresponding inductance matrix in the physical reference frame is

$$\boldsymbol{L}^{\mathrm{p}} = \begin{bmatrix} L_\Sigma + \frac{4}{3}L_{\Delta 0}\cos(2\varphi) & -\frac{2}{3}L_{\Delta 0}\cos\left(2\left(\varphi - \frac{4\pi}{3}\right)\right) & -\frac{2}{3}L_{\Delta 0}\cos\left(2\left(\varphi - \frac{2\pi}{3}\right)\right) \\ -\frac{2}{3}L_{\Delta 0}\cos\left(2\left(\varphi - \frac{4\pi}{3}\right)\right) & L_\Sigma + \frac{4}{3}L_{\Delta 0}\cos\left(2\left(\varphi - \frac{2\pi}{3}\right)\right) & -\frac{2}{3}L_{\Delta 0}\cos(2\varphi) \\ -\frac{2}{3}L_{\Delta 0}\cos\left(2\left(\varphi - \frac{2\pi}{3}\right)\right) & -\frac{2}{3}L_{\Delta 0}\cos(2\varphi) & L_\Sigma + \frac{4}{3}L_{\Delta 0}\cos\left(2\left(\varphi - \frac{4\pi}{3}\right)\right) \end{bmatrix}. \tag{4.136}$$

Since $L_{\mathrm{dd}} = L_{\mathrm{qq}}$, it is clear that no anisotropy information can be obtained through current measurements in this case; the admittance matrix in the 'αβ' frame becomes

$$\boldsymbol{Y}^{\mathrm{s}*} = \frac{1}{L_\Sigma^2}\begin{bmatrix} L_\Sigma & 0 \\ 0 & L_\Sigma \end{bmatrix} = \begin{bmatrix} 1/L_\Sigma & 0 \\ 0 & 1/L_\Sigma \end{bmatrix}. \tag{4.137}$$

The resulting inductance ratios, however, are

$$\kappa_\alpha = \frac{L_{\alpha\beta}L_{0\beta} - L_{\beta\beta}L_{0\alpha}}{L_{\alpha\alpha}L_{\beta\beta} - L_{\alpha\beta}^2} = \frac{-L_\Sigma L_{\Delta 0}\cos(2\varphi)}{L_\Sigma^2} = -\frac{L_{\Delta 0}}{L_\Sigma}\cos(-2\varphi) \tag{4.138}$$

$$\kappa_\beta = \frac{L_{\alpha\beta}L_{0\alpha} - L_{\alpha\alpha}L_{0\beta}}{L_{\alpha\alpha}L_{\beta\beta} - L_{\alpha\beta}^2} = \frac{L_\Sigma L_{\Delta 0}\sin(2\varphi)}{L_\Sigma^2} = -\frac{L_{\Delta 0}}{L_\Sigma}\sin(-2\varphi) \tag{4.139}$$

which means that the inductance ratio vector $\boldsymbol{\kappa}$ moves on a circle in the αβ-plane and would allow a straightforward position estimation. A motor that conforms to this inductance model seems therefore quite favorable for zero-sequence voltage based techniques, however this inductance model is clearly different from the conventional anisotropy model used in current-based techniques and for PMSMs in general.

It is worth to mention that for example in [MSG+17] it was stated that estimation using the zero-sequence voltage is not possible when $L_{\mathrm{dd}} = L_{\mathrm{qq}}$. As we have seen, this is true only with additional assumptions and cannot be generalized. This example illustrates the need for a thorough analysis of the requirements placed on the properties of the machine and a careful definition of what constitutes an anisotropy for zero-sequence voltage based techniques.

4.4. Voltage Vector Requirements

4.4.1. Voltage Vector Requirements When Using the Zero-Sequence Voltage

In the approach followed in this work, anisotropy information is obtained via transient excitation with discrete voltage vectors, which is achieved by applying modified pulse patterns to the switching inverter. In this section, the requirements for a certain number and orientation of discrete voltage vectors that must be applied for acquiring the components of the inductance ratio vector are considered. In the previous works that use a comparable estimation approach, such as [Jia00; Man13; Wer18], several possibilities have been presented for calculating the components from certain sets of voltage vectors, however the exact condition for the required number and orientation was not given. In fact, the previous works employed a higher number of measurements for the calculation of the inductance ratio vector than what is absolutely necessary.

As discussed in section 4.2.4, evaluating the difference between the zero-sequence voltages during different voltage vectors within a short period allows to eliminate the resistive and EMF related terms and obtain only the anisotropy related information. The differential zero-sequence voltage is the product of the inductance ratio vector and the vectorial difference of the respective voltage vectors:

$$\Delta u_{\mathrm{NAN}} = \begin{bmatrix} \kappa_\alpha & \kappa_\beta & 0 \end{bmatrix} \Delta \boldsymbol{u}^{\mathrm{s}}_{\mathrm{term}} \tag{4.140}$$

$$\Delta u_{\mathrm{NAN}} = \begin{bmatrix} \kappa_\mathrm{a} - \frac{1}{3} & \kappa_\mathrm{b} - \frac{1}{3} & \kappa_\mathrm{c} - \frac{1}{3} \end{bmatrix} \Delta \boldsymbol{u}^{\mathrm{p}}_{\mathrm{term}} \,. \tag{4.141}$$

Given that $\boldsymbol{\kappa}$ contains two-dimensional information, at least two linearly independent $\Delta \boldsymbol{u}_{\mathrm{term}}$ must be applied to solve the equations for κ_α and κ_β or, with the knowledge that $\kappa_\mathrm{a} + \kappa_\mathrm{b} + \kappa_\mathrm{c} = 1$, for κ_a, κ_b and κ_c respectively. For the discrete voltage vectors this means that *at least two linearly independent active vectors* and, *additionally, one other active or zero vector* are required. To ensure sufficient durations for these vectors at all times, modified modulation schemes are required, which are the subject of chapter 6.

4.4.2. Comparison with Requirements for Current-Based Techniques

Let us consider again the admittance matrix resulting from the fundamental wave inductance model,

$$\boldsymbol{Y}^{\mathrm{s}*} = \begin{bmatrix} Y^*_{\alpha\alpha} & Y^*_{\alpha\beta} \\ Y^*_{\alpha\beta} & Y^*_{\beta\beta} \end{bmatrix} = \frac{1}{L_\Sigma^2 - L_\Delta^2} \begin{bmatrix} L_\Sigma - L_\Delta \cos(2\varphi) & -L_\Delta \sin(2\varphi) \\ -L_\Delta \sin(2\varphi) & L_\Sigma + L_\Delta \cos(2\varphi) \end{bmatrix} . \tag{4.142}$$

Similar as for the zero-sequence voltage based approach, the requirements on the number and orientation of a suitable set of discrete voltage vectors for direct calculation of a position estimate shall be regarded. Using (4.80) and (4.83) we can write

$$\begin{bmatrix} \Delta \mathrm{d}i_\alpha/\mathrm{d}t \\ \Delta \mathrm{d}i_\beta/\mathrm{d}t \end{bmatrix} = \begin{bmatrix} Y^*_{\alpha\alpha} & Y^*_{\alpha\beta} \\ Y^*_{\alpha\beta} & Y^*_{\beta\beta} \end{bmatrix} \begin{bmatrix} \Delta u_\alpha \\ \Delta u_\beta \end{bmatrix} . \tag{4.143}$$

This means that when applying different voltage vectors in quick succession, the differences in the measured current derivatives from one vector to another are linearly related to the differences in the voltage vectors via the admittance matrix $\boldsymbol{Y}^{\mathrm{s}*}$. To determine the three unknowns in $\boldsymbol{Y}^{\mathrm{s}*}$, two linearly independent $\Delta\boldsymbol{u}_{\mathrm{term}}$ and therefore at least three different voltage vectors $\boldsymbol{u}_{\mathrm{term}}$ are required as a minimum. After the admittances have been determined, the electrical rotor position can be obtained (assuming $L_\Delta < 0$) by

$$\tilde{\varphi}_{\mathrm{Y}} = \frac{1}{2}\mathrm{atan2}\left(\; 2Y^*_{\alpha\beta}, \quad Y^*_{\alpha\alpha} - Y^*_{\beta\beta} \; \right) + k\pi \tag{4.144}$$

or, if we consider $Y^*_{\alpha\beta}$ being calculated separately from $Y^*_{\beta\alpha}$,

$$\tilde{\varphi}_{\mathrm{Y}} = \frac{1}{2}\mathrm{atan2}\left(\; Y^*_{\alpha\beta} + Y^*_{\beta\alpha}, \quad Y^*_{\alpha\alpha} - Y^*_{\beta\beta} \; \right) + k\pi \tag{4.145}$$

similar to the function used in [KKS+11]. At least in the sense of required voltage vectors the requirements placed on a modified modulation strategy are then identical. The original INFORM technique indeed inserted multiple active voltage vectors between regular SVM periods which fulfil this requirement. Further advancements in the area of current-based techniques have led to the concept of arbitrary injection. The main idea behind the concept of arbitrary injection is to consider the isotropic admittance

$$Y_\Sigma = \left(Y^*_{\alpha\alpha} + Y^*_{\beta\beta} \right)/2 = \frac{L_\Sigma}{L_\Sigma^2 - L_\Delta^2} \tag{4.146}$$

as a known and separately determined parameter and therefore effectively reduce the number of unknowns to two [Lan15, pp. 961-963]. Obviously, only two different voltage vectors are then required as a minimum and except for low magnitudes of the reference voltage vector, this requirement is already fulfilled by conventional space vector modulation. Additionally the use of oversampling and linear approximation for determining the current changes according to [Lan14] can reduce the minimum voltage vector durations needed for sufficient signal-to-noise ratios. The isotropic admittance may however need to be updated regularly during operation to account for varying levels of saturation [Pau14, p. 73], in which case three vectors are still required [Lan14, p. 46].

The conclusion that can be drawn from this is that the need to modify the SVM for zero-sequence voltage based techniques is certainly a drawback when compared to current-based techniques following the concept of arbitrary injection. This is owed to the fact that, at each time instant, the zero-sequence voltage can provide only one-dimensional information, whereas current measurements allow to acquire two-dimensional information.

4.5. Experimental Investigation of Parasitic Effects at the Neutral Point

This section discussses two effects that, during the work on this thesis, have shown to affect the measurement of the zero-sequence voltage considerably and that can generally be attributed to the existence of parasitic capacitances in the motor and the measuring system. The first effect is overshoot and ringing that occurs at the neutral point after a switching event. This effect is well-known and has previously been described for example in [HP04]. The second effect has, to the knowledge of the author, not yet been documented in the literature and relates to the coupling of external disturbances into the neutral point voltage over the motor housing.

In this thesis, three low power PMSMs are used for experimental investigations. Motor M1 is a prototype conveyor roll motor that was specifically optimized for sensorless control. Motor M2 and M3 are commercially available motors. In the case of M2, the neutral point has been made available by the manufacturer. Motor M3 has an accessible neutral point by default, which is quite rare. All three are external rotor motors. More information about the motors is provided in appendix A. Investigations are mainly carried out with motors M1 and M2, motor M3 is only used at one point in this thesis. The investigations in the two following sections are performed with motor M2.

4.5.1. Ringing of the Neutral Point Voltage

When the terminal voltages are switched by the inverter, the neutral point voltage changes according to (4.51) and thus also the zero-sequence voltage. However, in practice the voltage step at the neutral point is often accompanied by significant overshoot and ringing that is reflected in the zero-sequence voltage. This effect can best be observed in an isolated way by simultaneously switching all terminal voltages between the negative and positive potential of the DC link while monitoring the neutral point voltage on an oscilloscope, as shown in Fig. 4.4. Here, the three terminals of motor M2 were tied together and switched from the low potential – in the following simply referred to as ground – to the high potential of the DC link voltage by a single half-bridge of the inverter. Between neutral point and ground, a 10 kΩ resistor was connected to simulate a voltage divider in a measurement scenario.

The ringing can be attributed to the interaction between the motor inductances and parasitic capacitances, which create resonance at high frequencies. Besides capacitances within the motor, capacitances involving the measurement circuitry and the cables can also contribute to the ringing. Whether the motor is grounded or not showed to have a significant effect on the ringing of the neutral point. Grounding refers here to an electrical connection between the motor housing and the low potential of the DC link. An overshoot of more than 30 % can be observed for the grounded case. When the motor housing is isolated, the overshoot and ringing is significantly decreased and the neutral point settles faster compared to a grounded motor, as can be observed in Fig. 4.4. To make this general effect plausible, Fig. 4.5 shows a circuit diagram with two lumped capacitances located between the neutral point and the motor housing and between the housing and ground. It is clear that short-circuiting the capacitance C_{HG} increases the overall capacitance of this circuit.

It should be noted that while C_{NH} will be rather constant and a result of the machine structure, the capacitance C_{HG} can change during operation, e.g. when an electrical connection is made to other objects. It was found that even touching the motor with the hand resulted in a significant increase in overshoot and ringing, leading to a behavior somewhere between the isolated and the grounded state.

When designing a measurement circuit for the zero-sequence voltage, care should be taken to keep additional capacitances at the neutral point low and avoid increasing the ringing and the settling time further. The effect of placing an additional capacitance of 47 pF between the neutral point of motor M2 and ground is shown in Fig. 4.6.

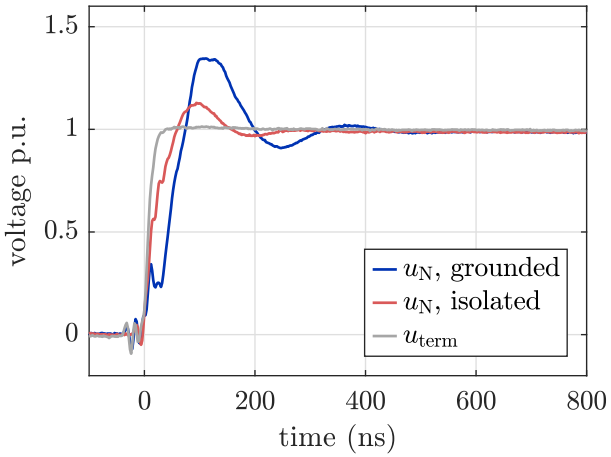

Figure 4.4.: Step response of the neutral point voltage for motor M2 in the grounded and in the isolated case.

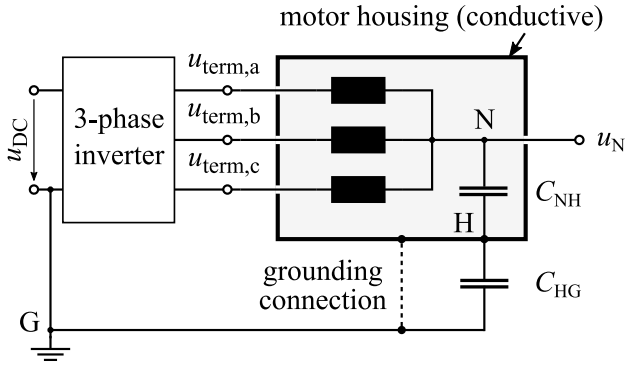

Figure 4.5.: Simplified circuit diagram with lumped capacitance at the neutral point. If a grounding connection exists, C_{HG} is bypassed and the overall capacitance increases.

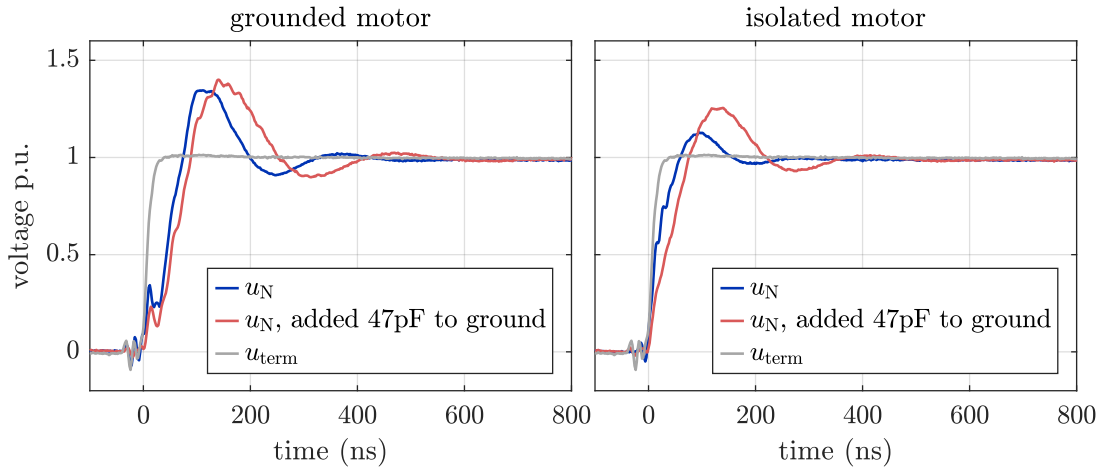

Figure 4.6.: Effect of additional capacitance of 47 pF between the neutral point and inverter ground, for grounded and isolated motor M2.

In the measurement circuit that will be used in the experimental parts of this work, the neutral point voltage is scaled down using a voltage divider. The size of the resistances must be chosen so that on one hand sufficient bandwidth is achieved in combination with measurement capacitances but on the other hand current flow through the neutral point remains small.

In Fig. 4.7, it can be seen that the overshoot decreases slightly with decreasing resistances from 1 MΩ to 10 kΩ. A significant reduction of the overshoot is visible for a resistance of 1 kΩ, however significant current would flow through the neutral point in this case and a small stationary offset is also noticable.

In addition to the main oscillation visible in the previous figures, significant additional higher frequency oscillations were reported in [HP04], apparently caused by reflections on long motor cables. The authors used an RC filter at the motor terminals to reduce these oscillations. It should be added, however, that the authors of this work sampled the zero-sequence voltage before the main oscillation had decayed.

4.5.2. Capacitive Coupling of External Disturbances

Besides the discussed ringing of the neutral point voltage, parasitic capacitances in the motor can also cause problems when parts of the motor are exposed to external electrical disturbances, e.g. when the motor is conductively connected to other electrical devices such as other motors through its flange connection or its shaft. Through the parasitic

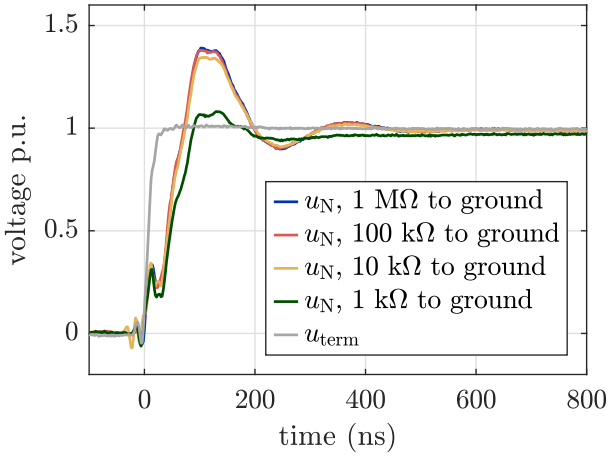

Figure 4.7.: Effect of different resistances between the neutral point and ground (housing grounded).

capacitances between housing and neutral point, disturbances can then couple onto the neutral point and corrupt the measurements of the zero-sequence voltage. In the best case this leads only to increased signal noise but in the worst case the machine can behave incorrectly. The latter was experienced for example in a setup of multiple conveyor roller motors that were mounted on a common conductive frame and were found to be mutually disturbing each other, leading to losses of the initially determined polarity and thus ongoing reversals of the generated torque.

To the knowledge of the author, the effect of a capacitive coupling of external disturbances has not yet been described in the scientific literature, except for a vague mention in [BDGL04] that shielding and grounding practices were observed to influence the used technique. The effect is demonstrated on an experimental setup shown in Fig. 4.8. It includes two exemplars of motor M2 that are mounted on an aluminum plate, through which their housings are conductively connected to each other. The three terminals of one motor are tied together and connected to an inverter which applies pulses of 2.5 µs duration to them. The second motor is used to observe resulting disturbances at its neutral point; its terminals are connected to the ground of the same inverter. Using a laboratory cable of 50 cm length, the aluminum plate can be optionally connected to ground.

On the left side of Fig. 4.9, the neutral point voltages of the driven and the disturbed motor are shown without ground connection. A significant oscillation can be observed at the neutral point of the disturbed motor that lasts approximately 400 ns. The problematic

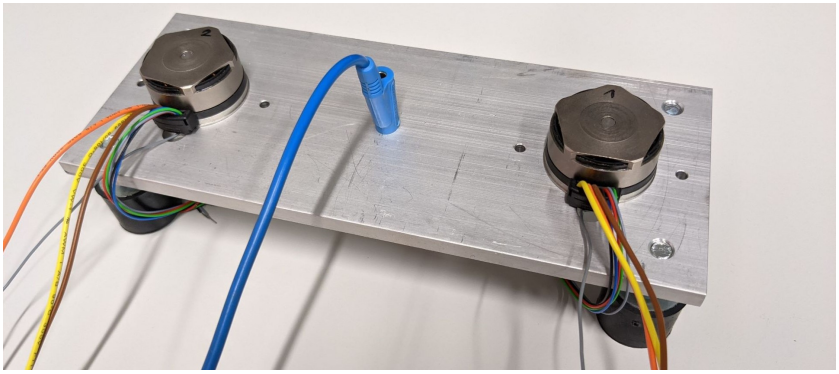

Figure 4.8.: Test setup for capacitive coupling of disturbances onto the neutral point. The blue cable connects the aluminum plate and therefore the two motors to the inverter ground.

aspect here is that such disturbances can happen anytime in the switching period of the disturbed motor. If the disturbance happens to fall into the sampling period of the measured u_{NAN} voltage, the measurements will clearly be corrupted.

There are two solutions to this problem. If possible, the motor housing can be electrically isolated from the environment, which is admittedly a trivial, yet effective solution. However, it can be assumed that this is probably not practical in most applications or may even be impossible. The more viable solution is then to provide an alternative low impedance path for the disturbance by grounding the motor, i.e. connecting the housing to a stable voltage potential such as the system ground. As illustrated in Fig. 4.10, disturbance currents are then diverted through the ground connection instead of coupling onto the neutral point. On the right side of Fig. 4.9, it can be seen that grounding the aluminum plate reduces the disturbance in size and, more importantly, only relatively high frequency oscillations remain as disturbance. A full elimination of disturbances cannot be expected due to the parasitic inductance of the ground connection. The remaining high frequency components can be suppressed by using a lowpass filter whose cutoff frequency is low enough to effectively remove the remaining oscillations but high enough to capture the transient behavior of the neutral point for the measurements. Without ground connection, a lower cutoff frequency would clearly be required. In the aforementioned conveyor roller setup, the grounding practice has proven successful in preventing any misbehavior.

As a conclusion, a coupling of external electrical disturbances onto the neutral point should be anticipated and can be prevented by isolating or grounding the motor. When

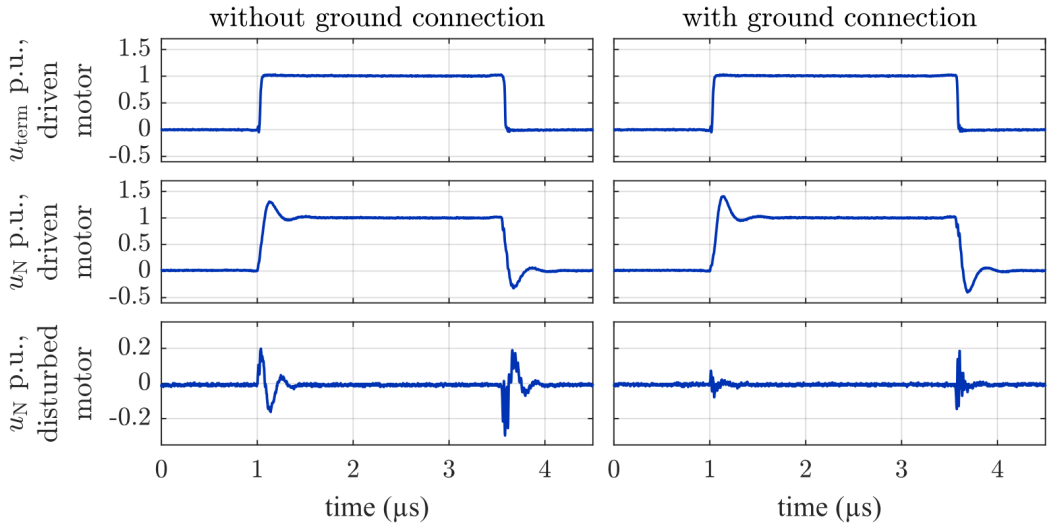

Figure 4.9.: Effect of grounding the motor housing. With the ground connection, capacitive couplings of disturbances onto the neutral point are significantly reduced to only the highest frequency oscillations.

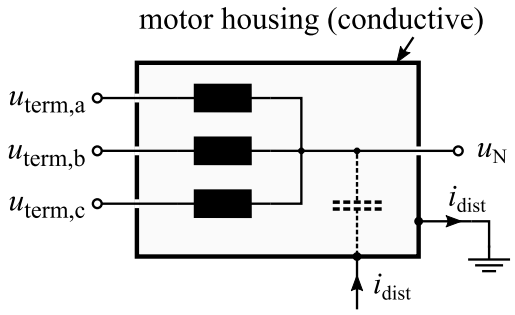

Figure 4.10.: By grounding the motor, disturbance currents are diverted to ground instead of coupling onto the neutral point.

grounding the motor, the inductance of the grounding connection will significantly determine up to which frequency disturbance currents are diverted through the grounding connection instead of coupling to the neutral point through the motor's parasitic capacitances. Therefore, such connection should generally be as short as possible.

4.6. Summary

In this chapter, the anisotropy information that can be obtained from the zero-sequence voltage was analyzed. For techniques using the zero-sequence voltage, the anisotropy information expresses itself in the form of position-dependent inductance ratios. Besides the desired anisotropy information, the zero-sequence voltage contains disturbing terms, namely resistive voltages and voltages induced by rotor movement. By applying different voltage vectors within a short time window and considering only the differences of the respective zero-sequence voltages, these slowly changing terms can be systematically eliminated and the inductance ratios can be determined. Accordingly, the (negative) zero-sequence voltage and the differences of it within short time periods are described in the 'abc' reference frame by

$$u_{\mathrm{NAN}} = -u_0 \quad = \boldsymbol{\kappa}_{\Delta}^{\mathrm{p}} \boldsymbol{u}_{\mathrm{term}}^{\mathrm{p}} - \boldsymbol{\kappa}^{\mathrm{p}} \boldsymbol{u}_{\mathrm{slow}}^{\mathrm{p}} \tag{4.147}$$

$$\Delta u_{\mathrm{NAN}} = -\Delta u_0 = \boldsymbol{\kappa}_{\Delta}^{\mathrm{p}} \Delta \boldsymbol{u}_{\mathrm{term}}^{\mathrm{p}} \tag{4.148}$$

with the inductance ratios

$$\boldsymbol{\kappa}^{\mathrm{p}} = \begin{bmatrix} \kappa_{\mathrm{a}} & \kappa_{\mathrm{b}} & \kappa_{\mathrm{c}} \end{bmatrix} \tag{4.149}$$

$$\boldsymbol{\kappa}_{\Delta}^{\mathrm{p}} = \begin{bmatrix} \kappa_{\mathrm{a}} - 1/3 & \kappa_{\mathrm{b}} - 1/3 & \kappa_{\mathrm{c}} - 1/3 \end{bmatrix} . \tag{4.150}$$

In the 'αβ0' reference frame they are described by

$$u_{\mathrm{NAN}} = -u_0 \quad = \boldsymbol{\kappa}_{\Delta}^{\mathrm{s}} \boldsymbol{u}_{\mathrm{term}}^{\mathrm{s}} - \boldsymbol{\kappa}^{\mathrm{s}} \boldsymbol{u}_{\mathrm{slow}}^{\mathrm{s}} \tag{4.151}$$

$$\Delta u_{\mathrm{NAN}} = -\Delta u_0 = \boldsymbol{\kappa}_{\Delta}^{\mathrm{s}} \Delta \boldsymbol{u}_{\mathrm{term}}^{\mathrm{s}} \tag{4.152}$$

with the inductance ratios

$$\boldsymbol{\kappa}^{\mathrm{s}} = \begin{bmatrix} \kappa_\alpha & \kappa_\beta & 1 \end{bmatrix} \tag{4.153}$$

$$\boldsymbol{\kappa}^{\mathrm{s}}_{\Delta} = \begin{bmatrix} \kappa_\alpha & \kappa_\beta & 0 \end{bmatrix} . \tag{4.154}$$

The analysis in the 'αβ0' frame showed that, different from the reduced admittance matrix, the inductance ratios are dependent also on the mutual inductances with the zero-sequence axis. To obtain anisotropy information, $L_{0\alpha}$ and $L_{0\beta}$ must be different from zero, which corresponds to mutually different variations of self- and mutual inductances in the 'abc' reference frame.

Starting from a general fundamental wave inductance matrix, the inductance ratios resulting for the general case and three special cases were discussed for additional insights. Table 4.1 sums up the anisotropy information contained in the zero-sequence voltage and in the currents for these cases in a comprehensive manner. In addition, the trivial case of an isotropic machine with $L_\Delta = L_{\Delta 0} = 0$ is also listed. One thing becomes very clear from the conducted analysis. Anisotropy information obtained via the zero-sequence voltage and anisotropy information obtained via currents or their derivatives cannot be regarded equivalent and depending on the inductance variations, motors can be more suitable for the one or the other. For extreme cases of a fundamental wave inductance matrix, the anisotropy information can at least theoretically vanish for either of the two. Moreover, a difference between L_{dd} and L_{qq} is *neither a sufficient nor a necessary condition* to obtain anisotropy signals via the zero-sequence voltage.

Further differences lie in the presence of 4φ-components in the inductance ratios and in the fact that zero-sequence voltage measurements can acquire only one-dimensional information per each time instant compared to two-dimensional information in the case of current measurements which does therefore not allow a relaxation of the voltage vector requirements similar to that achieved with the concept of arbitrary injection. At least two linearly independent active vectors and, additionally, one other active or zero vector are required to estimate the position in a way that slowly changing voltage terms are eliminated.

In addition to the analytical considerations, effects that arise from parasitic capacitances have been discussed. In particular, grounding the motor has been shown to have a significant effect on the transient behaviour of the neutral point voltage and its robustness against external disturbances.

Table 4.1.: Anisotropy information contained in the zero-sequence voltage and the currents in the 'αβ' frame for different special cases of the fundamental wave inductance matrix in (4.85).

Assumptions	Anisotropy information in zero-sequence voltage: $\begin{bmatrix}\kappa_\alpha & \kappa_\beta\end{bmatrix}^{\mathrm{T}}$	Anisotropy information in currents: $\boldsymbol{Y}^{\mathrm{s*}} = (\boldsymbol{L}^{\mathrm{s*}})^{-1}$
-	$\frac{1}{1-(L_\Delta/L_\Sigma)^2}\begin{bmatrix}-(L_{\Delta0}/L_\Sigma)\cos(-2\varphi)+\left(L_{\Delta0}L_\Delta/{L_\Sigma}^2\right)\cos(4\varphi)\\ -(L_{\Delta0}/L_\Sigma)\sin(-2\varphi)+\left(L_{\Delta0}L_\Delta/{L_\Sigma}^2\right)\sin(4\varphi)\end{bmatrix}$	$\frac{1}{L_\Sigma^2-L_\Delta^2}\begin{bmatrix}L_\Sigma-L_\Delta\cos(2\varphi) & -L_\Delta\sin(2\varphi)\\ -L_\Delta\sin(2\varphi) & L_\Sigma+L_\Delta\cos(2\varphi)\end{bmatrix}$
$L_{\mathrm{m}2}=0$ $\Leftrightarrow L_{\Delta0}=L_\Delta$	$\frac{1}{1-(L_\Delta/L_\Sigma)^2}\begin{bmatrix}-(L_\Delta/L_\Sigma)\cos(-2\varphi)+(L_\Delta/L_\Sigma)^2\cos(4\varphi)\\ -(L_\Delta/L_\Sigma)\sin(-2\varphi)+(L_\Delta/L_\Sigma)^2\sin(4\varphi)\end{bmatrix}$	$\frac{1}{L_\Sigma^2-L_\Delta^2}\begin{bmatrix}L_\Sigma-L_\Delta\cos(2\varphi) & -L_\Delta\sin(2\varphi)\\ -L_\Delta\sin(2\varphi) & L_\Sigma+L_\Delta\cos(2\varphi)\end{bmatrix}$
$L_{\mathrm{m}2}=L_2$ $\Leftrightarrow L_{\Delta0}=0$	$\begin{bmatrix}0\\0\end{bmatrix}$	$\frac{1}{L_\Sigma^2-L_\Delta^2}\begin{bmatrix}L_\Sigma-L_\Delta\cos(2\varphi) & -L_\Delta\sin(2\varphi)\\ -L_\Delta\sin(2\varphi) & L_\Sigma+L_\Delta\cos(2\varphi)\end{bmatrix}$
$L_{\mathrm{m}2}=-L_2/2$ $\Leftrightarrow L_\Delta=0$	$\begin{bmatrix}-(L_{\Delta0}/L_\Sigma)\cos(-2\varphi)\\ -(L_{\Delta0}/L_\Sigma)\sin(-2\varphi)\end{bmatrix}$	$\begin{bmatrix}1/L_\Sigma & 0\\ 0 & 1/L_\Sigma\end{bmatrix}$
$L_{\mathrm{m}2}=L_2=0$ $\Leftrightarrow L_\Delta=L_{\Delta0}=0$	$\begin{bmatrix}0\\0\end{bmatrix}$	$\begin{bmatrix}1/L_\Sigma & 0\\ 0 & 1/L_\Sigma\end{bmatrix}$

5. Position Estimation

In the previous chapter, the inductance ratio vector $\boldsymbol{\kappa}$ was identified to include the relevant anisotropy information that is available in the zero-sequence voltage. Its components can be obtained from a suitable sequence of measurements at different discrete voltage vectors, eliminating slowly changing voltage terms. This chapter discusses the estimation of the rotor position from the inductance ratios.

5.1. Angle Calculation

Based on the fundamental wave inductance model, the inductance ratios contain harmonic components of two and four times the electrical rotor position with respective phase shifts. If the inductance matrix corresponds to one of the two special cases described in sections 4.3.3 and 4.3.5, the position can be explicitly calculated without further knowledge about the machine. In the case $L_\Delta = 0$, the calculation is trivial, while for $L_\Delta = L_{\Delta 0}$ it is not as straightforward but still possible as will be shown.

It is clear that the inductance waveforms of real motors will match these special cases only to a certain extent. The ratio of the 2φ- and $4\varphi-$components in the inductance ratios can differ from the assumed ratio and additional harmonics of both the mechanical and electrical rotor position may be present. Additionally, the inductances and inductance ratios will also vary over the machine currents due to saturation of the core material. Because the stator flux adds to the permanent magnet flux, the saturation usually leads to significant shifts of the estimated axis from the actual position that must be considered. In addition, magnetic hysteresis [CLK11] and eddy currents [Lan14] are also known to have an effect on anisotropy-based estimation in general.

A typical approach to position estimation is to first find a function or structure that returns the correct position for a motor corresponding to the assumed inductance model. Ideally, this function or structure does not require knowledge of any machine parameters. Deviations from the model can then be accounted for by adding additional compensation elements. These may include parameters or datasets obtained by finite element method

(FEM) simulations or experiments to better describe the actual characteristics of the respective machine (type), including operation under varying load conditions and at different speeds. Following this approach, the following sections describe the calculation of the position estimate for the two special cases that allow a parameter-free position estimation. Aterwards, stator current dependence and approaches to address additional harmonics in the inductance ratios are discussed briefly. Because the position estimate obtained from the inductance ratio vector has an uncertainty of 180° electrical, a procedure for initial polarity estimation is finally given.

5.1.1. Calculation from Original Inductance Ratios

It has been discussed that for zero-sequence voltage based techniques, the anisotropy information is contained in position-dependent inductance ratios, the components of $\boldsymbol{\kappa}$. The most intuitive way to calculate a position estimate is certainly to calculate the orientation of the $\boldsymbol{\kappa}$ vector in the $\alpha\beta$-plane using the *arctangent* function. This approach was used already in [HJP97]. Note that the position has typically not been calculated actually from $\boldsymbol{\kappa}$ but from the directional zero-sequence voltage $\boldsymbol{u}_{\mathrm{NAN,dir}} = \boldsymbol{\kappa} u_{\mathrm{DC}}$, as this is what is directly obtained from the measurements.

In theory this approach provides a correct position estimate if the components of $\boldsymbol{\kappa}$ consist of a single harmonic component, which for PMSMs is the 2φ-component. According to the analysis in 4.3, this is the case only if

$$L_{\mathrm{m2}} = -L_2/2 \Leftrightarrow L_\Delta = 0 \tag{5.1}$$

in the inductance model. The α- and β-components of $\boldsymbol{\kappa}$ are then

$$\begin{aligned} \kappa_\alpha\left(L_\Delta = 0\right) &= -\frac{L_{\Delta 0}}{L_\Sigma}\cos\left(-2\varphi\right) \\ \kappa_\beta\left(L_\Delta = 0\right) &= -\frac{L_{\Delta 0}}{L_\Sigma}\sin\left(-2\varphi\right) \ . \end{aligned} \tag{5.2}$$

Accordingly, the position estimate can be calculated using

$$\tilde{\varphi}_\kappa = \begin{cases} -\frac{1}{2}\mathrm{atan2}\left(\kappa_\beta,\ \kappa_\alpha\right) + k\pi, & L_{\Delta 0} < 0 \\ -\frac{1}{2}\mathrm{atan2}\left(-\kappa_\beta,\ -\kappa_\alpha\right) + k\pi, & L_{\Delta 0} > 0 \ . \end{cases} \tag{5.3}$$

Because $L_\Delta = \left(L_{\mathrm{dd}} - L_{\mathrm{qq}}\right)/2$, assuming negligible L_Δ implies that this approach yields

best results for machines with small to no differences between L_{dd} and L_{qq}.

In contrast to this, most of the previous works have modelled the position dependence of the inductance matrix according to the special case with $L_\Delta = L_{\Delta 0}$ and still used the above estimation function. To nevertheless justify this approach, it has been argued that L_Δ is often relatively small in many machines so that the additional terms varying with 4φ can be neglected [Jia00, p. 62]. Since the appearance of the terms varying with 4φ concerns all techniques using the zero-sequence voltage, the same argumentation was also used in works using rotating [BDGG05] and alternating injection [XZ16a] approaches even though different signal processing is required there for position estimation. In [ITSA16], the neglection of the term has not been explicitly stated, but the components of $\boldsymbol{u}_{\mathrm{NAN,dir}}$ have been assumed to be approximately sinusoidal which ultimately leads to the same situation.

For motors that feature only small anisotropies, the neglection of the 4φ-components is indeed a viable option. Moreover, the two mentioned special cases coincide at $L_\Delta \approx L_{\Delta 0} \approx 0$ so that a distinction is no longer meaningful. Yet, this approach is not fully satisfactory. Especially for motors that exhibit larger inductance variations and should therefore actually be well suited for anisotropy-based position estimation, the systematic estimation errors can become quite significant. To demonstrate this, Fig. 5.1 shows the estimated position obtained for an inductance model with $L_\Delta = L_{\Delta 0}$ over the actual position for different values of $r = L_\Delta / L_\Sigma$. The maximum absolute errors increase almost proportionally with $|r|$ and reach a maximum of 15° at $|r| = 0.5$, as illustrated in Fig. 5.2.

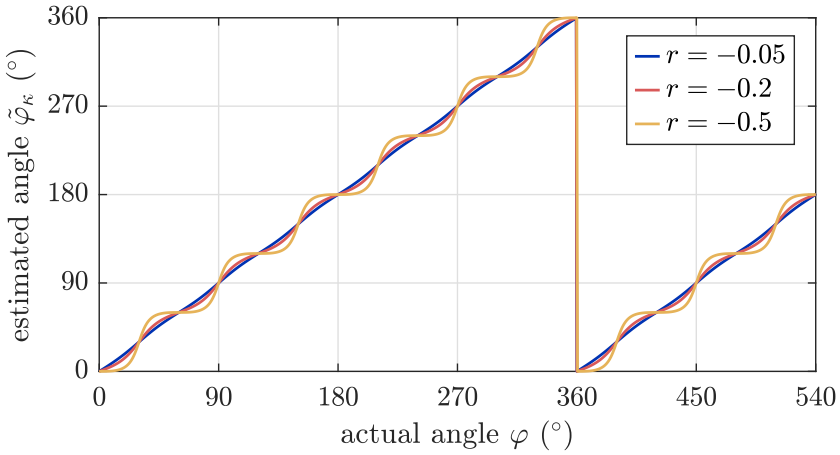

Figure 5.1.: Estimated angle $\tilde{\varphi}_\kappa$ under assumption of the inductance model with $L_\Delta = L_{\Delta 0}$ for different values of $r = L_\Delta / L_\Sigma$.

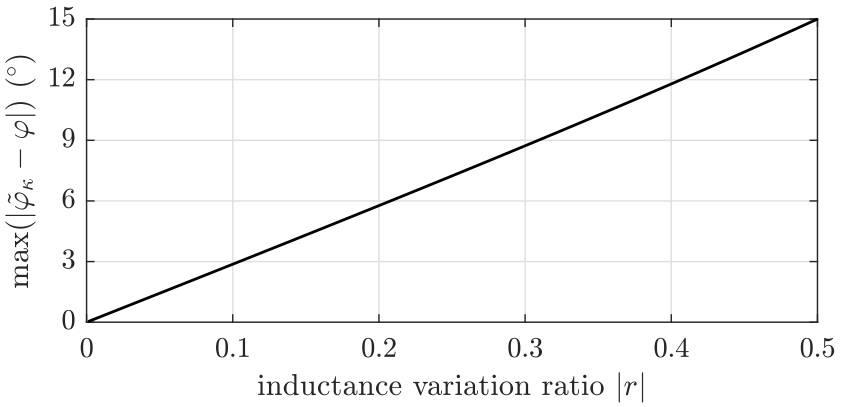

Figure 5.2.: Maximum estimation errors using $\tilde{\varphi}_\kappa$ for the inductance model with $L_\Delta = L_{\Delta 0}$.

5.1.2. Calculation from Transformed Inductance Ratios

It can be assumed that the 4φ-terms have been neglected in many works primarily because a function that can correctly calculate the position under consideration of these has been lacking. For the elimination of significant 4φ-terms, methods for the general compensation of secondary harmonics (see section 5.2) or methods like the harmonic activated neural network in [Wer18] can be used, but these increase the complexity of the estimation scheme and require identification of the harmonic components either online or offline. However, for the discussed special case with $L_\Delta = L_{\Delta 0}$ it is actually possible to reconstruct the correct rotor position analytically by relatively simple means and without knowledge of machine parameters as will be shown in this section. In this section, a method is described that transforms the inductance ratios into intermediate signals that have only terms varying with two times the rotor position and calculates the position from these. The transformation was originally found in [Man13]. Based on that transformation, a vector of transformed inductance ratios

$$\boldsymbol{\rho}^{\mathrm{p}} = \begin{bmatrix} \rho_{\mathrm{a}} \\ \rho_{\mathrm{b}} \\ \rho_{\mathrm{c}} \end{bmatrix}^{\mathrm{T}} = \frac{1}{\sqrt{3}} \begin{bmatrix} \sqrt{\kappa_{\mathrm{b}}\kappa_{\mathrm{c}}/\kappa_{\mathrm{a}}} \\ \sqrt{\kappa_{\mathrm{a}}\kappa_{\mathrm{c}}/\kappa_{\mathrm{b}}} \\ \sqrt{\kappa_{\mathrm{a}}\kappa_{\mathrm{b}}/\kappa_{\mathrm{c}}} \end{bmatrix}^{\mathrm{T}} \tag{5.4}$$

is defined. Compared to [Man13], the transformation is performed using the inductance ratios and not the directional zero-sequence voltages and a factor $1/\sqrt{3}$ is added to make the amplitude of the modified inductance ratios comparable to the original inductance

ratios. Without loss of generality, it is assumed for the mutual inductances that not only their variations L_{m2} but also their mean values L_{m0} in the 'abc' frame are zero. This leads to simpler inductance ratios

$$\boldsymbol{\kappa}^{\mathrm{p}} = \frac{1}{L_{\mathrm{bb}}L_{\mathrm{cc}} + L_{\mathrm{aa}}L_{\mathrm{cc}} + L_{\mathrm{aa}}L_{\mathrm{bb}}} \begin{bmatrix} L_{\mathrm{bb}}L_{\mathrm{cc}} \\ L_{\mathrm{cc}}L_{\mathrm{aa}} \\ L_{\mathrm{aa}}L_{\mathrm{bb}} \end{bmatrix}^{\mathrm{T}} \tag{5.5}$$

that can be inserted into (5.4), yielding

$$\boldsymbol{\rho}^{\mathrm{p}} = \frac{1}{\sqrt{3}} \begin{bmatrix} \sqrt{{L_{\mathrm{aa}}}^2 (L_{\mathrm{aa}}L_{\mathrm{bb}} + L_{\mathrm{bb}}L_{\mathrm{cc}} + L_{\mathrm{cc}}L_{\mathrm{aa}})} \\ \sqrt{{L_{\mathrm{bb}}}^2 (L_{\mathrm{aa}}L_{\mathrm{bb}} + L_{\mathrm{bb}}L_{\mathrm{cc}} + L_{\mathrm{cc}}L_{\mathrm{aa}})} \\ \sqrt{{L_{\mathrm{cc}}}^2 (L_{\mathrm{aa}}L_{\mathrm{bb}} + L_{\mathrm{bb}}L_{\mathrm{cc}} + L_{\mathrm{cc}}L_{\mathrm{aa}})} \end{bmatrix}^{\mathrm{T}} . \tag{5.6}$$

Based on the assumptions on the self-inductances, it can be seen that

$$L_{\mathrm{aa}}L_{\mathrm{bb}} + L_{\mathrm{bb}}L_{\mathrm{cc}} + L_{\mathrm{cc}}L_{\mathrm{aa}} = 3\left(L_{\Sigma}^2 - L_{\Delta}^2\right) \tag{5.7}$$

and therefore

$$\boldsymbol{\rho}^{\mathrm{p}} = \begin{bmatrix} \sqrt{L_{\mathrm{aa}}^2 \cdot 3\left(L_{\Sigma}^2 - L_{\Delta}^2\right)} \\ \sqrt{L_{\mathrm{bb}}^2 \cdot 3\left(L_{\Sigma}^2 - L_{\Delta}^2\right)} \\ \sqrt{L_{\mathrm{cc}}^2 \cdot 3\left(L_{\Sigma}^2 - L_{\Delta}^2\right)} \end{bmatrix}^{\mathrm{T}} . \tag{5.8}$$

Because

$$3\left(L_{\Sigma}^2 - L_{\Delta}^2\right) > 0 \tag{5.9}$$

and

$$L_{\lambda\lambda} > 0, \quad \lambda \in \{\mathrm{a}, \mathrm{b}, \mathrm{c}\} \tag{5.10}$$

one can rearrange (5.8) to

$$\boldsymbol{\rho}^{\mathrm{p}} = \frac{1}{3\sqrt{L_{\Sigma}^2 - L_{\Delta}^2}} \begin{bmatrix} \sqrt{L_{\mathrm{aa}}^2} \\ \sqrt{L_{\mathrm{bb}}^2} \\ \sqrt{L_{\mathrm{cc}}^2} \end{bmatrix}^{\mathrm{T}} \tag{5.11}$$

$$= \frac{1}{3\sqrt{L_{\Sigma}^2 - L_{\Delta}^2}} \begin{bmatrix} L_{\mathrm{aa}} \\ L_{\mathrm{bb}} \\ L_{\mathrm{cc}} \end{bmatrix}^{\mathrm{T}} \tag{5.12}$$

$$= \frac{1}{3\sqrt{L_{\Sigma}^2 - L_{\Delta}^2}} \begin{bmatrix} L_{\Sigma} + 2L_{\Delta}\cos\left(2\varphi\right) \\ L_{\Sigma} + 2L_{\Delta}\cos\left(2\left(\varphi - \frac{2\pi}{3}\right)\right) \\ L_{\Sigma} + 2L_{\Delta}\cos\left(2\left(\varphi - \frac{4\pi}{3}\right)\right) \end{bmatrix}^{\mathrm{T}} . \tag{5.13}$$

As can be seen, the components of $\boldsymbol{\rho}^{\mathrm{p}}$ have the same shape as the self-inductances. They do not contain a component varying with 4φ. Note that (5.13) is obtained also if $L_{\mathrm{m0}} \neq 0$; what changes in this case is the value of L_{Σ}.

The inductance variation ratio $r = L_{\Delta}/L_{\Sigma}$ can be used to simplify the expression so that

$$\boldsymbol{\rho}^{\mathrm{p}} = \frac{1}{3\sqrt{1 - \left(L_{\Delta}/L_{\Sigma}\right)^2}} \begin{bmatrix} 1 + 2\left(L_{\Delta}/L_{\Sigma}\right)\cos\left(2\varphi\right) \\ 1 + 2\left(L_{\Delta}/L_{\Sigma}\right)\cos\left(2\left(\varphi - \frac{2\pi}{3}\right)\right) \\ 1 + 2\left(L_{\Delta}/L_{\Sigma}\right)\cos\left(2\left(\varphi - \frac{4\pi}{3}\right)\right) \end{bmatrix}^{\mathrm{T}} \tag{5.14}$$

$$= \frac{1}{\sqrt{1 - r^2}} \begin{bmatrix} \frac{1}{3} & \frac{1}{3} & \frac{1}{3} \end{bmatrix} + \frac{2}{3}\frac{1}{\sqrt{1 - r^2}} \begin{bmatrix} r\cos\left(2\varphi\right) \\ r\cos\left(2\left(\varphi - \frac{2\pi}{3}\right)\right) \\ r\cos\left(2\left(\varphi - \frac{4\pi}{3}\right)\right) \end{bmatrix}^{\mathrm{T}} . \tag{5.15}$$

Using the same transformation as for the original inductance ratio vector, the modified inductance ratios can be transformed to the 'αβ0' frame:

$$\boldsymbol{\rho}^{\mathrm{s}} = \begin{bmatrix} \rho_{\alpha} \\ \rho_{\beta} \\ \rho_{0} \end{bmatrix}^{\mathrm{T}} = \rho^{\mathrm{p}} \boldsymbol{T}_{\mathrm{C}}^{-1} \tag{5.16}$$

$$= \frac{1}{\sqrt{1 - r^2}} \begin{bmatrix} r\cos\left(-2\varphi\right) \\ r\sin\left(-2\varphi\right) \\ 1 \end{bmatrix}^{\mathrm{T}} . \tag{5.17}$$

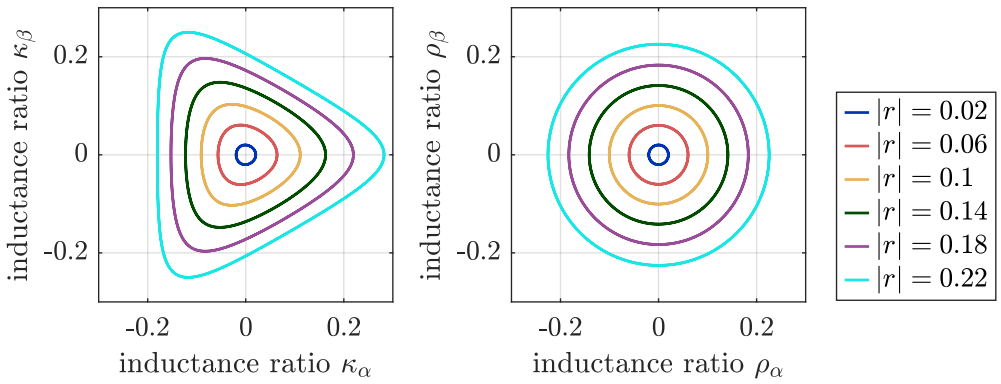

Figure 5.3.: Inductance ratios in αβ-plane, adapted from [SKMN21].

Similiarly, the inverse transform is given by

$$\boldsymbol{\rho}^{\mathrm{p}} = \boldsymbol{\rho}^{\mathrm{s}} \boldsymbol{T}_{\mathrm{C}} \,. \tag{5.18}$$

For comparison, $\boldsymbol{\kappa}^{\mathrm{s}}$ has been

$$\boldsymbol{\kappa}^{\mathrm{s}} = \frac{1}{1-r^2} \begin{bmatrix} -r\cos(-2\varphi) + r^2\cos(4\varphi) \\ -r\sin(-2\varphi) + r^2\sin(4\varphi) \\ 1-r^2 \end{bmatrix}^{\mathrm{T}} \tag{5.19}$$

under assumption of $L_\Delta = L_{\Delta 0}$ according to (4.119). For both vectors, the loci in the αβ-plane are shown in Fig. 5.3 for different values of $|r|$. While for $\boldsymbol{\kappa}$ the locus increasingly deviates from a circular shape with increasing $|r|$, the locus of $\boldsymbol{\rho}$ remains a circle with the radius

$$\hat{\rho} = \frac{|r|}{\sqrt{1-r^2}} \,. \tag{5.20}$$

After examining the differences in the loci of the two inductance ratio vectors, let us return to the calculation of the position estimate. Since the transformed inductance ratios in (5.19) contain only one harmonic component, it is clear that the estimated position can be calculated as

$$\tilde{\varphi}_\rho = \begin{cases} -\frac{1}{2}\mathrm{atan2}\left(-\rho_\beta,\ -\rho_\alpha\right) + k\pi, & L_\Delta = L_{\Delta 0} < 0 \\ -\frac{1}{2}\mathrm{atan2}\left(\rho_\beta,\ \rho_\alpha\right) + k\pi, & L_\Delta = L_{\Delta 0} > 0 \,. \end{cases} \tag{5.21}$$

The sign of L_Δ is the same as that of r and a negative L_Δ or r corresponds to $L_{\mathrm{dd}} < L_{\mathrm{qq}}$ for the assumed inductance model.

5.1.3. Computationally Efficient Alternative

Calculating the estimated position from the modified inductance ratios as described in the last section allows to obtain the correct position for the inductance model with $L_\Delta = L_{\Delta 0}$. In [SGN19], a different algorithm has been proposed which serves the same purpose. Since it skips the step of creating sinusoidal intermediate signals and therefore eliminates the calculation of square roots and divisions, it is less computationally intensive. The equivalency to the previous function is demonstrated in the following for the case of $L_\Delta = L_{\Delta 0} < 0$.

The alternative method is based on the reciprocal values of the inductance ratios which are transformed to the 'αβ' frame similar as with the other calculation functions and the *atan2* function is calculated:

$$\tilde{\varphi}_{\rho,\mathrm{alt}} = -\frac{1}{2}\mathrm{atan2}\left(-\left(\frac{\sqrt{3}}{2}\cdot\kappa_\mathrm{a}^{-1} - \frac{\sqrt{3}}{2}\kappa_\mathrm{c}^{-1}\right), -\left(\kappa_\mathrm{a}^{-1} - \frac{1}{2}\kappa_\mathrm{b}^{-1} - \frac{1}{2}\kappa_\mathrm{c}^{-1}\right)\right) + k\pi\ . \tag{5.22}$$

By multiplying both arguments of the *atan2* function with $2\kappa_\mathrm{a}\kappa_\mathrm{b}\kappa_\mathrm{c}$, the function is simplified and divisions are avoided without changing the result:

$$\tilde{\varphi}_{\rho,\mathrm{alt}} = -\frac{1}{2}\mathrm{atan2}\left(-\sqrt{3}\left(\kappa_\mathrm{a}\kappa_\mathrm{c} - \kappa_\mathrm{a}\kappa_\mathrm{b}\right), -2\kappa_\mathrm{b}\kappa_\mathrm{c} + \kappa_\mathrm{a}\kappa_\mathrm{c} + \kappa_\mathrm{a}\kappa_\mathrm{b}\right) + k\pi\ . \tag{5.23}$$

To show the equivalency to the estimation function (5.3), one can replace ρ_α and ρ_β in that equation by their counterparts in the 'abc' frame using (5.16) and obtain

$$\tilde{\varphi}_\rho = -\frac{1}{2}\mathrm{atan2}\left(-\left(\frac{\sqrt{3}}{2}\rho_\mathrm{b} - \frac{\sqrt{3}}{2}\rho_\mathrm{c}\right), -\left(\rho_\mathrm{a} - \frac{1}{2}\rho_\mathrm{b} - \frac{1}{2}\rho_\mathrm{c}\right)\right) \tag{5.24}$$

$$= -\frac{1}{2}\mathrm{atan2}\left(-\left(\frac{\sqrt{3}}{2}\cdot\sqrt{\kappa_\mathrm{a}\kappa_\mathrm{c}/\kappa_\mathrm{b}} - \frac{\sqrt{3}}{2}\sqrt{\kappa_\mathrm{a}\kappa_\mathrm{b}/\kappa_\mathrm{c}}\right), -\left(\sqrt{\kappa_\mathrm{b}\kappa_\mathrm{c}/\kappa_\mathrm{a}} - \frac{1}{2}\sqrt{\kappa_\mathrm{a}\kappa_\mathrm{c}/\kappa_\mathrm{b}} - \frac{1}{2}\sqrt{\kappa_\mathrm{a}\kappa_\mathrm{b}/\kappa_\mathrm{c}}\right)\right)\ . \tag{5.25}$$

By multiplying both arguments with $2\sqrt{\kappa_\mathrm{a}\kappa_\mathrm{b}\kappa_\mathrm{c}}$, one finally receives

$$\tilde{\varphi}_\rho = -\frac{1}{2}\mathrm{atan2}\left(-\sqrt{3}\left(\kappa_\mathrm{a}\kappa_\mathrm{c} - \kappa_\mathrm{a}\kappa_\mathrm{b}\right),\, -2\kappa_\mathrm{b}\kappa_\mathrm{c} + \kappa_\mathrm{a}\kappa_\mathrm{c} + \kappa_\mathrm{a}\kappa_\mathrm{b}\right) + k\pi \tag{5.26}$$

$$\tilde{\varphi}_\rho = \tilde{\varphi}_{\rho,\mathrm{alt}}\ . \tag{5.27}$$

The same can be shown for the case of $L_\Delta = L_{\Delta 0} > 0$. The two estimation functions obviously return exactly the same result, which under the assumption of the fundamental wave inductance model with $L_\Delta = L_{\Delta 0}$ is the correct position. The alternative estimation function considering both cases is

$$\tilde{\varphi}_{\rho,\mathrm{alt}} = \begin{cases} -\frac{1}{2}\mathrm{atan2}\left(-\sqrt{3}\left(\kappa_\mathrm{a}\kappa_\mathrm{c} - \kappa_\mathrm{a}\kappa_\mathrm{b}\right),\, -2\kappa_\mathrm{b}\kappa_\mathrm{c} + \kappa_\mathrm{a}\kappa_\mathrm{c} + \kappa_\mathrm{a}\kappa_\mathrm{b}\right) + k\pi, & L_\Delta = L_{\Delta 0} < 0 \\ -\frac{1}{2}\mathrm{atan2}\left(\sqrt{3}\left(\kappa_\mathrm{a}\kappa_\mathrm{c} - \kappa_\mathrm{a}\kappa_\mathrm{b}\right),\, 2\kappa_\mathrm{b}\kappa_\mathrm{c} - \kappa_\mathrm{a}\kappa_\mathrm{c} - \kappa_\mathrm{a}\kappa_\mathrm{b}\right) + k\pi, & L_\Delta = L_{\Delta 0} > 0\ . \end{cases} \tag{5.28}$$

If only the estimated position is of relevance, the functions in (5.21) and (5.28) are obviously equivalent. Which algorithm should be used is mainly a question of whether the calculation of the intermediate signals is desired. This can be the case if the $\boldsymbol{\rho}$ vector shall be used as the basis for a vector decoupling of secondary anisotropies (see section 5.2). Furthermore, calculating and plotting $\boldsymbol{\rho}$ is often useful to analyze and illustrate the underlying anisotropy information.

5.1.4. Choice of the Anisotropy Vector and Estimation Function

Obviously, the function required to correctly calculate the estimated position depends on the assumed inductance model. For a fundamental wave inductance model according to section 4.3, L_Δ and $L_{\Delta 0}$ are the decisive parameters. If $L_\Delta = 0$, a circular locus of $\boldsymbol{\kappa}$ is obtained and the estimation function (5.3) is the appropriate choice. If $L_\Delta = L_{\Delta 0}$, a circular locus can be obtained by transformation to $\boldsymbol{\rho}$ and the estimation functions (5.21) and (5.28) are the appropriate choice. For motors that exhibit small inductance variations, comparable results are to be expected for the loci of the inductance ratio vectors and the estimated positions because the two cases coincide at $L_\Delta \approx L_{\Delta 0} \approx 0$. Given that L_Δ and $L_{\Delta 0}$ are not parameters that are usually provided in a datasheet, it appears purposeful to perform measurements on the actual machine and compare the two resulting inductance ratio vectors as well as the respective position estimates.

Motors M2 and M3 showed only subtle differences between the usage of $\boldsymbol{\kappa}$ and $\boldsymbol{\rho}$ which can be attributed to their generally small inductance variations. For Motor M1 however,

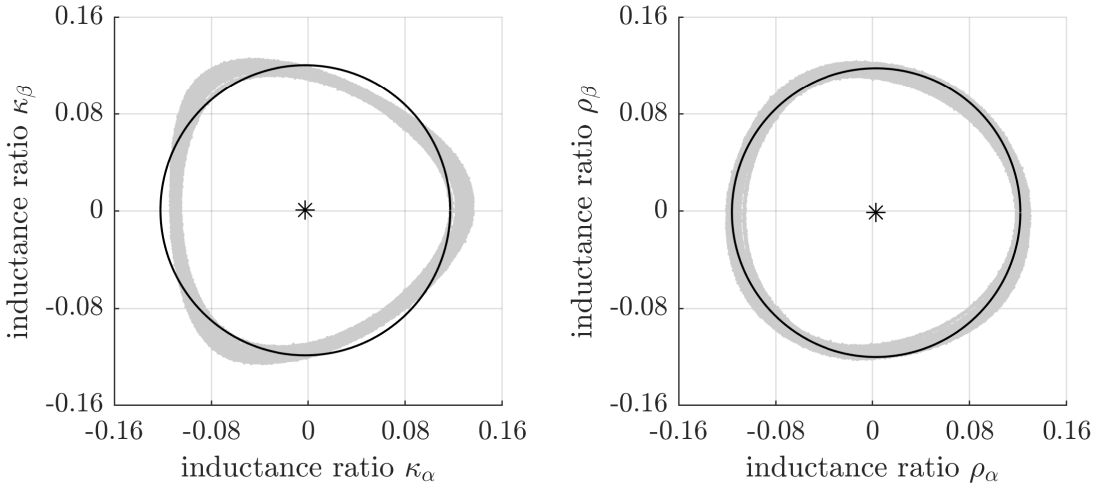

Figure 5.4.: Measured anisotropy vectors $\boldsymbol{\kappa}$ and $\boldsymbol{\rho}$ in the αβ-plane for motor M1 at $n = 10\,\mathrm{r/min}$ and current controlled to zero, showing a more circular shape for $\boldsymbol{\rho}$.

the usage of $\boldsymbol{\rho}$ clearly led to a significantly more circular locus as can be seen in Fig. 5.4[1]. To aid in identifying the differences in shape, the figure includes circular fits that have been calculated using the Pratt method [Che20]. Further results that support the usage of $\boldsymbol{\rho}$ as the preferable anisotropy vector, including position estimation results, will be shown as part of the experimental investigations in chapter 7. As a consequence, and to avoid an excessive number of figures, only $\boldsymbol{\rho}$ will mostly be shown in this thesis to illustrate the anisotropy information and $\tilde{\varphi}_\rho$ will be used as the primary position estimate.

5.1.5. Other Position Estimation Functions

In [TMH+11a; Man13], two other estimation functions have been suggested that can rather be considered approximative estimation functions that are not based on a fundamental wave inductance model. The authors refer to these as "calculation based on the highest value" and "calculation based on the lowest value". While the functions do not involve geometric functions and are therefore rather computationally light, harmonic

[1]The inductance ratios in Fig. 5.4 were obtained using the modulation strategy mSVM5, which is described in section 6.3.2

errors in the estimated position must be expected [Man13], [SGN19].

5.2. Saturation Effects and Secondary Anisotropies

Up to this point, a simplified machine model has mostly been considered. Real machines with their different designs conform to such models only to a certain extent. In practice, there are different physical effects which affect the zero-sequence voltage that are not covered by the simplified model and that one must be aware of. In section 4.5, parasitic capacitances have already been identified to affect the neutral point voltage and therefore the zero-sequence voltage. Beside these, there are effects that are generally existent in anisotropy-based techniques such as saturation, secondary anisotropies [BD11], magnetic hysteresis [CLK11] and eddy currents [Lan14]. Saturation effects and secondary anisotropies may be considered the most relevant due to their impact on the estimated position and the possibility to determine and compensate them with reasonable effort using experimental or simulation data. Therefore, they will be discussed in more detail in this section. The effects of hysteresis and eddy currents are generally more difficult to analyze and quantify. However, one effect that is likely attributable to magnetic hysteresis will be discussed in section 7.1.1.

It is generally well-known in the scientific literature that magnetic saturation has a large impact on anisotropy-based techniques. In the simplified machine model, the self- and mutual inductances were assumed to have a DC component and a component varying with two times the rotor position, however the inductances were solely a function of the rotor position and did not depend on the currents in the machine. In reality, however, the magnetic flux created by the stator currents changes the magnetic saturation state of the machine's iron core and thus affects the inductances and inductance ratios.

Provided that the motor generally shows saturation effects, the following effects can be expected in principle. In the d-axis of a machine, the magnetic flux is biased by the permanent magnets which shift the starting point on the saturation curve upwards (see Fig. 3.1(b)). As a result of this and the geometry of the iron core, L_{dd} is typically smaller than L_{qq}. A positive current in the d-axis will then increase this difference and vice versa. Accordingly, a current in this direction can be expected to weaken or strengthen the anisotropy signals depending on the sign of the current. This effect can advantageously be exploited for initial rotor polarity detection, but it must also be considered when operation with field-weakening is desired. In contrast, a current in the q-axis creates a flux that is perpendicular to the flux of the permanent magnets, thereby shifting the

direction of the resulting flux vector away from the d-axis. Therefore, it can generally be expected that phase shifts occur in the anisotropy signals and the estimated position with increasing q-axis current. These can be compensated by correction functions or lookup tables.

Additionally, real PMSMs will however often contain not only the main anisotropy that rotates with -2φ but also additional harmonic components. For zero-sequence voltage based techniques, terms varying with 4φ are introduced even when the self- and mutual inductances have only harmonic components of 2φ as discussed in section 4.3. The harmonic content present in anisotropy signals or in the resulting estimation error can be determined by Fourier analysis. Similar to the main anisotropy, the secondary anisotropies can be considered as caused by geometry or by saturation [SEP13]. Depending on the specific machine design, compensation of such secondary anisotropies, often also called secondary saliencies, may be necessary if they are of significant magnitude [BD11]. For induction machines, decoupling of secondary anisotropies has played an even more important role in the scientific literature as there are always two pronounced anisotropies existent, one resulting from saturation and another one resulting from the rotor bars or slotting [Pau14].

To compensate the effect of secondary anisotropies, different methods have been proposed for example in [DL98; PLKK13; Pau14] which are not limited to a specific sensorless technique and may therefore be used also with the approach of position estimation that is pursued in this thesis. Generally, the secondary anisotropies can be modelled as a Fourier series of which the coefficients are determined a priori for one type of motor in a commissioning procedure and at different operating conditions, in particular varying load currents. One possibility is then to use a scalar compensation of the position error caused by the secondary anisotropies ("scalar decoupling"). This is possible as long as the raw estimated position remains monotonous. Another possibility is to decouple the harmonics directly from the anisotropy vector ("vector decoupling") which remains possible also for larger secondary anisotropies. For more details, refer to [DL98; PLKK13; Pau14]. It is worth adding that a compensation of secondary anisotropies in PMSMs is usually pursued only for harmonics of one or even two times the electrical spatial frequency but not for harmonics of the mechanical spatial frequency. This is because the absolute mechanical position is usually not known, making compensation of mechanical harmonics significantly more difficult. However, harmonics of the mechanical spatial frequency may still be present, resulting for example from fractional-slot machine designs or from imperfect manufacturing.

The motors used in this thesis showed relatively small secondary anisotropies. Since the compensation of secondary anisotropies is not a focus of this work, no compensation of secondary anisotropies has been implemented. The harmonic content present in the anisotropy signals of motor M1 and M2, as well as dependencies of the anisotropy signals and resulting position estimates on the currents, will be shown and discussed in chapter 7.

5.3. Phase-Locked Loop Filtering of the Estimated Position

The inductance ratios obtained through the measurements of the zero-sequence voltage usually have a signal-to-noise ratio which is high enough to enable direct calculation of the position using the functions provided in sections 5.1.1-5.1.3. The resulting position information is limited only in sample rate but not in bandwidth and can usually be used directly for driving the motor without additional filtering for motors that exhibit a reasonable amount of anisotropy.

However, it was found useful during this work to add a PLL-type filter to further smoothen the estimated position. The noise can then be further reduced and, as a usually beneficial side effect, harmonic content in the estimated position is reduced at higher rotor speeds, which improves the behavior of the drive. The PLL-type filter consists of a PI controller and an integrator that are part of the feedback loop shown in Fig. 5.5. Structures like this are commonly used in many works related to sensorless control; in [HN00], it was described as part of a general position and speed estimation algorithm. They are also part of the techniques for decoupling secondary anisotropies.

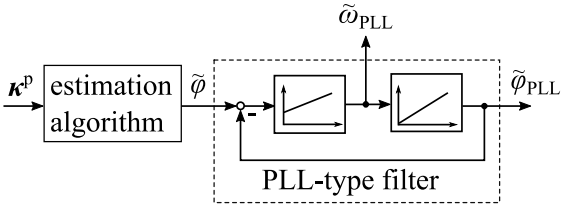

Figure 5.5.: PLL-type filter for the estimated position.

The equations of the PLL-type filter can be formulated in the Laplace domain as

$$\tilde{\omega}_{\mathrm{PLL}}(s) = \left(k_{\mathrm{P}} + k_{\mathrm{I}}\frac{1}{s}\right)\left(\tilde{\varphi}(s) - \tilde{\varphi}_{\mathrm{PLL}}(s)\right) \tag{5.29}$$

$$\tilde{\varphi}_{\mathrm{PLL}}(s) = \frac{1}{s}\tilde{\omega}_{\mathrm{PLL}}(s) \tag{5.30}$$

where the PI controller is formulated in parallel form. The transfer function for the position estimate is given by

$$\frac{\tilde{\varphi}_{\mathrm{PLL}}(s)}{\tilde{\varphi}(s)} = \frac{k_{\mathrm{P}}s + k_{\mathrm{I}}}{s^2 + k_{\mathrm{P}}s + k_{\mathrm{I}}}\,. \tag{5.31}$$

When $s^2 = 0$, the transfer function equals one. Therefore, the PLL introduces no phase lag when the second derivative of the position is zero, i.e. at constant speed. The structure can also be interpreted as a simple mechanical observer, in which case estimated load torques can be inserted into the structure as in [DL98]. To avoid reducing the dynamic performance of the drive, the bandwidth of the PLL should be chosen sufficiently high. For this work it was set to 200 Hz, the parameters of the PLL were $k_{\mathrm{P}} = 1014$ and $k_{\mathrm{I}} = 257.06 \cdot 10^3$.

The speed information required for the control of the machine can be obtained from $\tilde{\omega}_{\mathrm{PLL}}$. Alternatively, if no PLL shall be used, the speed can be obtained by calculating the derivative of the estimated position instead.

5.4. Initial Polarity Detection

The estimated position exhibits an uncertainty of 180° electrical that must be resolved before operation of the drive is started, otherwise the torque could be generated in the wrong direction. The uncertainty of 180° is common to all anisotropy-based techniques with only few exceptions like the one in [CSTT00]. The simplest solution to resolve the uncertainty is to bring the motor to a known position, for example by applying a constant voltage vector to align the rotor to this vector. However, the resulting movement is often undesirable. Initial polarity detection procedures are therefore commonly performed at the startup of the drive to remove the uncertainty. Typically, these procedures exploit the magnetic saturation of the iron core [MT94; Sch96; Hol06; KKS+11; Man13; XZ17]. For motors that do not exhibit significant saturation effects, an alternative approach was proposed in [TZP+18] that evaluates the rotor movement when applying small voltage

pulses in the q-axis.

The concept of using the magnetic saturation for initial polarity detection was already described early in [Sch88] and can be outlined as follows. By producing a stator current in the initially assumed d-axis, a stator flux component is generated either in the actual direction of the rotor flux or in the direction opposite to it. If the current is applied in the actual d-axis, the saturation is increased in this axis and L_{dd} decreases. If the current is applied in the opposite direction of the real d-axis, L_{dd} increases. Because the current is applied in the estimated d-axis, no significant torque is generated and rotor movement is thus minimized.

Similar to the position estimation itself, most known initial polarity detection procedures rely on current measurements to capture the effects of the resulting inductance changes. In [Sch88], the initial polarity detection was performed by comparing the current changes that result from certain voltage vectors with a bias current in both directions of the assumed d-axis. A very similar approach was used in [Hol06] and compares the size of the current pulse resulting from applying voltage pulses in both directions of the assumed d-axis.

Because the position estimation described in this work is based on the measurement of the zero-sequence voltage, it was found more convenient to base also the initial polarity detection on this information. However, there exists only few literature that conduct initial polarity detection using the zero-sequence voltage. In [XZ17], two different methods are presented involving the use of alternating or rotating injection signals. In the case of alternating injection, the amplitude of the zero-sequence voltage is evaluated. In the case of rotating injection signals, either the amplitude or the secondary harmonics in the zero-sequence voltage are evaluated. As already described in chapter 3, analog filters are typically necessary to separate the response of the zero-sequence voltage to the injected signal from components introduced by the inverter switching, so that such approach would require additional circuitry.

[Man13, pp. 71-76] appeared to be the only work describing an initial polarity detection procedure using the zero-sequence voltage and an excitation via discrete voltage vectors. The author suggested to individually compare the a-, b- and c-components of the directional zero-sequence voltages – which the author refers to as flux linkage signals – that result from the application of positive and negative d-axis current. Depending on the position, the individual components either increase, decrease or do not change at all. With this kind of implementation, inconsistencies can occur in the components if the separation is poor, in which case the polarity cannot be resolved unambiguously. While

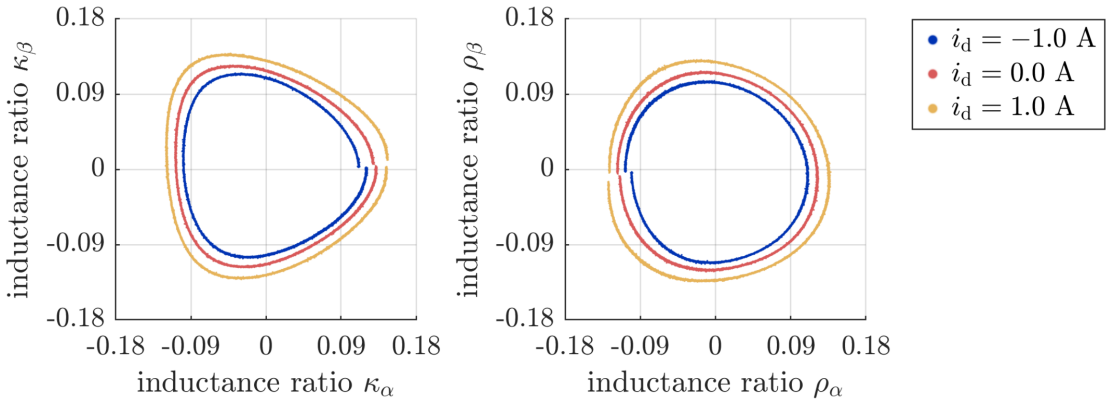

Figure 5.6.: Effect of d-axis current on inductance ratios for motor M1.

the author suggested to consider only the two components that are most likely to vary, this approach seems rather suboptimal overall.

In the following, an approach is described that evaluates the magnitude of the anisotropy vector in the αβ-plane instead. It is a slightly refined version of the procedure published in [SGN19]. The refinements lie in the use of the inductance ratio vectors $\boldsymbol{\kappa}$ or $\boldsymbol{\rho}$ instead of the directional zero-sequence voltages and in a more comprehensible calculation of the magnitude of the anisotropy vector.

As can be seen in Figs. 5.6 and 5.7, the application of a current in the assumed d-axis increases or decreases the magnitude of the inductance ratios depending on the sign of the current in the actual d-axis. Motor M2 has shown significantly stronger saturation effects compared to motor M1. Either the magnitude of the inductance ratio vector $\boldsymbol{\kappa}$ or $\boldsymbol{\rho}$ can be used for polarity detection. Due to the more circular shape especially for motor M1, the vector $\boldsymbol{\rho}$ is again chosen here as for the angle calculation. The more circular shape can be expected to make the polarity detection somewhat more robust against changes in magnitude that occur due to possible movement of the rotor during the procedure.

The procedure for initial polarity detection is performed as follows. Using the same modified space vector modulation and measurements as during normal operation, the initial estimated position with the initial 180° uncertainty is calculated. The initial position estimate lies within a half electrical period, here between 0° and 180°. A small voltage is first applied in the positive direction of the assumed d-axis for a short period and then in the negative direction for an equal duration. Assuming no mutual inductance

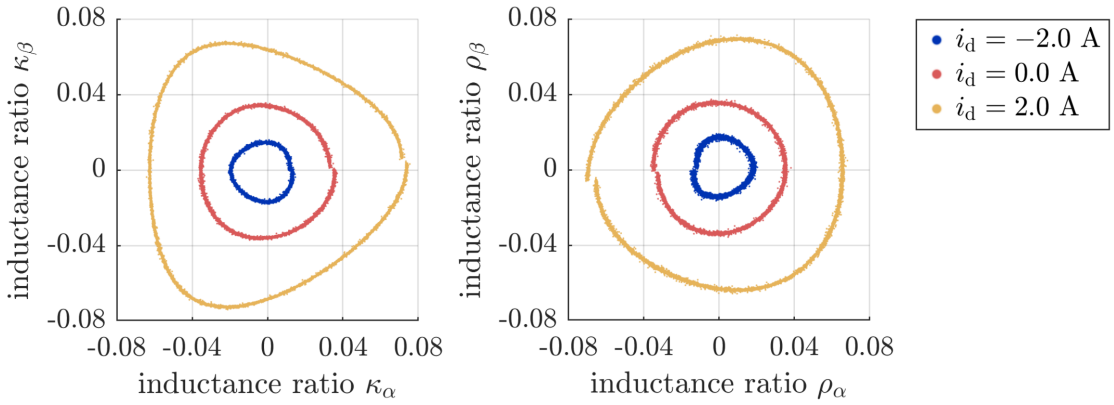

Figure 5.7.: Effect of d-axis current on inductance ratios for motor M2.

between d- and q-axis and no rotor movement, the current will then rise solely in the direction of the d-axis according to (2.77). Alternatively, the current can be *controlled* to lie in the d-axis. However, this was not considered necessary here and was omitted in favor of a simpler implementation.

Throughout the procedure, the inductance ratios are calculated and the estimated position is updated to keep the voltage in the d-axis even when small rotor movements occur. After a small transition time allowing the current to change, the magnitude of the inductance ratio vector is calculated from the Clarke-transformed inductance ratios

$$\hat{\rho}^\mathrm{s} = \sqrt{\rho_\alpha^2 + \rho_\beta^2}\,. \tag{5.32}$$

Alternatively, it can also be calculated by projecting the inductance ratios in the 'abc' frame onto the already calculated estimated position using

$$\hat{\rho}^\mathrm{s} = \cos\left(-2\tilde{\varphi}_\rho\right)\cdot\rho_\mathrm{a} + \cos\left(-2\tilde{\varphi}_\rho - \tfrac{2\pi}{3}\right)\cdot\rho_\mathrm{b} + \cos\left(-2\tilde{\varphi}_\rho - \tfrac{4\pi}{3}\right)\cdot\rho_\mathrm{c}\,. \tag{5.33}$$

similar to the approach described in [SGN19]. For the inductance model with $L_\Delta = L_{\Delta 0}$, one finds that

$$\hat{\rho}^\mathrm{s} = \frac{r}{\sqrt{1-r^2}} \tag{5.34}$$

which features no dependence on the rotor position and where r would now vary over the d-axis current due to saturation. By averaging the values of $\hat{\rho}^\mathrm{s}$ obtained during the application of the assumedly positive d-axis voltage, $\hat{\rho}^\mathrm{s}_+$ is calculated and analogously $\hat{\rho}^\mathrm{s}_-$ is calculated by averaging the values obtained during the assumedly negative d-axis

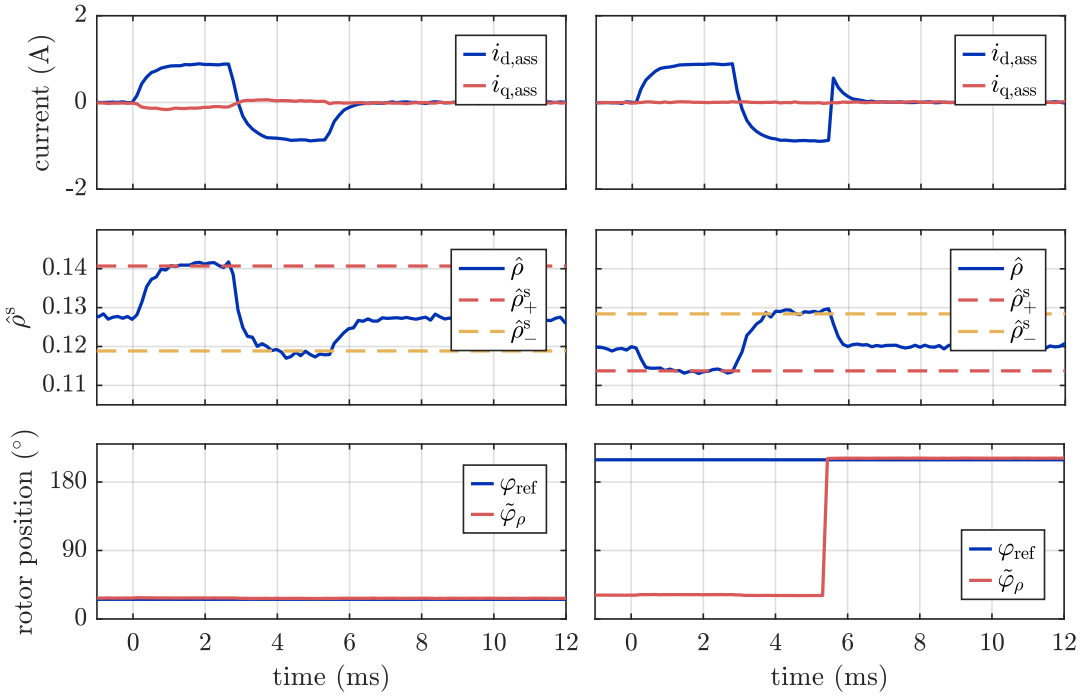

Figure 5.8.: Initial polarity detection performed at two different positions: on the right side, the initially assumed polarity was wrong and is corrected at the end of the procedure.

voltage. If $\hat{\rho}^s_+ > \hat{\rho}^s_-$, then the initially assumed polarity was correct. Otherwise, 180° have to be added to the electrical position to correct the assumed polarity. The voltage levels and durations for the application of the positive and negative voltages must be chosen sufficiently high to ensure proper separation of positive and negative polarity. Figure 5.8 shows how polarity detection is performed for motor M1. The (anti-)correlation between the applied current and the amplitude of the inductance ratios is clearly visible. It can be seen that the initial polarity is detected reliably; the whole initialization procedure takes about 6 ms here.

5.5. Summary

To estimate the rotor position from measured inductance ratios, three calculation functions have been discussed in this chapter. They are based on special cases of a fundamental wave inductance model and allow, under neglection of saturation and other effects, to calculate the rotor position in a parameter-free way.

For the inductance model with

$$L_\Delta = 0 \Leftrightarrow L_{\mathrm{m}2} = -L_2/2 \; . \tag{5.35}$$

the inductance ratio vector $\boldsymbol{\kappa}$ consists only of harmonic components of 2φ and is circular in the $\alpha\beta$-plane. Therefore, the position can be calculated directly by applying the *atan2* function on κ_α and κ_β without further ado.

Under the assumption of the inductance model with

$$L_\Delta = L_{\Delta 0} \Leftrightarrow L_{\mathrm{m}2} = 0 \tag{5.36}$$

the calculation of the correct position is less trivial but still possible. One possiblity is a nonlinear transformation of the inductance ratios. It leads to the transformed inductance ratios ρ_α and ρ_β, from which the correct position is then obtained again via the *atan2* function. An alternative estimation function has been provided, which essentially skips the step of calculating ideal purely sinusoidal, transformed inductance ratios. Since this step involves the calculation of square roots and divisions (which typically require significantly more processor cycles than additions or multiplications), avoiding it reduces the computational effort and may therefore be useful for microcontroller implementations.

A given motor will likely not have fully circular shapes for either vector, but the choice of the estimation function should preferably be made according to which of the two above assumptions is closest to being satisfied. The differences between the first and the other two estimation functions will be small for motors with small inductance variations but becomes significant especially for motors that feature pronounced inductance variations and are therefore well suited for anisotropy-based techniques.

As for any anisotropy-based technique, the anisotropy signals of real motors will deviate from the modeled signals, especially due to saturation effects and the presence of secondary anisotropies, which are also closely related to each other. Additional measures, such as lookup-tables, correction functions or decoupling structures may therefore be necessary to infer the rotor position as accurately as possible.

To resolve the initial 180° uncertainty of the estimated position, an initial polarity detection is required. Procedures that exploit magnetic saturation are preferable to avoid rotor movement. By evaluating the magnitude of the inductance ratio vector during the application of positive and negative pulses in the estimated d-axis of the machine, the same anisotropy information as for the position estimation can be used for the initial polarity detection and additional measurements or circuitry are avoided.

6. Modified Space Vector Modulation

In the following chapter, modulation strategies are discussed. In the sensorless control approach pursued in this thesis, a modulation strategy and the pulse pattern resulting from it serves two purposes. On the one hand it shall apply the reference voltage vector to the machine that is calculated by the upstream current control. On the other hand, it creates the transient excitation used to measure the desired anisotropy information and sufficient durations must be ensured for the discrete voltage vectors during which the zero-sequence voltage measurements shall be performed. It should be remembered at this point that the discrete voltage vectors result directly from the possible inverter switching states according to Table 2.2.

This chapter is substantially based on the work already published in [SKMN21] and is structured as follows. First, it is discussed why standard space vector modulation cannot be used and modified modulation strategies are necessary. Then a total of five modified modulation strategies are described and compared, including two novel modulation strategies. Fundamental characteristics such as the update rate of the anisotropy information and achievable voltage utilization are discussed for each strategy and the equations to calculate the inductance ratios from the measurements are provided. After this, a spectral analysis is conducted to compare the introduction of additional voltage harmonics by the different modulation strategies. Additionally, differences in the obtained inductance ratios and position estimates are investigated based on experimental data. Finally, the results are summarized.

6.1. Necessity of Modified Space Vector Modulation

In section 4.4.1 it was discussed that in order to measure the inductance ratios while eliminating terms related to EMF and resistive imbalances, a suitable set of discrete voltage vectors must be applied. The discrete voltage vectors during which the measurements of the zero-sequence voltage are performed will be referred to as *measurement vectors*. As a minimum requirement, two linearly independent active measurement vectors and,

additionally, one other active or zero measurement vector are necessary.

Additionally, minimum durations T_{mv} must be guaranteed for the measurement vectors involved so that

$$T_{\mathrm{mv}} \geq T_{\mathrm{mv,min}} \ . \tag{6.1}$$

Three factors can be named that determine the required minimum duration. The first is the overshoot and ringing of the neutral point voltage that is caused by parasitic capacitances in the machine as discussed in section 4.5.1. Measurements should not be taken directly after a switching event because they would be distorted by the transient behavior. Secondly, the dead-time between switching off one switch and switching on the other switch in one inverter leg that is necessary to prevent short-circuiting the DC link voltage introduces a current dependence to the effective switching instant and the voltage slope. Especially the combination of ringing and current-dependent delays of the switching instant suggests that a certain amount of time should be allowed for the neutral point voltage to settle to a reliable value. And finally, the ADC requires a certain amount of time to sample u_{NAN} before conversion.

If standard SVM is used, the requirement for a given minimum duration will not be fulfilled in certain regions of the hexagon of applicable voltage vectors. These regions are highlighted in red in Fig. 6.1. Two different kinds of regions can be identified. The regions of the one kind are the regions interconnecting two sectors of the SVM, where the time for which the more distant active vector is applied becomes too small. As these regions coincide in the origin, the requirement for a minimum duration will not be fulfilled for small reference voltage vectors independently of their direction. For the regions of this kind, estimation can however be enabled by suitable modification of the modulation

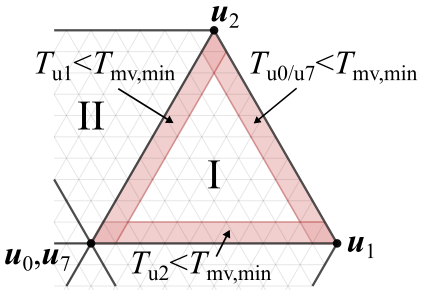

Figure 6.1.: Regions where minimum durations are not fulfilled for a reference voltage vector in sector I when using standard SVM. From [SKMN21].

strategy. The regions of the other kind are located at the outline of the hexagon where the time for the two zero vectors becomes too small. For these regions, estimation cannot be enabled by modified modulation strategies, because the two adjacent active vectors must be applied for up to the entire switching period, leaving insufficient time for the application of other vectors.

Accordingly, the modifications from a standard SVM shall ensure that minimum durations are guaranteed for a set of measurement vectors in particular at low voltages and for reference voltage vectors that lie near the border of two voltage sectors. The modified modulation strategies will be referred to as modified SVM (mSVM). Besides ensuring minimum durations, the modified SVMs will on the other hand lead to a reduction of the applicable voltage magnitude in comparison to a standard SVM. In previous research, little attention has been paid to the actual amount of reduction resulting from modified modulation strategies. This is probably because the works often focused mostly on low-speed operation, where voltage utilization is typically low as well. However, for broader applicability that includes operation up to high speed it is important to specify and compare the voltage magnitudes that can be achieved with different modified modulation strategies. The actual voltage reduction will therefore be given for each of the modified modulation strategy under investigation.

Before that, one can already determine the voltage reduction that is achievable in a best-case scenario. The maximum voltage magnitude is defined here as the highest magnitude that can be realized in any direction of the αβ-plane, meaning that so-called overmodulation is not considered. When using standard SVM, the highest achievable voltage magnitude without overmodulation is then

$$\hat{u}_{\mathrm{max,standard}} = \frac{2}{3} u_{\mathrm{DC}} \cdot \cos(30^\circ) = \frac{2}{3} u_{\mathrm{DC}} \cdot \frac{\sqrt{3}}{2} = \frac{1}{\sqrt{3}} u_{\mathrm{DC}} \,. \tag{6.2}$$

To specify the amount of reduction in achievable voltage magnitude that occurs when using different modified SVMs, a voltage reduction factor k_{red} is defined here, where

$$\hat{u}_{\mathrm{max,mod}} = (1 - k_{\mathrm{red}})\, \hat{u}_{\mathrm{max,standard}} \,. \tag{6.3}$$

It is assumed here that the modified SVM is used repeatedly in all switching periods. Otherwise the achievable voltage amplitude would differ between periods which is likely undesirable. Let us define an estimation period T_{est} that is required to fully update the inductance ratio vector so that a new position estimate can be calculated. T_{est} is equal

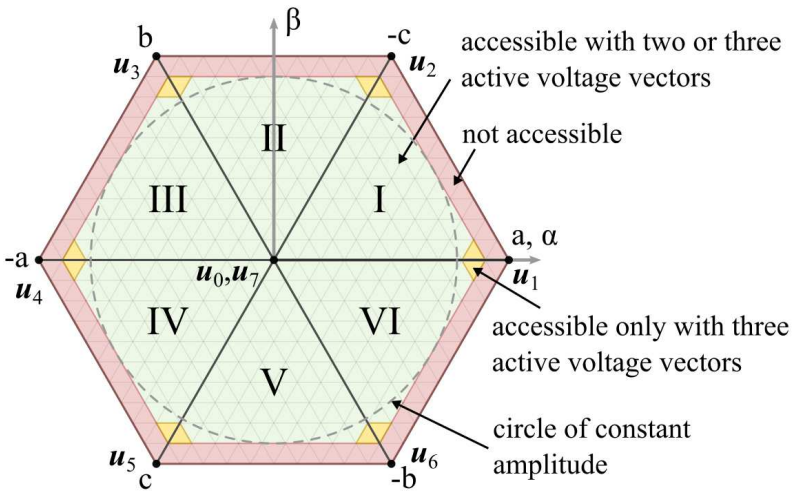

Figure 6.2.: Theoretically accessible voltage regions for modified modulation strategies, resulting from the requirement of minimum durations for suitable measurement vectors. Shown for an exemplary ratio of $T_{\mathrm{mv,min}}/T_{\mathrm{est}} = 0.1$. From [SKMN21].

to one or multiple switching periods. It can quickly be recognized that in the best case the reduction factor is

$$k_{\mathrm{red,min}} = \frac{1 \cdot T_{\mathrm{mv,min}}}{T_{\mathrm{est}}} \tag{6.4}$$

because in addition to the two adjacent active voltage vectors at least one zero vector or one additional active voltage vector must be applied for $T_{\mathrm{mv,min}}$ in every estimation period (see section 4.4.1). These additional vectors do not contribute towards the direction of the reference vector and therefore reduce the achievable voltage amplitude. Note that this is a best-case consideration. The actual reduction depends on the design of the modified SVM as will be further discussed.

It is worth to mention that the yellow regions in Fig. 6.2 can only be reached if the three active vectors closest to the reference voltage vector are used as measurement vectors. For low ratios of $T_{\mathrm{mv}}/T_{\mathrm{est}}$, these regions are of little importance since they lie outside the circle of constant amplitude. The threshold at which the yellow regions start

to limit the achievable voltage magnitude can be geometrically derived using

$$\frac{2}{3}u_{\mathrm{DC}} \cdot \cos(30^\circ)\,(1 - T_{\mathrm{mv}}/T_{\mathrm{est}}) = \frac{2}{3}u_{\mathrm{DC}} \cdot (1 - 2T_{\mathrm{mv}}/T_{\mathrm{est}}) \tag{6.5}$$

$$\frac{\sqrt{3}}{2}\,(1 - T_{\mathrm{mv}}/T_{\mathrm{est}}) = (1 - 2T_{\mathrm{mv}}/T_{\mathrm{est}}) \tag{6.6}$$

which leads to

$$T_{\mathrm{mv}}/T_{\mathrm{est}} = \frac{1 - \sqrt{3}/2}{2 - \sqrt{3}/2} \approx 0.118 \tag{6.7}$$

Beyond this threshold it would be necessary to use the mentioned three active vectors as measurement vectors to achieve the highest possible voltage utilization.

There exist many possibilities for how the modulation strategy can be modified compared to a standard SVM. In addition to the mandatory requirements to guarantee minimum durations for the measurement of the zero-sequence voltage, some additional characteristics can be formulated which an ideal modified modulation strategy should fulfill, including:

- high update rate of the anisotropy information
- high voltage utilization
- high rejection of systematic estimation errors such as
  - errors arising from the low-frequency part $\boldsymbol{u}_{\mathrm{slow}}$
  - errors due to non-linear machine behaviour
  - errors due to acquiring the components of the anisotropy vector at different time instants
  - varying common modes of u_{N} and u_{AN} causing errors due to common mode gain in analog subtraction
- low harmonic content in the resulting phase currents
- low complexity of implementation, i.e.
  - low computational effort
  - low hardware capability requirements

An additional aspect of using modified space vector modulation shall be at least mentioned here. Ensuring minimum durations for at least two linearly independent active vectors enables also the measurement of the currents via a single current sensor placed in series with the DC link as discussed in [BPJT97], which may be a beneficial side effect in applications with very strict cost requirements.

In the following sections, a total of five different modified modulation strategies will be discussed and compared concerning the characteristics listed above. First, three modulation strategies are discussed that were adopted from other scientific works. After that, two newly proposed modulation strategies are considered.

6.2. Modified Modulation Strategies in Previous Works

6.2.1. mSVM1: Alternating Opposing Vector Insertion

References [JH97; Jia00] are likely the first publications describing an anistropy-based sensorless technique which uses an excitation by discrete voltage vectors and measurements of the zero-sequence voltage during these vectors. To obtain sufficient durations for the measurements, the modulation was modified from a standard SVM, however the actual implemented modified modulation strategy was described only textually in [Jia00, pp. 66-71]. It is stated that the duration of one active vector in a switching period is prolonged by a certain amount which is compensated for by application of the opposing active vector in the switching period that follows. However, in standard SVM only up to two active vectors are used which implies that for each axis the duration of at least one voltage vector will be "prolonged" from a starting value of zero. Because it is also described that the opposing measurement vectors were applied in direct succession, it can be assumed that a pulse pattern as shown in Fig. 6.3 was used. As illustrated, one active measurement vector is added at the end of one switching period and followed by the opposing vector at the beginning of the next switching period. The axis of the measurement vectors alternates every two switching periods, leading to a total of six switching periods to obtain measurements for all three axes. Even though ways to estimate the position using only one or two axes of measurements are described, the opposing vector insertion is preferably repeated in all three axes as was indicated in [Jia00, pp. 72-74] and as will be confirmed by experimental results in section 6.7.

The remaining parts of two successive switching periods are mirrored to avoid additional switching events. As illustrated in Fig. 6.3, the switching periods can be considered as divided into two separate blocks. The sequence of the two opposing measurement vectors form one block that is independent of the reference vector and which is referred to here as the measurement block. The duration for which each measurement vector is applied is equal and constant so that each measurement block has a constant duration of $2T_{\mathrm{mv}}$. The actual modulation takes place exclusively in the remaining part of a switching

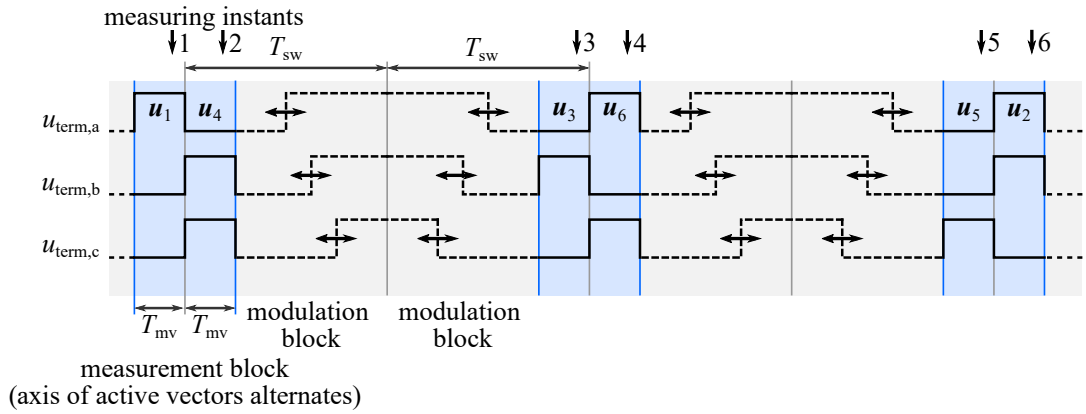

Figure 6.3.: Pulse pattern with insertion of alternating opposing vectors (mSVM1).

period which shall therefore be referred to as the modulation block. In these blocks, the positions of the pulse edges vary; the shares of zero and active vectors are selected so that, on average, the desired reference vector is obtained. This systematic of dividing the switching period into contiguous measurement and modulation blocks will consistently be used in this chapter to compare the five investigated modulation strategies in a clear and visual way.

The mirror-image arrangement of the adjacent modulation blocks result in center-aligned pulses in these. Accordingly, the pulse pattern can also be seen as the result of a center-aligned standard SVM which has the opposing measurement vectors inserted between the original switching periods. The inserted vectors double the switching frequency compared to a standard center-aligned SVM. Generally, this modulation strategy features strong similarities to the original current-based INFORM technique, which also inserts opposing voltage vectors for the measurements, as can be well seen for example in [RS04]. Placing the measurement vectors in direct succession offers three essential advantages. First of all, since the measurements are performed as close to each other as possible, the slowly changing voltage $\boldsymbol{u}_{\mathrm{slow}}$ can be eliminated most effectively. Second, since opposing voltage vectors are used in this case, they compensate each other almost immediately and additional current ripple is therefore minimized. Finally, placing the measurement vectors at a fixed position in the switching period simplifies the creation of the pulsed signals, allows simple and consistent triggering of the measurements and a consistent time instant at which the measured information becomes available.

Next, the calculation of the inductance ratios from the measurements will be considered.

Each measurement block yields two measurements of u_{NAN}, one from each of the two opposing measurement vectors. From each pair of measurements, one component of a directional voltage vector $\Delta\boldsymbol{u}^{\mathrm{p}}_{\mathrm{NAN}}$ in the 'abc' reference frame can be calculated according to (4.67)-(4.71):

$$\begin{aligned}
\Delta u_{\mathrm{NAN,a}} &= (\kappa_{\mathrm{a}} - 1/3) \cdot u_{\mathrm{DC}} = \big(u_{\mathrm{NAN},2} - u_{\mathrm{NAN},1}\big)/2 \\
\Delta u_{\mathrm{NAN,b}} &= (\kappa_{\mathrm{b}} - 1/3) \cdot u_{\mathrm{DC}} = \big(u_{\mathrm{NAN},4} - u_{\mathrm{NAN},3}\big)/2 \\
\Delta u_{\mathrm{NAN,c}} &= (\kappa_{\mathrm{c}} - 1/3) \cdot u_{\mathrm{DC}} = \big(u_{\mathrm{NAN},6} - u_{\mathrm{NAN},5}\big)/2 \,.
\end{aligned} \tag{6.8}$$

Here, $u_{\mathrm{NAN},j}$ refers to the value of u_{NAN} at measuring instant j according to Fig. 6.3. Subsequently, the inductance ratios can be calculated as

$$\kappa_{\mathrm{a}} = \frac{\Delta u_{\mathrm{NAN,a}}}{u_{\mathrm{DC}}} + \frac{1}{3} \tag{6.9}$$

$$= \frac{1}{2u_{\mathrm{DC}}} \big(u_{\mathrm{NAN},2} - u_{\mathrm{NAN},1}\big) + \frac{1}{3} \tag{6.10}$$

and

$$\kappa_{\mathrm{b}} = \frac{1}{2u_{\mathrm{DC}}} \big(u_{\mathrm{NAN},4} - u_{\mathrm{NAN},3}\big) + \frac{1}{3} \tag{6.11}$$

$$\kappa_{\mathrm{c}} = \frac{1}{2u_{\mathrm{DC}}} \big(u_{\mathrm{NAN},6} - u_{\mathrm{NAN},5}\big) + \frac{1}{3} \,. \tag{6.12}$$

It is worth to mention that the use of opposing measurement vectors leads to the highest possible magnitude of $\Delta\boldsymbol{u}_{\mathrm{term}}$ and therefore the largest transient excitation.

In the next step, the achievable voltage amplitude shall be considered. Per each of the six switching periods that form a complete measurement sequence, a single duration T_{mv} is reserved for the respective measurement vector. Therefore, the voltage reduction factor is

$$k_{\mathrm{red}} = \frac{6T_{\mathrm{mv}}}{6T_{\mathrm{sw}}} = 1\frac{T_{\mathrm{mv}}}{T_{\mathrm{sw}}} \tag{6.13}$$

which means that the achievable voltage magnitude is only slightly reduced. The accessible voltage region is shown in Fig. 6.4 for $T_{\mathrm{mv}}/T_{\mathrm{sw}} = 0.1$. For this exemplary ratio, a voltage utilization of 90 % would be possible. However, the relatively high achievable voltage goes at the cost of the update rate of the anisotropy information. Presumably the main downside of this approach is that the estimation is spread over a total of six switching periods. Only one component of the inductance ratios in the 'abc' frame is determined

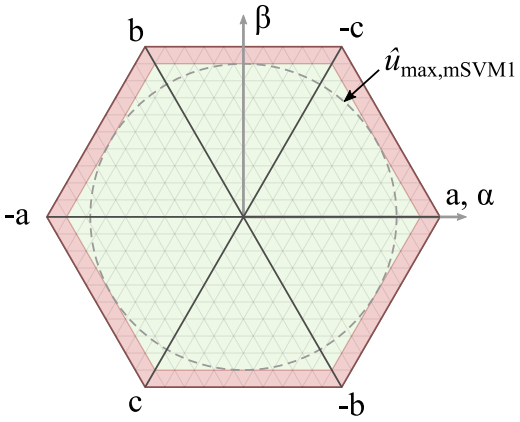

Figure 6.4.: Accessible voltage region when using mSVM1, for $T_{\mathrm{mv}}/T_{\mathrm{sw}} = 0.1$.

for each two switching periods. Therefore, it takes six switching periods until all three components are updated. At high speed, it is possible that the rotor position changes considerably between successive measurement blocks. However, the suggested PLL-type filter largely eliminates the high-frequency harmonics in the estimated position that are caused by the staggered measurements.

6.2.2. mSVM2: Successive Pulse Shift

A different approach to guarantee fixed durations for a suitable set of measurement vectors is to use a modified edge-aligned pulse pattern in which the leading edges of the three phases are shifted towards each other as described in [TMH+11a] and [Man13, pp. 16-20]. This results in a total of four measurement vectors: a zero vector, the two neighboring active vectors that result from the shifted pulses and the second zero vector. To compensate the active measurement vectors, the trailing edges in the modulation block must be shifted by the same amount as the ones in the modulation block. The pulse pattern is shown in Fig. 6.5.

Using the differences between the measured u_{NAN} before and after every switching instant in the measurement block, the components of $\Delta\boldsymbol{u}^{\mathrm{p}}_{\mathrm{NAN}}$ can again be calculated:

$$\begin{aligned}
\Delta u_{\mathrm{NAN,a}} &= (\kappa_{\mathrm{a}} - 1/3) \cdot u_{\mathrm{DC}} = u_{\mathrm{NAN},2} - u_{\mathrm{NAN},1} \\
\Delta u_{\mathrm{NAN,b}} &= (\kappa_{\mathrm{b}} - 1/3) \cdot u_{\mathrm{DC}} = u_{\mathrm{NAN},3} - u_{\mathrm{NAN},2} \\
\Delta u_{\mathrm{NAN,c}} &= (\kappa_{\mathrm{c}} - 1/3) \cdot u_{\mathrm{DC}} = u_{\mathrm{NAN},4} - u_{\mathrm{NAN},3} \ .
\end{aligned} \tag{6.14}$$

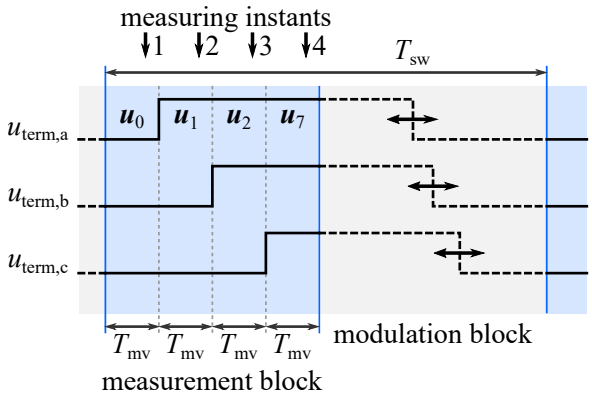

Figure 6.5.: Pulse pattern with successive pulse shift (mSVM2).

Accordingly, the inductance ratios in the 'abc' reference frame are obtained as

$$\begin{aligned} \kappa_a &= \frac{1}{u_{DC}} \left(u_{NAN,2} - u_{NAN,1} \right) + \frac{1}{3} \\ \kappa_b &= \frac{1}{u_{DC}} \left(u_{NAN,3} - u_{NAN,2} \right) + \frac{1}{3} \\ \kappa_c &= \frac{1}{u_{DC}} \left(u_{NAN,4} - u_{NAN,3} \right) + \frac{1}{3} \, . \end{aligned} \tag{6.15}$$

This modulation strategy offers the advantage that all three components of the inductance ratio vector in the physical frame are updated at every switching period and from one contiguous measurement block. At the same time, however, it limits the achievable voltage magnitude significantly. Since a duration of $4T_{mv}$ is spent for the four measurement vectors, the diameter of the accessible hexagon is reduced: compared to standard SVM, the relative reduction is $4 \cdot T_{mv}/T_{sw}$. Furthermore, because the two active measurement vectors are not chosen in dependence of the voltage sector, the region of applicable voltage is biased towards these active vectors as shown in Fig. 6.6. As can clearly be seen, the achievable amplitude is limited by the sector on the opposite side of the active measurement vectors. In the illustrated case it is sector IV, and the overall reduction factor can be given as

$$k_{red} = 6 \frac{T_{mv}}{T_{sw}} \, . \tag{6.16}$$

Unless T_{mv} can be kept very small in relation to T_{sw}, this will often be a substantial reduction in achievable voltage magnitude. For the same exemplary ratio of $T_{mv}/T_{sw} = 0.1$, only 40 % of the voltage achievable with standard SVM would be usable.

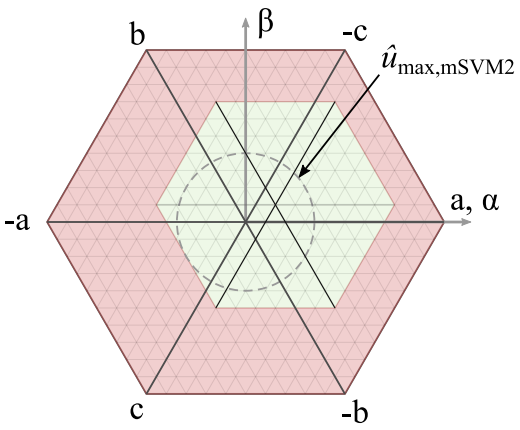

Figure 6.6.: Accessible voltage region when using mSVM2, for $T_{\mathrm{mv}}/T_{\mathrm{sw}} = 0.1$.

6.2.3. mSVM3: Alternating Single Edge or Pulse Shift

Another possibility to modify the SVM was described in [Man13, p. 63f]. At the beginning of a switching period, a zero measurement vector is again applied. However, instead of successively shifting all of the leading edges of an edge-aligned standard SVM towards each other, only the leading edge of one phase is shifted ahead of the other two. The phase to be shifted is alternated each time, resulting in a recurring sequence of three switching periods each. In each period, two measurements of u_{NAN} are taken during the zero measurement vector and the active measurement vector resulting from the shifted edge.

Since the process is repeated in all of the three axes, a total of six measurements is taken for one estimation period as shown in Fig. 6.7. Similar to mSVM1, the directional Δu_{NAN} voltages are calculated from each pair of measurements according to

$$\begin{aligned} \Delta u_{\mathrm{NAN,a}} &= (\kappa_{\mathrm{a}} - 1/3) \cdot u_{\mathrm{DC}} = u_{\mathrm{NAN},2} - u_{\mathrm{NAN},1} \\ \Delta u_{\mathrm{NAN,b}} &= (\kappa_{\mathrm{b}} - 1/3) \cdot u_{\mathrm{DC}} = u_{\mathrm{NAN},4} - u_{\mathrm{NAN},3} \\ \Delta u_{\mathrm{NAN,c}} &= (\kappa_{\mathrm{c}} - 1/3) \cdot u_{\mathrm{DC}} = u_{\mathrm{NAN},6} - u_{\mathrm{NAN},5} \end{aligned} \tag{6.17}$$

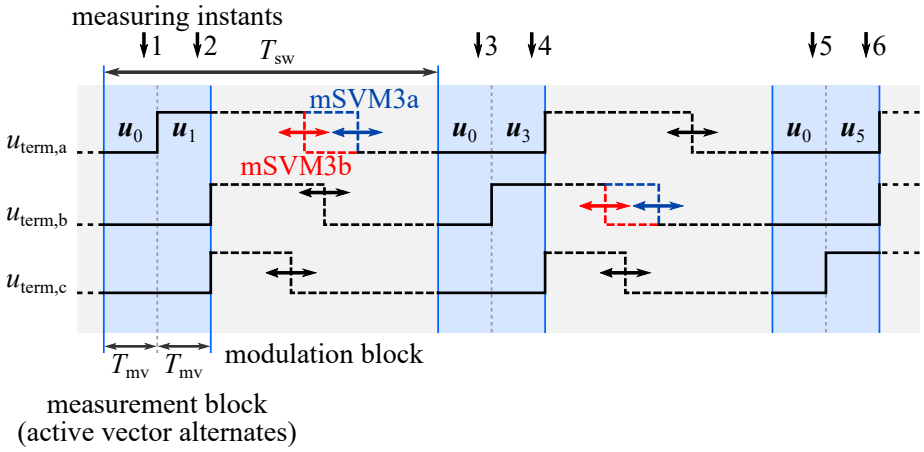

Figure 6.7.: Pulse pattern with alternating single edge or pulse shift (mSVM3).

and the inductance ratios are obtained as

$$\begin{aligned} \kappa_a &= \frac{1}{u_{DC}} \left(u_{NAN,2} - u_{NAN,1} \right) + \frac{1}{3} \\ \kappa_b &= \frac{1}{u_{DC}} \left(u_{NAN,4} - u_{NAN,3} \right) + \frac{1}{3} \\ \kappa_c &= \frac{1}{u_{DC}} \left(u_{NAN,6} - u_{NAN,5} \right) + \frac{1}{3} \,. \end{aligned} \tag{6.18}$$

However, compared to the six switching periods required for mSVM1, it takes only three and therefore half the switching periods to update all of the anisotropy signals.

For this modulation strategy, the voltage reduction depends on how the compensation of the active measurement vectors is realized. Two variants are conceivable in principle. The first possibility is to let the active measurement vectors compensate each other over a total of three switching periods. This variant will be referred to as mSVM3a. Compared to an edge-aligned standard SVM, *only the leading edge* of a phase is shifted for each period. The voltage reduction in this case is

$$k_{red} = \frac{6T_{mv}}{3T_{sw}} = 2\frac{T_{mv}}{T_{sw}} \,. \tag{6.19}$$

When considering a single switching period, the reference vector to be generated on average is not exactly obtained with this variant. The second possibility is to shift the *whole pulse* of one phase, so that the measurement vectors are compensated for in

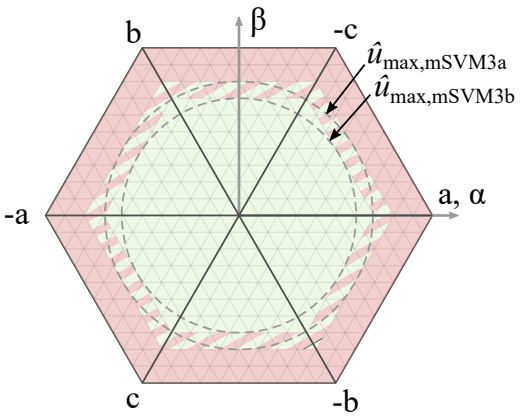

Figure 6.8.: Accessible voltage region when using one of the two variants of mSVM3, for $T_{\mathrm{mv}}/T_{\mathrm{sw}} = 0.1$.

the modulation block of the same switching period. This variant will be referred to as mSVM3b. The reference vector is then exactly obtained for each switching period, however the voltage reduction is increased to

$$k_{\mathrm{red}} = \frac{9T_{\mathrm{mv}}}{3T_{\mathrm{sw}}} = 3\frac{T_{\mathrm{mv}}}{T_{\mathrm{sw}}} \ . \tag{6.20}$$

The voltage reduction for both variants is illustrated in Fig. 6.8.

6.2.4. Discussion of the Known Modified Modulation Strategies

When using mSVM1 or mSVM3, the inductance ratios that are required for calculating the position estimate are acquired over three separate measurement blocks, distributed over six (mSVM1) or three (mSVM3) switching periods. While this is unproblematic at standstill or low speeds, it can have a negative impact at higher speeds because the rotor position may have considerably changed between the measurement of the a-, b- and c-component. Additional complexities in the estimation results at high speed can therefore be expected. An obvious drawback of mSVM2 instead is that the utilizable voltage is much more significantly reduced compared to the other two strategies. This directly reduces also the speed up to which a machine can be operated with the sensorless technique by a significant amount. In the following section, two novel modified modulation strategies are presented that aim to address these drawbacks.

A last thing shall be discussed here concerning the calculation of the position estimate

when using one of the previous modulation strategies. As has been discussed before, a minimum of three measurement vectors is required to acquire the inductance ratios. Because the modulation strategies mSVM1, mSVM2 and mSVM3 use more measurement vectors than necessary, the set of equations is overdetermined and κ_a, κ_b and κ_c may not exactly sum to one but contain an offset

$$\kappa_{0,\mathrm{off}} = \frac{1}{3}\left(\left(\kappa_{\mathrm{a},} + \kappa_\mathrm{b} + \kappa_\mathrm{c}\right) - 1\right) \ . \tag{6.21}$$

If position estimation based on κ_α and κ_β is performed, the offset has no impact on the estimated position because the offset adds only to κ_0. However, if position estimation using ρ_α and ρ_β is desired, calculating and removing this offset from the inductance ratios may slightly affect the estimation results. In the conducted experiments the offsets were always removed. From examining the measured data, the differences between the estimated electrical angle with and without offset removal were found to be less than 0.01°. Therefore, the effect of the offset removal on the experimental data presented in this thesis can be considered negligible.

6.3. Novel Modified Modulation Strategies

The modulation strategies mSVM1, mSVM2 and mSVM3 use either four or six measurement vectors per estimation period to obtain the inductance ratios. In the following, two novel modified modulation strategies are described. Both use only the minimum number of three measurement vectors and calculate all three inductance ratios from a single contiguous measurement block. As a result, both allow high voltage utilization and update rate of the anisotropy information. The first strategy that is presented uses a zero vector and the two active vectors that are naturally used in standard SVM as measurement vectors to allow for the maximum possible voltage utilization. The second strategy uses three active measurement vectors that are displaced by 120° from each other in the αβ-plane.

6.3.1. mSVM4: Sector-Dependent Successive Pulse Shift

The first novel modulation strategy, mSVM4, uses a pulse pattern that is very similar to that of mSVM2, however only one zero vector is used and the two active measurement vectors are not kept fixed. Instead, they are chosen as those that are naturally used in

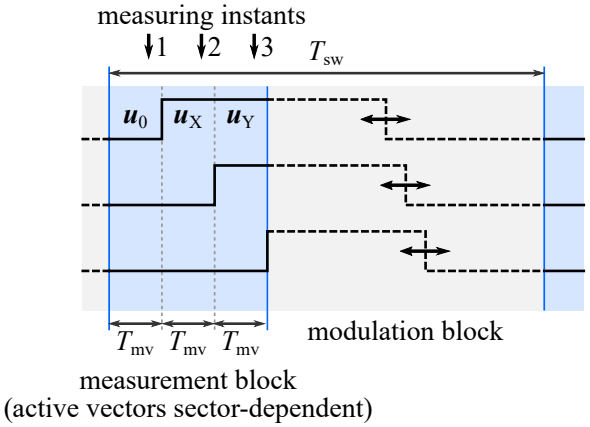

Figure 6.9.: Pulse pattern with sector-dependent successive edge shift (mSVM4). The shown waveform corresponds to sector I.

standard SVM so that the composition of the measurement block becomes dependent on the voltage sector.

For sector I, the determination of the inductance ratios is almost similar to the procedure for mSVM2, with the only difference that the measurement $u_{\mathrm{NAN},4}$ is replaced by $u_{\mathrm{NAN},1}$:

$$\begin{aligned}
\Delta u_{\mathrm{NAN,a}} &= (\kappa_{\mathrm{a}} - 1/3) \cdot u_{\mathrm{DC}} = u_{\mathrm{NAN},2} - u_{\mathrm{NAN},1} \\
\Delta u_{\mathrm{NAN,b}} &= (\kappa_{\mathrm{b}} - 1/3) \cdot u_{\mathrm{DC}} = u_{\mathrm{NAN},3} - u_{\mathrm{NAN},2} \\
\Delta u_{\mathrm{NAN,c}} &= (\kappa_{\mathrm{c}} - 1/3) \cdot u_{\mathrm{DC}} = u_{\mathrm{NAN},1} - u_{\mathrm{NAN},3} \; .
\end{aligned} \tag{6.22}$$

Accordingly, the inductance ratios are

$$\begin{aligned}
\kappa_{\mathrm{a}} &= \frac{1}{u_{\mathrm{DC}}} \left(u_{\mathrm{NAN},2} - u_{\mathrm{NAN},1} \right) + \frac{1}{3} \\
\kappa_{\mathrm{b}} &= \frac{1}{u_{\mathrm{DC}}} \left(u_{\mathrm{NAN},3} - u_{\mathrm{NAN},2} \right) + \frac{1}{3} \\
\kappa_{\mathrm{c}} &= \frac{1}{u_{\mathrm{DC}}} \left(u_{\mathrm{NAN},1} - u_{\mathrm{NAN},3} \right) + \frac{1}{3} \; .
\end{aligned} \tag{6.23}$$

For the other sectors, the calculations are obtained analogously. The full inductance ratio vector is updated with every switching period.

The voltage reduction of this modified modulation strategy is given by

$$k_{\mathrm{red}} = \frac{1T_{\mathrm{mv}}}{1T_{\mathrm{sw}}} = 1\frac{T_{\mathrm{mv}}}{T_{\mathrm{sw}}} \tag{6.24}$$

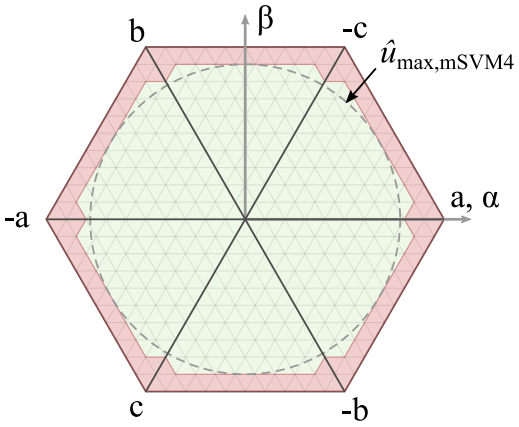

Figure 6.10.: Accessible voltage region when using mSVM4, for $T_{\mathrm{mv}}/T_{\mathrm{sw}} = 0.1$.

which is due to the one zero vector that is applied for T_{mv} in every measurement block. The accessible voltage region is shown in Fig. 6.10. For

$$T_{\mathrm{mv}}/T_{\mathrm{sw}} > \frac{1-\cos(30°)}{2-\cos(30°)} = \frac{1-\sqrt{3}/2}{2-\sqrt{3}/2} \approx 0.118 \tag{6.25}$$

however, the voltage reduction becomes

$$k_{\mathrm{red}} = \frac{1}{\cos(30°)} - \frac{2}{\cos(30°)}\frac{T_{\mathrm{mv}}}{T_{\mathrm{sw}}} \tag{6.26}$$

$$= \frac{2}{\sqrt{3}} - \frac{4}{\sqrt{3}}\frac{T_{\mathrm{mv}}}{T_{\mathrm{sw}}}\,. \tag{6.27}$$

due to the reason mentioned in section 6.1.

Compared to the other modified modulation strategies, this strategy can be considered a discontinuous strategy because the active vectors in the measurement block change abruptly at the transition to another voltage sector. To prevent a high-frequency switching back and forth, a hysteresis logic should be implemented. Depending on the size of the hysteresis band and the ratio $T_{\mathrm{mv}}/T_{\mathrm{sw}}$, additional voltage reduction may occur.

6.3.2. mSVM5: Triaxial Vector Insertion

The second novel modulation strategy, referred to as mSVM5, uses a measurement block with three active vectors, one in each of the three axes, that result in a zero vector on average. The modulation blocks are mirrored as with mSVM1, so that a pulse pattern as

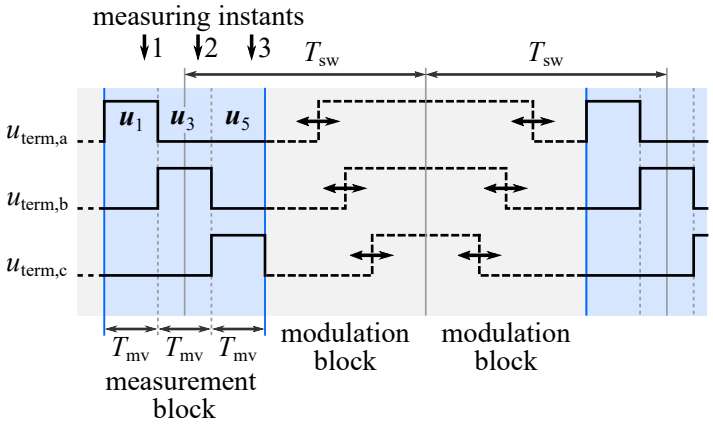

Figure 6.11.: Pulse pattern with triaxial vector insertion (mSVM5).

shown in Fig 6.11 is obtained. Similar to mSVM1, it can be regarded as a center-aligned standard SVM that has the described measurement block inserted between its pulses.

For this modulation strategy, the inductance ratios in the physical frame cannot be calculated from only two measurements each. Starting from

$$\kappa_{\Delta}^{\mathrm{p}} \boldsymbol{u}_{\mathrm{term}}^{\mathrm{p}} - \boldsymbol{\kappa}^{\mathrm{p}} \mathbf{u}_{\mathrm{slow}}^{\mathrm{p}} = u_{\mathrm{NAN}} \tag{6.28}$$

and inserting the active vectors $\boldsymbol{u}_1$, $\boldsymbol{u}_3$ and $\boldsymbol{u}_5$ into $\boldsymbol{u}_{\mathrm{term}}^{\mathrm{p}}$, the following equations are obtained:

$$\text{I:}\ \ (\kappa_{\mathrm{a}} - 1/3) \cdot u_{\mathrm{DC}} - \boldsymbol{\kappa}^{\mathrm{p}} \boldsymbol{u}_{\mathrm{slow}}^{\mathrm{p}} = u_{\mathrm{NAN},1} \tag{6.29}$$

$$\text{II:}\ \ (\kappa_{\mathrm{b}} - 1/3) \cdot u_{\mathrm{DC}} - \boldsymbol{\kappa}^{\mathrm{p}} \boldsymbol{u}_{\mathrm{slow}}^{\mathrm{p}} = u_{\mathrm{NAN},2} \tag{6.30}$$

$$\text{III:}\ \ (\kappa_{\mathrm{c}} - 1/3) \cdot u_{\mathrm{DC}} - \boldsymbol{\kappa}^{\mathrm{p}} \boldsymbol{u}_{\mathrm{slow}}^{\mathrm{p}} = u_{\mathrm{NAN},3} \tag{6.31}$$

It should be recalled that $\kappa_{\mathrm{a}} + \kappa_{\mathrm{b}} + \kappa_{\mathrm{c}} = 1$. Using $((2 \cdot \mathrm{I} - \mathrm{II} - \mathrm{III})/3$, $\boldsymbol{u}_{\mathrm{slow}}^{\mathrm{p}}$ is eliminated, yielding

$$(\kappa_{\mathrm{a}} - 1/3) \cdot u_{\mathrm{DC}} = \left(2u_{\mathrm{NAN},1} - u_{\mathrm{NAN},2} - u_{\mathrm{NAN},3}\right)/3 \tag{6.32}$$

and κ_{a} is finally obtained as

$$\kappa_{\mathrm{a}} = \frac{1}{u_{\mathrm{DC}}} \left(2u_{\mathrm{NAN},1} - u_{\mathrm{NAN},2} - u_{\mathrm{NAN},3}\right) + \frac{1}{3} \,. \tag{6.33}$$

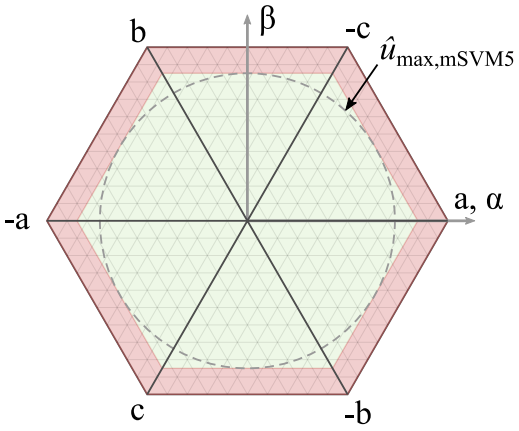

Figure 6.12.: Accessible voltage region when using mSVM5, for $T_{\mathrm{mv}}/T_{\mathrm{sw}} = 0.1$.

The same is done for κ_{b} and κ_{c}, yielding

$$\kappa_{\mathrm{b}} = \frac{1}{u_{\mathrm{DC}}} \left(2u_{\mathrm{NAN},3} - u_{\mathrm{NAN},1} - u_{\mathrm{NAN},2}\right) + \frac{1}{3} \tag{6.34}$$

$$\kappa_{\mathrm{c}} = \frac{1}{u_{\mathrm{DC}}} \left(2u_{\mathrm{NAN},2} - u_{\mathrm{NAN},3} - u_{\mathrm{NAN},1}\right) + \frac{1}{3} \,. \tag{6.35}$$

Due to the three measurement vectors that are applied for T_{mv} each and inserted once per two switching periods, the voltage reduction is described by

$$k_{\mathrm{red}} = \frac{3T_{\mathrm{mv}}}{2T_{\mathrm{sw}}} = \frac{3}{2}\frac{T_{\mathrm{mv}}}{T_{\mathrm{sw}}} \,. \tag{6.36}$$

The accessible voltage region for $T_{\mathrm{mv}}/T_{\mathrm{sw}} = 0.1$ is shown in Fig. 6.12.

A side effect of this novel modulation strategy is that all measurements are performed with the same common mode voltage $u_{\mathrm{term},0}$, making the measurements less susceptible to common mode errors.

Taking a closer look at Fig. 6.11, one can see that some of the periods denoted with T_{sw} feature three edges whereas others feature only one edge. Because of this, the implementation of this pulse pattern can be somewhat more complex compared to the other strategies.

6.4. Other Modified SVM Strategies and Concepts

Besides the described modulation strategies, there are some other strategies and concepts which should at least be mentioned in this scope. In [NKPK15], a modified pulse pattern has been shown for an estimation using the neutral point voltage where the leading edge for one phase is aligned to the beginning of a switching period and the trailing edge for a second phase to its end. This leads to a total of up to five active vectors and no zero vector, however no information was provided about the actual measuring instants that should be used.

A work published in [PSB03] goes in a similar direction and proposed a modulation strategy with six active vectors and no zero vectors. Such modulation leads to high ripple in the phase currents. The work used an estimation based on current changes, therefore the high current ripple was intended to increase the evaluable signal magnitudes. In contrast, u_{NAN} stays approximately constant per each discrete voltage vector, therefore prolonging the durations of active vectors beyond the required minimum is not purposeful for techniques like the one looked at in this thesis. In general, it should be remembered that active vectors which do not contribute towards the reference vector reduce the achievable voltage utilization depending on the duration of their application. Therefore, such strategies are clearly not the best choice for operation up to high speeds.

Besides, one may argue that the measurement vectors do not necessarily have to form contiguous measurement blocks and that they could also be distributed throughout a switching period. Moreover, works like [NKPK15; ITSA16] used modification of standard SVM only when necessary, i.e. only in those voltage regions where the requirements for minimum durations are not fulfilled. While this may sound advantageous at first, there are some disadvantages that have not been mentioned in these works but can be expected. Similar to mSVM4, different measurement vectors have to be used in different regions of the voltage plane and may lead to discontinuities in the measurements as will be shown in section 6.7. In addition, however, the time instants at which measurements may be performed become dependent on the reference voltage vector, increasing the overall complexity. The effectiveness of an elimination of the low frequency part $\boldsymbol{u}_{\mathrm{slow}}$ is also reduced with increasing time between individual measurements. In fact, the authors in [ITSA16] focused on low-speed operation and acquired the anisotropy signals from single measurements of u_{NAN} during the application of active vectors, without elimination of $\boldsymbol{u}_{\mathrm{slow}}$. Due to the mentioned expectable disadvantages, the author of this thesis has decided not to pursue the approach of modifying the modulation “on demand only”.

Modifying the SVM will usually require access to a relatively low system level such as timers that create the pulsed waveforms. However, when commercially available inverter hardware must be used, such low level access may not be available. In [Wer18], the modification was therefore realized in a way that requires no access to the implementation of the modulator. Certain switching periods of a standard SVM were used solely for measurement purposes, while the others were used as normal switching periods that synthesize the voltage references from the current control. It is clear that this significantly limits either the applicable voltage, the sample rate of the anisotropy information, or both, depending on the ratio of measurement and switching periods. Therefore, this approach was also not further pursued here.

6.5. Spectral Analysis of Modified SVMs

The described modified SVMs guarantee sufficient durations for the measurements of the zero-sequence voltage but they also have an impact on the harmonic content in the phase currents. Besides increasing losses, additional harmonics can in particular lead to audible noise. Depending on whether the machine is operated in proximity to people or animals, this noise may be unacceptable. To compare the investigated modified SVMs in terms of harmonic content, a spectral analysis is conducted. For this purpose, they have been implemented in MATLAB Simulink and a discrete Fourier transformation was applied to one of the line-to-line voltages, i.e. the voltage between two motor terminals, resulting from the waveforms generated. The input for the modulation was a rotating reference voltage vector of constant magnitude – the fundamental voltage.

In Figs. 6.13 and 6.14, calculated spectra are shown for $T_{\mathrm{mv}} = 0.05 \cdot T_{\mathrm{sw}}$ and fundamental voltages that represent voltage utilizations of 5 % and 50 % of the voltage available with standard SVM and no overmodulation. Note that the left columns represent the standard SVM with center-aligned pulses and the modified strategies that are most comparable to it whereas the right column shows the strategies most comparable to edge-aligned standard SVM. The ratio between the fundamental frequency of the reference voltages and the switching frequency was $f_{\mathrm{f}}/f_{\mathrm{sw}} = 120$. To allow for better comparisons in the cases of mSVM1 and mSVM5, the center aligned standard SVM is shown additionally also for $f_{\mathrm{f}}/f_{\mathrm{sw}} = 60$. mSVM4 was simulated without a hysteresis logic. Therefore, the switching of the measurement vectors happens exactly at the border between two voltage sectors in the simulation.

The following observations can be made: The spectra for mSVM2 and mSVM5 are

relatively close to the ones for standard SVM with edge- and center-aligned pulses respectively, even though additional peaks can be identified at multiples of f_{sw} for mSVM2 and at multiples of $f_{\mathrm{sw}}/2$ for mSVM5. The spectrum for mSVM1 essentially shows additional harmonics located at $f/f_{\mathrm{sw}} = \frac{1}{6}, \frac{2}{6}, \frac{4}{6}, \frac{5}{6}, \frac{7}{6}, \ldots$. Similarly, mSVM3a and mSVM3b show additional harmonics at $f/f_{\mathrm{sw}} = \frac{1}{3}, \frac{2}{3}, \frac{4}{3}, \frac{5}{3}, \frac{7}{3}, \ldots$, but to a significantly larger extent. In fact, mSVM3a and mSVM3b have been observed in practice to cause the most significant audible noise when these harmonics fall into the audible range. For mSVM4, the spectrum looks rather different, with harmonics distributed throughout the frequency range. These findings help to understand how the switching frequency must be selected to keep harmonic components outside the audible range or which modulation strategies can be expected to produce audible noise for a given switching frequency.

A common measure to quantify the harmonic content caused by modulation techniques is the weighted total harmonic distortion [HL03, pp. 91-93], defined by

$$\mathrm{WTHD} = \frac{1}{u_1}\sqrt{\sum_{k=2}^{\infty}\left(\frac{u_k}{k}\right)^2} \tag{6.37}$$

where u_k is the amplitude of the k-th harmonic of the fundamental voltage $u_1 = u_{\mathrm{f}}$ in the line-to-line voltage. Weighting the voltage harmonics by their harmonic order aims to provide a measure of the expectable harmonic content in the currents for an inductive load such as an electric motor as the harmonics in the currents are usually of greater importance than those in the voltages [HL03, pp. 91-93]. What is important to note, however, is that the WTHD is not a measure of audible noise and that a higher WTHD is not necessarily associated with a subjectively perceived higher audible noise.

Calculated WTHDs are shown in Table 6.1. It can be seen that, in particular at low voltage utilization, mSVM1 and mSVM5 result in the lowest WTHD among the investigated modified modulation strategies. This can likely be attributed to the fact that the inserted voltage vectors largely compensate each other within the measurement block. Further, it can be seen that the differences in the harmonic content become less pronounced for the higher voltage utilization of $u_{\mathrm{f}} = 0.5 \cdot u_{\mathrm{DC}}/\sqrt{3}$. This can be attributed to the constant duration of the measurement vectors becoming small in relation to those of the active vectors in the modulation block. The WTHD of all modified modulation strategies except for mSVM4 become then approximately two times the WTHD of a center aligned SVM with equal switching frequency. The WTHD of mSVM4 lies between that of an edge-aligned and a center-aligned standard SVM. This can be explained by the

structure of the pulse pattern that lies generally somewhere between these two, mainly differing by the distribution of the active vectors between the beginning and the end of a switching period.

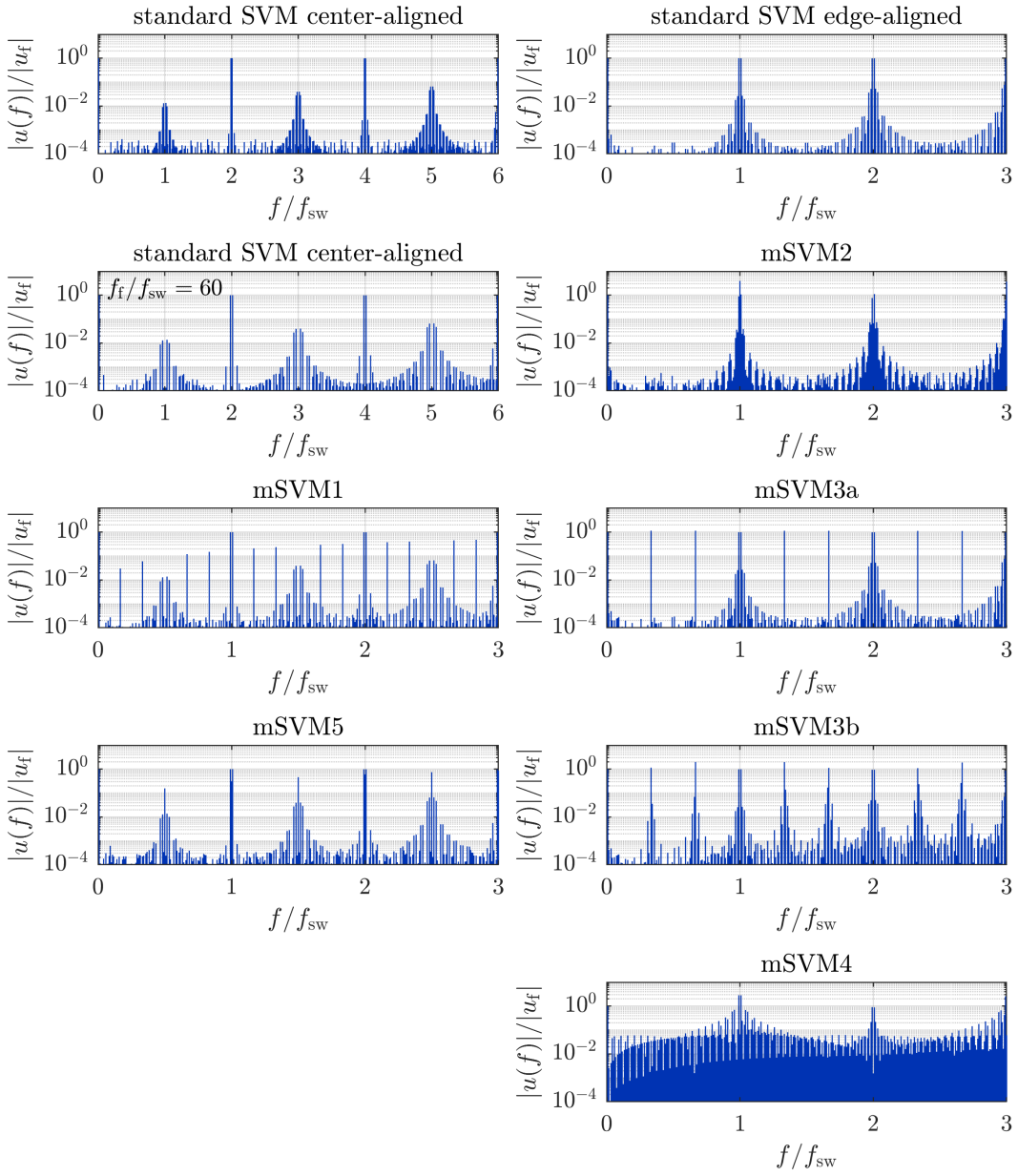

Figure 6.13.: Spectra of the line-to-line voltage for standard SVM and the modified modulation strategies under investigation. $u_f = 0.05 \cdot u_{DC}/\sqrt{3}$, $T_{mv} = 0.05 \cdot T_{sw}$, $f_f/f_{sw} = 120$ (except for the second spectrum on the left).

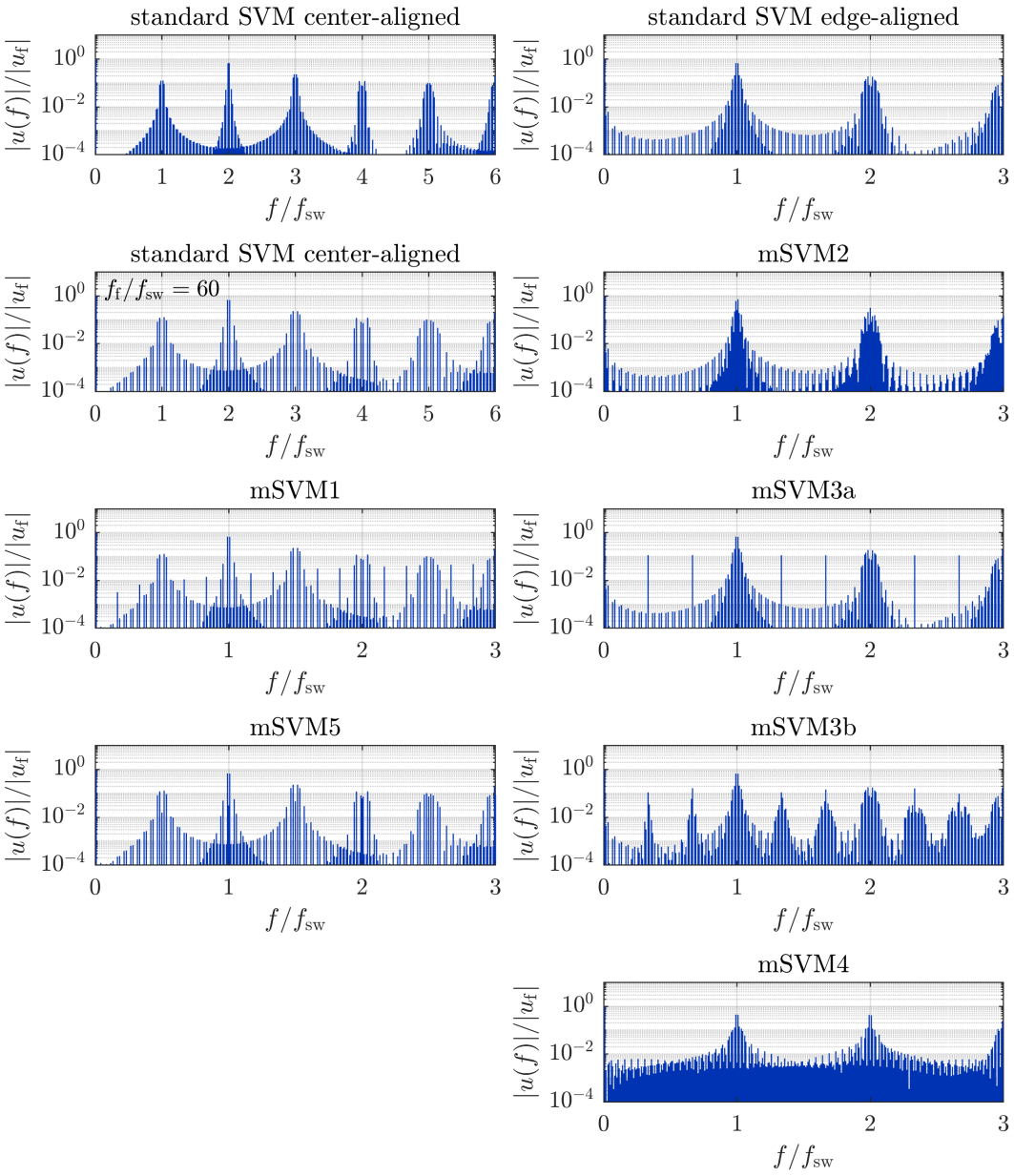

Figure 6.14.: Spectra of the line-to-line voltage for standard SVM and the modified modulation strategies under investigation. $u_f = 0.5 \cdot u_{DC}/\sqrt{3}$, $T_{mv} = 0.05 \cdot T_{sw}$, $f_f/f_{sw} = 120$ (except for the second spectrum on the left).

Table 6.1.: Weighted total harmonic distortions for standard SVM and the modified modulation strategies under investigation. $T_{\mathrm{mv}} = 0.05 \cdot T_{\mathrm{sw}}$.

	$f_{\mathrm{f}}/f_{\mathrm{sw}}$	WTHD $u_{\mathrm{f}} = 0.05 \cdot u_{\mathrm{DC}}/\sqrt{3}$	WTHD $u_{\mathrm{f}} = 0.5 \cdot u_{\mathrm{DC}}/\sqrt{3}$
Standard SVM center-aligned	120	0.71 %	0.460 %
Standard SVM center-aligned	60	1.43 %	0.921 %
mSVM1	120	1.64 %	0.924 %
mSVM5	120	1.72 %	0.926 %
Standard SVM edge-aligned	120	1.45 %	0.921 %
mSVM2	120	3.79 %	0.949 %
mSVM3a	120	3.74 %	0.983 %
mSVM3b	120	4.41 %	0.992 %
mSVM4	120	4.20 %	0.693 %

6.6. Experimental Test Setup

The following section describes the experimental setup that was used for most of the experimental investigations presented in the further course of this thesis. A schematic of the overall setup is presented in Fig. 6.15.

The motor under test is driven by a custom motor control board, shown in Fig. 6.16. The core of this board is an STM32H753xx microcontroller that features an ARM Cortex-M7 running at 400 MHz and three 16-bit ADCs. It performs all the measurements and calculations that are necessary for the sensorless control of the machine. The implementation on a microcontroller offers high flexibility and hardware level access that was beneficial to implement the various modified modulation strategies used in this thesis and synchronize the pulse patterns with the ADC measurements precisely. The board includes also the three-phase inverter featuring a gate driver and six 40 V rated MOSFETs. Furthermore, the phase currents are measured using three shunt resistors placed in series with the inverter outputs and three AD8418A current sense amplifiers. In the experiments, the housing of the motor under test is electrically connected to the system ground, i.e. the negative supply rail of the DC link voltage that is provided by a DC power supply. The switching frequency is 32 kHz for motors M1 and M2 and 64 kHz for motor M3, considering its smaller time constant. The duration for the measurement vectors is $T_{\mathrm{mv}} = 2\,\mu\mathrm{s}$ for all motors. The software implementing the control of the motor under test including the generation of the modified pulse patterns and the position estimation algorithms has been written in C code.

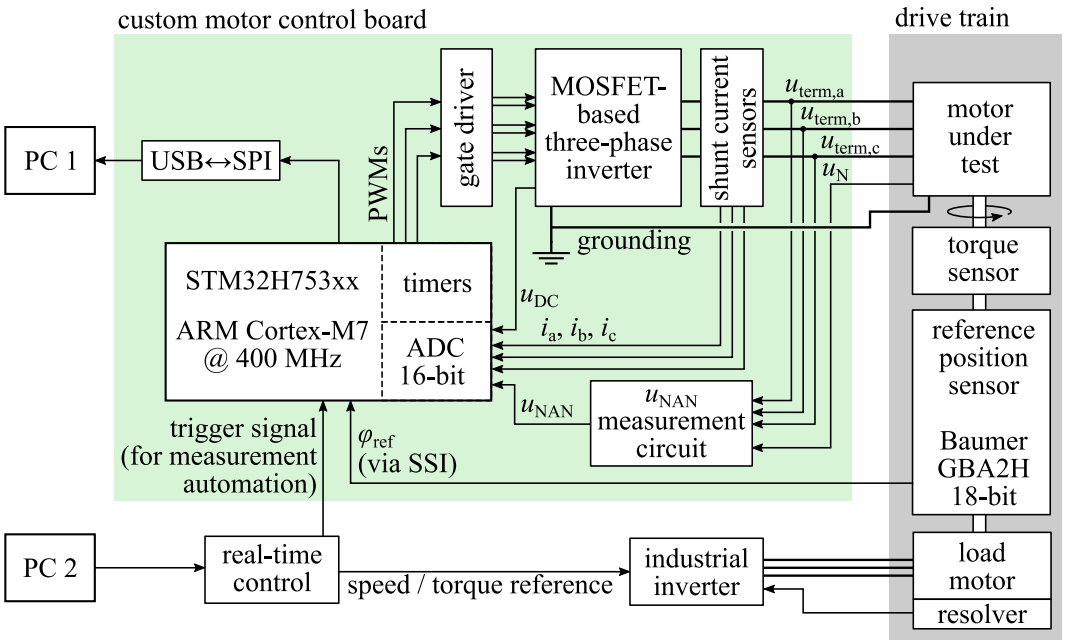

Figure 6.15.: Experimental test environment.

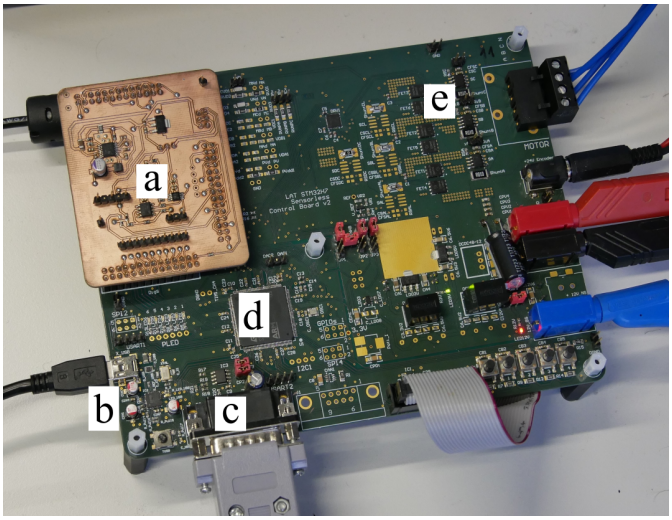

Figure 6.16.: Custom motor control board: (a) u_{NAN} measurement circuit (b) USB interface (c) position sensor interface (d) STM32H753xx microcontroller (e) inverter and shunt current sensors. From [SKMN21].

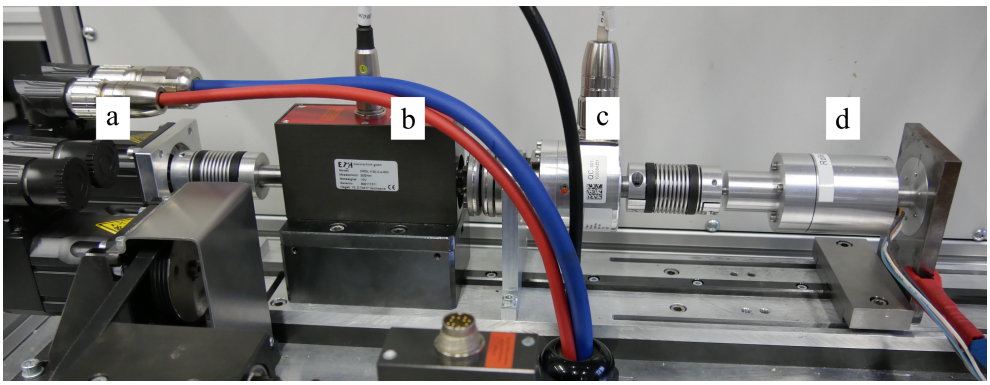

Figure 6.17.: Drive train as part of the experimental test setup with motor M1 mounted: (a) load motor, (b) torque sensor, (c) reference position sensor and (d) motor under test.

The motor under test is mounted in the drive train of the test setup, which can be seen in Fig. 6.17. Besides the motor under test, the drive train includes a load motor, a torque sensor and a reference position sensor. The reference position sensor is an optical encoder GBA2H from Baumer, which provides the absolute mechanical position with a resolution of 18 bits and a specified accuracy of ±0.01°. It is read by the custom control board via SSI (Synchronous Serial Interface). The load motor is driven by an industrial inverter and receives speed or, in some cases, torque references from a real-time control and measurement unit, which is connected to a desktop PC via Ethernet. The torque sensor was used only for validation purposes.

An essential part of the custom motor control board is the measurement circuit for the zero-sequence voltage. A principal schematic of the measurement circuit is shown in Fig. 6.18. It consists of a scaling stage and a subtraction stage. In the scaling stage, u_{N} is scaled down using a voltage divider (gain 1:15). The artificial neutral point is created and scaled down using a network of four resistors. The subtraction stage consists of two voltage followers for u_{N} and u_{AN} and the actual subtractor. For the voltage followers, an ADA4807-2 from Analog Devices was used, whereas the subtractor was realized using an LMH6609 from Texas Instruments with a gain of +5. These operational amplifiers are high bandwidth amplifiers that allow tracking the fast transients occuring at u_{N} and u_{AN} during the switching events.

In Fig. 6.19, the dynamic response and transient common mode rejection are demonstrated by differential- and common-mode step responses. Using a function generator (Hameg HM8150), voltage steps of 0.3 V were applied directly to the inputs of the sub-

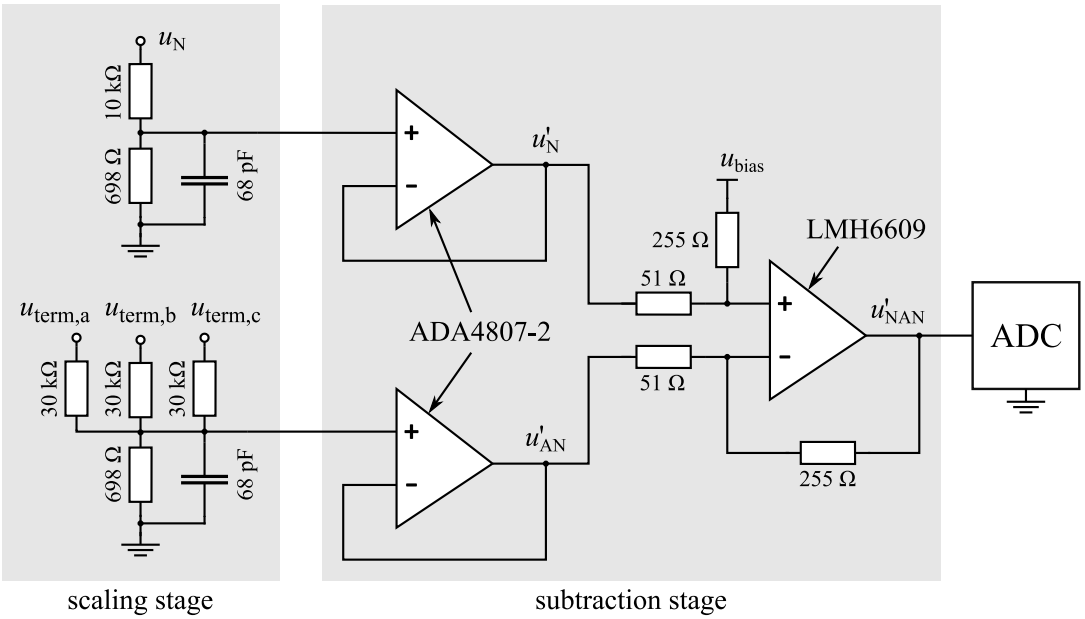

Figure 6.18.: Used measurement circuit for u_{NAN}. Output voltages of amplifiers are denoted with accent as distinction from the actual voltages.

traction stage. The scaling stage was not connected in this experiment. u'_{N} and u'_{AN} are the outputs of the voltage followers. In the shown courses, the subtractor gain of 5 and the bias voltage for u_{NAN} are already removed. It can be seen that the subtractor reacts quickly to a change of the differential voltage. For a change in the common-mode voltage, there is a small transient error of about 0.5 % that decays within less than 1 µs. Static common-mode errors are practically negligible. It should be mentioned that depending on which voltage vectors are used for the measurements, common-mode errors that might occur in a subtraction stage, for example due to resistor mismatch, will also cancel out partly due to the subtraction of successive measurements of u_{NAN}.

As discussed in section 4.5.1, steps of the neutral point voltage are often accompanied by overshoot and ringing. The artificial neutral point voltage, on the other hand, closely resembles the mean voltage of the three terminal voltages. Its dynamic response is therefore almost the same as that of the terminal voltages. Therefore, it usually rises faster than the neutral point voltage and has no or at least significantly less overshoot. This results in additional temporary differences between the real and artificial neutral point directly after a switching event which can be significantly larger than those caused

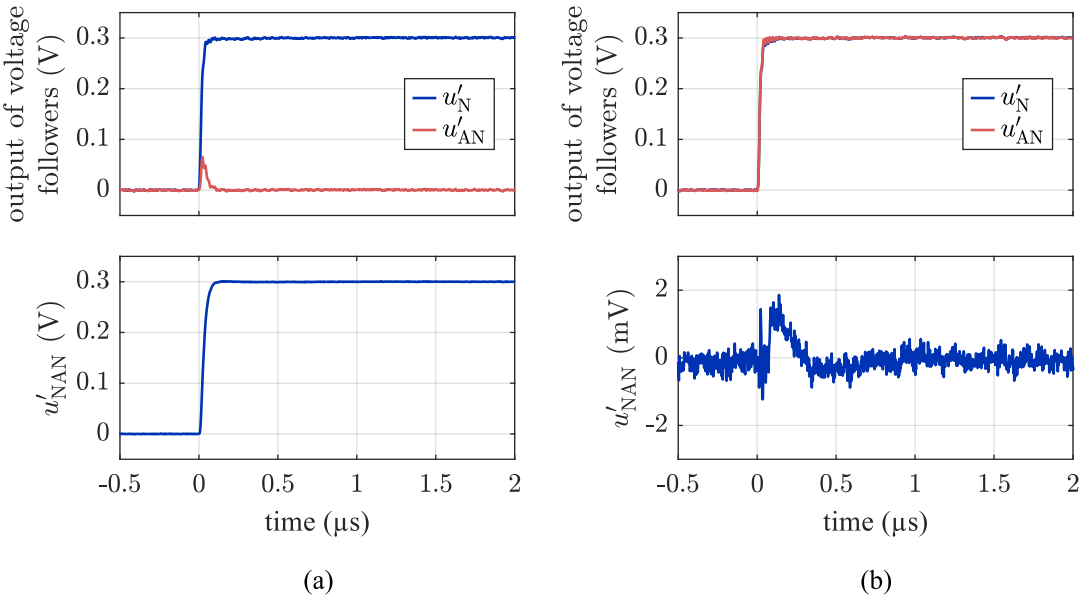

Figure 6.19.: Oscilloscope measurements of the differential- and common-mode step responses of the subtractor stage for a 0.3 V step: (a) differential-mode step response (b) common-mode step response.

by the position-dependent inductance ratios. By placing an additional capacitor at the voltage divider, u_N and u_{AN} are slightly lowpass-filtered which reduces these temporary differences and also cuts off very high frequency components including those potentially caused by external disturbances (see section 4.5.2).

Fig. 6.20 shows an oscilloscope measurement of the signal that is produced by the measurement circuit during operation. Here, motor M2 was rotated at $n = 1000\,\mathrm{r/min}$ and current-controlled to $i_q = 3.2\,\mathrm{A}$. The modulation strategy mSVM5 was used.

6.7. Differences Due to the Use of Measurement Vectors in Two or in Three Axes

With (4.152), a linear relationship has been established between the differences of two or more voltage vectors and the respective differences in the zero-sequence voltage via the inductance ratio vector $\boldsymbol{\kappa}_\Delta$. On this basis, the actual measurement vectors used should not have much of an impact on the measured inductance ratios and the estimated position. This applies especially to low speeds, where the voltages induced by rotor movement

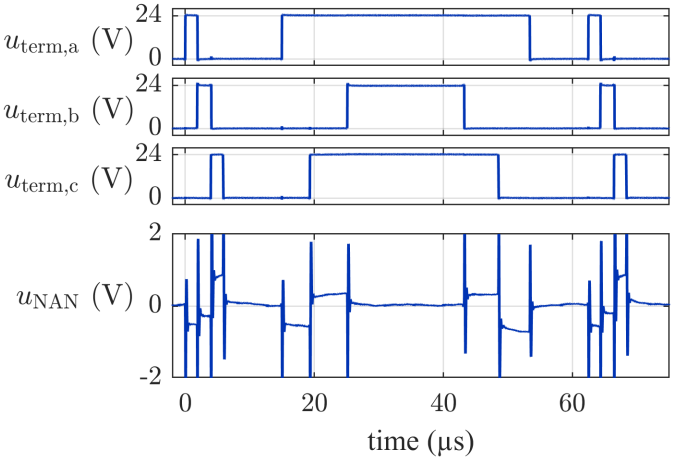

Figure 6.20.: Oscilloscope measurements of terminal voltages and u_{NAN} for motor M2 at $n = 1000\,\text{r/min}$ and $i_{\text{q}} = 3.2\,\text{A}$, using mSVM5. u_{NAN} is measured at the output of the measurement circuit.

are negligible and where the position hardly changes between successive measurements. Yet, during the work on this thesis, it was experienced that the actually measured inductance ratios and the resulting position estimates can differ considerably between the investigated modulation strategies, even at low speeds. Moreover, these differences appeared to be of systematic nature. A major portion of the differences showed to be attributable to whether measurement vectors in only two or in all three of the axes were used to calculate the inductance ratios. This effect is discussed in this section, following what was already published in [SKMN21].

To investigate the observed phenomena, experiments have been performed using the test setup described in the previous section. Motor M1 and motor M2 were driven by the load motor at a moderate speed of 20 Hz electrically, with their currents controlled to zero. The moderate speed was chosen to obtain voltage magnitudes that are sufficient for generating sector changes for mSVM4 despite the implemented hysteresis logic. The estimated position was used to control the motors under test.

Fig. 6.21 shows deviations of the estimated positions from the reference position resulting from the five different modulation strategies. For mSVM3, only the variant mSVM3b is shown; the results for mSVM3a were almost identical. It can be seen that the curves for mSVM1, mSVM3b and mSVM5 are highly coincidental, whereas the curves for mSVM2 and mSVM4 deviate noticeably. What is particularly noticeable for mSVM4

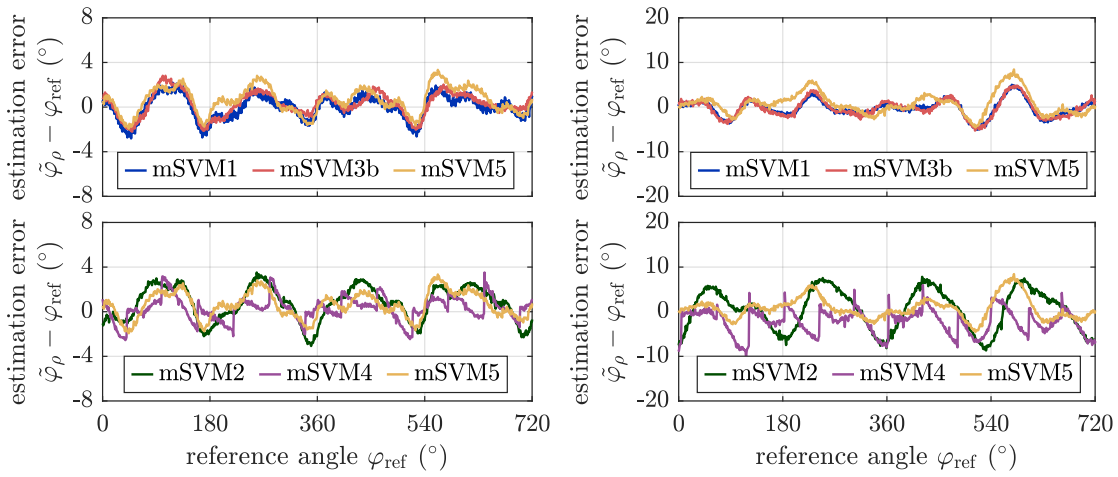

Figure 6.21.: Estimation errors resulting from the five modulation strategies under investigation. (left) motor M1, n = 150 r/min, (right) motor M2, n = 171.4 r/min. Currents were controlled to zero for both motors.

are the jumps that occur roughly every 60°. From the five investigated modulations strategies, mSVM4 is the only one where the measurement vectors depend on the voltage sector, introducing discontinuity to the estimation. A closer look at the data confirmed that the jumps take place at the time of the sector changes. It should be mentioned that at higher speeds such discontinuities are smoothed by the PLL-type filter. At low speeds, however, the smoothing effect of the PLL is small, so that the discontinuities have the greatest effect here.

More insight can be obtained by examining the measured inductance ratio vectors in the αβ-plane. Fig. 6.22 shows scatter plots of the inductance ratios obtained for motor M2 together with circle fits that were again calculated using the Pratt method from [Che20]. Similar to the estimated positions, significant differences are observable mainly for mSVM2 and mSVM4. For mSVM2, the main difference is a noticeable shift of the circle's center in comparison to the other modulation strategies. For mSVM4, the measured data appears to be separated into three different segments, reaffirming the discontinuity caused by the sector-dependent measurement vectors. What the two modulation strategies have in common is that, different from the other strategies, measurement vectors in only two of the three physical axes are used for calculating the inductance ratios.

To further analyze the effect of the measurement vectors used, another experiment has been conducted. In this experiment, that involved also motor M3, a modulation

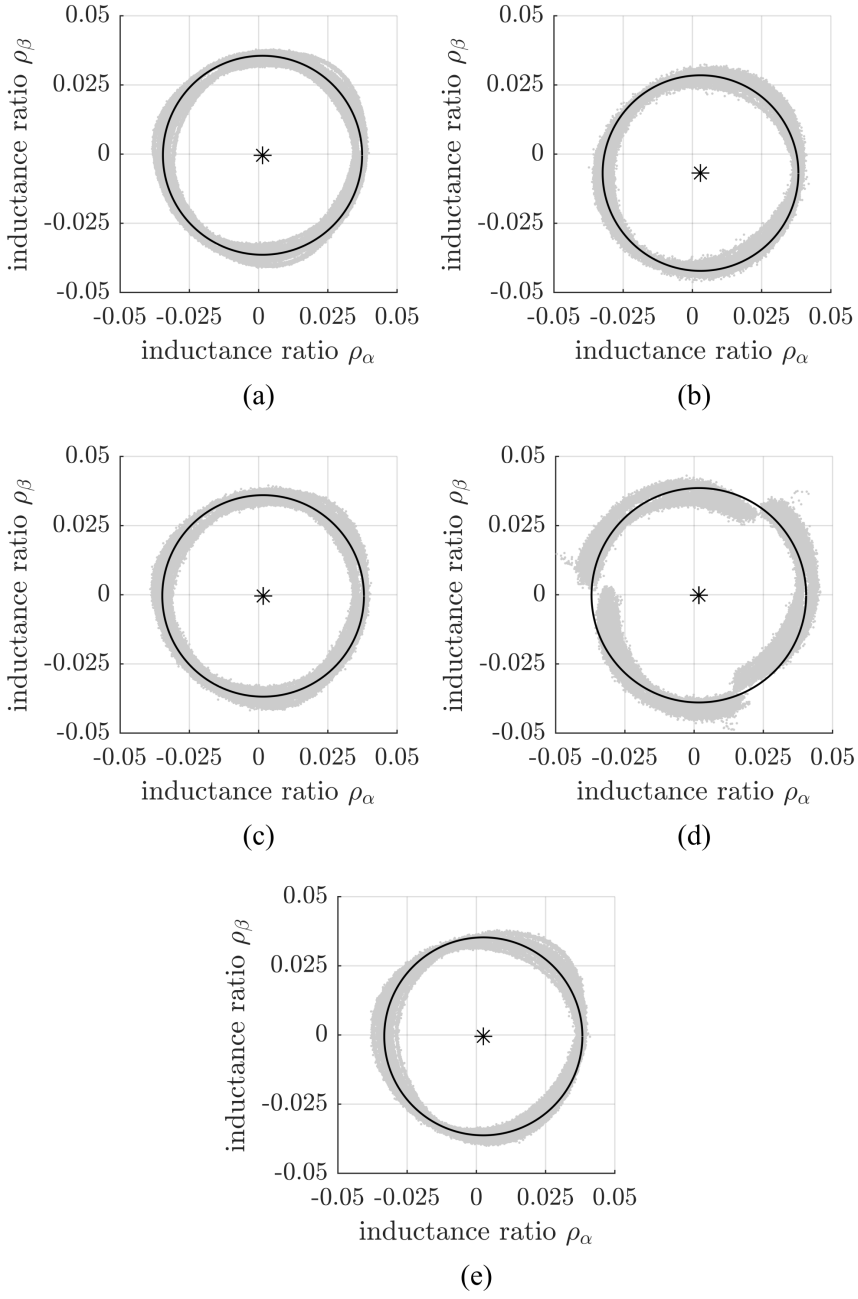

Figure 6.22.: Measured data and circle fits of the inductance ratio vector $\boldsymbol{\rho}$ in the $\alpha\beta$-plane, using different modulation strategies: (a) mSVM1, (b) mSVM2, (c) mSVM3b, (d) mSVM4, (e) mSVM5. Motor M2 is used, running at $n = 171.4\,\mathrm{r/min}$ with currents controlled to zero. From [SKMN21].

strategy similar to mSVM4 was used in which, however, the pairs of active measurement vectors were hold constant for the duration of a test. This allowed to acquire continuous measurements of the inductance ratios for each vector pair regardless of the reference voltage vector. Due to motor M3 being too small to be mounted on the drive train of the experimental setup, the experiment was conducted with only the motors. Accordingly, they were running in sensorless operation without external load and were speed-controlled to a very low speed of 1 r/min.

The results of this experiment are shown in Fig. 6.23. For motors M2 and M3, significant offsets can be observed in the calculated circle fits. Obviously, these depend systematically on the active measurement vectors used in the respective test. The varying offsets lead to discontinuities in the calculated values of ρ_α and ρ_β; which further lead to the discontinuities that have been observed in the estimated position. However, the dependence of the inductance ratios on the used measurement vectors clearly contradicts the linear model in (4.152) and can also not be explained by general common-mode errors in the measurement circuit which are anyway almost negligible as shown in the previous section. Instead, it demonstrates the limitations of the simplified model, which does not take into account the nonlinear properties of real machines. It seems likely that effects like saturation, hysteresis and/or eddy currents, in combination with the "asymmetric measurement" in only two of the three axes, lead to the observed offsets in the $\alpha\beta$-plane, while using measurement vectors in three axes seems to compensate for most of this behavior.

This assumption was further verified by using mSVM1 but considering only the measurements from two of the three axes. As shown in Fig. 6.24, a very similar effect on the inductance ratios could be observed. Note that the modulation pattern itself was not changed. Instead, the measurements from only two of the three axes were used in each case to calculate ρ_α and ρ_β and estimate the position.

However, the extent to which varying offsets occur showed to be strongly dependent on the machine. As can be seen in Fig. 6.23, motor M1 showed to be least affected. This might be due to the fact that this motor generally has higher inductance variations, which are also less current-dependent. However, further investigations are necessary to gain further insight into the physical background of the effect.

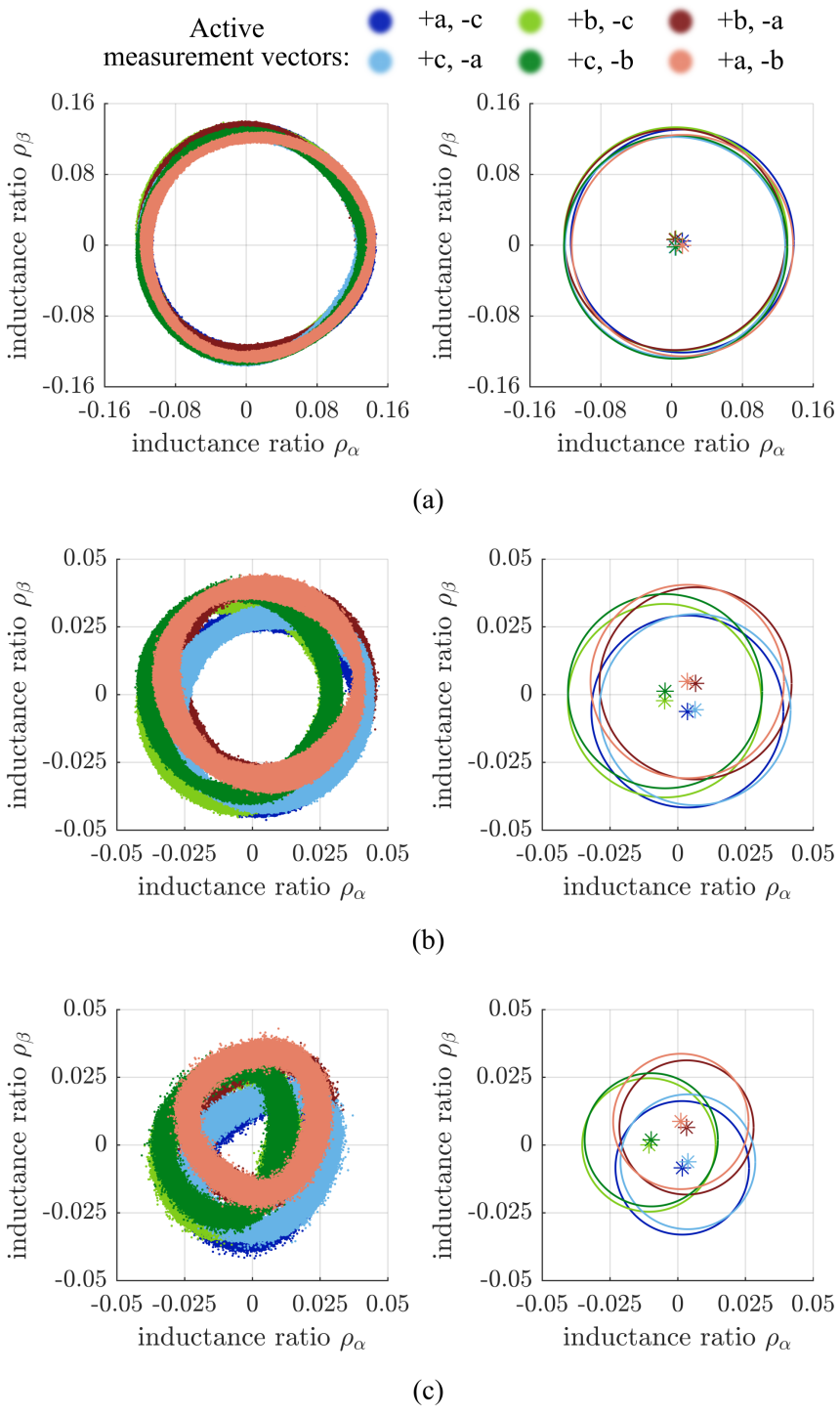

Figure 6.23.: Scatter plots (left) and corresponding circle fits (right) of inductance ratio vector $\boldsymbol{\rho}$ in the αβ-plane for (a) motor M1, (b) motor M2 and (c) motor M3, using modulation similar to mSVM4 but with fixed measurement vectors at $n = 1\,\mathrm{r/min}$ and no external load. For motors M2 and M3, the usage of active measurement vectors in only two axes leads to significant offsets. From [SKMN21].

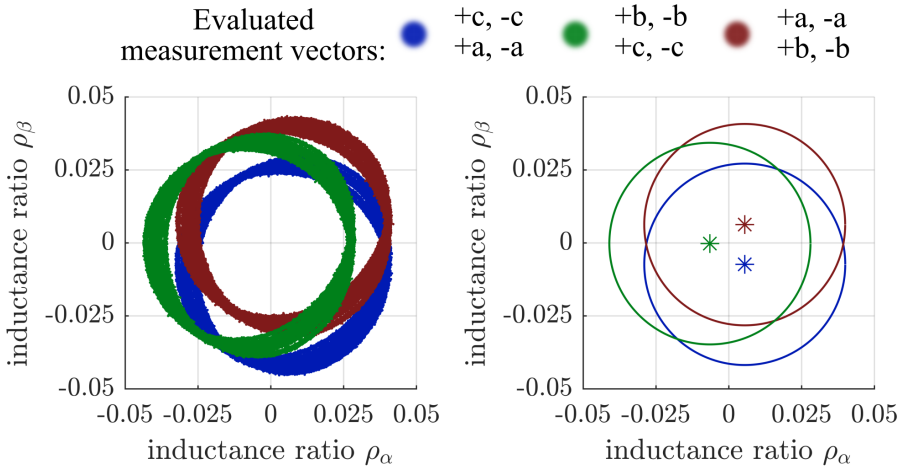

Figure 6.24.: Scatter plot and corresponding circle fit of inductance ratio vector $\boldsymbol{\rho}$ in the αβ-plane for motor M2 when using mSVM1 but discarding the measurements from one of the three axes at $n = 1\,\mathrm{r/min}$ and no external load. From [SKMN21]

6.8. Summary

To acquire the desired anisotropy information, minimum durations must be ensured for the discrete voltage vectors during which measurements of the zero-sequence voltage are to be made. With standard SVM, this requirement is not fulfilled in the high voltage regions and the regions interconnecting two neighboring voltage sectors. Modified modulation strategies are therefore necessary. Five different strategies were discussed and compared in this chapter, including two new strategies that use only the minimum number of three discrete voltage vectors for acquiring the inductance ratios. All investigated strategies place at least two measurement vectors in contiguous blocks that were referred to as measurement blocks. Such placement has the advantage that voltages caused by resistive imbalances and voltages induced by rotor movement are eliminated most effectively. Additionally, the positions of the measurement vectors within a switching period are fixed, which is useful for implementation.

Some fundamental properties of the five modified modulation strategies are summarized in Table 6.2. Moreover, the most important differences that were identified between the various strategies can be summarized under the following four aspects:

- **Achievable voltage utilization** – while the modified modulation strategies enable the measurement of two-dimensional anisotropy information for reference voltage vectors of any direction, they still reduce the achievable voltage magnitude. This limits in particular the speed up to which the machine can be operated. The respective voltage utilizations are illustrated in Fig. 6.25 for given ratios of $T_{\mathrm{mv}}/T_{\mathrm{sw}}$. mSVM1 and mSVM4 allow for the highest voltage utilization, whereas mSVM2 limits the voltage amplitude particularly significantly.

- **Update rate of the anisotropy vector** – mSVM1 and mSVM3 acquire only one component of the inductance ratio vector in the 'abc' reference frame per measurement block, whereas the others acquire the entire vector. The update rate can be described by the number of switching periods required to update the entire inductance ratio vector (= $T_{\mathrm{est}}/T_{\mathrm{sw}}$ in Table 6.2). mSVM2 and mSVM4 require only one switching period and thus the fewest to update the entire vector, whereas mSVM1 with six switching periods requires the most.

- **Harmonics in the line-to-line voltages** – they can lead in particular to audible noise. mSVM3 performs worst here as it introduces significant harmonics at

$f/f_{\mathrm{sw}} = \frac{1}{3}, \frac{2}{3}, \frac{4}{3}, \frac{5}{3}, \frac{7}{3}, \ldots$, whereas mSVM2 introduces the fewest harmonics below the switching frequency.

- **Differences in the estimation results** – experimental investigations showed that using measurement vectors in only two of the three physical axes can have a considerable effect on the inductance ratio vector $\boldsymbol{\rho}$. Offsets in the αβ-plane were observed which led to increased harmonics in the estimated position for mSVM2 and discontinuous position estimates for mSVM4. The offsets can be attributed to nonlinear properties of a machine and differed in intensity for the three investigated motors. The use of measurement vectors in all three axes, in contrast, seems to compensate the offsets almost completely in the case of the other strategies.

As can be concluded from the above, none of the strategies performs best under all aspects. The two newly proposed modulation strategies, mSVM4 and mSVM5, allow to both utilize a wide range of the DC link voltage and estimate the position with a high update rate. Both strategies also update the full inductance ratio vector with each measurement block which avoids inconsistencies at high rotor speeds. mSVM4 uses one zero vector and the two active vectors that are naturally used in standard SVM to measure the zero-sequence voltage during these. As a result, mSVM4 offers both the highest voltage utilization (for $T_{\mathrm{mv}}/T_{\mathrm{sw}} \leq 0.118$) and update rate. However, the sector-dependent measurement vectors can lead to varying offsets of $\boldsymbol{\rho}$ in the αβ-plane and therefore discontinuous position estimates. This is most noticeable at low speeds when the PLL does not provide much smoothing effect. mSVM5, on the other hand, inserts three active vectors that are evenly distributed in the αβ-plane. Because mSVM5 does not exhibit discontinuities in the estimated position but still offers relatively high voltage utilization and a good update rate, it is a well-balanced modulation strategy that does not show any significant weaknesses under any of the aspects considered. For these reasons, it is also selected for the further experimental investigations in the following chapter.

Table 6.2.: Fundamental properties of the five modified modulation strategies under investigation.

Abbreviation	mSVM1	mSVM2	mSVM3a / mSVM3b	mSVM4	mSVM5
References	[Jia00]	[TMH+11a]	[Man13]	-	-
Nr. of axes with active measurement vectors	3	2	3	2	3
Nr. of measurement vectors per T_{est}	6	4	6	3	3
$T_{\text{est}}/T_{\text{sw}}$	6	1	3	1	2
Voltage reduction factor in $T_{\text{mv}}/T_{\text{est}}$	6	6	6 / 9	1*	3
Voltage reduction factor in $T_{\text{mv}}/T_{\text{sw}}$	1	6	2 / 3	1*	1.5
Alignment in the modulation blocks	center	edge	edge	edge	center
	*: For $T_{\text{mv}}/T_{\text{sw}} \leq 0.118$, see section 6.3.1				

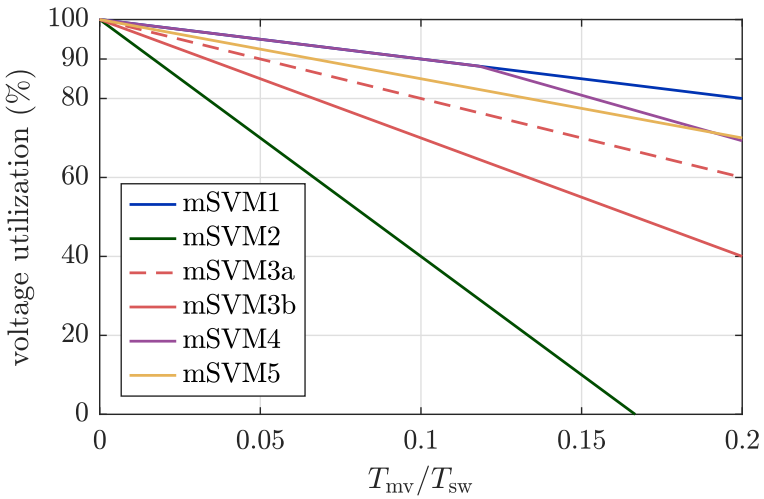

Figure 6.25.: Achievable voltage utilization without overmodulation for the investigated modulation strategies.

7. Experimental Results

In this chapter, experimentally obtained estimation results as well as the underlying inductance ratios are presented and analyzed for the motors M1 and M2. All experiments are conducted using mSVM5. The majority of the experiments are conducted at stationary operation, which are shown in the first section. Thereafter, results under transient conditions are shown.

7.1. Stationary Operation

The following experiments were performed through automated test procedures with the previously described experimental test setup. The load motor is speed-controlled to different constant speeds while the motor under test is operated with current control. At each speed, the current in the d- or q-axis is varied in equidistant steps, with the current in the respective other axis held at zero. The reference position is used to control the motor under test.

7.1.1. Inductance Ratios and Estimation Results at Selected Operating Points

Fig. 7.1 shows measured inductance ratios $\kappa_{\Delta,\mathrm{a}}$, $\kappa_{\Delta,\mathrm{b}}$, $\kappa_{\Delta,\mathrm{c}}$ for motor M1 and motor M2 at 10 r/min and zero current. Data from one electrical period is shown, however, the data was collected over several mechanical revolutions. Figs. 7.2 and 7.3 show the corresponding inductance ratio vectors $\boldsymbol{\rho}$ in the αβ-plane that are calculated from the inductance ratios in the first half of these periods as well as the resulting estimated positions and position errors. The locus of the inductance ratio vector is additionally shown for a full mechanical period. In the latter case, the inductance ratio vector completes one revolution per half electrical period. Each one follows a slightly different path and therefore creates a, at least apparently, wider trail in the αβ-plane. The estimated position from before the PLL-type filter is shown. Already at this point, it is evident that the estimation

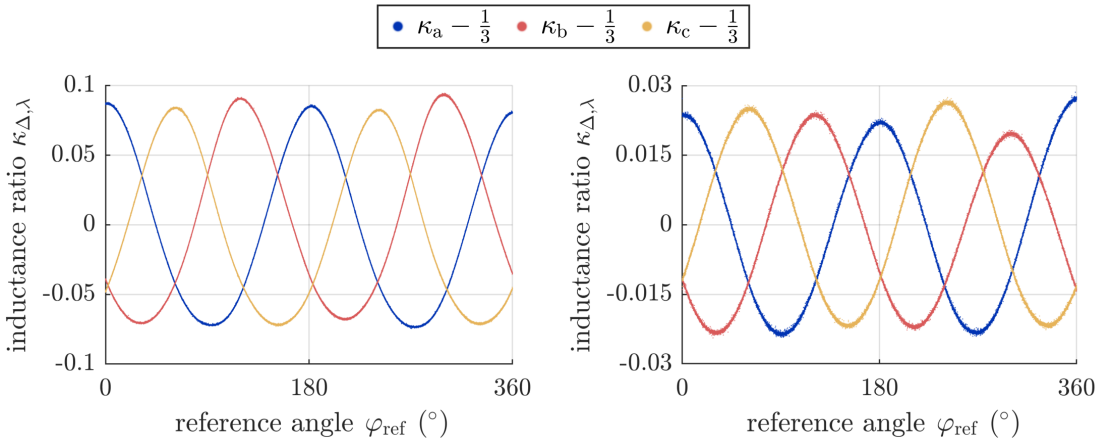

Figure 7.1.: Inductance ratios $\kappa_{\Delta,\lambda}$ at $n = 10\,\mathrm{r/min}$ and zero current: (left) motor M1, (right) motor M2.

error includes only small amounts of noise and is instead mainly caused by harmonic components.

Fig. 7.4 shows motor M2 at a relatively high speed of 3000 r/min and a q-axis current of 3.2 A. It can be seen that the results are not fundamentally different, even though an offset occurs in the estimated position that is mainly current-related. Compared to 7.3, larger magnitudes can be observed for $\boldsymbol{\rho}$.

7.1.2. Harmonic Analysis of Measured Inductance Ratios

Before the influence of the speed and q-axis current on the estimated position is investigated in detail, a harmonic analysis on the measured inductance ratios for motors M1 and M2 shall be conducted. For this purpose, a discrete Fourier transform (DFT) is performed on the inductance ratios over the reference rotor angle, which makes it a spatial DFT. With a DFT over time, speed fluctuations in the drive train could distort the signals and thus falsify the results. Since the regularly sampled reference angles are not equidistant, a non-uniform DFT must be used.

According to [Wik21], a non-uniform DFT is defined as

$$\mathcal{F}_k(x) = X_k = \sum_{h=0}^{N-1} x_h e^{-2\pi j w_h f_k} \tag{7.1}$$

where x_h are the samples of the signal to be transformed, which will be κ_α or ρ_α here. It

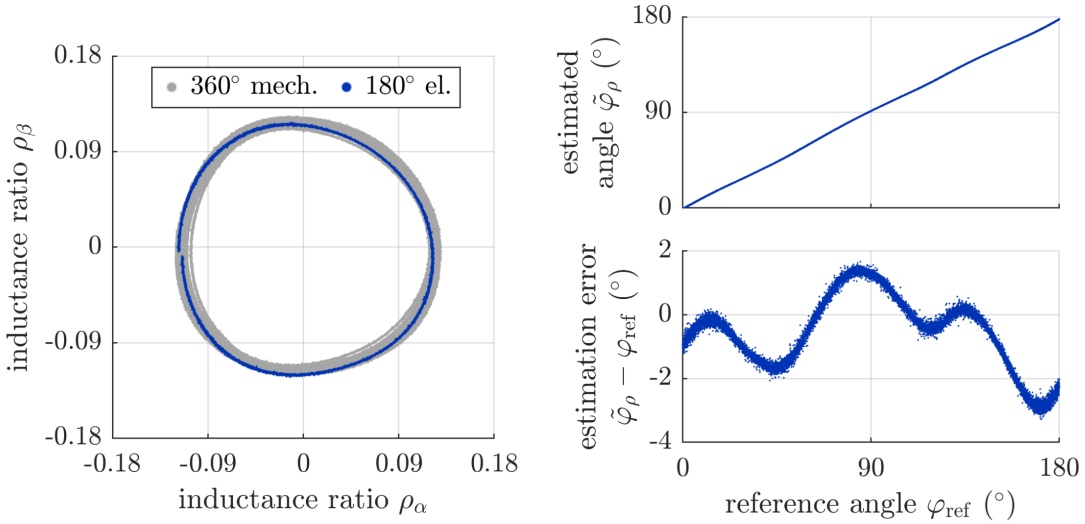

Figure 7.2.: Inductance ratios and resulting position estimates for motor M1, n = 10 r/min, $i_\mathrm{q} = 0$.

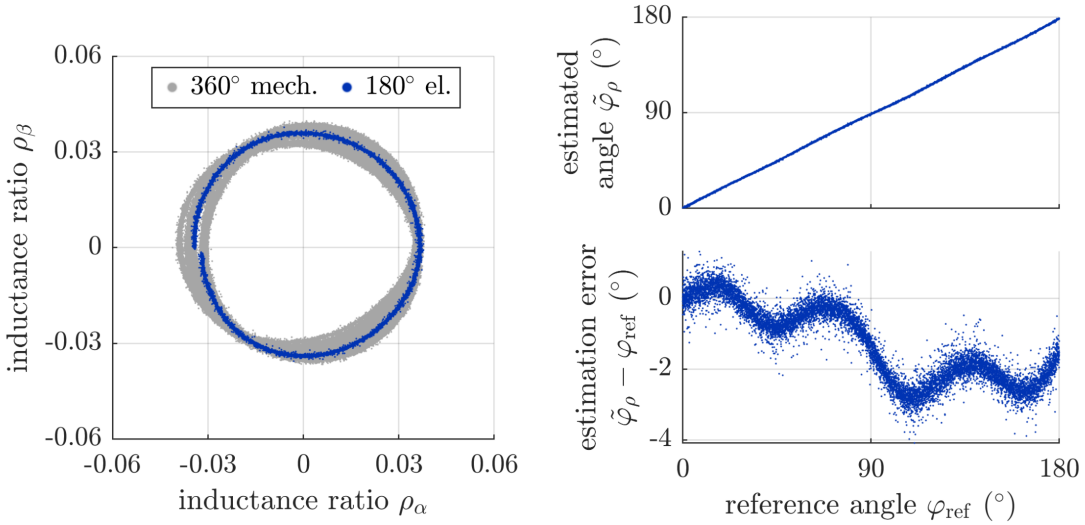

Figure 7.3.: Inductance ratios and resulting position estimates for motor M2, n = 10 r/min, $i_\mathrm{q} = 0$.

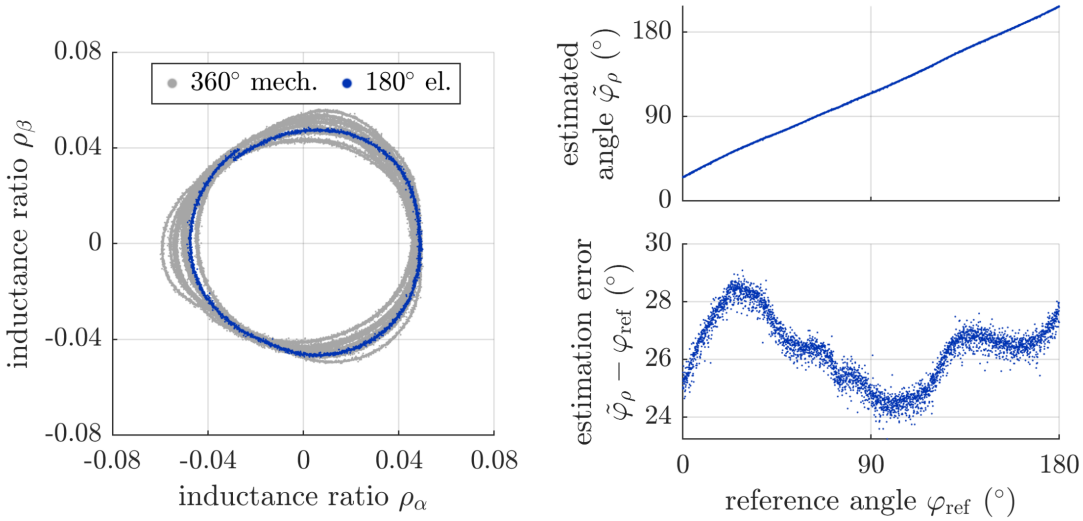

Figure 7.4.: Inductance ratios and resulting position estimates for motor M2, n = 3000 r/min, i_{q} = 3.2 A.

was verified that the β-component contains almost identical harmonics (except for the offset component at $k = 0$), so that a separate presentation is omitted. Further, the index h ranges from 0 to $N - 1$, where N is the total number of samples. w_h are the sample points. To perform a spatial DFT over the mechanical reference position, we set

$$2\pi w_h = \varphi_{\mathrm{m,ref},h} \tag{7.2}$$

where $\varphi_{\mathrm{m,ref},h}$ is the mechanical reference position at the sample point w_h. f_k are the spatial frequencies. Assuming stationary operation, i.e. constant speed and constant d- and q-axis currents, the measured anisotropy signals are periodic signals that repeat with each mechanical revolution. Accordingly, only integer harmonics of the mechanical spatial frequency can appear, so that f_k can be chosen as k (see NUDFT type II in [Wik21]). The final transformation is given by

$$\mathcal{F}_k(x) = \sum_{h=0}^{N-1} x_h e^{-j\varphi_{\mathrm{m,ref},h}k} \tag{7.3}$$

$$= \sum_{h=0}^{N-1} x_h \cdot \left[\cos\left(-\varphi_{\mathrm{m,ref},h} \cdot k\right) + j \cdot \sin\left(-\varphi_{\mathrm{m,ref},h} \cdot k\right)\right] . \tag{7.4}$$

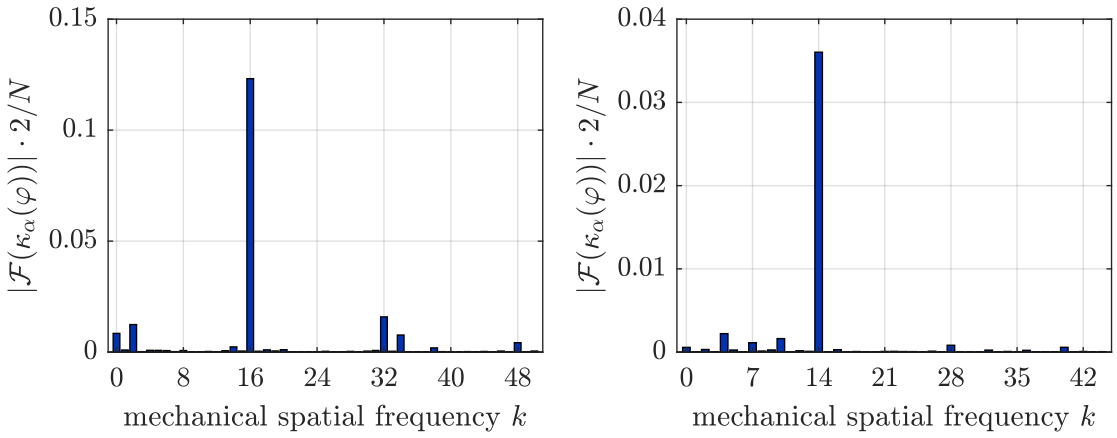

Figure 7.5.: Spatial DFT of κ_α: (left) motor M1 (right) motor M2; $n = 10\,\mathrm{r/min}$ and current controlled to zero for both motors.

Resulting amplitude spectra of κ_α are shown in Fig. 7.5. For both motors, the main harmonic component is located at $k = 2p$ as expected. Especially for motor M1, there is also a distinct component located at $k = 4p$. Besides, further harmonics of the mechanical position exist that are not multiples of the number of polepairs. As discussed earlier, these components are usually neglected, because they are difficult to compensate.

In the following, only harmonics of the electrical spatial frequency $f_k = k/p$ shall be considered, in particular the 2^{nd} and 4^{th} harmonics. By looking at the spectra of κ_α and ρ_α in Figs. 7.6 and 7.7, one can see that the main difference between the two lies in the amplitude of the 4^{th} harmonic component, whereas the other components remain more or less unchanged. Besides the 2^{nd} and 4^{th} harmonic component and the stationary offsets, there are only small secondary anisotropies visible for the electrical spatial frequencies, such as a 6^{th} harmonic for motor M1 and a fundamental component for motor M2.

Since the machine currents have a strong impact on the measured inductance ratios, the dependence of the 2^{nd} and 4^{th} harmonic coefficients on the d- and q-axis current are shown in Figs. 7.8 and 7.9. Obviously the 4^{th} harmonic component is smaller in $\boldsymbol{\rho}$ compared to $\boldsymbol{\kappa}$ in almost all of the shown operating points. The only exceptions are operating points with negative d-axis current for motor M2 where the magnitude of the inductance ratio vector becomes very small. Again, one can observe that the d-axis current has a strong impact on the amplitudes of the harmonic components due to saturation. This is particularly true for motor M2, where the amplitude of the 2^{nd} harmonic component increases by more than a factor of three at $i_\mathrm{d} = 4\,\mathrm{A}$ and vanishes

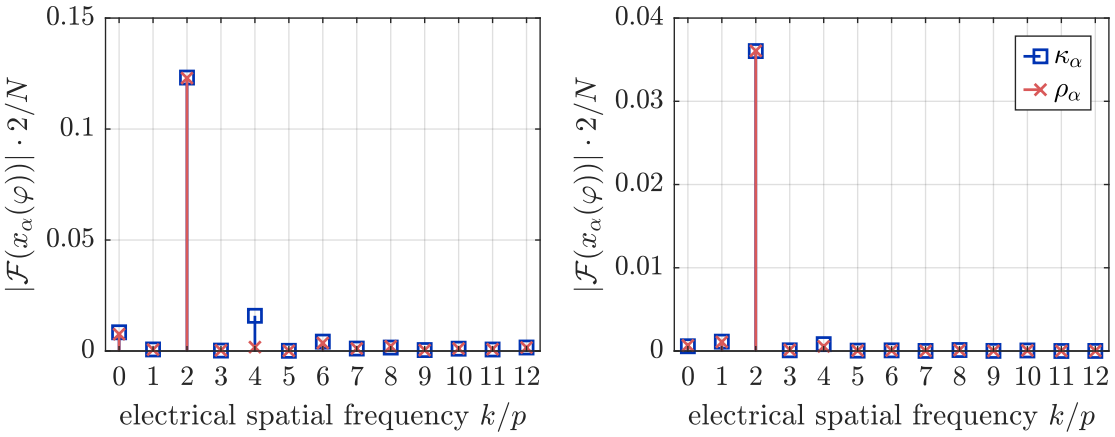

Figure 7.6.: Electrical spatial DFT of κ_α and ρ_α: (left) motor M1 (right) motor M2; $n = 10\,\mathrm{r/min}$ and current controlled to zero for both motors.

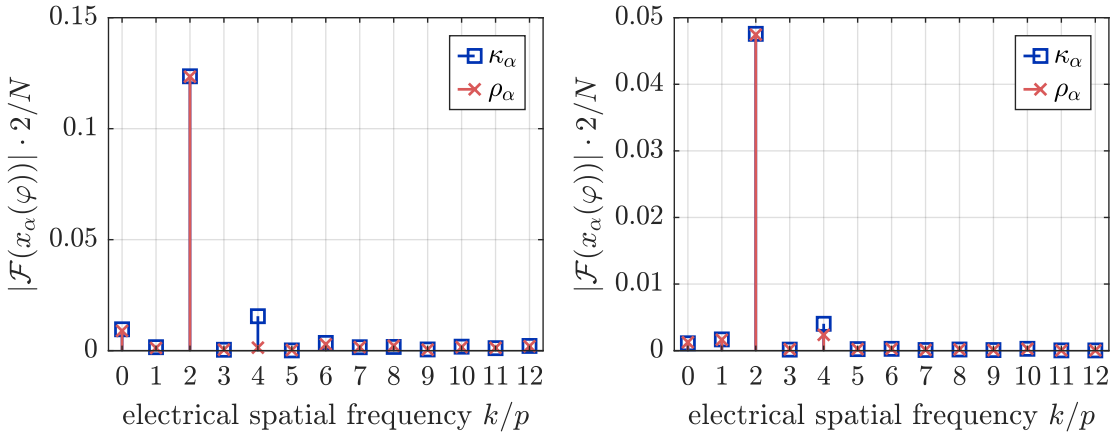

Figure 7.7.: Electrical spatial DFT of the κ_α and ρ_α under load: (left) motor M1 at $i_\mathrm{q} = 1.5\,\mathrm{A}$, (right) motor M2 at $i_\mathrm{q} = 3.2\,\mathrm{A}$; $n = 10\,\mathrm{r/min}$ for both motors.

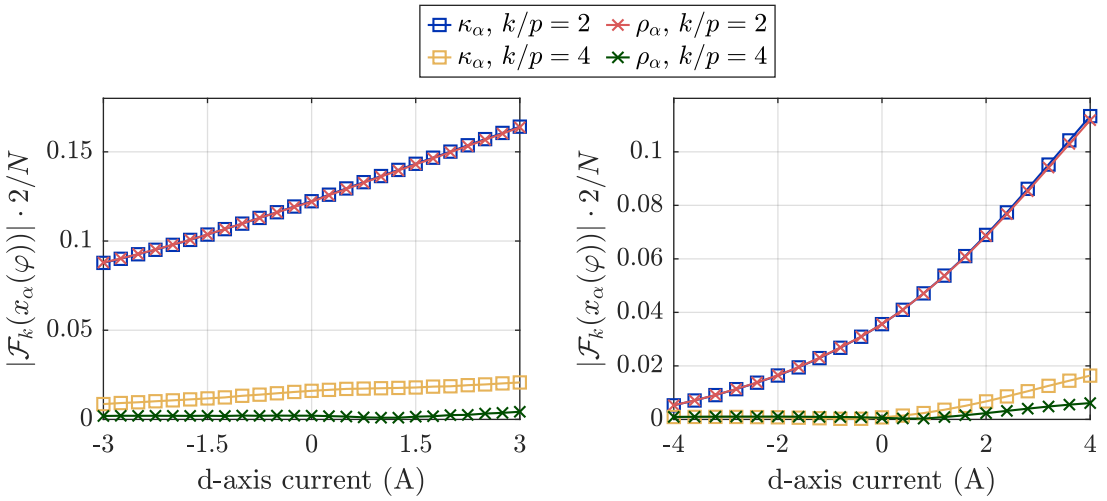

Figure 7.8.: 2^{nd} and 4^{th} harmonic coefficients for κ_α and ρ_α at different d-axis currents and $n = 10\,\text{r/min}$. (left) motor M1, (right) motor M2

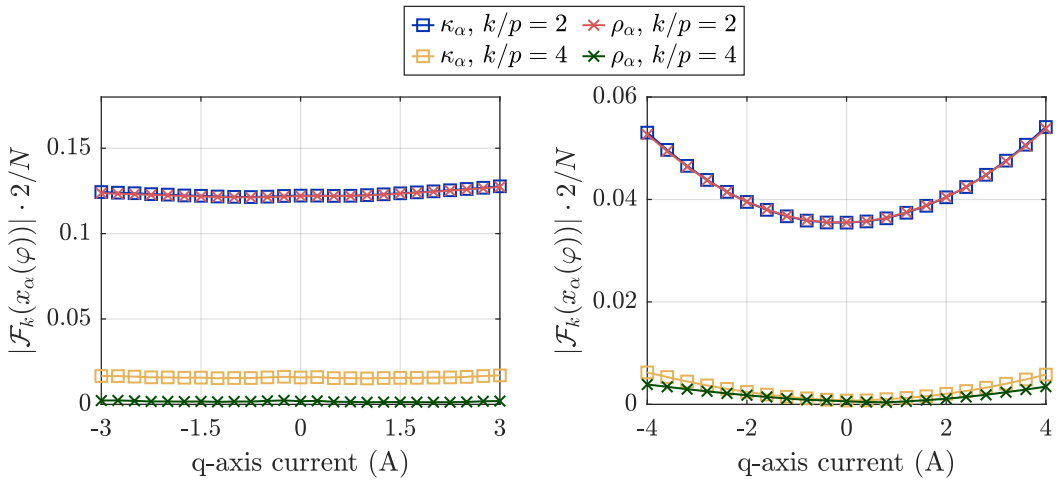

Figure 7.9.: 2^{nd} and 4^{th} harmonic coefficients for κ_α and ρ_α at different q-axis currents and $n = 10\,\text{r/min}$. (left) motor M1, (right) motor M2.

almost entirely at $i_\text{d} = -4\,\text{A}$. The influence of the q-axis current is considerably smaller. For motor M1, it is almost nonexistent, whereas for motor M2, the amplitudes of the 2^{nd} and 4^{th} harmonic increase considerably with increasing absolute value.

7.1.3. Analysis of the Estimation Error

In this section, an analysis of the estimation error under stationary operation is conducted. Two main objectives are pursued. The first is to break down the estimation error into stationary offsets, harmonic estimation errors and noise, and to enable an assessment of the contributions of each. The second objective is to investigate the influence of the rotor speed and the q-axis current on these parts of the estimation error.

The mean, minimum and maximum estimation errors at different current levels and for two different speeds are shown in Fig. 7.10 for motor M1 and in Fig. 7.11 for motor M2. Current-dependent shifts in the estimated position are clearly visible and can be attributed to magnetic saturation effects. Again, it can be seen that motor M2 is evidently more prone to saturation effects because the shifts are much larger. It should be emphasized that the span between the minimum and maximum estimation error is mainly caused by harmonic components as a result of secondary anisotropiess, which will become more apparent in the course of this section. Additionally, the rotor speed also shows to have some effect on the estimated position, however thanks to the elimination of low frequency terms in the zero-sequence voltage its impact on the mean estimation error is relatively small compared to that of the q-axis current.

However, an interesting aspect has been found when examining the speed dependence of the estimation error. In Fig. 7.12, the mean estimation error over speed is shown

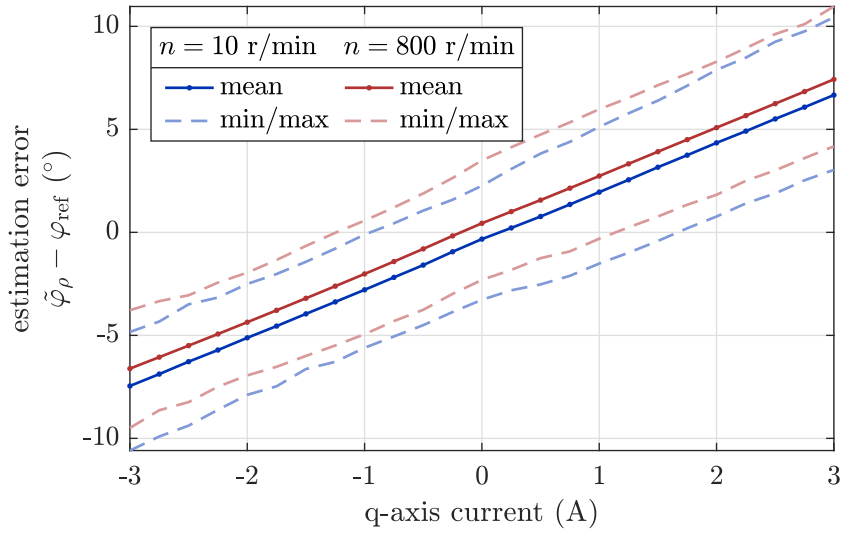

Figure 7.10.: Mean, minimum and maximum estimation errors at different q-axis currents and two different speeds for motor M1.

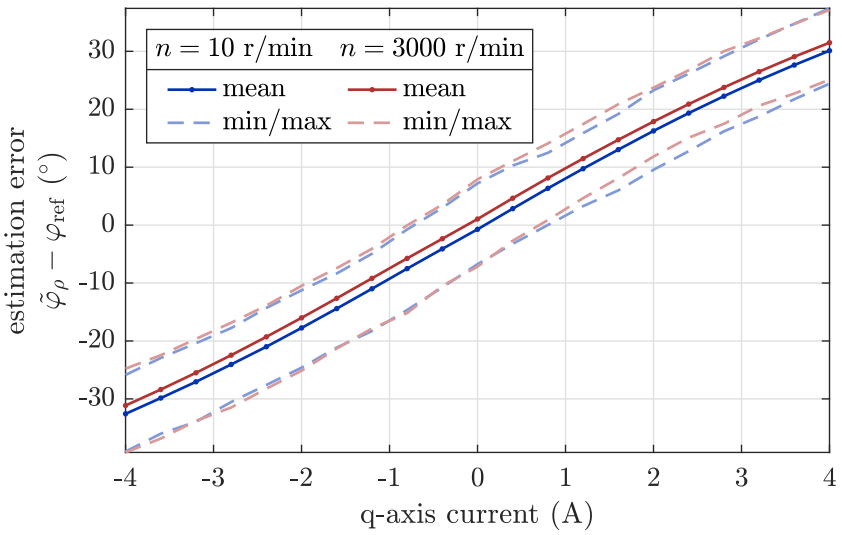

Figure 7.11.: Mean, minimum and maximum estimation errors at different q-axis currents and two different speeds for motor M2.

for motor M2 at zero current. One can observe a clear discontinuity at $n = 0\,\mathrm{r/min}$. Obviously, the rotational direction has a noticeable impact, which may be unexpected at first. The reason for this is probably magnetic hysteresis, since the magnetization history depends on the direction of movement and leads to a hysteresis also in the estimated position. For further verification, an experiment was conducted where the motor under test was rotated back and forth at low speeds of $\pm 1\,\mathrm{r/min}$ by the load motor, again with currents controlled to zero. The resulting reference and estimated angles are shown in Fig. 7.13. Especially in the estimation error, a hysteretic behavior becomes clearly visible. Moreover, the differences between positive and negative rotational direction are in the same range as the jump in Fig. 7.12. For motor M1, a similar effect was observed. However, it is somewhat surprising in Fig. 7.12 that the estimation error changes its trend already slightly before the directional inversion, which cannot yet be explained and offers room for further investigation.

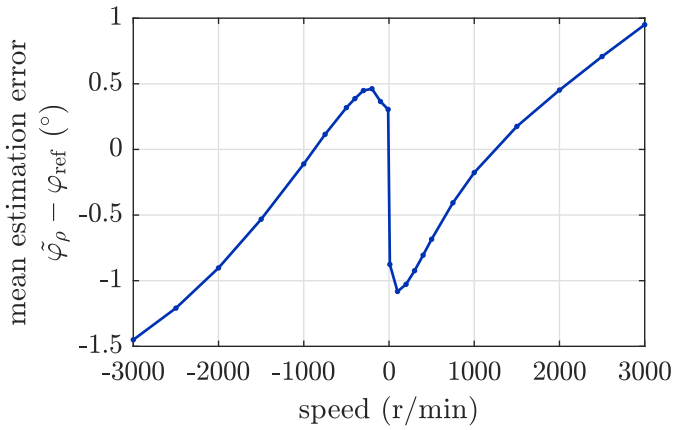

Figure 7.12.: Discontinuity of the estimation error at reversal of direction for motor M2 at $i_\mathrm{d} = i_\mathrm{q} = 0$, likely caused by magnetic hysteresis.

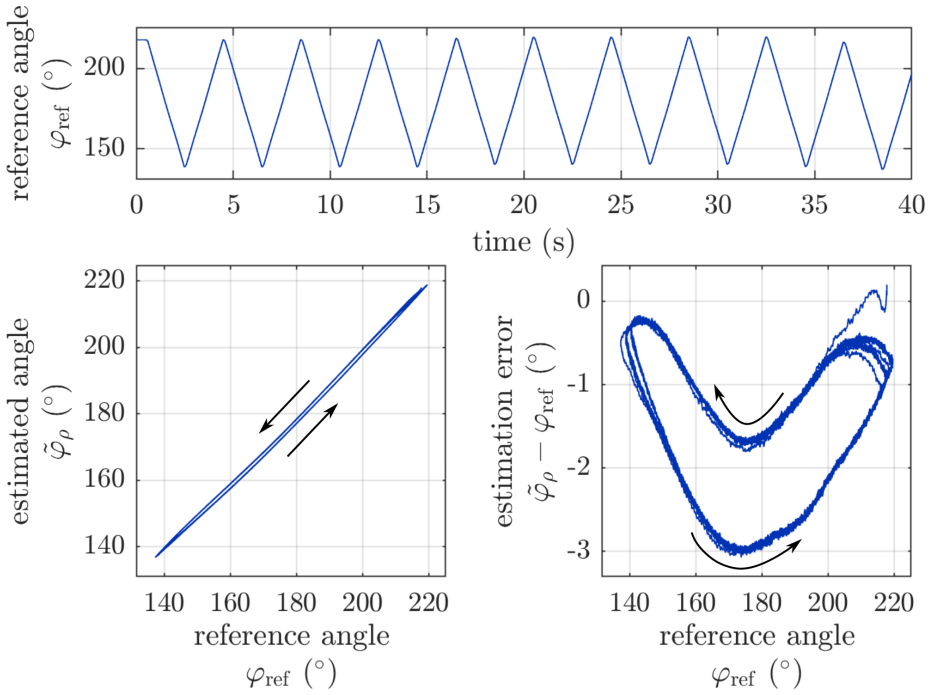

Figure 7.13.: Hysteresis effect in the estimated position for motor M2 which is rotated back and forth at $n = \pm 1$ r/min and whose current is controlled to zero.

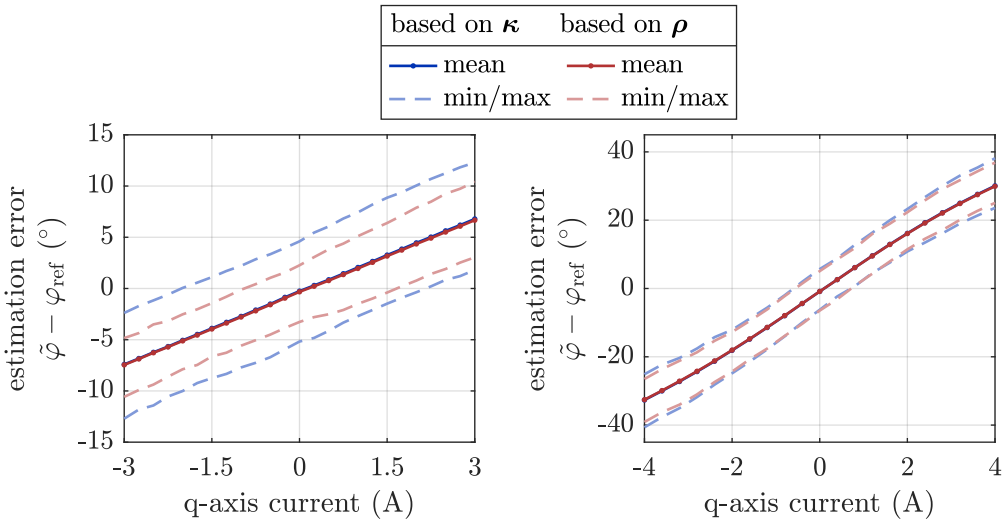

Figure 7.14.: Effect of the estimation algorithm on the estimation error ($n = 10\,\mathrm{r/min}$). (left) motor M1, (right) motor M2.

The measurements in the previous section have already shown that 4φ-components are indeed smaller in $\boldsymbol{\rho}$ compared to $\boldsymbol{\kappa}$ for the used motors. As discussed in chapter 5, the estimation should therefore preferably be based on one of the functions given in (5.21) and (5.28). Fig. 7.14 supports this statement by showing mean, minimum and maximum estimation errors that result from $\tilde{\varphi}_{\boldsymbol{\kappa}}$ and $\tilde{\varphi}_{\boldsymbol{\rho}}$. For motor M1, the estimation function involving the transformed inductance ratios $\boldsymbol{\rho}$ clearly leads to significant reductions in the spread between minimum and maximum estimation errors. For motor M2, the use of this estimation function still leads to improvements, however the effect is smaller due to the generally smaller variations in the inductance ratios.

Besides stationary offsets, the estimation error features harmonic components and noise. Under ideal conditions, the harmonic errors are deterministic and repeat with each mechanical revolution, whereas the noise is random. Both can be seen in Figs. 7.15 and 7.16, where the influence of the q-axis current and the speed is also visible. Obviously, both current and speed affect the harmonic estimation errors. Accordingly, functions for the compensation of harmonic errors should take both into account. Additionally, it can be seen that Motor M1 exhibited generally smaller harmonic errors that are also less dependent on current and speed.

Lastly, the noise in the estimation error shall be quantified. For this purpose, the noise was separated by high-pass-filtering the estimation error. Similar to the harmonic

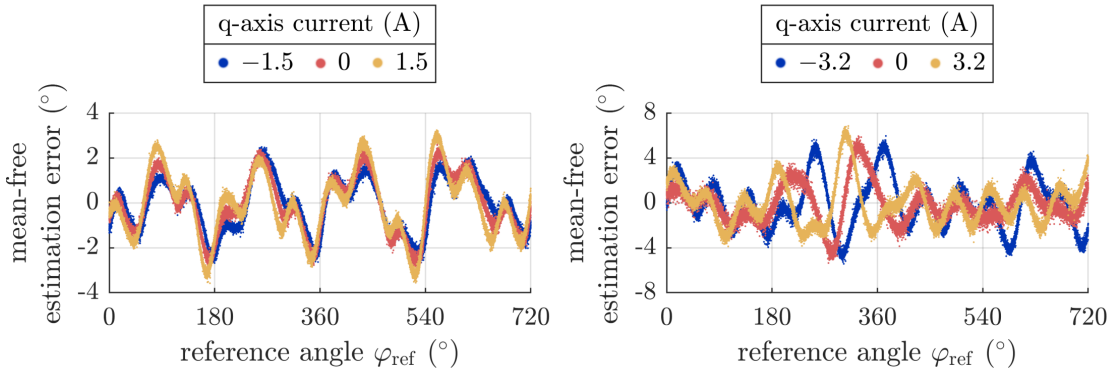

Figure 7.15.: Mean-free estimation error at different currents for $n = 10\,\mathrm{r/min}$: (left) motor M1, (right) motor M2.

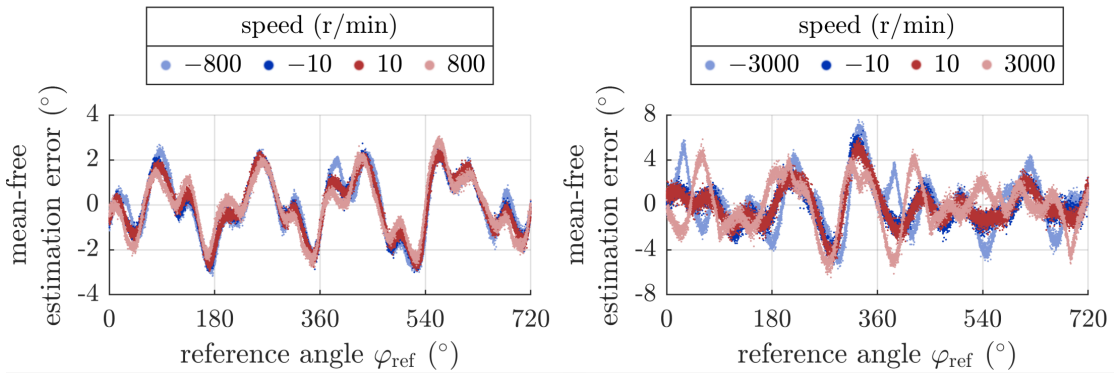

Figure 7.16.: Mean-free estimation error at different speeds for $i_{\mathrm{q}} = 10\,\mathrm{r/min}$: (left) motor M1, (right) motor M2.

analysis, the filtering was performed over the reference position and not over time. Using the *highpass*-function in MATLAB, harmonic components with a spatial frequency of less than 60/(360 °el), i.e. harmonic components that feature less than 60 periods per electrical period were removed from the estimation error. As can be seen in the example in Fig. 7.17, this leads to signals that are well representative of the noise in the estimation error. To quantify the noise, standard deviations of these high-pass filtered signals were calculated. The results are shown in Fig. 7.18. It can be seen that the standard deviations are less than 0.1° for motor M1 and less than 0.27° for motor 2 for the considered points of operation, which again confirms that the technique provides position estimates with low noise content.

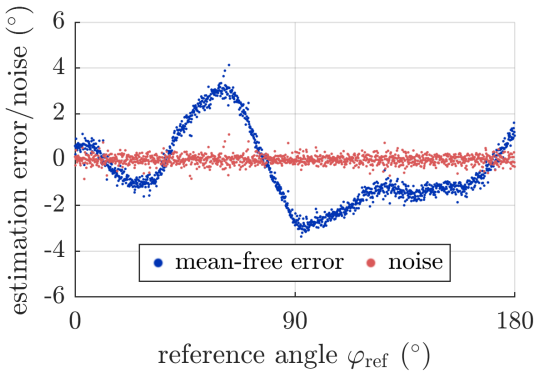

Figure 7.17.: Estimation noise obtained through high-pass filtering, for motor M2 at 1000 r/min, $i_{\mathrm{q}} = 0$.

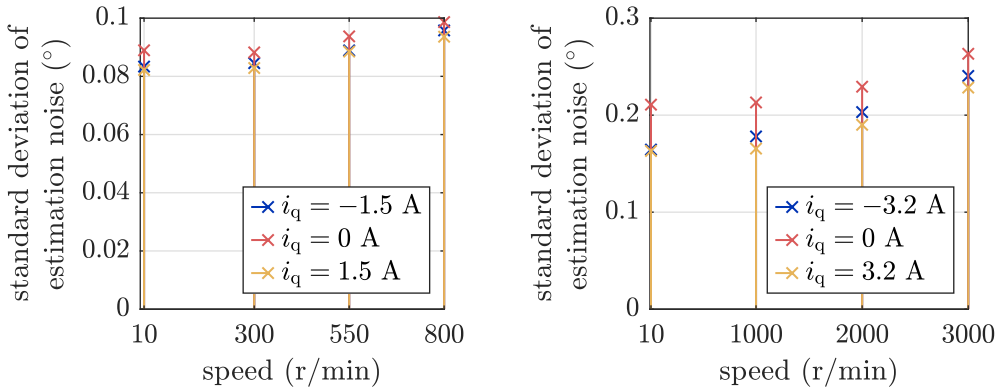

Figure 7.18.: Estimation noise at different speeds and q-axis currents for (left) motor M1, (right) motor M2.

7.2. Transient Operation

In this section, the behavior of a sensorless speed control under speed and load torque steps is demonstrated using motor M2. One experiment each is performed using the measured and the estimated position for controlling the motor under test to allow a comparison of the resulting behavior. The estimated position is compensated using a look-up table with linear interpolation over the q-axis current to remove the stationary shifts in the position. The lookup table includes mean errors similar to the ones shown in Fig. 7.11, with the exception that mean errors from both $n = 10$ r/min and $n = -10$ r/min

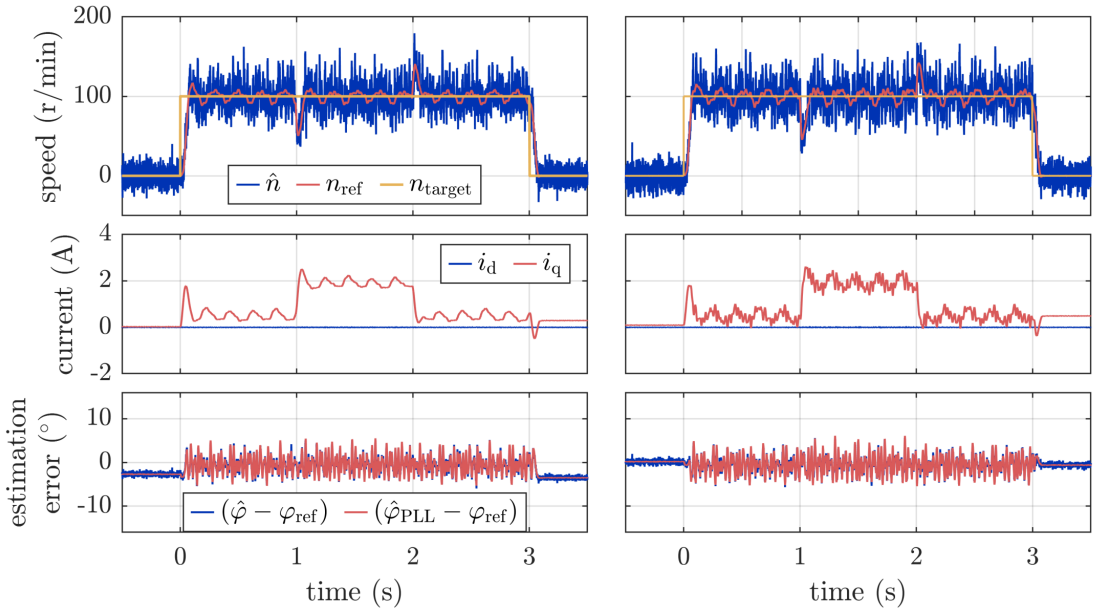

Figure 7.19.: Speed step from 0 to 100 r/min and back and torque step of 0.05 N m and back: (left) controlled using the reference position, (right) controlled using the estimated position.

were averaged. For better distinction, a current-compensated estimated position

$$\hat{\varphi} = \tilde{\varphi}_{\rho} - \varphi_{\mathrm{comp}}(i_{\mathrm{q}}) \tag{7.5}$$

is introduced. This position is fed into the PLL-type filter discussed in section 5.3, which then returns $\hat{\varphi}_{\mathrm{PLL}}$ and the estimated speed $\hat{n}$, which are used in the speed and current control loop. The reference speed is obtained via a similarly parameterized PLL-type filter.

Results at low speed are shown in Fig. 7.19, where the following procedure was used. At $t = 0$, a speed step from 0 to 100 r/min is commanded to the motor under test. From $t = 1\,\mathrm{s}$ to $t = 2\,\mathrm{s}$, an additional torque of $M_{\mathrm{ld}} = 0.05\,\mathrm{N\,m}$ is applied via the load motor. At $t = 3\,\mathrm{s}$, the target speed is returned to zero. It can be seen that the machine behaves as one would expect and that the curves for speed, q-axis current and estimation error are very similar between the control using the estimated and the control using the measured position. Generally, the speed obtained from the estimated position has significantly higher fluctuations as a result of noise and, when the machine is rotating,

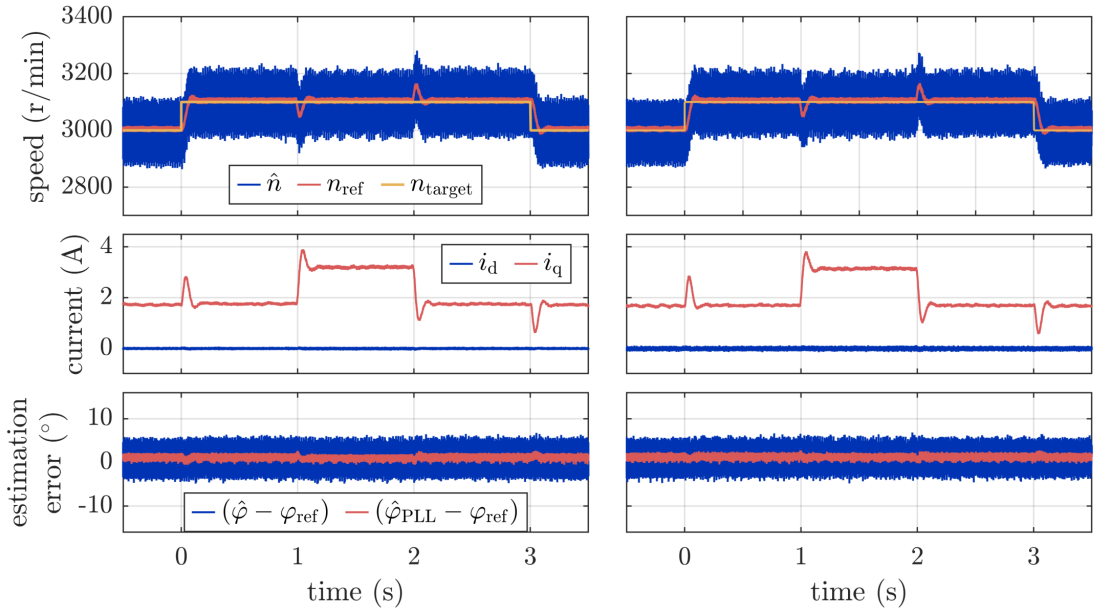

Figure 7.20.: Speed step from 3000 to 3100 r/min and back and torque step of 0.05 N m and back: (left) controlled using the reference position, (right) controlled using the estimated position.

the harmonic parts in the estimated position. The latter result also in higher fluctuations in the q-axis current, since the speed controller tries to compensate for the supposed speed fluctuations. It is clear that the harmonics in the estimated position largely affect the maximum bandwidth of the speed control that can be set before instabilities occur. Compensation of secondary anisotropies is therefore useful also with regard to achieving high dynamics in speed control.

The same experiments were performed for a speed step from 3000 to 3100 r/min and back. An identical load torque was applied in this case. As can be seen in Fig. 7.20, the PLL-type filter considerably smoothes out the harmonic errors at high speeds like this. At the same time, the speed fluctuations caused by the harmonic errors are also less significant in relation to the total speed. As a result, the behavior in this case is almost identical for operation with and without sensor.

7.3. Summary

The shown experimental results demonstrated the capabilities of an anisotropy-based position estimation using the zero-sequence voltage, which provides anisotropy signals and position estimates with low noise content. As could be expected from other works in the field of anisotropy-based position estimation, the anisotropy signals show clear dependencies on the d- and q-axis currents which can be attributed to saturation effects. Most importantly, significant shifts appear in the mean estimated position with increasing q-axis current. Speed and rotational direction also have a measurable effect on the mean estimated position, but it is rather small compared to the current dependence. Beyond stationary offsets, the remaining estimation errors are mainly of harmonic nature and, therefore, repeat with each mechanical revolution. By definition, this is the error that is caused by secondary anisotropies. The harmonic parts of the estimation error showed to vary with speed and current so that possible compensation functions should ideally take both into account. In comparison to harmonic parts, the contribution of noise to the total error was significantly lower.

In accordance with the theoretical considerations presented earlier, it could be observed that the harmonic components of 4φ are clearly reduced in $\boldsymbol{\rho}^{\mathrm{s}}$ compared to $\boldsymbol{\kappa}^{\mathrm{s}}$. As a result, harmonic estimation errors in $\tilde{\varphi}_{\rho}$ are reduced over $\tilde{\varphi}_{\kappa}$ as well. Therefore, using this estimation function is clearly preferable for the used motors and, according to the analysis in sections 4.3.1 and 5.1, the same should apply to all motors that are sufficiently well represented by the general wave inductance model and that have small variations in the mutual inductances in the 'abc' reference frame.

The performance of the position estimation has been demonstrated also under transient conditions. The only differences that could be observed between the use of the measured position and the estimated position for the control of the machine can be attributed to harmonic errors in the estimated signals that arise from secondary anisotropies. To further improve control behavior, a determination and compensation of secondary anisotropies, taking into account relevant factors such as currents and speed, is therefore recommendable for practical implementation. In general, however, the estimation technique is clearly suitable for use in field-oriented control from standstill to high speed and under varying load conditions.

8. Conclusion

To enable position estimation for PMSMs at any speed, anisotropy-based techniques that measure the zero-sequence voltage are an interesting alternative to the more common techniques that use current measurements. Measuring the zero-sequence voltages requires access to the neutral point and is therefore not immediately applicable to most commercially available machines. However, in applications where the neutral point can be made accessible, it can enable position estimation with high signal-to-noise ratio with manageable effort and cost. This work focused on an excitation through modified pulse patterns, which does not require the use of analog bandpass-filters and leads to a high update rate for the anisotropy signals while also avoiding audible noise at frequencies significantly below the switching frequency. In the following, the main results of this work are summarized.

8.1. Summary

Physically, the technique under investigation is based on magnetic anisotropies, generally caused by rotor geometry and magnetic saturation, which generate a zero-sequence voltage in the machine phases. The zero-sequence voltage was analyzed using a simplified mathematical model in the two stationary reference frames 'abc' and '$\alpha\beta 0$'. This provided insights into general relations of the anisotropy information and allowed basic comparisons with current-based techniques. The anisotropy information in the zero-sequence voltage expresses itself in position-dependent inductance ratios. Generally, the anisotropy information contained in these inductance ratios is not identical to the one obtainable via current measurements and – at least theoretically – anisotropy information may even be available only by one kind of measurement but not by the other. As a consequence that is probably of greater practical relevance, small differences in the estimated position are to be expected, depending in particular on the variations of self- and mutual inductances in the 'abc' reference frame. A further difference exists in the fact that measurements of the zero-sequence voltage provide only one-dimensional

information per time instant as opposed to two-dimensional information in the case of current measurements. This has implications, in particular, on the requirements placed on the number and orientation of voltage vectors that need to be applied. At least when compared with current-based techniques using the concept of arbitrary injection, the requirements on the applied voltage vectors are more strict for techniques based on the zero-sequence voltage.

The measurement of the zero-sequence voltage can advantageously be performed by subtracting a reference voltage generated by an artificial neutral point. The housing of the machine should preferably be grounded through a connection with low inductance or, if possible, electrically isolated from its environment. Otherwise, disturbances that arise for example from other motors may couple onto the neutral point through parasitic capacitances within the motor and corrupt ongoing measurements. Generally, parasitic capacitances from within the motor, but also from the connected cables or the measurement circuit can lead to overshoot and ringing at the neutral point in combination with the machine inductances. Therefore, care sould be taken not to unnecessarily increase parasitic capacitances at the neutral point.

As part of the analytical considerations, two simplified anisotropy models were discussed which both allow a parameter-free calculation of the estimated position. The more common one leads to harmonic components of 4φ in the inductance ratios and therefore requires less trivial functions to calculate the correct position. Two such functions were considered: a function based on intermediate signals of sinusoidal shape and a function with reduced computational cost. In particular for motors that feature more pronounced magnetic anisotropy, these can help to reduce harmonic errors in the estimated position.

As with most anisotropy-based techniques, the estimated electrical position contains an uncertainty of 180°. To resolve the uncertainty, an initial polarity detection procedure should be performed at the startup of the drive. A suitable procedure that evaluates the magnitude of the (transformed) inductance ratio vector during the application of positive and negative voltage pulses in the estimated d-axis has been proposed. Since the procedure uses the same anisotropy information used for the position estimation technique, additional measurements are avoided.

The necessity of using modified modulation strategies to ensure minimum durations for the measurements of the zero-sequence voltage was discussed and five modulation strategies were investigated in detail. For this purpose, a systematic that divides the switching periods into measurement and modulation blocks has been introduced. Different aspects have been considered in the investigation, including in particular the achievable

voltage utilization, the update rate of the anisotropy vector, the introduction of harmonics in the line-to-line voltages and differences in the estimation results. Concerning the estimation results, differences were especially identified between the strategies that use measurement vectors in all of the three physical axes and those that use measurement vectors in only two axes. In the latter case, offsets of the inductance ratio vectors in the αβ-plane were observed which can be attributed to nonlinear properties of a machine. The investigated modulation strategies included two novel modulation strategies that calculate the inductance ratios using a contiguous block of three measurement vectors. The first one, mSVM4, allows for an excellent voltage utilization and update rate of the position information, but can lead to discontinuities in the position estimates due to the use of only two active measurement vectors. The second one, mSVM5, still features relatively high voltage utilization and a good update rate with no significant weaknesses in any of the examined properties.

Using mSVM5, the estimation technique has been validated using two low power machines: a custom prototype PMSM and a commercially available PMSM. The influence of rotor speed as well as the one of the d- and q-axis currents were analyzed. Generally, the anisotropy signals and the estimated position exhibited low noise content and relatively little dependence on rotor speed. In particular the low noise content is seen as a key benefit of the considered technique. Standard deviations of less than 0.1° for motor M1 and less than 0.27° for motor M2 were observed in the estimation noise isolated through high-pass filtering. Even with only a relatively simple angle compensation in dependence of the q-axis current, the motors could successfully be controlled in sensorless operation under varying speed and load conditions. However, in order to achieve a behavior that is on par with high-resolution position sensors, the challenge lies particularly in proper compensation of harmonic errors. For motors that feature more significant secondary anisotropies than the motors used here, this aspect is even more important. This compensation of so-called secondary anisotropies is, however, a common issue for all anisotropy-based techniques, therefore one can refer to solutions already existing in the scientific literature. Ideally, the compensation should take into account dependencies on current and speed. It should be stressed that, when designing a motor for anisotropy-based techniques, particular attention should be paid to the harmonics of the mechanical position which are not integer multiples of the electrical position, since these are particularly difficult to compensate.

8.2. Outlook

In this thesis, the investigations have been performed with the motors as 'black boxes'. The investigations revealed effects that are not covered by the simplified mathematical model, such as a dependence of the measured inductance ratios on the used voltage vectors or hysteretic effects in the estimated position. Future research could additionally investigate the physical background through simulations using the finite-elements method.

Additional potential is seen in the development of efficient procedures to identify secondary anisotropies and, in combination, current and speed dependencies of given machines. The use of the anisotropy signals for purposes beyond the control of the machine, such as condition monitoring, represents another interesting area for future research.

A. Motors Used in Experiments

In Table A.1, further information is provided for the three PMSMs that were used for the investigations within this work. The values for M2 and M3 are taken from the manufacturer's data sheets [DS1; DS2]. It should be noted that both manufacturers specify their motors for operation with six-step block commutation. Assuming a sinusoidal waveform for the permanent magnet flux linkage, Ψ_{PM} was approximated as

$$\Psi_{\mathrm{PM}} = \frac{k_{\mathrm{M}} \cdot \pi}{p \cdot \sqrt{3} \cdot 3} \tag{A.1}$$

(see [Bol12, pp. 445-450]) for motors M2 and M3. Here, k_{M} is the torque constant provided in the respective data sheet. All three motors are depicted in Fig. A.1.

Table A.1.: Motors used in experiments

Motor	M1	M2	M3
Manufacturer	-	Faulhaber	maxon
Motor type	prototype conveyor roller motor	4221G024BXTR	EC 20 flat 9V sensorless
Nominal voltage	24 V	24 V	9 V
Nominal power	70 W	100 W	3 W
Nominal speed	800 r/min	4180 r/min	4140 r/min
Nominal current	1.5 A	3.17 A	0.478 A
Phase resistance R	1.1 Ω	0.37 Ω	4.7 Ω
Mean inductance L_{Σ}	0.435 mH	0.332 mH	0.65 mH
Permanent magnet flux linkage Ψ_{PM}	9.89 mV s	3.26 mV s	1.27 mV s
Number of polepairs p	8	7	4

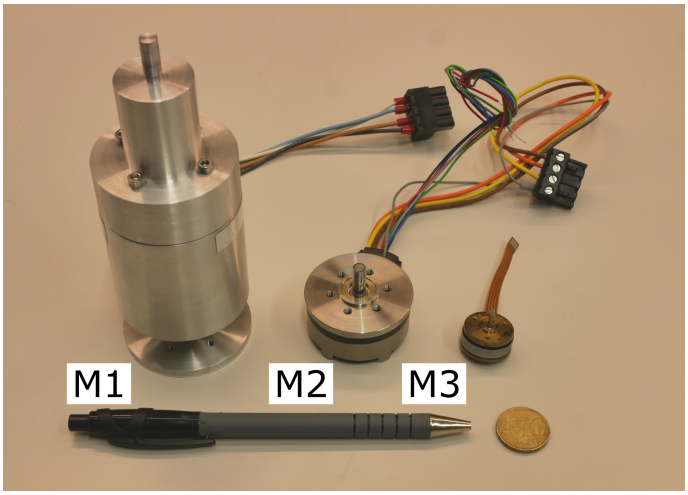

Figure A.1.: Motors used in experiments, with pen and 10 euro cent coin as size comparison.

B. Nomenclature

Conventions:

X, x	variable
X, x	designation
$\boldsymbol{X}$	matrix
$\boldsymbol{x}$	vector

General:

$\boldsymbol{I}$	identity matrix
j	imaginary unit

Machine model:

$\boldsymbol{u}$	phase voltage vector
$\boldsymbol{u}_{\mathrm{term}}$	terminal voltage vector
$\boldsymbol{i}$	phase current vector
$\boldsymbol{\Psi}$	total flux linkage vector
$\boldsymbol{\Psi}_{\mathrm{s}}$	vector of flux linkages due to stator currents
$\boldsymbol{\Psi}_{\mathrm{PM}}$	vector of flux linkage vector due to permanent magnets
$\boldsymbol{L}$	inductance matrix
$\boldsymbol{R}$	resistance matrix
$\boldsymbol{T}_{\mathrm{C}}$	Clarke transformation matrix
$\boldsymbol{T}_{\mathrm{P}}$	clockwise rotation matrix (Park transformation)
$\boldsymbol{J}$	clockwise 90° rotation matrix
J	moment of inertia
φ	electrical rotor angle
φ_{m}	mechanical rotor angle
ω	electrical angular frequency

Reference frames - superscripts for vectors and matrices:

p	physical reference frame 'abc'
s	stator reference frame 'αβ0'
r	rotor reference frame 'dq0'
s$*$	reduced stator reference frame 'αβ'
r$*$	reduced rotor reference frame 'dq'

Reference frames - subscripts for scalars:

a, b, c	components of physical 'abc' reference frame
α, β, 0	components of the 'αβ0' reference frame
d, q, 0	components of the 'dq0' reference frame

Space vector modulation:

$\boldsymbol{u}_0$, $\boldsymbol{u}_1$, ... $\boldsymbol{u}_7$	discrete voltage vectors of a two-level three-phase switching inverter
u_{DC}	DC link voltage
f_{sw}	switching frequency
T_{sw}	switching period $T_{\mathrm{sw}} = 1/f_{\mathrm{sw}}$
T_{mv}	duration for each measurement vector
T_{est}	estimation period

Anisotropy-based position estimation:

L_0	mean value of self inductances in the 'abc' reference frame
L_2	variation of self inductances in the 'abc' reference frame
L_{m0}	mean value of mutual inductance in the 'abc' reference frame
L_{m2}	variation of mutual inductances in the 'abc' reference frame
L_Δ	variation of inductances in the 'αβ' reference frame
$L_{\Delta 0}$	variation of mutual inductances with the zero-sequence axis
L_Σ	mean value of self inductances in the 'αβ' reference frame
$L_{\Sigma 0}$	(mean value of) self inductance in the zero-sequence axis
r	inductance variation ratio, $r = L_\Delta/L_\Sigma$ (for case $L_\Delta = L_{\Delta 0}$)
u_{N}	voltage between machine neutral point and inverter reference
u_{AN}	voltage between artificial neutral point and inverter reference
u_{NAN}	voltage between machine and artificial neutral point
Δu_{NAN}, Δu_0	differences of u_{NAN} or u_0 within short time periods
$\boldsymbol{u}_{\mathrm{NAN,dir}}$	directional zero-sequence voltage, $\boldsymbol{u}_{\mathrm{NAN,dir}} = \boldsymbol{\kappa} u_{\mathrm{DC}}$
$\boldsymbol{Y}$	admittance matrix
$\boldsymbol{\kappa}$	inductance ratio vector
$\boldsymbol{\rho}$	transformed inductance ratio vector
$\boldsymbol{\kappa_\Delta}$	anisotropic part of $\boldsymbol{\kappa}$
$\boldsymbol{\rho_\Delta}$	anisotropic part of $\boldsymbol{\rho}$
φ_{ref}	reference electrical rotor angle from position sensor
$\tilde{\varphi}$	raw estimated electrical rotor angle
$\hat{\varphi}$	estimated electrical rotor angle after current-correction function
$\hat{\varphi}_{\mathrm{PLL}}$	estimated electrical rotor angle after current-compensation and PLL

Acronyms:

ADC	analog-to-digital converter
BEMF	back-electromotive force
FEM	finite element method
INFORM	Indirect Flux detection by Online Reactance Measurement
MOSFET	metal–oxide–semiconductor field-effect transistor
mSVM	modified space vector modulation
PLL	phase-locked loop
PMSM	permanent magnet synchronous machine
SVM	space vector modulation

Bibliography

[AFG+16] A. Athavale, H. Flieh, B. S. Gagas, T. S. Slininger, and R. D. Lorenz, "Machine design for self-sensing," in *2016 IEEE Symposium on Sensorless Control for Electrical Drives (SLED)*, Nadi, Fiji, Jun. 2016, pp. 1–10. DOI: 10.1109/SLED.2016.7518789.

[BCC+14] F. Betin *et al.*, "Trends in electrical machines control: Samples for classical, sensorless, and fault-tolerant techniques," *IEEE Industrial Electronics Magazine*, vol. 8, no. 2, pp. 43–55, Jun. 2014. DOI: 10.1109/MIE.2014.2313752.

[BD11] F. Briz and M. W. Degner, "Rotor position estimation," *IEEE Industrial Electronics Magazine*, vol. 5, no. 2, pp. 24–36, Jun. 2011. DOI: 10.1109/MIE.2011.941118.

[BDGG05] F. Briz, M. W. Degner, P. Garcia, and J. M. Guerrero, "Rotor position estimation of AC machines using the zero-sequence carrier-signal voltage," *IEEE Transactions on Industry Applications*, vol. 41, no. 6, pp. 1637–1646, Nov. 2005. DOI: 10.1109/TIA.2005.857469.

[BDGL04] F. Briz, M. W. Degner, P. Garcia, and R. D. Lorenz, "Comparison of saliency-based sensorless control techniques for AC machines," *IEEE Transactions on Industry Applications*, vol. 40, no. 4, pp. 1107–1115, Jul. 2004. DOI: 10.1109/TIA.2004.830768.

[BG10a] O. Benjak and D. Gerling, "Review of position estimation methods for IPMSM drives without a position sensor part II: Adaptive methods," in *The XIX International Conference on Electrical Machines - ICEM 2010*, Rome, Italy, Sep. 2010, pp. 1–6. DOI: 10.1109/ICELMACH.2010.5607980.

[BG10b] O. Benjak and D. Gerling, "Review of position estimation methods for PMSM drives without a position sensor, part III: Methods based on saliency and signal injection," in *2010 International Conference on Electrical Machines and Systems*, Incheon, Korea, Oct. 2010, pp. 873–878.

[Bol12] E. Bolte, *Elektrische Maschinen*. Berlin, Germany: Springer Berlin Heidelberg, 2012, ISBN: 978-3-642-05485-3. DOI: 10.1007/978-3-642-05485-3.

[BPJT97] F. Blaabjerg, J. Pedersen, U. Jaeger, and P. Thoegersen, "Single current sensor technique in the DC link of three-phase PWM-VS inverters: A review and a novel solution," *IEEE Transactions on Industry Applications*, vol. 33, no. 5, pp. 1241–1253, Oct. 1997. DOI: 10.1109/28.633802.

[Che20] N. Chernov, *Circle fit (Pratt method)*, MATLAB Central File Exchange, Apr. 2020. [Online]. Available: https://de.mathworks.com/matlabcentral/fileexchange/22643-circle-fit-pratt-method (visited on 04/21/2020).

[CLK11] J. Cordier, P. Landsmann, and R. Kennel, "The influence of magnetic hysteresis on HF injection based inductance calculation," *2011 IEEE Energy Conversion Congress and Exposition*, 2011. DOI: 10.1109/ECCE.2011.6063829.

[CST99] A. Consoli, G. Scarcella, and A. Testa, "A new zero frequency flux position detection approach for direct field oriented control drives," in *1999 IEEE Industry Applications Conference*, Phoenix, AZ, USA, Oct. 1999, pp. 2290–2297. DOI: 10.1109/IAS.1999.799163.

[CSTT00] A. Consoli, G. Scarcella, G. Tutino, and A. Testa, "Zero frequency rotor position detection for synchronous PM motors," in *2000 IEEE 31st Annual Power Electronics Specialists Conference*, Galway, Ireland, 2000, pp. 879–884. DOI: 10.1109/PESC.2000.879930.

[DL98] M. Degner and R. Lorenz, "Using multiple saliencies for the estimation of flux, position, and velocity in AC machines," *IEEE Transactions on Industry Applications*, vol. 34, no. 5, pp. 1097–1104, Sep. 1998. DOI: 10.1109/28.720450.

[DS1] Dr. Fritz Faulhaber GmbH & Co. KG, *Faulhaber 4221 ... BXT R*, data sheet, Feb. 2018. [Online]. Available: https://www.faulhaber.com/fileadmin/Import/Media/EN_4221_BXTR_DFF.pdf (visited on 05/19/2020).

[DS2] maxon motor ag, *maxon EC 20 flat 3W*, catalog page, Mar. 2021. [Online]. Available: https://www.maxongroup.co.uk/medias/sys_master/root/8882562138142/EN-21-287.pdf (visited on 03/12/2022).

[GMKN19] E. Grasso, R. Mandriota, N. König, and M. Nienhaus, "Analysis and exploitation of the star-point voltage of synchronous machines for sensorless operation," *Energies*, vol. 12, no. 24 (article number 4729), Jan. 2019. DOI: 10.3390/en12244729.

[HJP97] J. Holtz, J. Jiang, and H. Pan,
"Identification of rotor position and speed of standard induction motors at low speed including zero stator frequency,"
in *IECON'97 23rd International Conference on Industrial Electronics, Control, and Instrumentation*, vol. 2, New Orleans, LA, USA, Nov. 1997, pp. 971–976.

[HL03] D. G. Holmes and T. A. Lipo,
Pulse Width Modulation for Power Converters: Principles and Practice.
Hoboken, NJ, USA: John Wiley & Sons, Oct. 2003,
ISBN: 978-0-471-20814-3.

[HN00] L. Harnefors and H.-P. Nee, "A general algorithm for speed and position estimation of AC motors," *IEEE Transactions on Industrial Electronics*, vol. 47, no. 1, pp. 77–83, Feb. 2000. DOI: 10.1109/41.824128.

[Hol06] J. Holtz, "Initial rotor polarity detection and sensorless control of PM synchronous machines," in *Conference Record of the 2006 IEEE Industry Applications Conference Forty-First IAS Annual Meeting*,
vol. 4, Tampa, FL, USA, Oct. 2006, pp. 2040–2047.
DOI: 10.1109/IAS.2006.256816.

[HP02] J. Holtz and H. Pan, "Elimination of saturation effects in sensorless position controlled induction motors," in *Conference Record of the 2002 IEEE Industry Applications Conference. 37th IAS Annual Meeting*,
vol. 3, Pittsburgh, PA, USA, Oct. 2002, pp. 1695–1702.
DOI: 10.1109/IAS.2002.1043762.

[HP04] J. Holtz and H. Pan, "Acquisition of rotor anisotropy signals in sensorless position control systems," *IEEE Transactions on Industry Applications*, vol. 40, no. 5, pp. 1379–1387, Oct. 2004.
DOI: 10.1109/TIA.2004.834053.

[ITSA16] Y. Iwaji, R. Takahata, T. Suzuki, and S. Aoyagi, "Position sensorless control method at zero-speed region for permanent magnet synchronous motors using the neutral point voltage of stator windings,"
IEEE Transactions on Industry Applications, vol. 52, no. 5,
pp. 4020–4028, Sep. 2016. DOI: 10.1109/TIA.2016.2582118.

[JH97] J. Jiang and J. Holtz, "Accurate estimation of rotor position and speed of induction motors near standstill," in *Proceedings of Second International Conference on Power Electronics and Drive Systems*,
vol. 1, Singapore, May 1997, pp. 1–5.

[Jia00] J. Jiang, *Drehgeberlose feldorientierte Regelung für Asynchronmaschinen bei Ständerfrequenz Null*. Aachen, Germany: Shaker, 2000,
ISBN: 978-3-8265-7534-1.

[JL95] P. L. Jansen and R. D. Lorenz, "Transducerless position and velocity estimation in induction and salient AC machines," *IEEE Transactions on Industry Applications*, vol. 31, no. 2, pp. 240–247, Mar. 1995. DOI: 10.1109/28.370269.

[KEZ91] J. Kolar, H. Ertl, and F. Zach, "Influence of the modulation method on the conduction and switching losses of a PWM converter system," *IEEE Transactions on Industry Applications*, vol. 27, no. 6, pp. 1063–1075, Nov. 1991. DOI: 10.1109/28.108456.

[KKB02] M. P. Kaźmierkowski, R. Krishnan, and F. Blaabjerg, *Control in Power Electronics: Selected Problems* (Academic Press Series in Engineering). Amsterdam, Netherlands: Academic Press, 2002, ISBN: 978-0-12-402772-5.

[KKS+11] S. Kim, Y. Kwon, S. Sul, J. Park, and S. Kim, "Position sensorless operation of IPMSM with near PWM switching frequency signal injection," in *8th International Conference on Power Electronics - ECCE Asia*, Jeju, Korea (South), May 2011, pp. 1660–1665. DOI: 10.1109/ICPE.2011.5944422.

[KN17] S. Kleen and M. Nienhaus, "Impact of the embedding of magnets on a sensorless drive method," in *Innovative Small Drives and Micro-Motor Systems; 11th GMM/ETG-Symposium*, Saarbrücken, Germany, Sep. 2017, pp. 1–5.

[Kri01] R. Krishnan, *Electric Motor Drives — Modeling, Analysis, and Control*. Upper Saddle River, NJ, USA: Prentice Hall, Feb. 2001, ISBN: 0-13-091014-7.

[Lan14] P. Landsmann, "Sensorless control of synchronous machines by linear approximation of oversampled current," Dr.-Ing. dissertation, Technische Universität München, Munich, Germany, Jun. 2014.

[Lan15] P. Landsmann, "Anisotropie-basierte Schätzung der Rotorlage," in *Elektrische Antriebe—Regelung von Antriebssystemen*, D. Schröder, Ed., Berlin, Germany: Springer, 2015, pp. 943–984, ISBN: 978-3-642-30096-7. DOI: 10.1007/978-3-642-30096-7_15.

[LKH03] M. Linke, R. Kennel, and J. Holtz, "Sensorless speed and position control of synchronous machines using alternating carrier injection," in *IEEE International Electric Machines and Drives Conference, 2003. IEMDC'03.*, vol. 2, Jun. 2003, pp. 1211–1217. DOI: 10.1109/IEMDC.2003.1210394.

[Man13] C. Mantala, "Sensorless control of brushless permanent magnet motors," Dr.-Ing. dissertation, University of Bolton, Bolton, UK, 2013. [Online]. Available: http://ubir.bolton.ac.uk/625/ (visited on 09/03/2018).

[MSG+17] T. Müller, C. See, A. Ghani, A. Bati, and P. Thiemann, "Direct flux control – sensorless control method of PMSM for all speeds – basics and constraints," *Electronics Letters*, vol. 53, no. 16, pp. 1110–1111, 2017. DOI: 10.1049/el.2017.1772.

[MT94] N. Matsui and T. Takeshita, "A novel starting method of sensorless salient-pole brushless motor," in *Proceedings of 1994 IEEE Industry Applications Society Annual Meeting*, vol. 1, Denver, CO, USA, Oct. 1994, pp. 386–392. DOI: 10.1109/IAS.1994.345475.

[NHHS14] T. Nenning, M. Hofer, M. Hutterer, and M. Schrödl, "Setup with two self-sensing magnetic bearings using differential 3-active INFORM," presented at the 22nd International Conference on Magnetically Levitated Systems and Linear Drives, Aug. 2014, pp. 689–692.

[NKPK15] A. Niederer, G. Knecht, S. Paulus, and M. Koerner, "Control device and method for determining the rotor angle of a synchronous machine," U.S. Patent 9214882B2, Dec. 2015. [Online]. Available: https://patents.google.com/patent/US9214882B2/en?oq=US+9.214%2c882+B2 (visited on 01/14/2019).

[Pau14] D. Paulus, "Beliebige Injektion für permanent erregte Synchronmaschinen," Dr.-Ing. dissertation, Technische Universität München, Munich, Germany, Sep. 2014.

[PLK11] D. Paulus, P. Landsmann, and R. Kennel, "Sensorless field- oriented control for permanent magnet synchronous machines with an arbitrary injection scheme and direct angle calculation," in *2011 Symposium on Sensorless Control for Electrical Drives*, Birmingham, UK, Sep. 2011, pp. 41–46. DOI: 10.1109/SLED.2011.6051543.

[PLK12] D. Paulus, P. Landsmann, and R. Kennel, "Saliency based sensorless field- oriented control for permanent magnet synchronous machines in the whole speed range," in *3rd IEEE International Symposium on Sensorless Control for Electrical Drives (SLED 2012)*, Milwaukee, WI, USA, Sep. 2012, pp. 1–6. DOI: 10.1109/SLED.2012.6422802.

[PLKK13] D. Paulus, P. Landsmann, S. Kuehl, and R. Kennel, "Arbitrary injection for permanent magnet synchronous machines with multiple saliencies," in *2013 IEEE Energy Conversion Congress and Exposition*, Denver, CO, USA, Sep. 2013, pp. 511–517. DOI: 10.1109/ECCE.2013.6646744.

[PSB03] V. Petrovic, A. M. Stankovic, and V. Blasko, "Position estimation in salient PM synchronous motors based on PWM excitation transients," *IEEE Transactions on Industry Applications*, vol. 39, no. 3, pp. 835–843, May 2003. DOI: 10.1109/TIA.2003.811776.

[RS04] E. Robeischl and M. Schroedl, "Optimized INFORM measurement sequence for sensorless PM synchronous motor drives with respect to minimum current distortion," *IEEE Transactions on Industry Applications*, vol. 40, no. 2, pp. 591–598, Mar. 2004. DOI: 10.1109/TIA.2004.824510.

[Sch15] D. Schröder, *Elektrische Antriebe—Regelung von Antriebssystemen*, 4th ed. Berlin, Germany: Springer Vieweg, 2015, ISBN: 978-3-642-30096-7.

[Sch88] M. Schrödl, "Detection of the rotor position of a permanent magnet synchronous machine at standstill," presented at the Int. Conf. on Electrical Machines (ICEM), Pisa, Italy, 1988, pp. 195–197.

[Sch96] M. Schroedl, "Sensorless control of AC machines at low speed and standstill based on the INFORM method," in *IAS '96. Conference Record of the 1996 IEEE Industry Applications Conference Thirty-First IAS Annual Meeting*, vol. 2, San Diego, CA, USA: Institute of Electrical and Electronics Engineers, Oct. 1996, pp. 270–277. DOI: 10.1109/IAS.1996.557028.

[SEP13] M. Seilmeier, S. Ebersberger, and B. Piepenbreier, "PMSM model for sensorless control considering saturation induced secondary saliencies," in *2013 IEEE International Symposium on Sensorless Control for Electrical Drives and Predictive Control of Electrical Drives and Power Electronics (SLED/PRECEDE)*, ISSN: 2166-6733, Munich, Germany, Oct. 2013, pp. 1–8. DOI: 10.1109/SLED-PRECEDE.2013.6684519.

[SGN19] K. Schuhmacher, E. Grasso, and M. Nienhaus, "Improved rotor position determination for a sensorless star-connected PMSM drive using Direct Flux Control," *The Journal of Engineering*, vol. 2019, no. 17, pp. 3749–3753, 2019. DOI: 10.1049/joe.2018.8055.

[SKMN21] K. Schuhmacher, S. Kleen, C. May, and M. Nienhaus, "Modulation strategies for anisotropy-based position estimation of PMSMs using the neutral point voltage," *IEEE Access*, vol. 9, pp. 68 445–68 460, May 2021. DOI: 10.1109/ACCESS.2021.3077695.

[SKN19] K. Schuhmacher, S. Kleen, and M. Nienhaus, "Comparison of anisotropy signals for sensorless control of star-connected PMSMs," in *2019 IEEE 10th International Symposium on Sensorless Control for Electrical Drives (SLED)*, Turin, Italy, Sep. 2019, pp. 1–6. DOI: 10.1109/SLED.2019.8896351.

[Str19] R. Strothmann, "Device and method for determining the rotational position of a rotor in an electric machine," European pat. 1961107 (B1), Oct. 2019. [Online]. Available: https://worldwide.espacenet.com/publicationDetails/biblio?FT=D&date=20191016&DB=&locale=de_EP&CC=EP&NR=1961107B1&KC=B1&ND=5 (visited on 11/22/2019).

[TMH+11a] P. Thiemann *et al.*, "New sensorless rotor position detection technique of PMSM based on direct flux control," in *International Conference on Power Engineering, Energy and Electrical Drives (POWERENG), 2011*, J. A. Aguado, Ed., Malaga, Spain, May 2011, pp. 1–6. DOI: 10.1109/PowerEng.2011.6036516.

[TMH+11b] P. Thiemann *et al.*, "PMSM sensorless rotor position detection for all speeds by direct flux control," in *IEEE International Symposium on Industrial Electronics (ISIE), 2011*, Gdansk, Poland, Jun. 2011, pp. 673–678. DOI: 10.1109/ISIE.2011.5984238.

[TMM+12] P. Thiemann, C. Mantala, T. Mueller, R. Strothmann, and E. Zhou, "PMSM sensorless control with direct flux control for all speeds," in *2012 IEEE Symposium on Sensorless Control for Electrical Drives*, Milwaukee, WI, USA, Sep. 2012, pp. 1–6. DOI: 10.1109/SLED.2012.6422812.

[TZP+18] M. Tanaskovic, C. Zhao, F. Percacci, P. Gnos, S. Mariethoz, and D. Frick, "Rotor polarity detection and tracking for slotless permanent magnet synchronous motors," in *2018 IEEE 9th International Symposium on Sensorless Control for Electrical Drives (SLED)*, Helsinki, Finland, Sep. 2018, pp. 102–107. DOI: 10.1109/SLED.2018.8486065.

[VCC+00] A. Vagati, A. Canova, M. Chiampi, M. Pastorelli, and M. Repetto, "Design refinement of synchronous reluctance motors through finite-element analysis," *IEEE Transactions on Industry Applications*, vol. 36, no. 4, pp. 1094–1102, Jul. 2000, Conference Name: IEEE Transactions on Industry Applications. DOI: 10.1109/28.855965.

[Wer18] T. Werner, *Geberlose Rotorlagebestimmung in elektrischen Maschinen*. Wiesbaden, Germany: Springer Fachmedien Wiesbaden, 2018, (also Dr.-Ing. dissertation, Gottfried Wilhelm Leibniz Universität Hannover, Hannover, Germany), ISBN: 978-3-658-22271-0. DOI: 10.1007/978-3-658-22271-0.

[Wik21] Wikipedia contributors, *Non-uniform discrete Fourier transform*, in *Wikipedia, The Free Encyclopedia*, Jul. 22, 2021. [Online]. Available: https://en.wikipedia.org/w/index.php?title=Non-uniform_discrete_Fourier_transform&oldid=1034819158 (visited on 08/22/2021).

[WVS19] G. Wang, M. Valla, and J. Solsona, "Position sensorless permanent magnet synchronous machine drives—a review," *IEEE Transactions on Industrial Electronics*, vol. 67, no. 7, pp. 5830–5842, Nov. 2019. DOI: 10.1109/TIE.2019.2955409.

[XZ16a] P. L. Xu and Z. Q. Zhu, "Novel carrier signal injection method using zero-sequence voltage for sensorless control of PMSM drives," *IEEE Transactions on Industrial Electronics*, vol. 63, no. 4, pp. 2053–2061, Apr. 2016. DOI: 10.1109/TIE.2015.2506146.

[XZ16b] P. L. Xu and Z. Q. Zhu, "Novel square-wave signal injection method using zero-sequence voltage for sensorless control of PMSM drives," *IEEE Transactions on Industrial Electronics*, vol. 63, no. 12, pp. 7444–7454, Dec. 2016. DOI: 10.1109/TIE.2016.2593657.

[XZ17] P. Xu and Z. Q. Zhu, "Initial rotor position estimation using zero-sequence carrier voltage for permanent-magnet synchronous machines," *IEEE Transactions on Industrial Electronics*, vol. 64, no. 1, pp. 149–158, Jan. 2017. DOI: 10.1109/TIE.2016.2596703.